Alma Mater Studiorum – Università di Bologna

DOTTORATO DI RICERCA IN

GEOFISICA

Ciclo 32

Settore Concorsuale: 04/A4 - GEOFISICA

Settore Scientifico Disciplinare: GEO/12 - OCEANOGRAFIA E FISICA DELL'ATMOSFERA

TOWARDS A BROADER UNDERSTANDING OF THE EFFECTS OF TIDAL
FORCING ON THE GLOBAL OCEAN CIRCULATION

Presentata da: Federica Borile

Coordinatore Dottorato

Nadia Pinardi

Supervisore

Simona Masina

Co-Supervisori

Doroteaciro Iovino

Nadia Pinardi

Paola Cessi

Esame finale anno 2022

Acknowledgments

Firs of all, I would like to express my sincere gratitude to my supervisors, who supported me throughout the journey of this Ph.D.. I would like to thank dott. Simona Masina and dott. Dorotea Iovino for their expertise, constant encouragements and patience in answering all my doubts. I'm also very grateful to prof. Nadia Pinardi and prof. Paola Cessi for teaching me how details make the difference in a good job and pushing me towards new goals. They all four shared their huge knowledge of Oceanography with me, making constructive comments and suggestions to improve my work.

I'm extremely grateful to my husband Luca, who encouraged, supported and picked me up so many times in this long Ph.D. marathon. He always believed in me and listened calmly to all my research hurdles, being my personal "ironman".

Special thanks to my sons Giosue', Samuele and who will come, because they are my big source of energy, inspiration (desperation), happiness and curiosity. They made this journey more challenge and the studying time more precious.

I'm grateful to all my big family, from the youngest to the eldest member, because they encouraged me day by day. I would like to thank especially my mum because she helped me the best, being next to me regardless of the physical distance.

A special gratitude to my friend Chiara, who always brings a smile into our home. She joined our family in small steps and gave me the huge opportunity to build my personal and professional life at the same time.

My sincere thanks also to the colleagues of the CMCC Foundation and the other Ph.D. students, who shared this experience with me and made my research more fun.

Finally, I'm grateful to prof. Steve Shore, because at the beginning of my scientific career he taught me the importance of Curiosity, regardless of the topic. His questions were precious to let me understand who I wanted to become.

Abstract

The study of tides and their interactions with the complex dynamics of the global ocean represents a crucial and important challenge in ocean modelling. This thesis aims to deepen the study of tides from a dynamical point of view, analysing what are their effects on the general circulation of the ocean. We perform different experiments of a mesoscale-permitting global ocean model forced by both atmospheric fields and astronomical tidal potential, including a broad spectrum of 11 tidal constituents. Given the importance of internal tides in the energy distribution of the open ocean, we implement a topographic wave drag into the barotropic momentum equation to include a dissipative term for internal tides. The parametrization follows the formulation proposed by Shakespeare et al. (2020) for a locally dissipating wave motion at the semidiurnal frequency and is based on the computation of unresolved roughness and bottom water stratification. Moreover, we include a parametrization to simulate the gravitational self-attraction and earth-loading effects induced by ocean tides, and we modify the bottom friction numerical formulation to improve its coherency with the analytical definition.

On the global scale, the modelled tidal solutions are compared with TPXO global tidal model atlases. At regional scales, instead, we select two regions of interest to assess the model accuracy with a set of tide gauges data: the North-West Atlantic Ocean and the Indonesian region. After a preliminary phase of model assessment, we study the impact of tides in the general circulation of the ocean focusing on the Atlantic basin. We compute the meridional streamfunction in different experiments with and without tidal forcing and we find that tides weaken the overturning circulation during the analysed period from 1981 to 2007, even though the interannual differences strongly change in both amplitude and phase. Furthermore, the reduction is even stronger in the tidal experiment with the topographic wave drag, suggesting that internal tides contribute to the overturning strength.

The zonally integrated momentum balance shows that the presence of tides changes the water stratification at the zonal boundaries of the domain, modifying the pressure and therefore the geostrophic balance over the entire basin. Since the overturning circulation is geostrophically balanced, we identify the diapycnal tidal processes as the main drivers of the overturning weakening.

Moreover, we perform an additional experiment using a mesoscale-resolving configuration forced by tides, and we compare the simulated tides both with the previous simulations and observed data. The increased resolution allows to resolve more intense internal tides both at

the diurnal and semidiurnal frequencies. Nevertheless, the accuracy of modelled tidal amplitude strongly depends on the region of interest and the considered harmonic component.

Finally, we describe the overturning circulation in the Mediterranean Sea computing the meridional and zonal streamfunction both in the traditional, Eulerian, and residual frameworks. The circulation is characterised by different cells, and their forcing processes are described with particular emphasis to the role of mesoscale and a transient climatic event. We complete the description of the overturning circulation giving evidence for the first time to the connection between meridional and zonal cells.

Contents

Chapter 1

Introduction

Ocean tides are the periodic movement of water masses caused by the gravitational attraction of the Moon and the Sun over the Earth system. The overall response to the tide-generating forces takes the form of waves travelling across the ocean, called *tidal components*, which are characterised by a set of harmonic constants.Tides are then classified according to their cyclical period: components with one or two cycles per day, called *diurnal* or *semidiurnal*, have typically the largest amplitudes, while components with period longer than one day, called *long period*, are smaller.

The tidal phenomenon has been documented and studied for centuries with in situ observations on tide gauges stations (Cartwright, 1999), but only during the last three decades an accurate mapping of the tidal elevations has become possible thanks to the acquisition of satellite altimeter data (Le Provost et al., 1995). Therefore, tides are now simulated at global scale, both by numerical barotropic models (Egbert and Erofeeva, 2002; Lyard et al., 2021) and hydrodynamical general circulation models (Arbic et al., 2010; Müller et al., 2010; Rocha et al., 2016; Madec and the NEMO team, 2016). The barotropic tidal contribution to the ocean circulation is derived by solving the Laplace's tidal equations (Laplace, 1776):

$$
\begin{aligned}
\frac{\partial \boldsymbol{u}}{\partial t} &= -f\hat{\boldsymbol{k}} \times \boldsymbol{u} - g\nabla\left(\eta + \eta_{eq}\right) \\
\frac{\partial \eta}{\partial t} &= -\nabla(H\boldsymbol{u})
\end{aligned}
\tag{1.1}
$$

where $\boldsymbol{u} = (u, v)$ is the horizontal velocity field, t is the time, f is the Coriolis parameter, g is the gravitational acceleration, H is the ocean depth, η is the sea surface elevation and η_{eq} is the sea level equilibrium height. In particular, the variable η_{eq} represents the tidal forcing function (Schureman, 1958) and is defined by a linear superposition of tidal waves.

Each wave is defined by frequency ω, amplitude A and phase χ, forming the overall forcing

$$
\begin{aligned}
\eta_{eq}(\lambda, \phi, t) = {} & \cos^2 \phi \sum_i A_i \cos\left(\omega_i t + \chi_i + 2\lambda\right) \\
& + \sin 2\phi \sum_j A_j \cos\left(\omega_j t + \chi_j + \lambda\right) \\
& + (1 - 3\sin^2 \phi) \sum_k A_k \cos\left(\omega_k t + \chi_k\right)
\end{aligned}
\tag{1.2}
$$

where (λ, ϕ) are the geographical coordinates and (i, j, k) are the indexes referred respectively to semidiurnal, diurnal and long period tides.

Despite the simple formulation of the forcing, simulating the tidal phenomena in a well definite place is very challenging since each harmonic changes strongly in space, especially in shallow waters and coastal regions with complex coastlines and steep bathymetry (Aiken, 2008; Reef et al., 2020). The grid spacing size is one of the main sources of error in tidal numerical models at the global scale, and the simpler method to minimise the biases is to increase the spatial resolution. Other sources of error come from the unresolved tidally-induced phenomena, such as the formation of baroclinic tides, the self-attraction of the ocean, the earth-loading effect, the interaction of tides with bottom topography or the observed enhanced mixing (Arbic, 2021). In the present work we use a purely hydrodynamical global ocean model to analyse tides, comparing two configurations with different spatial resolutions and using the coarser one to implement two tidal parametrizations.

1.1 Internal tides in the ocean

In the absence of bottom topography, tides propagate in the ocean as a periodic and purely barotropic motion, but when they flow over topographic features they perturb the background flow and lose a portion of their energy. A first part of energy is directly lost through local dissipation and mixing, while another part is converted into baroclinic energy generating motion at smaller horizontal scales, such as bottom turbulence, hydraulic effects (Winters and Armi, 2014) or internal waves (Garrett and Kunze, 2007; Falahat and Nycander, 2015). These waves are called *internal tides* since they are a special example of internal gravity waves, as perturbations on a stratified fluid with a gravitational restoring force at the tidal frequency (Bell, 1975). These motions are observed in several open ocean areas and are mainly associated with three types of topography, corresponding to: oceanic islands, oceanic trenches and mid-ocean ridges (Egbert and Ray, 2000; Garrett and Kunze, 2007). All the structures have in common slopes that vary over a wide range of spatial scales and, in turn, generate internal tides at different scales:

- small-scale waves are associated with high vertical modes and tend to dissipate near the generation site breaking into turbulence. St. Laurent and Garrett (2002) estimates that around 1/3 of the generated energy flux contributes to the local mixing through the breaking of this class of tides, and the driving processes are mainly shear instability, wave-wave

interaction, or topographic scattering (Lueck and Mudge, 1997; Thorpe, 2001; Nikurashin and Legg, 2011). An example has been detected in the abyssal Brazil Basin, where mixing rates are enhanced over rough topography and modulate at spring-neap tidal frequency (Ledwell et al., 2000);

- large-scale waves are associated with low vertical modes that radiate over hundreds or thousands of kilometers far from the generation site before dissipating (Dushaw et al., 1995). The induced mixing is due to mechanisms like wave-wave interaction, scattering by abyssal hills or dissipation at critical slopes (Bühler and Holmes-Cerfon, 2011; Legg, 2014). Waves like these sometimes reach the shelf, where the slope scatter or amplify them as they propagate toward shallower water. Typical examples are propagating waves from the Hawaiian Ridge (Zhao et al., 2010).
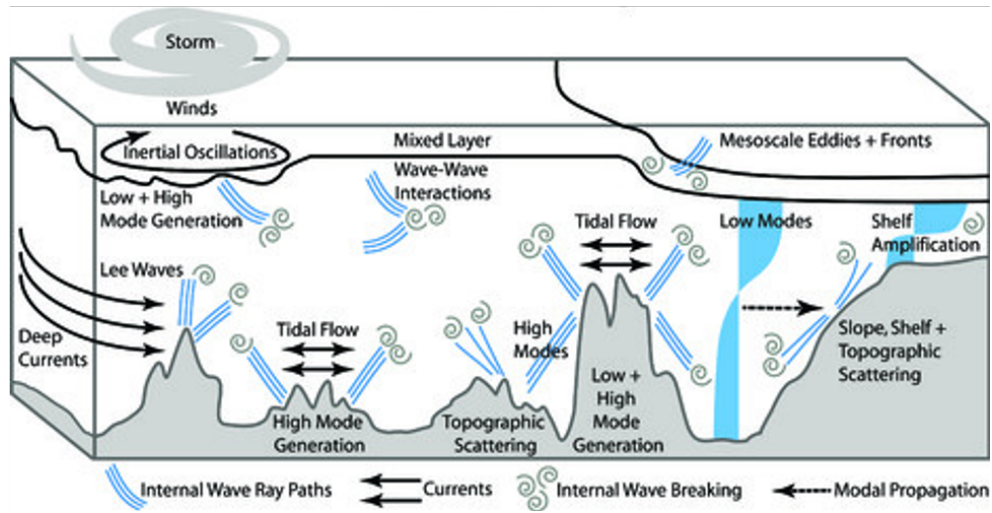
Figure 1.1: Schematic of internal wave mixing processes in the open ocean. Reproduced from MacKinnon et al. (2017).

Figure 1.1 summarises the complex system of internal waves mixing processes occurring in the open ocean and Arbic (2021) proposed a detailed review about their simulation within ocean general circulation models. Indeed, since the presence of mixing processes is relevant for the whole dynamical system, many efforts have been made to reproduce them in numerical models.

Regional models are particularly useful to study the generation and early propagation of internal tides at high resolution (Carter et al., 2012), whereas multi-scale processes are difficult to resolve on a global domain, where the resolution is typically lower. Current state-of-the-art global ocean models reproduce only the mixing processes related to lower-mode waves, leaving the rest to be parametrised as an explicit damping of internal tides energy (Arbic et al., 2010). To reach this target, many parametrizations have been proposed following two possible approaches: the former one parametrises the unresolved topographic stress that causes internal tides (Jayne and St. Laurent, 2001; Arbic et al., 2004; Egbert et al., 2004; Garner, 2004; Zaron and Egbert, 2006; Green and Nycander, 2013; Shakespeare et al., 2020), while the latter one includes the unresolved mixing processes (Melet et al., 2016; de Lavergne et al., 2020).

In this thesis we assessed the accuracy of simulated tides in an eddy-permitting global general circulation model and we implemented a topographic wave drag and self-attraction and loading parametrization, analysing their impact on the modelled sea surface height and global kinetic energy.

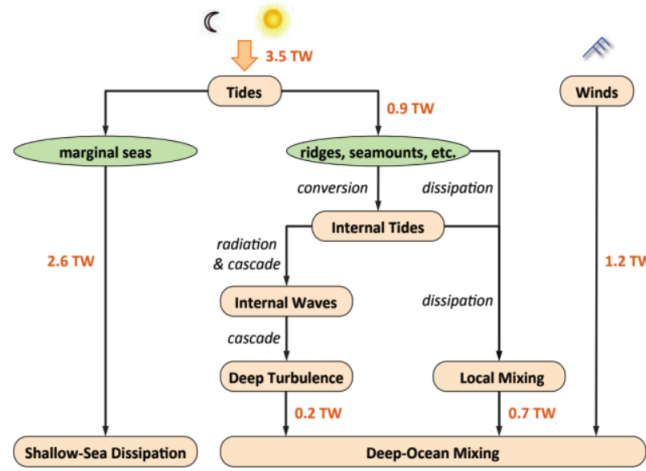## 1.2 Tidal energy distribution and large scale circulation

Figure 1.2: Global energy flux budget based on Munk and Wunsch (1998). Reproduced from Kang (2012).

From the energetic point of view, tides are a source of barotropic energy for the global ocean and their contribution has been quantified with near-astronomical accuracy to 3.5 TW (Munk and Wunsch, 1998). Most of the energy is lost in shallow seas and on the continental shelf, where tidal currents are stronger and therefore increase the bottom friction (Kantha, 1995; Munk, 1997; Lyard et al., 2021). The remaining part (25-30% of the total) is dissipated in the deep ocean through the interaction processes described above (Egbert and Ray, 2000).

Figure 1.2 summarises the energy flux budget computed by Munk and Wunsch (1998), where the cascade of tidal energy from larger to smaller scales involves the interaction between internal tides and background flow, composed by mean currents and mesoscale structures. The reciprocal effect that internal tides have on mesoscale eddies or fronts was extensively analysed during the last decades (Chavanne et al., 2010; Callendar et al., 2011; Dunphy and Lamb, 2014; Jensen et al., 2018). Likewise, many studies described how the mean flow modifies the propagation of baroclinic tides, modifying their wavelength or blocking their coastward propagation (Pereira et al., 2007; Kelly and Lermusiaux, 2016; Dossmann et al., 2020). On the other hand, only few studies focused on the impact of tidal waves on the mean flow, and they are mainly limited to coastal areas (Xuan et al., 2016) or near abyssal hills (Shakespeare and Hogg, 2019).

Regardless of the interaction processes, a description of the role of tides in the general circulation of the ocean is still lacking. Indeed, barotropic and baroclinic tides have all the characteristics to efficiently contribute to the general circulation: they propagate over large distances across the ocean, interact with topography and other dynamical structures at the mesoscale, and finally

change the water properties through diapycnal mixing at local scales. Similarly, the global ocean circulation is described by overturning cells that are sensitive, in intensity and pathway, to wind-driven upwelling in the Southern Ocean (looking at regional scales) as well as deep water formation in the Labrador and Nordic Seas (as a local scale process). Kuhlbrodt et al. (2007) proposed an extensive review of the processes driving the overturning circulation, completing the above list with internal waves propagation and heat and freshwater fluxes at the surface.

Since tidal propagation and dissipation processes are suitable to affect the overturning, we focused our analysis on the circulation of the Atlantic Ocean, especially in the northern part of the basin, where internal tides are extensively documented.

Given the importance of the overturning circulation in the climate system, we analyzed it also in a regional basin, as the Mediterranean Sea. In this thesis we described the zonal and meridional overturning cells that characterise the basin computing the streamfunctions both in the classical, Eulerian, and in the residual frameworks (Andrews et al., 1987; Marshall and Radko, 2003). The concept of residual zonal (meridional) circulation has never been applied in this region and adds to the mean flow the contribution of dynamical structures with zero time or meridional (zonal) averages but nonzero fluxes, leading to a more inclusive representation of the transports across the basin.

1.3   Thesis objectives

To address the above mentioned issues we used different configurations of the NEMO model with and without tidal forcing, stressing the attention on the role of internal tides. The scientific question that we investigate is then formalised as follow:

what are the effects of tidal forcing on the global general circulation?

However, before digging into the study of the tides, the thesis started with a different question:

what is the overturning circulation in a marginal sea?

Both questions require to investigate the behavior of the ocean at large scale, and in order to provide answers we have considered the effects of dynamical processes at smaller temporal and spatial scales: the internal tides in the Atlantic Ocean and the mesoscale features in the Mediterranean Sea.

The specific objectives of the chapters are:

Chapter 2

- to assess the accuracy of tides in an eddy-permitting configuration of the NEMO global ocean model, validating the results in two regions of interest;

- to implement a parametrization to include the self-attraction and loading effects induced by barotropic tides;

- to implement a new parametrization and modify the numerical formulation of the bottom friction to include the dissipation of internal tides over unresolved rough topography;

Chapter 3

- to evaluate the impact of tidal forcing on the Atlantic meridional overturning circulation;

- to analyse the zonally integrated momentum balance in the Atlantic Ocean, focusing on the interaction between internal tides and mesoscale structures;

Chapter 4

- to describe the overturning circulation in the Mediterranean Sea in both the Eulerian and the residual frameworks;

- to illustrate the fundamental forcing which drives the overturning circulation in the basin;

Chapter 5

- to assess the accuracy of tides in an eddy-resolving configuration of the NEMO global ocean model, comparing the results to the eddy-permitting configuration.

Chapter 2

The implementation of tidal parametrizations in NEMO

When tides are implemented in a baroclinic ocean model the entire water column is forced by a source of energy that contributes to the ocean circulation. In the present chapter we analyse the simulation of barotropic and baroclinic tides in a global eddy-permitting configuration of the NEMO ocean model with $1/4°$ horizontal resolution. Following the method proposed by Shakespeare et al. (2020), we describe the implementation of a new parametrization to dissipate tidal energy over unresolved bathymetry, and we analyse the results comparing the modelled sea surface height (SSH) with observed data from tide gauges and the TPXO data-constrained barotropic tidal model. The same approach is proposed to analyse a second parametrization, describing the self-attraction and earth-loading effects induced by ocean tides using the formulation proposed by Accad and Pekeris (1978).

2.1 Theoretical framework

2.1.1 Global ocean simulations with tides

During the last decades, observed data have demonstrated that tides are fundamental to understand and properly simulate both the sea surface oscillations and the interior mixing of the ocean (Munk and Wunsch, 1998; Egbert and Ray, 2000; Wunsch and Ferrari, 2004). Unlike other forcings such as wind stress or buoyancy exchange with the atmosphere, the spatial and temporal structures of the tidal forcing is reproducible with high accuracy according to the simple relation between the astronomical potential, Π^A, and the generated sea surface displacement

$$\Pi^A(\boldsymbol{x}, t) = -g\, \eta_{eq}(\boldsymbol{x}, t) \tag{2.1}$$

where g is the gravitational acceleration and η_{eq} is the so called *equilibrium tide* defined in (1.2). Nevertheless, while the tidal input of energy is widely used in numerical ocean models through the implementation of (2.1) in the momentum equation, the issue about how and where tides are dissipated is still a debated topic. An overview of the mechanisms that produce energy conversion

from the barotropic to the baroclinic modes is proposed in Section 1.1, and a complete review is provided by Arbic (2021).

Egbert and Ray (2000) demonstrated that barotropic tides lose energy over topographic features at rates that are inconsistent with the simulated tides, thus barotropic tidal models need an additional energy conversion term to properly reproduce data near rough topography. The tidally induced stress $\boldsymbol{\tau}^{tide}$ is found to be proportional to the tidal velocity and differs from the traditional bottom friction $\boldsymbol{\tau}_b$

$$\boldsymbol{\tau}_b = \rho_0 \, C_d \, |\boldsymbol{u}_{-H}| \cdot \boldsymbol{u}_{-H} \tag{2.2}$$

$$\boldsymbol{\tau}^{tide} = \rho_0 \, \mathbb{C} \cdot \boldsymbol{u}^{tide} \tag{2.3}$$

where ρ_0 is the reference density, C_d is the dimensionless bottom drag coefficient derived from the law of the wall (Von Karman, 1931), $\boldsymbol{u}_{-H}$ is the bottom velocity, $\mathbb{C}$ is the internal wave drag tensor dependent on topography and stratification, and $\boldsymbol{u}^{tide}$ is the barotropic tidal velocity.

Many authors have proposed formulations of $\boldsymbol{\tau}^{tide}$ (Jayne and St. Laurent, 2001; Arbic et al., 2004; Egbert et al., 2004; Garner, 2004; Zaron and Egbert, 2006; Schiller and Fiedler, 2007; Arbic et al., 2010; Green and Nycander, 2013; Shakespeare et al., 2020), and hereafter we summarize those that contributed the most to the present work.

Jayne and St. Laurent (2001) included a parametrization for internal wave drag over rough topography for a hydrodynamic barotropic tidal model. Their work is based on a scaling relation of the energy flux lost by barotropic tides following the analogous atmospheric phenomenon of "orographic drag" (Palmer et al., 1986). They added a dissipative term to the classical bottom friction (2.2)

$$\boldsymbol{\tau}^{tide} = \rho_0 \frac{\pi}{L} h^2 N \overline{\boldsymbol{u}} \tag{2.4}$$

where (L, h) are the typical bathymetric wavelength and amplitude, N is the Brünt-Väisälä frequency, and $\overline{\boldsymbol{u}}$ is the barotropic velocity. The parametrization is only used in regions deeper than 100 m, and L is tuned to minimise the misfit between the modelled elevations and those of data-constrained models. They found that a wavelength of 10 km makes the global dissipation in the deep ocean in close agreement with the measured value of 1 TW (Egbert and Ray, 2000). It is worth noting that, even though this formulation is based on a simple scale relation, it is the most used by numerical tidal models.

Arbic et al. (2004) showed that the accuracy of simulated surface tides depends on the parametrized dissipation and proposed a topographic drag parametrization for a baroclinic two-layer tidal model. They tried to limit the tidal dissipation only to the bottom stress induced by friction in (2.2) and demonstrated that only physically implausible values of C_d of $\mathcal{O}(10^{-1})$ produce consistent tidal elevations.

A topographic drag was then implemented following Garner (2004), that developed a parametrization for quasi-steady background flows in the atmosphere and then extended it to the oscillatory case relevant for tides. The formulation proposed by Arbic et al. (2004) is applied in regions

deeper than 1000 m where a tensor $\chi(\boldsymbol{x})$ is defined as

$$\chi(\boldsymbol{x}) = -N \frac{\sqrt{\omega^2 - f^2}}{\omega} \iint \frac{\hat{h}(\boldsymbol{k})}{|\boldsymbol{k}|} e^{(i\boldsymbol{k}\cdot\boldsymbol{x})}\, dk\, dl \tag{2.5}$$

with ω the tidal frequency, $\hat{h}$ the topography roughness in the Fourier domain and $\boldsymbol{k} = (k, l)$ the correspondent horizontal wavenumbers. The implemented topographic drag is then

$$\boldsymbol{\tau}^{tide} = \lambda \left[\overline{\rho}\, \nabla\chi \left(\nabla h\right)^T \right] \boldsymbol{u}_2 \tag{2.6}$$

where $\overline{\rho}$ is the mean density, $\boldsymbol{u}_2$ is the velocity of the second (bottom) layer of the model, and λ is a tunable factor to obtain optimal tidal elevations. An important innovation in (2.6) compared to (2.4) is that here the wave drag intensity depends on the tidal frequency of interest.

Trying to simplify the formulation, **Arbic et al. (2010)** replaced the tensor with a scalar, variable in space according to energy considerations from the previous study. In this case, the topographic drag is applied just to the tidal flow where the tidal waves decay time is shorter than 30 days, and an implicit linear stress formulation is used in the total momentum equation over the bottom 500 m of the water column

$$\boldsymbol{\tau}^{tide} = \lambda\, r \left(\boldsymbol{u} - \widetilde{\boldsymbol{u}}_{-H} \right) \tag{2.7}$$

where r is the scalar drag coefficient variable in space with dimensions of $(\text{kg/m}^2\text{s})$, and $\widetilde{\boldsymbol{u}}_{-H}$ is the detided bottom flow.

Shakespeare et al. (2020) analysed the tidal bottom drag generated by different types of waves in a baroclinic tidal model. The authors pointed out that baroclinic tidal waves could stress the barotropic flow with mechanisms that do not induce dissipation. Looking at regional domains, they deduced a complex scalar coefficient of stress

$$r^* = \frac{1}{4\pi A} \int_0^{+\infty} |\hat{h}(K)|^2 \frac{K^2}{|\omega|} \sqrt{(N^2 - \omega^2)(\omega^2 - f^2)} \coth(imH + \gamma H)\, dK \quad . \tag{2.8}$$

where A is the area of interest, $\hat{h}$ is the topographic roughness in the Fourier space with (K, m) horizontal and vertical wavenumbers, and γ is a decay-weighted vertical wavenumber.
This topographic wave stress has therefore a very general formulation to parametrise different tidal waves according to their frequency, vertical mode and decay time, together with local roughness and water stratification. The momentum exchange between mean and tidal flows is then

$$\boldsymbol{\tau}^{tide} = \rho_0\, r^*\, \overline{\boldsymbol{u}}_{tide} \tag{2.9}$$

where $\overline{\boldsymbol{u}}_{tide}$ is the barotropic tidal velocity (more details of the scheme demonstration are provided in Appendix A). We found this work as the most inclusive to parametrise different types of interactions between rough topography and barotropic oscillating flows, thus we selected it to be implemented in the NEMO model. It impacts the barotropic momentum equation, and we now analyse which terms are involved from the analytical point of view.

2.1.2 Analytical barotropic momentum

The horizontal momentum equation is now considered with the aim to study the tidal effect on the ocean circulation from the analytical point of view. We focused the attention on the vertically integrated equation and its boundary terms in order to recall how the tidal flow interacts with the bottom of the ocean.

Here we propose the horizontal momentum equation and its boundary conditions at the ocean surface, $\eta(\boldsymbol{x}, t)$, and solid bottom, $-H(\boldsymbol{x})$, with the addition of the tidal forcing (2.1)

$$\frac{\partial \boldsymbol{u}}{\partial t} = -f \hat{\boldsymbol{k}} \times \boldsymbol{u} + \nabla \Pi^A - \frac{1}{\rho_0} \nabla p + \frac{1}{\rho_0} \frac{\partial}{\partial z} \left(A_v \frac{\partial \boldsymbol{u}}{\partial z} \right) + \boldsymbol{\mathcal{A}} \qquad (2.10\text{a})$$

$$A_v \frac{\partial \boldsymbol{u}}{\partial z} \bigg|_{\eta} = \boldsymbol{\tau}_w \qquad (2.10\text{b})$$

$$A_v \frac{\partial \boldsymbol{u}}{\partial z} \bigg|_{-H} = \boldsymbol{\tau}_b \qquad (2.10\text{c})$$

where p is the total pressure, A_v the vertical eddy viscosity, $\boldsymbol{\mathcal{A}}$ summarises advection and lateral viscosity terms, $\boldsymbol{\tau}_w$ represents the wind stress at the surface and $\boldsymbol{\tau}_b$ the bottom stress.

When the vertical integral is applied between the bottom and the surface of the ocean, the kinematic boundary conditions (2.10b-c) are used to write

$$\int_{-H}^{\eta} \frac{\partial \boldsymbol{u}}{\partial t} \, dz = -f \hat{\boldsymbol{k}} \times \int_{-H}^{\eta} \boldsymbol{u} \, dz + (H + \eta) \nabla \Pi^A - \frac{1}{\rho_0} \int_{-H}^{\eta} \nabla p \, dz + \frac{1}{\rho_0} (\boldsymbol{\tau}_w - \boldsymbol{\tau}_b) + \int_{-H}^{\eta} \boldsymbol{\mathcal{A}} \, dz \quad (2.11)$$

or its equivalent formulation

$$\int_{-H}^{\eta} \frac{\partial}{\partial t} (\overline{\boldsymbol{u}} + \boldsymbol{u}') \, dz = -(H + \eta) f \hat{\boldsymbol{k}} \times \overline{\boldsymbol{u}} + (H + \eta) \nabla \Pi^A - \frac{1}{\rho_0} \int_{-H}^{\eta} \nabla p \, dz + \frac{1}{\rho_0} (\boldsymbol{\tau}_w - \boldsymbol{\tau}_b) + \int_{-H}^{\eta} \boldsymbol{\mathcal{A}} \, dz$$
$$(2.12)$$

where the horizontal velocity has been decomposed into its barotropic and baroclinic components

$$\boldsymbol{u} = \overline{\boldsymbol{u}} + \boldsymbol{u}' \quad \text{and the former is given by} \quad \overline{\boldsymbol{u}} = \frac{1}{H + \eta} \int_{-H}^{\eta} \boldsymbol{u} \, dz \quad . \qquad (2.13)$$

Equation (2.12) shows that the tidal forcing term is applied to the entire water column. This information is hidden inside the depth integrated terms that are now further analysed:

- the integrated term on the left of (2.12) can be decomposed according to the Leibniz integration rule as

$$\int_{-H}^{\eta} \frac{\partial}{\partial t} (\overline{\boldsymbol{u}} + \boldsymbol{u}') \, dz = \frac{\partial}{\partial t} [(H + \eta) \overline{\boldsymbol{u}}] - (\overline{\boldsymbol{u}} + \boldsymbol{u}'_\eta) \frac{\partial \eta}{\partial t} \qquad (2.14)$$

  where the last term refers to the SSH variability. This term is usually small and therefore neglected in numerical ocean models, but this assumption is not valid in shallow water regions with high tidal amplitude (Haley and Lermusiaux, 2010), or where baroclinic tides reach the sea surface (Ray and Mitchum, 1996; Lahaye et al., 2019). We plan to further analyse its contribution on the momentum balance in future research projects;

- the first integrated term on the right of (2.12) represents the pressure contribution to the barotropic momentum. The total pressure can be decomposed in three different terms

$$p(\boldsymbol{x}, z, t) = p_a(\boldsymbol{x}, t) + \rho_0 g(\eta - z) + p'(\boldsymbol{x}, z, t) \tag{2.15}$$

where the first term describes the atmospheric pressure applied to the ocean as a boundary condition, the second one the hydrostatic pressure and the last term represents the dynamical pressure which is defined as

$$p'(\boldsymbol{x}, z, t) \equiv g \int_z^0 \left[\rho(\boldsymbol{x}, z', t) - \rho_0 \right] dz' \qquad . \tag{2.16}$$

The pressure term in (2.12) can be then decomposed as

$$-\frac{1}{\rho_0} \int_{-H}^{\eta} \nabla p \, dz = -\frac{1}{\rho_0}(H + \eta)\nabla p_a - g(H + \eta)\nabla\eta - \frac{1}{\rho_0} \int_{-H}^{\eta} \nabla p' \, dz \tag{2.17}$$

and the integrated dynamical pressure component can be further decomposed as

$$-\frac{1}{\rho_0} \int_{-H}^{\eta} \nabla p' \, dz = -\frac{1}{\rho_0} \nabla \int_{-H}^{\eta} p' \, dz + \frac{1}{\rho_0} p'_{-H} \nabla H \tag{2.18}$$

where the term p'_η is neglected according to p' definition.

In this case $p'_{-H}\nabla H$ represents a bottom boundary term and physically describes the interaction between the bottom dynamical pressure and rough topography (Bell, 1975). In a stably stratified fluid, the oscillation of pressure over bathymetric obstacles leads the generation of internal waves that convert kinetic energy from the barotropic to the baroclinic modes (Kang and Fringer, 2012; Müller, 2013). The last term of (2.18) is then essential to understand the behavior of internal tides near the ocean floor, and to predict how they stress the circulation.

Considering these decompositions, the final form of the barotropic momentum equation is

$$\frac{\partial}{\partial t} \left[(H + \eta)\overline{\boldsymbol{u}} \right] = -(H + \eta)f\hat{\boldsymbol{k}} \times \overline{\boldsymbol{u}} + (H + \eta)\nabla\Pi^A - \frac{1}{\rho_0}(H + \eta)\nabla p_a - g(H + \eta)\nabla\eta$$

$$+ (\overline{\boldsymbol{u}} + \boldsymbol{u}'_\eta)\frac{\partial\eta}{\partial t} - \frac{1}{\rho_0}\nabla \int_{-H}^{\eta} p' \, dz + \frac{1}{\rho_0}p'_{-H}\nabla H + \frac{1}{\rho_0}\left(\boldsymbol{\tau}_w - \boldsymbol{\tau}_b \right) + \int_{-H}^{\eta} \boldsymbol{\mathcal{A}} \, dz \tag{2.19}$$

where the ocean dynamics at the vertical boundaries is overall described by four terms: $\boldsymbol{\tau}_w$ and $(\overline{\boldsymbol{u}} + \boldsymbol{u}'_\eta)\frac{\partial\eta}{\partial t}$ at the surface, $\boldsymbol{\tau}_b$ and $p'_{-H}\nabla H$ at the bottom.

Even though the presence of tides can strongly affect the ocean dynamics at the surface (especially in coastal regions where semidiurnal tides may exceed 10 m of amplitude), in the present work we investigate the bottom boundary terms that describe the generation and possible dissipation or propagation of internal tides in the open ocean.

2.1.3 Self-attraction and loading effects

The barotropic momentum equation above described does not include effects of yielding of the solid Earth to tide-generating forces or to weight of the oceanic tidal column, as well as oceanic gravitational self-attraction effects. However, as tides started to be implemented in numerical models, it became clear that these phenomena perturb the gravitational tidal potential by changing pressure on the ocean floor. According to that, Hendershott (1972) added a new term on the momentum equation using a simplified form of (2.19)

$$\frac{\partial \overline{\boldsymbol{u}}}{\partial t} + f\hat{\boldsymbol{k}} \times \overline{\boldsymbol{u}} = -g\nabla \left(\eta - \eta_{sal} - \eta_{eq}\right) + \boldsymbol{\mathcal{F}} \tag{2.20}$$

where the self-attraction and loading (SAL hereafter) effects are defined as

$$\eta_{sal} = \sum_n (1 + k'_n - h'_n) \frac{3\rho_0}{\rho_{earth}(2n+1)} \eta_n \tag{2.21}$$

with k'_n and h'_n Love and load numbers respectively, ρ_{earth} the mean density of the solid Earth and η_n the spherical harmonic components of the sea surface displacement.

Many authors pointed out that this formulation is computationally impractical in numerical models, since it should be implemented at each time step as a convolution of η with a SAL Green's function. Then, different procedures for handling the SAL term have been proposed over the years, with the simpler one developed by Accad and Pekeris (1978) and called "scalar approximation". They proposed to neglect the degree dependence in (2.21) and use only one term of the series, implying the assumption that the SAL effects are dominated by a specific spatial scale

$$\eta_{SAL} = \beta\eta \tag{2.22}$$

where β is a scalar coefficient generally set within a range between 0.6 and 1.1.

This approximation is widely used (Kodaira et al., 2016; Einšpigel and Martinec, 2017; Shihora et al., 2022) despite it is generally prone to large errors, especially near the coasts and on shelf areas where the coefficient varies with the dominant tidal component (Ray, 1998; Kuhlmann et al., 2011). Aware of the limits, we chose to implement this formulation in our tidal configuration, considering it as a first step toward the analysis of this tidal phenomena in our model, where we plan to implement a more accurate procedure in the future following an iterative approach (Egbert et al., 2004; Arbic et al., 2004).

2.2 Model configuration and experiments

The simulation of tides is performed using the global ocean general circulation model NEMO v3.6 (Madec and the NEMO team, 2016). All the experiments are configured on a global tripolar grid ORCA025 at 1/4° of horizontal resolution. The vertical discretization is based on 75 unevenly spaced levels with partial steps representing the bottom topography (Barnier et al., 2006). In particular, the z^* vertical coordinate system is used (Stacey et al., 1995; Adcroft and Campin,

2004)

$$z^* = H(\boldsymbol{x}) \frac{z - \eta(\boldsymbol{x}, t)}{H(\boldsymbol{x}) + \eta(\boldsymbol{x}, t)} \tag{2.23}$$

where z is the standard vertical coordinate, $\eta(\boldsymbol{x}, t)$ is the sea surface elevation and $H(\boldsymbol{x})$ is the total ocean depth at rest. This formulation allows the vertical thickness of each layer to be rescaled at every model time step, accounting for the varying fluid height.

The model bathymetry is based on the combination of the ETOPO1 data set (Amante and Eakins, 2009) in the open ocean and GEBCO (IOC and BODC, 2003) in coastal regions (Figure 2.1). The bottom friction formulation follows (2.2) and is computed as

$$\boldsymbol{\tau}_b = \rho_0 \, C_d \, \sqrt{|\boldsymbol{u}_{-H}|^2 + e_b} \, \boldsymbol{u}_{-H} = \rho_0 \, c_b^{\boldsymbol{u}} \, \boldsymbol{u}_{-H} \tag{2.24}$$

where $c_b^{\boldsymbol{u}}$ is the bottom friction parameter, and e_b represents the bottom turbulent kinetic energy parameter due to unresolved processes that characterise the bottom layer (tides, internal waves breaking and other short time scale currents). The bottom friction coefficient C_d is variable in space according to the law of the wall (Von Karman, 1931)

$$C_d = \left[\frac{\kappa}{\log(0.5 dz_{bot}/dz_{0b})} \right]^2 \tag{2.25}$$

where $\kappa = 0.4$ is the von-Karman constant, dz_{bot} is the last layer thickness, and dz_{0b} is a roughness length set equal to 3 mm.

The momentum and tracer equations are solved with a time step Δt of 600 s, whereas the sea surface elevation and the barotropic transports equations are computed using a shorter time step through the split-explicit time stepping scheme summarised in Section 2.3.
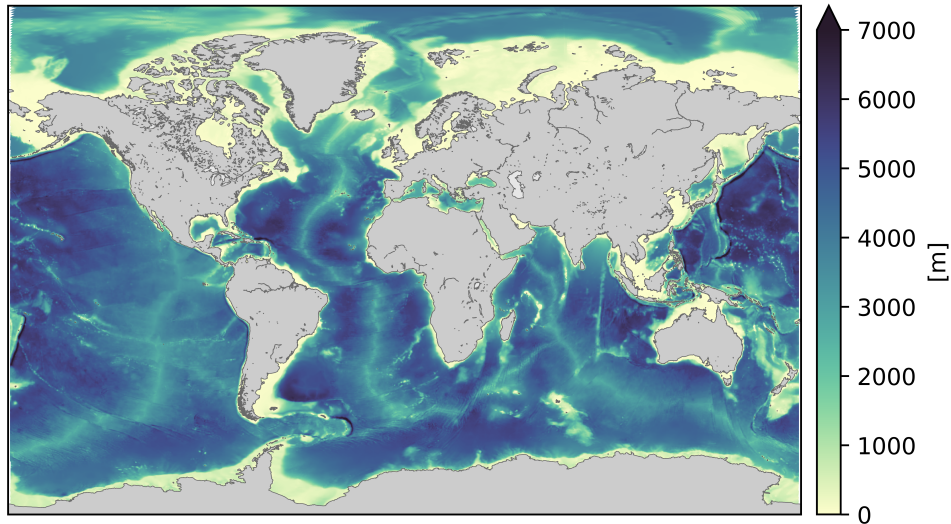

Figure 2.1: Global bathymetry on ORCA025 tripolar grid.

2.2.1 Description of the experiments

The first experiment is called CTRL025 and simulates the ocean general circulation without the tidal forcing. The model was initialised in January 2016 and integrated for two years up to December 2017. The initial conditions were provided by temperature and salinity climatologies from the World Ocean Atlas dataset (WOA13_v12) (Locarnini et al., 2013; Zweng et al., 2013), and the ocean started from a rest state. The coupled sea ice model LIM2 has no specific observed initial conditions, thus the climatological sea surface temperature is used to initialise the sea ice concentration. The surface forcing was provided by JRA55-do v1.4 reanalysis data (Tsujino et al., 2018), with frequency of three hours for atmospheric fields and one day for river runoff. The horizontal viscosity was bi-Laplacian with a value of 1.8×10^{11} m^4/s, and the tracer advection used a total variance dissipation (TVD) scheme (Zalesak, 1979). Laplacian lateral tracer mixing was along isoneutral surfaces with a coefficient of 300 m^2/s, whereas the vertical mixing of tracers and momentum was parameterized using the turbulent kinetic energy (TKE) scheme (Blanke and Raynaud, 1997). Without tides, the bottom turbulent kinetic energy paramenter in (2.24) was set at 2.5×10^{-3} m^2/s^2.

The second simulation, TIDE025, was configured as the previous one, with the addition of the tidal forcing associated with 11 tidal components. In this experiment we tried to simulate the most comprehensive set of tides including as many components as possible: 4 semidiurnal components (M2, N2, S2, K2), 4 diurnal components (K1, O1, P1, Q1), 2 long period tides (Mm, Mf) and one compound (M4). More information about the period and the description of these tidal components are provided in Table 2.1.

Tidal component	Period (hours)	Description	Tidal class
M2	12.42	principal lunar	
S2	12.00	principal solar	semidurnal
N2	12.66	larger lunar elliptic	
K2	11.97	luni-solar	
K1	23.93	luni-solar diurnal	
O1	25.82	principal lunar diurnal	diurnal
Q1	26.87	larger lunar elliptic	
P1	24.07	principal solar diurnal	
Mm	661.30 ($\sim$27d)	lunar monthly	long term
Mf	327.90 ($\sim$14d)	lunar fortnightly	
M4	6.21	–	compound

Table 2.1: Tidal components implemented in NEMO.

In a preliminary run, numerical instabilities arose in areas where tides are stronger (Gulf of Biscay, Hudson Strait, Drake passage, Amundsen and Weddell Seas in the Antarctic region), and to avoid this problem we applied a Shapiro filter of the fourth order in those particular areas; then we implemented the same changes on CTRL025 in order to have the same bathymetry in both the experiments. In addition, TIDE025 supposed to have no bottom turbulent kinetic energy, according to previous studies on tides using NEMO on regional scales (Agresti, 2018). Note that this experiment setup has been maintained in all the tidal experiments described below.

After a preliminary comparison between CTRL025 and TIDE025, we assessed many other simulations to study the possible implementation of a topographic wave drag (TWD hereafter).

In the NEMO ocean model community, a first step forward was proposed by de Lavergne et al. (2020) using an energy-constrained parametrization of mixing due to the local breaking of high-mode internal tides and the remote dissipation of low-mode internal tides. This parametrization was based on the work by Jayne and St. Laurent (2001) and required to know a priori the distribution of the tidal energy dissipation of the unresolved baroclinic modes. In our opinion, this is a strong constrain since we did not know a priori how many tidal modes are solved over the global domain, so we tried to implement a new TWD formulation that did not require any tidal information.

Since the tidal amplitude of TIDE025 was higher than observations (see Section 2.4), we started adding a stress term to the total momentum equation in a new experiment, called TIDE025_LIN. In this experiment we used the implicit bottom friction formulation as proposed by Arbic et al. (2010), and we added a linear term to the general formulation of the bottom stress (2.2)

$$\boldsymbol{\tau}_b = \rho_0 \, C_d \, |\boldsymbol{u}_b| \cdot \boldsymbol{u}_b + \rho_0 \frac{H}{T_d} \theta(H > H_*) \, \boldsymbol{u}_b \qquad (2.26)$$

where H is the ocean depth, H_* is a threshold depth here fixed at 1000 m, and T_d is a decay time of 10 days, set as constant over the entire domain. These quantities were chosen following Arbic et al. (2010), where the TWD e-folding time on the main topographic structures has the order of magnitude of tens of days. From TIDE025_LIN we learned that the TWD should be variable in space otherwise it is too dissipative and does not localise near rough topography as observed by Egbert and Ray (2000). Moreover, we observed that the new bottom stress formulation in (2.26) not only increases the stress magnitude where it is applied, but also decreases the stress on the continental shelves. This phenomenon is not confirmed by observed data, nevertheless it is worth noting the indirect relationship between the bottom friction formulation in the open ocean and the values obtained on the shelf. Despite that, we neglected the TIDE025_LIN experiment and tried to implement a formulation for the TWD based on rough topography information.

Since the NEMO model does not contain a dissipative term like the TWD, the first step toward its implementation was to check the dissipative bottom term already implemented in the code. In the TIDE025_BFR experiment, we changed the bottom friction parameter inside the barotropic mode (see section 2.3.1) to improve the model consistency with the analytical formulation. This experiment did not change the physics of the model but just changed the numerical computation of the bottom friction. Even though this improvement slightly changed the bottom stress term in the total momentum balance, we considered it as necessary in tidal simulations, so we kept it even in the following experiments.

Then, we implemented in the model a TWD parametrization from the ones described in Section 2.1.1. The formulation proposed by Garner (2004) and Arbic et al. (2004) in (2.6) was based on an analytical demonstration, but their TWD tensor had non-diagonal terms that are in principle non-negligible and difficult to be implemented in NEMO. On the other hand, Shakespeare et al. (2020) parametrized the TWD under the hypothesis of isotropic bathymetry, and reached a simplified formula keeping solid analytical assumptions. We chose the latter one as the best suitable in NEMO implementation. According to that, we run a new simulation TIDE025_TWD,

where the TWD of Shakespeare et al. (2020) was implemented limited to the dissipative waves regime. This experiment represents our best simulation of the interaction between barotropic tides and bathymetry, and more details about the TWD implementation are provided in section 2.3.2.

Finally, in TIDE025_TWD_SAL we completed the parametrization of tidal phenomena including the SAL term as proposed in (2.20). Since SAL effects are less analysed in the literature than the TWD ones, we chose to implement the scalar approximation defined in (2.22) with a β coefficient constant in space and equal to 0.1 as roughly proposed in Arbic (2021).

Table 2.2 summarises the main characteristics of the experiments that are analysed in the following sections.

Experiment	tidal forcing	bottom fr. correction	TWD	SAL	IC	Period	$e_b(m^2/s^2)$
CTRL025	NO	NO	NO	NO	climatology	2016 - 2017	2.5×10^{-3}
TIDE025	YES	NO	NO	NO	climatology	2016 - 2017	0
TIDE025_TWD	YES	YES	YES	NO	climatology	2016 - 2017	0
TIDE025_TWD_SAL	YES	YES	YES	YES	climatology	2016 - 2017	0

Table 2.2: Description of the simulations performed at $1/4°$ of horizontal resolution and analysed in section 2.4.

2.3 Barotropic momentum equation improvements in NEMO

When the split-explicit time stepping (*time splitting*) scheme is used (Shchepetkin and McWilliams, 1995), the barotropic momentum and free surface equations are solved with a different time step $\Delta t_{BT} = \Delta t/M$ with M an integer number. Using this approach, the barotropic time step, t^m, is shorter than the baroclinic one, t^n, and external gravity waves are allowed as possible solution of the horizontal momentum equation.

In the analysed configuration, we set a centred time integration, meaning that each barotropic mode spans between t^{n-1} ($m = 0$) and t^{n+1} (m=2M), and we fixed M equal to 100 in order to have a time interval of 6 seconds.

This scheme imposes that slowly varying terms of the momentum equation (2.19) are updated just at the beginning of the mode (i.e. t^{n-1}) and kept constant inside: in NEMO this is the case of the advection, the lateral mixing, the atmospheric and dynamical pressure gradients and the wind stress. Similarly, the bottom friction associated with the baroclinic bottom velocity is fixed to the centered baroclinic time step (t^n). The remaining terms are updated inside the barotropic mode and contribute to the barotropic transport balance. Using a_l and c_l as weighting

coefficients, the following notations for a generic variable ξ are used

$$\xi^{m+\frac{1}{2}} = a_1\xi^m + a_2\xi^{m-1} + a_3\xi^{m-2} \tag{2.27a}$$

$$\xi^* = c_0\xi^{m+1} + c_1\xi^m + c_2\xi^{m-1} + c_3\xi^{m-2} \tag{2.27b}$$

and the discretised formulation of the zonal barotropic momentum equation for a generic grid point (i,j,k) is then

$$
\begin{aligned}
\frac{\left[\overline{u}^{m+1}(H+\eta^{m+1})\right]_{i,j} - \left[\overline{u}^m(H+\eta^m)\right]_{i,j}}{\Delta t_{BT}} &= + \left(H + \eta^{m+\frac{1}{2}}\right)_{i,j} \left[f\,\overline{v}^{m+\frac{1}{2}}\right]_{i,j} \\
&\quad - g\,(H+\eta^*)_{i,j}\,\frac{1}{\Delta x_{i,j}}\left(\eta^*_{i+1,j} - \eta^*_{i,j}\right) \\
&\quad + g\left(H + \eta^{m+\frac{1}{2}}\right)_{i,j}\frac{1}{\Delta x_{i,j}}\left(\eta^{eq,m}_{i+1,j} - \eta^{eq,m}_{i,j}\right) \\
&\quad + \left(H + \eta^{m+\frac{1}{2}}\right)_{i,j}\left[c_b^{\mathbf{u},n}\frac{1}{H+\eta^m}\left(\overline{u}^m + u'^n_{-H}\right)\right]_{i,j} \\
&\quad + \mathcal{B}^{x,n-1}_{i,j}
\end{aligned} \tag{2.28}
$$

where u'^n_{-H} is the baroclinic component of the bottom velocity at t^n, and $\mathcal{B}^x$ contains all the slowly varying terms mentioned above.

Figure 2.2: Schematic of the split-explicit time stepping scheme for the barotropic and baroclinic modes with centred time integration. In this example $M = 5$. The quantities at $t + \Delta t$ are obtained using the $<>$ operator, where a time filter of boxcar averaging window over barotropic time steps is used (with a_l coefficients, blue vertical bars), whereas $<<>>$ operator computes time averaged transports to advect tracers (using c_l coefficients, red vertical bars). Reproduced from Madec and the NEMO team (2016).

2.3.1 Correction to the bottom friction

First, we checked the computation of the already implemented dissipation terms, and in particular the bottom friction as implemented in the official release of NEMO 3.6. In the NEMO barotropic mode, the coefficient $c_b^{\mathbf{u}}$ of (2.24) is fixed to the centered time step, t^n, even though the barotropic component of the bottom velocity changes. The resulting discretised bottom stress

for a generic time t^m is then

$$\boldsymbol{\tau}_b^m = c_b^{\boldsymbol{u},n} (\overline{\boldsymbol{u}}^m + \boldsymbol{u'}_{-H}^n) \tag{2.29a}$$

$$c_b^{\boldsymbol{u},n} = C_d \sqrt{|\overline{\boldsymbol{u}}^n + \boldsymbol{u'}_{-H}^n|^2 + e_b} \tag{2.29b}$$

This choice is justified by the possibility to remove at the beginning of the barotropic mode the portion of bottom friction induced by the barotropic velocity, and to update it at each barotropic time step using the correct barotropic component. However, in our opinion this formulation causes incoherence between terms in (2.29a) and (2.29b) because the two formulas are linked even though computed with different values of barotropic velocity. Since the presence of tides enhances the barotropic velocity variability, we changed the bottom friction coefficient inside the barotropic mode starting from the TIDE025_BFR experiment, and we updated the above formulas as follows

$$\boldsymbol{\tau}_b^m = c_b^{\boldsymbol{u},m} (\overline{\boldsymbol{u}}^m + \boldsymbol{u'}_{-H}^n) \tag{2.30a}$$

$$c_b^{\boldsymbol{u},m} = C_d \sqrt{|\overline{\boldsymbol{u}}^m + \boldsymbol{u'}_{-H}^n|^2 + e_b} \tag{2.30b}$$

making the bottom stress formulation more coherent with its analytical form (2.24).

2.3.2   Topographic wave drag implementation

The second step towards an "updated" simulation of tides in NEMO is to include the interaction processes between tides and rough topography in the model. The conversion and dissipation of barotropic tidal energy at the ocean floor is described in (2.18) by the $\frac{1}{\rho_0} p'_{-H} \nabla H$ term. According to the horizontal resolution of the model, this term could be in turn split into two components

$$\frac{1}{\rho_0} p'_{-H} \nabla H = \mathcal{P}_{mod} + \mathcal{P}_{twd} \tag{2.31}$$

where $\mathcal{P}_{mod}$ describes the processes resolved by the model and $\mathcal{P}_{twd}$ represents all the unresolved processes. Arbic et al. (2010) pointed out that numerical models at any resolution do not resolve the actual breaking of internal tides even though they reproduce a part of it ($\mathcal{P}_{mod}$), therefore a parametrization to include $\mathcal{P}_{twd}$ is required to properly reproduce tides.

In the TIDE025_TWD experiment, we implemented in the general circulation model NEMO the topographic wave drag induced by waves that are dissipated before interacting with the ocean surface. Following Shakespeare et al. (2020), these waves belong to the locally dissipating waves regime with a stress coefficient r^* in (2.8) that is real and positive inducing a sink of energy and momentum to the barotropic flow (see Appendix A for more details).

Before implementing the formulation in NEMO, we stressed the attention on some important differences between the model configuration we used and the one described in Shakespeare et al. (2020). First, the authors analysed the case of purely oscillatory flow at the tidal frequency, thus the general circulation of the ocean is suppressed, unlike our configuration where atmospheric and tidal forcings act on the ocean together. Secondly, they tested the parametrization in an open

ocean region of well-known tide conversion (Atlantic ridge), whereas our domain is global thus contains different interaction regimes.

Aware of these differences, we computed the scalar field r^* limited to the regime of dissipative waves and obtained

$$r^* = \frac{1}{2} N_b h_{rms}^2 \overline{K} F_1(\omega) \tag{2.32}$$

where h_{rms} is the roughness root-mean-square, and $\overline{K}$ is its height-weight-mean wavenumber, N_b is the bottom buoyancy frequency, ω is the tidal frequency of the principal component, and $F_1(\omega)$ is a weighting function defined as

$$F_1(\omega) = \frac{\sqrt{(N_b^2 - \omega^2)(\omega^2 - f^2)}}{N_b |\omega|} \tag{2.33}$$

We finally implemented the following formula in the barotropic momentum equation

$$\boldsymbol{\mathcal{P}}_{twd} = r^* \, \theta(H > H_*) \left(\overline{\boldsymbol{u}} - \langle \overline{\boldsymbol{u}} \rangle \right) \tag{2.34}$$

where θ is a Heaviside function to apply the drag only in regions deeper than a threshold value H_*, and $\langle \overline{\boldsymbol{u}} \rangle$ is the *detided* barotropic velocity that makes the parametrization effective just for the tidal velocity component.

Hereafter, we describe the procedure performed to compute the variables required by $\boldsymbol{\mathcal{P}}_{twd}$ to dissipate tidal waves at the semidiurnal frequency of the M2 component, considered as the most energetic on the global scale.

Roughness

The definition of *roughness* is a key point to be addressed in order to derive the topographic parameters required by (2.32) and it is here expressed as the thickness associated to the model unresolved bathymetry. Therefore, we used the GEBCO bathymetry dataset at 1' as reference to identify the topographic structures neglected by the ORCA025 grid, and we computed their difference in height, h, subtracting from the original GEBCO dataset its smoothed version obtained using the Shapiro filter of the second order

$$h = H_{GEBCO}^{orig} - H_{GEBCO}^{smooth} \simeq H_{GEBCO}^{orig} - H_{ORCA025} \tag{2.35}$$

where the filter was iterated 200 times to make the main topographic features qualitatively comparable to the model ones (Figure 2.3b).

Figure 2.3 shows that the roughness is typically absent on the continental shelves due to the high presence of sediments, whereas it characterises oceanic trenches, ridges and continental slopes with a global mean value of 80 m. It is worth noting that the roughness obtained on continental slopes is here associated with the filtering process that smooths the slope generating artificial values, thus a Heaviside function is included in $\mathcal{P}_{twd}$ to limit the roughness of interest.
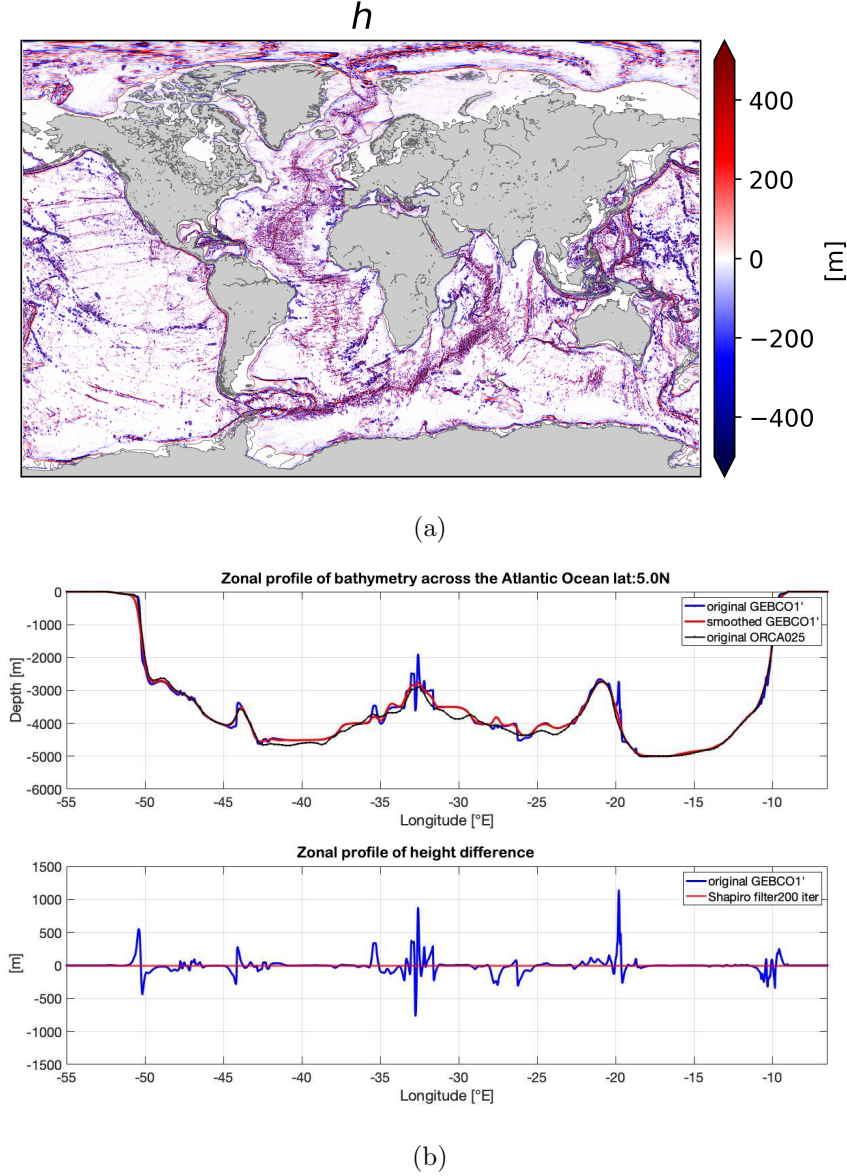
(a)

(b)

Figure 2.3: (a) Global map of topographic difference in height on the GEBCO 1' grid, computed using (2.35) with 200 iterations of the Shapiro filter on the GEBCO original bathymetry. (b) *Top*: bathymetry section in the Atlantic Ocean at 5°N. The model bathymetry at $1/4°$ (black) is compared with the original (blue) and filtered (red) GEBCO bathymetry at 1'. *Bottom*: Height difference section at the same latitude.

The threshold value H^* is fixed to consider roughness only in open ocean regions deeper than 500 m (Green and Nycander, 2013). The roughness root-mean-square, h_{rms}, and height-weight-mean wavenumber, $\overline{K}$, are then computed in the Fourier space as

$$h_{rms} = \sqrt{\frac{1}{4A\pi^2} \int_{-\infty}^{\infty} \int_{-\infty}^{\infty} |\hat{h}|^2 dk\,dl} \tag{2.36}$$

$$\overline{K} = \frac{1}{h_{rms}^2} \frac{1}{4A\pi^2} \int_{-\infty}^{\infty} \int_{-\infty}^{\infty} K\,|\hat{h}|^2 dk\,dl \tag{2.37}$$

where the hat operator represents the Fast Fourier Transform (FFT) algorithm applied to h, A

is the regional area where it is computed, and (k, l) are the wavenumbers.

The h_{rms} and $\overline{K}$ variables are interpolated on the model grid proceeding by steps:

1. the roughness FFT was computed on regular boxes of size 5° x 5°. For each GEBCO point a relative box was settled around, and the correspondent value of h_{rms} and $\overline{K}$ was saved. Different box sizes with different overlapping lengths were tested, starting from smaller boxes of 5° on each side up to bigger ones of 20°, as proposed by Shakespeare et al. (2020) in their implementation test. Boxes without overlapping seem to be the worst choice applied to the global domain because they are characterised by big gradients between each others causing numerical instabilities; therefore, finally, the finer box with the maximum overlapping was chosen as the best to maintain the level of accuracy on the GEBCO grid and avoid numerical issues;

2. the obtained fields were regridded from the regular GEBCO to the tripolar ORCA025 grid, computing for each target cell the average of the correspondent points from the source grid;

3. finally, the results were smoothed with 30 iterations of the Shapiro filter to remove gradients due to the limited dimension of the FFT boxes. It is worth saying that no window function was applied to the FFT analysis to keep the entire roughness spectrum on the GEBCO source grid and filter it only on the ORCA025 target grid.

The resulting h_{rms} field (Figure 2.4a) presents the higher values along the mean topographic features and has a mean value of 145 m on the global scale. Even though the FFT analysis was performed only on wet points, the highest values were located near the coast, especially on the Peru-Chile trench, on the Mexico coasts, along Greenland and in the Antarctic region (Figure 2.4). The boxes shape is visible also on the $\overline{K}$ field (Figure 2.4b), and according to (2.37) lower values are placed where h_{rms} is higher.
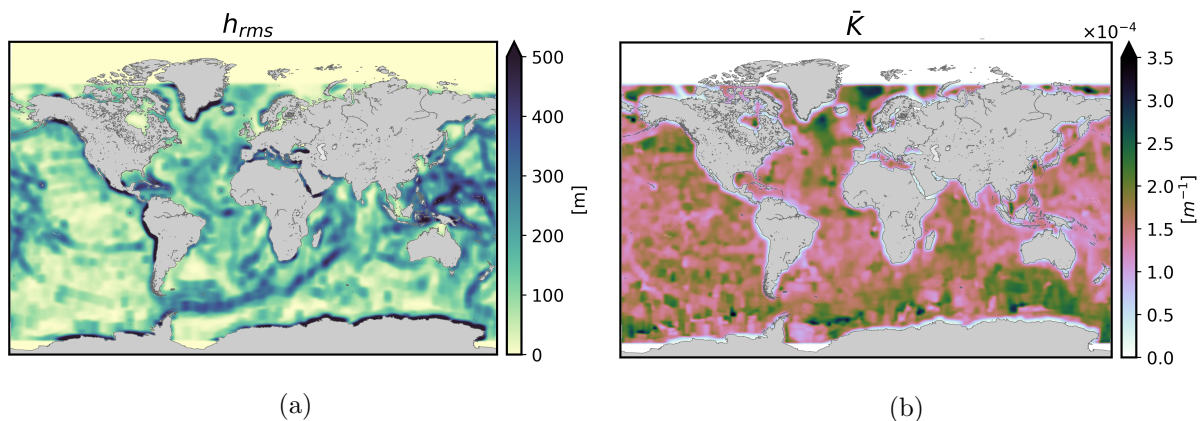

Figure 2.4: Global maps of (a) h_{rms} and (b) $\overline{K}$ computed from the GEBCO roughness and interpolated on the ORCA025 grid. In both cases 30 iterations of the Shapiro filter are applied to smooth the obtained fields and the results are masked further north (south) than 75°N (75°S) since the TWD is not applied at these latitudes due to the $F_1(\omega)$ function.

Bottom buoyancy frequency

The information about the fluid stratification at the bottom was computed from the CTRL025 experiment without tides. The obtained bottom Brünt-Väisälä frequency was averaged over 60 winter days and smoothed with 50 iterations of the Shapiro filter (Figure 2.5a). The filtering procedure was applied to avoid unstable stratification on local scales and to reach a spatial resolution comparable to h_{rms} and $\overline{K}$ fields.

Weighting function

The TWD proposed by Shakespeare et al. (2020) was weighted by the relation between the tidal frequency of interest, the fluid stratification and the inertial frequency. The weighting function $F_1(\omega)$ was then included in (2.32) as part of r^* and had real values when $f < \omega < N_b$. Figure 2.5b shows that the weight increases with the bottom fluid stratification and moving towards the equator.
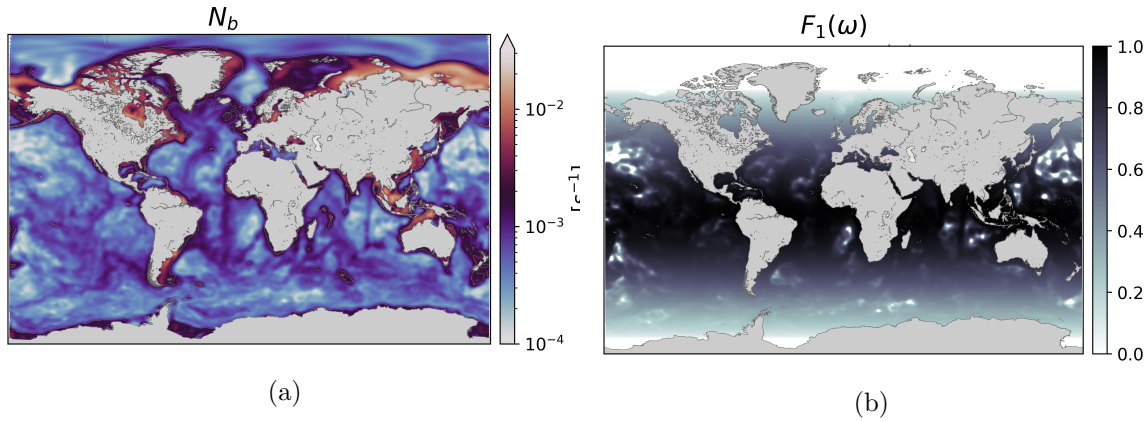
Figure 2.5: (a) Global map of N_b computed from the CTRL025 experiment as the average of 60 days wintertime. The field was filtered with 50 iterations of the Shapiro filter to avoid local instabilities and strong regional gradients. (b) Global map of the weighting function $F_1(\omega)$ for the M2 tidal frequency.

The fields described so far compose the time independent coefficient of $\mathcal{P}_{twd}$ that is presented in Figure 2.6. According to Arbic et al. (2010), TWD higher values are placed where the roughness unresolved by the model is higher, as in the Southwest Indian ridge, northeast of Madagascar and in the Indonesian region. Nevertheless, not always high values of roughness correspond to a strong TWD, as in the case of the Mid-Atlantic ridge that is characterised by a widespread roughness, or the case of the western part of the North Pacific Ocean where the bottom stratification is very weak. It is interesting to notice the high TWD values near the La Romanche fracture zone in the equatorial Atlantic Ocean. Moving poleward, the TWD is mainly weighted by latitude, almost absent in the polar regions.

Tidal barotropic velocity

The present parametrization is applied to tidal flows at the semidiurnal frequency of M2, that is the tidal component with higher amplitude on global scale (see Figure 2.10) and thus the most
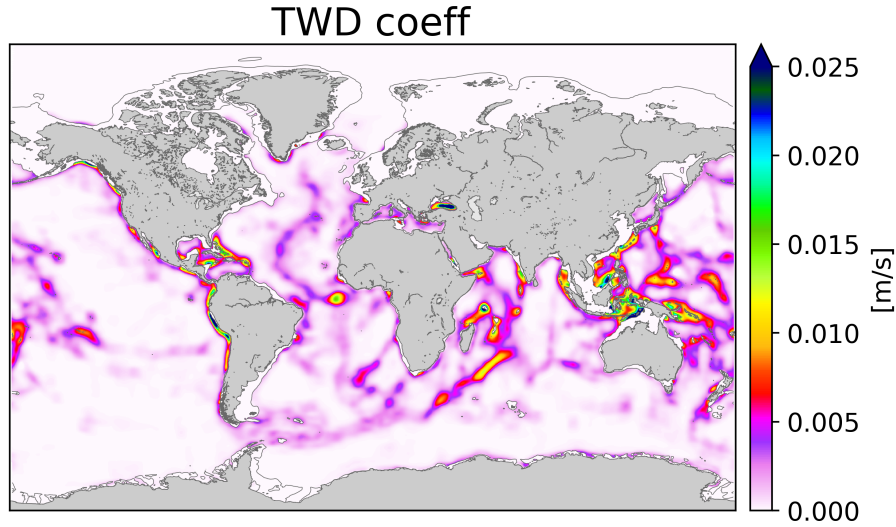
TWD coeff

Figure 2.6: Global map of $r^*\theta(H > H^*)$ on the ORCA025 grid. It corresponds to the constant coefficient in the TWD formulation (2.34). Contour grey line represents the isoline of $H^* = 500m$.

energetic to be dissipated. A key point to be addressed is then the definition of the tidal flow interested in the TWD: according to (2.34) it is computed as the runtime difference between the total barotropic velocity, $\overline{\boldsymbol{u}}$, and its 25-hour average, $\langle\overline{\boldsymbol{u}}\rangle$ corresponding to twice the M2 period. The average uses hourly instantaneous fields on temporal boxes with 1 hour of overlapping, and the obtained flows filter out in a rough way the semidiurnal tides effect.

2.4 Results

Hereafter we analyse the experiments summarised in Table 2.2 looking at the total kinetic energy (hereafter KE), the bottom stress and the SSH. We considered one year of spin up to reach a dynamical equilibrium of the ocean after the initial state of rest, thus the analysed data were extracted from the second year of simulation. The main objective of the proposed implementations is to reduce the net tidal energy input to the global budget and improve the SSH simulation compared to observed and modelled reference data.

2.4.1 Kinetic energy analysis

The KE is integrated on the global domain during the period from January to December 2017 as

$$KE = \int_{V_{tot}} \frac{1}{2}\rho_0(\boldsymbol{u} \cdot \boldsymbol{u}) \, dV \tag{2.38}$$

where V_{tot} is the volume of the ocean. This quantity is computed runtime and then averaged every 5 days (Figure 2.7), so it includes the contribution of all the dynamical structures resolved by the model.

The CTRL025 mean value of KE is 2.5×10^{18} kg m^2/s^2 and corresponds to a global KE density of 1.87 kg/m s^2. These values match the results of Iovino et al. (2016) where global NEMO

configurations were analysed at different resolutions. Adding the astronomical potential, all the tidal simulations increase the mean KE value and show the same oscillation phase due to spring and neap tides. In TIDE025 the KE increases by about 18% compared to CTRL025, while part of the energy is dissipated by the TWD in TIDE025_TWD and TIDE025_TWD_SAL, limiting the increment to 14% and 15% respectively. On the global scale the impact of SAL is then to slightly restore the tidal energy removed by the TWD, but further analysis is required to support this hypothesis.
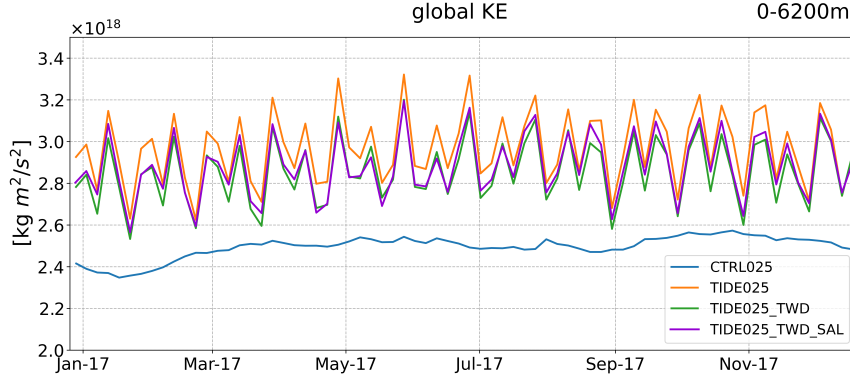
Figure 2.7: Timeseries of global KE during the period from January to December, 2017.

To evaluate whether and where the tidal forcing and related parametrizations have the stronger impact on the ocean, the KE density for different layers is computed as

$$KEd = \frac{1}{V_k} \int_{V_k} \frac{1}{2} \rho_0 (\boldsymbol{u} \cdot \boldsymbol{u}) \, dV \tag{2.39}$$

where V_k is the volume of the layer of interest. The surface layer is defined above 100 m, the intermediate ocean from 100 m to 500 m, the deep ocean from 500 m to 3000 m, and the abyssal ocean from 3000 m down to the bottom.

The resulting timeseries are presented in Figure 2.8 and the correspondent mean values are summarised in Table 2.3. Moving downward from the surface, the ocean KE decreases according to the weaker velocity magnitude, but the differences between experiments remains qualitatively the same. The KE root-mean-square difference with and without tides is then computed for each layer as

$$\Delta_{rms} = \sqrt{\frac{1}{N} \sum_{n=1}^{N} (KEd_{TIDE}^n - KEd_{CTRL}^n)^2} \tag{2.40}$$

where N is the amount of data in the period of interest.

The KE density of TIDE025_TWD is weaker than TIDE025 in each layer, as we expected applying the TWD to the barotropic flow: the relative difference between the two experiments changes with depth and has maximum values below 500 m depth, where the decrease is about 4% for the deep layer and 5% for the bottom layer. Indeed, the upper ocean is characterised by eddies, gyres and dynamical fronts that interact with internal tides reflecting or refracting them (Kelly et al., 2016) and their KE could be then indirectly modified by the TWD. The internal
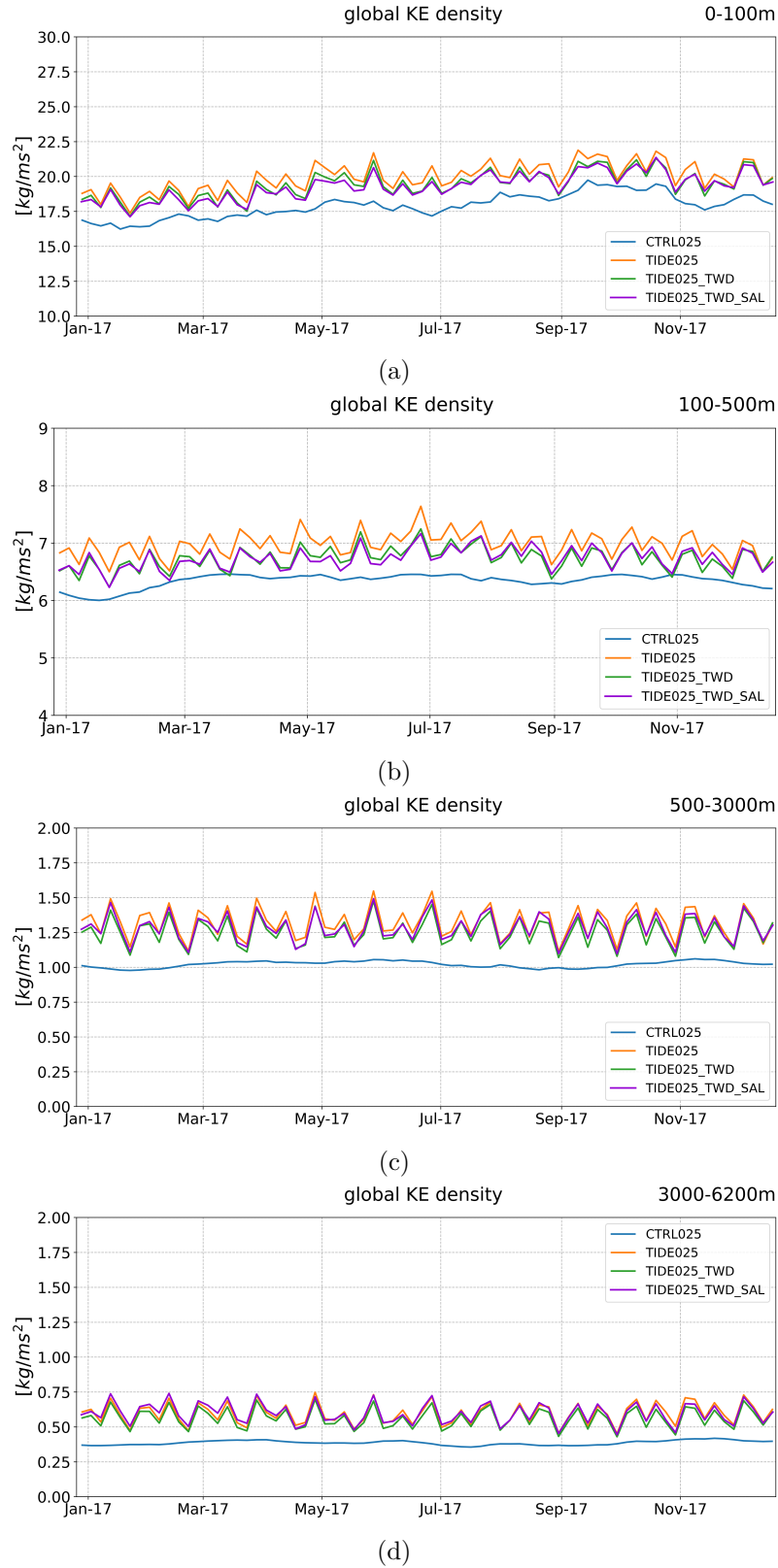
24

Figure 2.8: Timeseries of global KE density during the period from January to December, 2017, computed on different layers: (a) 0-100 m, (b) 100-500 m, (c) 500-3000 m, (d) 3000-6200 m.

tides dissipation has then a direct effect on the KE, but also an indirect effect on the dynamical structures that should be further examined on basin scales (see Chapter 3 for the North Atlantic case).

The SAL effect on the water column could be analysed comparing TIDE025_TWD_SAL with TIDE025_TWD: moving downward it reduces the KE density of 1% in the upper layer, has a negligible impact between 100 m and 500 m, and increases the KE in the deeper part of the ocean. This result confirms that the SAL parametrization reduces the tidal energy near the surface, as expected applying (2.22) in (2.20) where the SAL term decreases the sea surface displacement, but it also points out a baroclinic behaviour of the first mode, with an increase of energy near the bottom.

Experiment	0-100 m		100-500 m		500-3000 m		3000-6200 m		0-6200 m	
	KEd	Δ_{rms}	KEd	Δ_{rms}	KEd	Δ_{rms}	KEd	Δ_{rms}	KEd	Δ_{rms}
CTRL025	17.90	-	6.34	-	1.02	-	0.39	-	1.87	-
TIDE025	19.93	2.13	6.98	0.67	1.32	0.32	0.59	0.22	2.22	0.37
TIDE025_TWD	19.44 (-2%)*	1.6 5	6.73 (-3%)*	0.43	1.26 (-4%)*	0.26	0.56 (-5%)*	0.19	2.14 (-4%)*	0.29
TIDE025_TWD_SAL	19.30 (-1%)**	1.49	6.73 (0%)**	0.43	1.28 (+2%)**	0.28	0.60 (+6%)**	0.22	2.16 (+1%)**	0.31

Table 2.3: Temporal mean of the KE density (kg/ms^2) computed on different layers and the entire volume. Δ_{rms} values are computed using CTRL025 as reference. (*) Difference in percentage between TIDE025_TWD and TIDE025. (**) Difference in percentage between TIDE025_TWD_SAL and TIDE025_TWD.

2.4.2 Bottom stress analysis

The four experiments are compared using the bottom stress averaged over a period of 25 days, corresponding to an integer number of M2 tidal periods. Figure 2.9a shows the reference pattern of τ_b, with stronger values on the continental shelves and in the region of the Antarctic Circumpolar Current. When tides are implemented (TIDE025), the barotropic current increases everywhere and reaches the highest values in shallow water areas, where the tidal energy is felt by a smaller volume of water. These changes have the principal effect to increase the bottom friction of the ocean as demonstrated by Figure 2.9b, where the bottom stress is enhanced in regions of typical high tidal amplitude as the European shelf, the Hudson Strait, the Patagonian shelf, the Indonesian region, the East China Sea and the Bering Sea. Higher values are located even on the western boundaries of the global ocean. The overall trend on the open ocean is to slightly decrease the bottom friction (it is the case of the Pacific and Indian oceans), except near rough topography.

The differences become interesting when the TIDE025_TWD experiment is compared to TIDE025 (Figure 2.9c): in this case a dissipative term is added to the barotropic flow in regions deeper than 500 m, but the main differences are overall located on the continental shelves. Indeed, in the same regions where TIDE025 enhances the bottom friction, the TWD dissipates part of the tidal energy and weakens again the barotropic flow. Even though we could expect major differences near rough topography, this behaviour confirms that the dissipation of internal tides in the open ocean has a detectable impact also along the coasts.
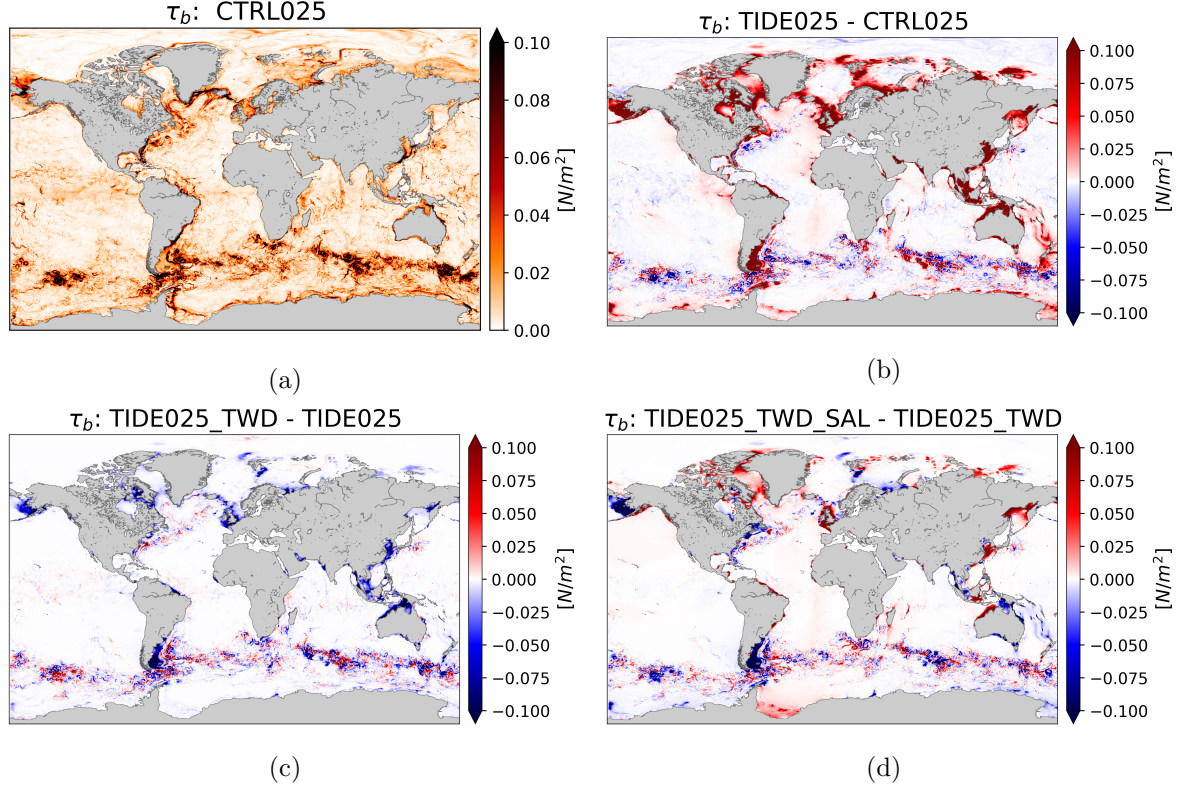
Figure 2.9: (a) Global map of bottom stress τ_b computed from the CTRL025 experiment averaged over 25 days from 25 April 2017 to 20 May 2017. The analysed period corresponds to an integer number of M2 periods. Differences between (b) TIDE025 and CTRL025, (c) TIDE025_TWD and TIDE025, (d) TIDE025_TWD_SAL and TIDE025_TWD during the same period.

Also the implementation of SAL produces the strongest effects in shallow water areas (Figure 2.9d), but the differences between TIDE025_TWD_SAL and TIDE025_TWD change sign according to the region of interest. This result is probably related to large errors due to the choice of using the SAL scalar approximation (Ray, 1998; Kuhlmann et al., 2011), rather than to physical reasons. Indeed, we made a strong assumption taking the β coefficient constant in (2.22), while it varies in space and time especially near the coasts (Kuhlmann et al., 2011). Aware of the limits of this parametrization, hereafter we analyse the SAL and TWD effects focusing on the SSH. This impact is quantified in the next section, comparing the modelled SSH with observed data looking at the tidal amplitudes on global and regional scales.

2.4.3 Sea level analysis

A global overview of the modelled tidal amplitudes in NEMO is presented in Figure 2.10 using the TPXO atlas as a reference. The TPXO data-assimilative barotropic tidal model was developed so as to assimilate altimeter and tide gauges data and obtaining information about the main tidal harmonic constituents (Egbert et al., 1994; Egbert and Erofeeva, 2002). The last version available, TPXO9_v02, provides a global atlas of 15 tidal harmonic constituents with a regular horizontal resolution of 1/30°. Despite TPXO shows its own errors compared to observations, its coastlines are much more realistic than in the ORCA025 grid, and the bottom topography is composed of

small scales features that are totally missing in our model at 1/4° of resolution.

The NEMO output is here analysed using the method of Foreman et al. (2009) to compute the harmonic analysis on hourly data for the period from April 24th to December 20th, 2017. The SSH timeseries are then decomposed into sinusoidal components to extrapolate from the total signal the implemented 11 tidal constituents, and the main semidiurnal (M2, S2) and diurnal (K1, O1) components are here discussed. Hereafter, the TIDE025 experiment is compared with TXPO, whereas TIDE025_TWD is analysed looking at the differences with respect to TIDE025, and TIDE025_TWD_SAL with respect to TIDE025_TWD.

The principal semidiurnal lunar component, M2, shows higher amplitudes almost everywhere in the open ocean (Figures 2.10a-b), whereas near the coasts the main differences between TIDE025 and TPXO are located offshore of Panama, Chile and Peru, in the Arabian Sea, in the Gulf of Benguela and offshore of New Zealand. Contrary to the general trend, M2 amplitude is lower in TIDE025 with respect to TPXO on the Kamchatka coast and in the Weddell Sea. The amphidromic points are generally well placed except for those in the Antarctic region. In particular, TIDE025 places an amphidromic point in the Southern ocean around 150°E, which is absent in TPXO.

The principal semidiurnal solar component, S2, is the worse simulated tidal harmonic, with double amplitude in regions of maxima in TPXO (Figures 2.10c-d). The main differences are placed at high latitudes, especially in the North Atlantic and in the Weddell Sea, where the presence of sea ice can change tidal oscillation. Indeed, one of the major sources of error in modelling tides in these regions is the inaccurate definition of the coastlines and the shape of the cavity geometry beneath ice shelves (Maraldi et al., 2007), that are poorly reproduced or even absent in our model. Accordingly, the presence of sea ice is probably underestimated in TIDE025, making the tidal amplitudes stronger in polar regions. Moreover, even the amphidromic points poorly match in the Pacific Ocean, with four points proposed by TPXO that are missing in TIDE025.

If the semidiurnal amplitudes present strong differences between the NEMO and TPXO models, on the other hand the diurnal components K1 and O1 are more similar (Figures 2.10e-f and 2.10g-h), with amplitude differences that are localised mainly in the Antarctic region. Other biases are found in the South China Sea, where the K1 amplitude is higher in TIDE025, or in the Arabian Sea, around Australia and on the European shelf, where our model overestimates the O1 component. Contrary to the general trend O1 is underestimated by NEMO in the Gulf of Alaska. The amphidromic points associated with diurnal tides have many differences between the two experiments, because TPXO has more points for each tidal constituent.

The general behaviour of TIDE025 is then to overestimate the TPXO tidal amplitude at all frequencies and to place the amphidromic points in the correct areas. These errors are mainly due to the different resolution of the two models, in agreement with many authors who described the close relationship between barotropic tides and bottom bathymetry (Kantha, 1995; He and Wilkin, 2006).
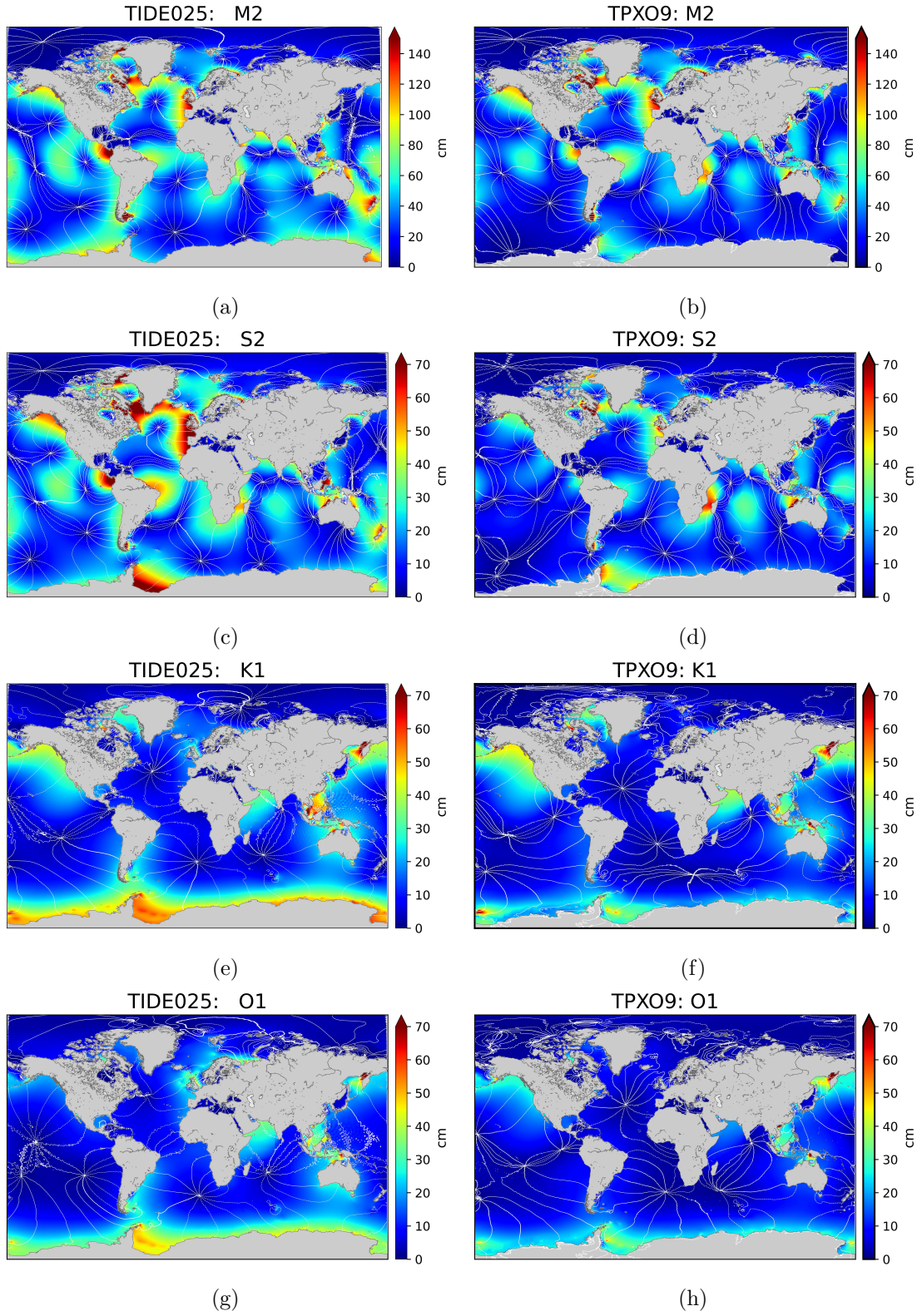
Figure 2.10: Global maps of tidal amplitudes and phases in TIDE025 (*left* column) and TPXO9_v2 (*right* column).

The analysis of TIDE025_TWD is proposed now as the relative difference of each tidal component with respect to TIDE025. Indeed, the differences between the two NEMO experiments are negligible compared to the ones with respect to TPXO. Figure 2.11 demonstrates that the tidal amplitude globally decreases for all the analysed frequencies even though the TWD is weighted just for the M2 component. Relative increments are mostly placed near the amphidromic points and associated nearby with a decrease of the same order of magnitude, meaning that the points of zero amplitude are shifted in space from one experiment to the other. It is worth noting that the diurnal tides show a wave-like pattern in the South China and Philippines Seas spreading through the North Pacific Ocean. When this signal is related to a decrease in amplitude, it demonstrates that the TWD dissipates part of the internal waves before they reach the sea surface.

The effects induced by SAL parametrization, instead, are more intense all around the globe as pointed out by the difference between TIDE025_TWD_SAL and TIDE025_TWD (Figure 2.12), with larger or smaller tidal amplitudes depending on the analysed component. As expected from the literature, the impact of these phenomena are detectable both in the open ocean and in shallow areas (Hendershott, 1972; Ray, 1998; Kuhlmann et al., 2011), but we found relative differences that are too large to be realistic, with values higher than 50% compared to the expected 10%. The M2 amplitude is enhanced almost everywhere, with values that are up to double in the Pacific and Southern Oceans. On the contrary, SAL generally weakens the S2 signal with a homogeneous pattern in the Atlantic Ocean, whereas it enhances the amplitude in the Indian and North Pacific Oceans. Looking at the diurnal frequencies, SAL weakens the K1 component in the Southern hemisphere and in the Atlantic Ocean, except for the North-West Atlantic coast, the Gulf of Mexico and the Gulf of Guinea. Finally, the O1 amplitude is doubled in most of the Pacific Ocean, whereas it is generally weakened in the rest of the global domain. This complex pattern suggests that the chosen formulation of SAL is probably too simplified to be realistic, implying the necessity of a more rigorous formulation weighted by the modelled SSH harmonics (Ray, 1998).

Sea level coastal analysis

The capability of NEMO to model tidal waves in coastal areas is assessed through a comparison with both observations and the TPXO barotropic tidal model. In particular, we performed the model validation in two regions of interest: the North-West Atlantic Ocean and the Indonesian Seas. Indeed, both regions are characterised by strong tidal waves: the former is well known for the dissipative regime of internal waves on the mid-Atlantic ridge (Zilberman et al., 2009), while the latter is characterised by a very complex bathymetry and represents a challenge region to test new tidal implementations limits (Ray et al., 2005; Nugroho et al., 2018).

We compared the model output with data taken from the University of Hawai'i Sea Level Centre (UHSLC) tide gauges database (Caldwell et al., 2015). The selected tide gauges are characterised by hourly data continuously recorded for 9 months, from April to December 2017 (Appendix B reports the complete list), and a map of the locations is given in Figure 2.13: 32 sites satisfy the required conditions on the North-West Atlantic coast, and 19 tide gauges are used in the Indonesian area even though few of them are placed in the interior seas.
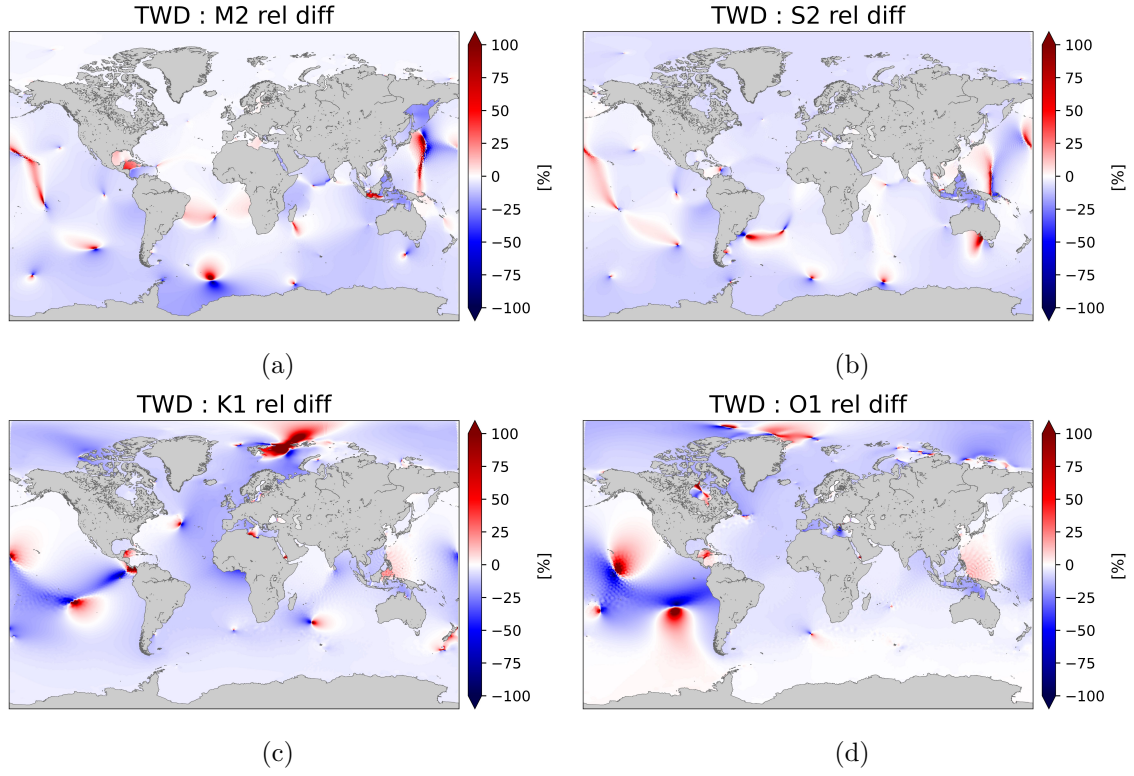
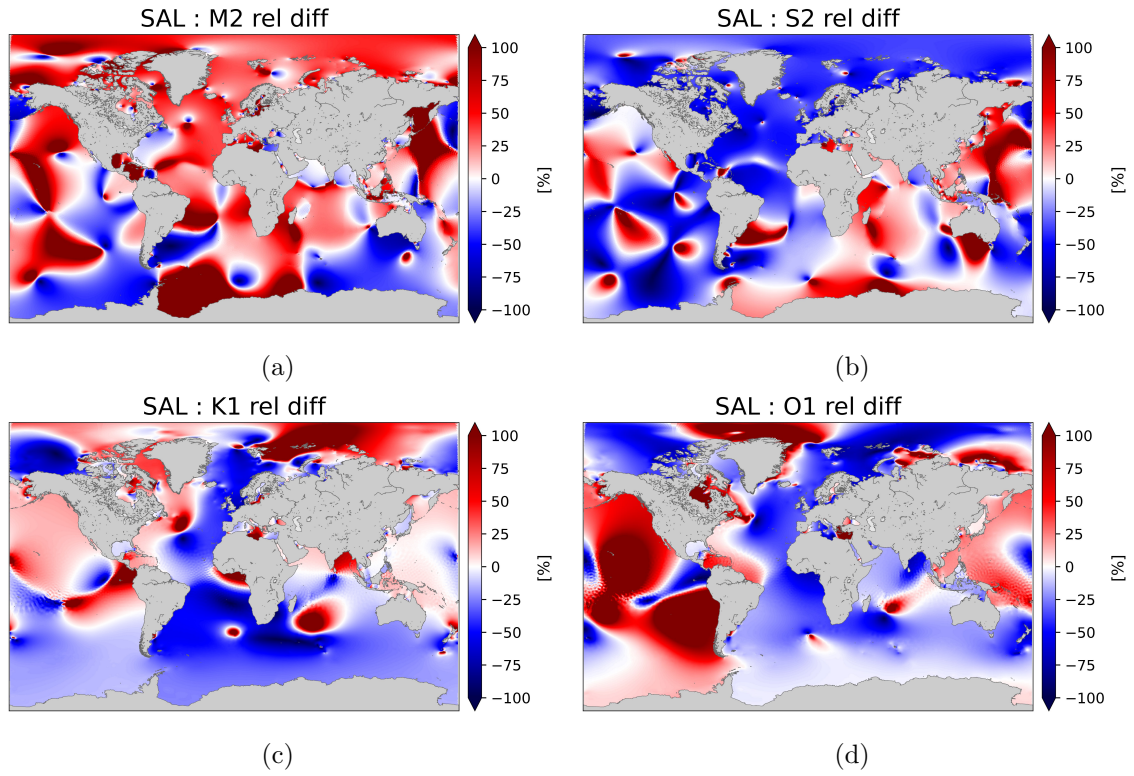Figure 2.11: Global maps of tidal amplitude relative differences between TIDE025_TWD and TIDE025.

Figure 2.12: Global maps of tidal amplitude relative differences between TIDE025_TWD_SAL and TIDE025_TWD.

2. The implementation of tidal parametrizations in NEMO

In order to validate the simulation, we compared the model output with observed data along the coasts. As for the open ocean case, the general behaviour was studied comparing TIDE025 and observations through scatter plots of amplitude and phase values, whereas specific comments are proposed on TIDE025_TWD and TIDE025_TWD_SAL to appreciate the effects of the TWD and the SAL. respectively. The differences between simulated and observed tides are quantified comparing for each site the vectorial distance computed as (Shriver et al., 2012)

$$d = \sqrt{\frac{1}{2}\left|A_m e^{i\phi_m} - A_o e^{i\phi_o}\right|^2} \tag{2.41}$$

where (A_m, ϕ_m) are the modelled tidal amplitude and phase, and (A_o, ϕ_o) the observed ones, and comparing for each area the root-mean-square distance computed as

$$RMSD = \sqrt{\frac{\sum_k^{TG} d_k^2}{N_{TG}}} \tag{2.42}$$

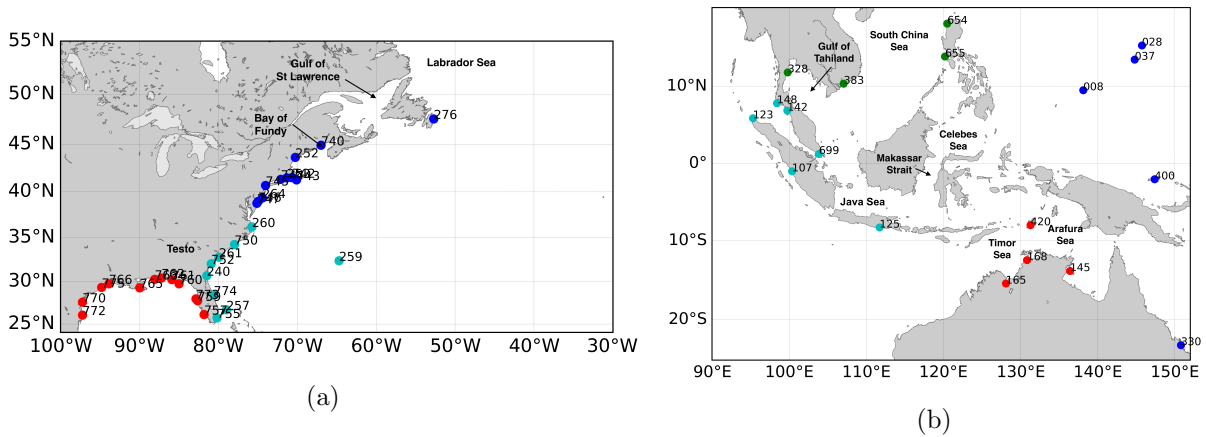where N_{TG} is the number of considered tide gauges.

Figure 2.13: Maps of the selected tide gauges in the (a) North-West Atlantic region and (b) Indonesian region.

North-West Atlantic region

Focusing on the North-West Atlantic region, the semidiurnal tides are dominant in the SSH signal, and Figure 2.14 shows a strong bias between TIDE025 and TPXO in the S2 component. Our model simulates greater amplitudes all around the basin from the open ocean to the coast, with maximum values in the Gulf of St. Lawrence and the Labrador Sea, where TIDE025 simulates waves of about 50 cm whereas in TPXO they are of about 15 cm. On the other hand, the M2 tides have a good match in the open ocean further south than 45°N, but they increase near the coasts moving toward the polar region. Differently, the K1 and O1 components are overestimated at lower latitudes (Fgures 2.14e-f and Figures 2.14g-h), especially in the Gulf of Mexico, and the amphidromic points of TIDE025 are positioned further north than TPXO.

It is interesting to notice the difference between TIDE025 and TIDE025_TWD presented in Figure 2.15. When the TWD is applied the tidal amplitudes decrease almost everywhere, with
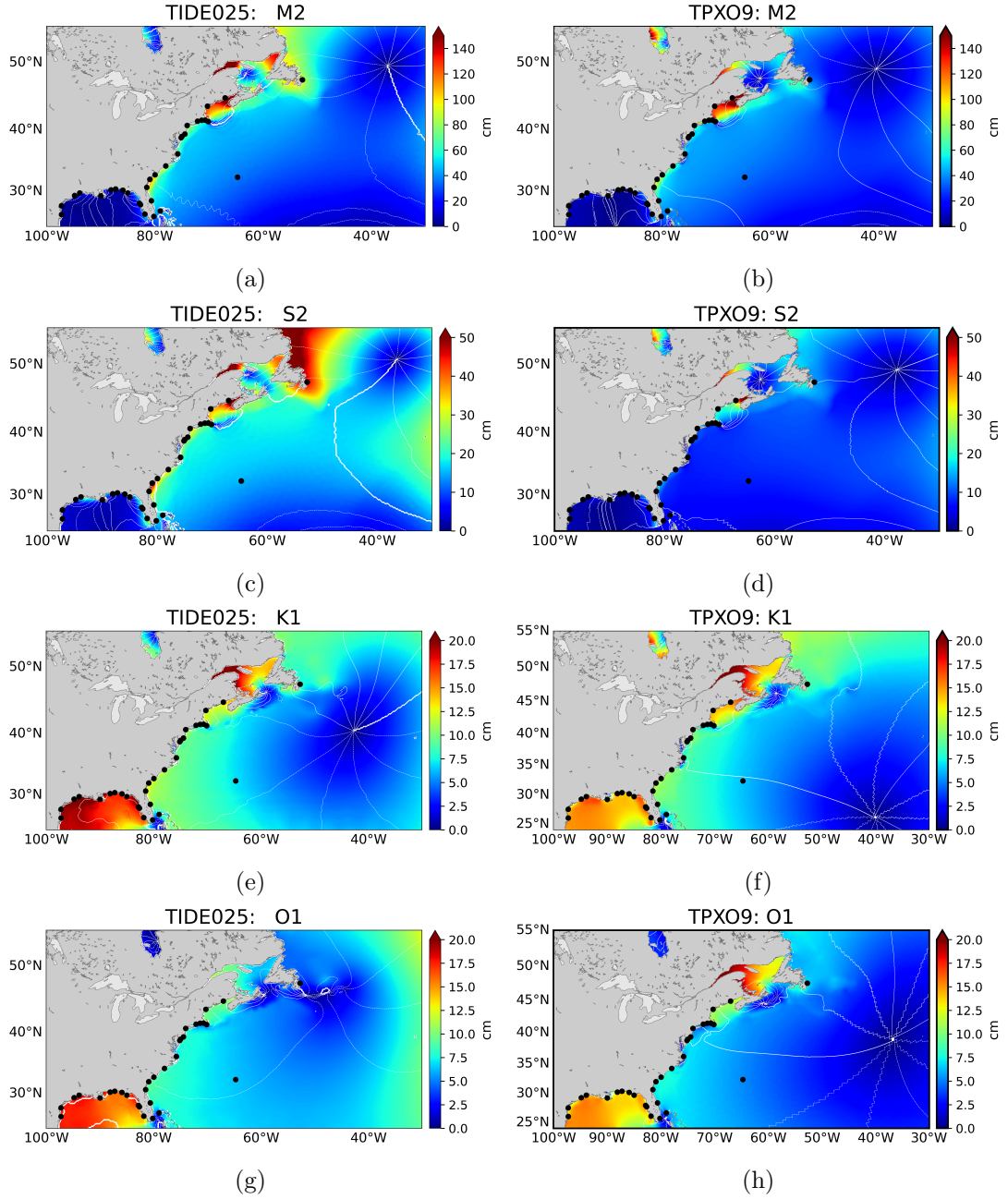
Figure 2.14: Maps of tidal amplitude and phase in the North-West Atlantic region in TIDE025 (*left* column) and TPXO9_v2 (*right* column).

the sole exceptions of the Gulf of Mexico for the M2 component, and the areas around diurnal amphidromic points. Nevertheless, the most notable difference involves semidiurnal tides outside of the New England continental shelf, where internal waves are dissipated by the TWD. The presence of internal tides in this region has been observed by Colosi et al (2001), and the TWD is particularly efficient due to the presence of the Gulf Stream that flows over the New England seamounts.

The differences between TIDE025_TWD_SAL and TIDE025_TWD are proposed in Figure 2.16: these maps show that the impact of SAL parametrization on the simulated tidal amplitude is
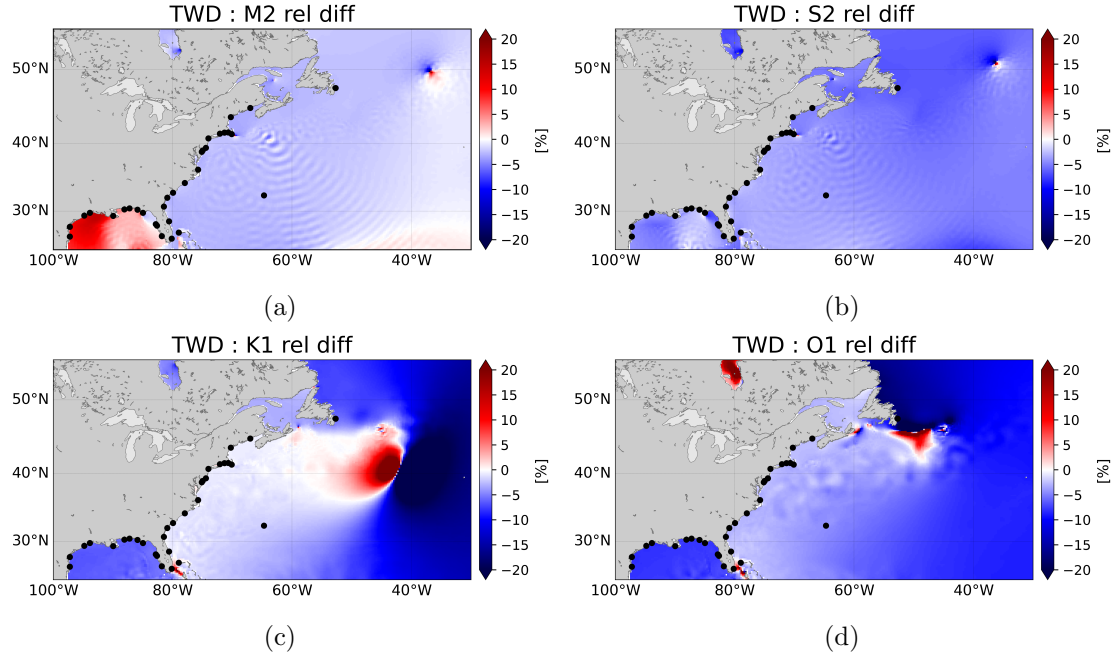
Figure 2.15: Maps of tidal amplitude relative differences between TIDE025_TWD and TIDE025 in the North-West Atlantic region.
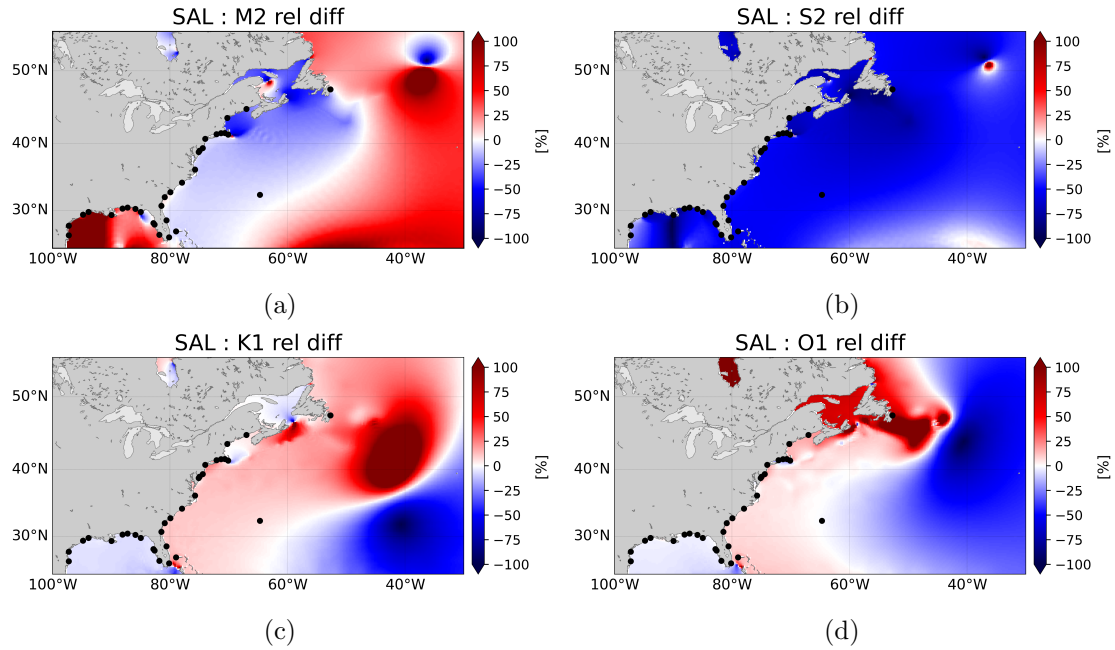

Figure 2.16: Maps of tidal amplitude relative differences between TIDE025_TWD_SAL and TIDE025_TWD in the North-West Atlantic region.

stronger than the TWD one (note the different palette compared to Figure 2.15). Diurnal tides generally increase near the coasts and weaken offshore, while the M2 component behaves in the opposite way. The S2 component is the only one that changes uniformly in space, decreasing by about 50-70% of its amplitude.
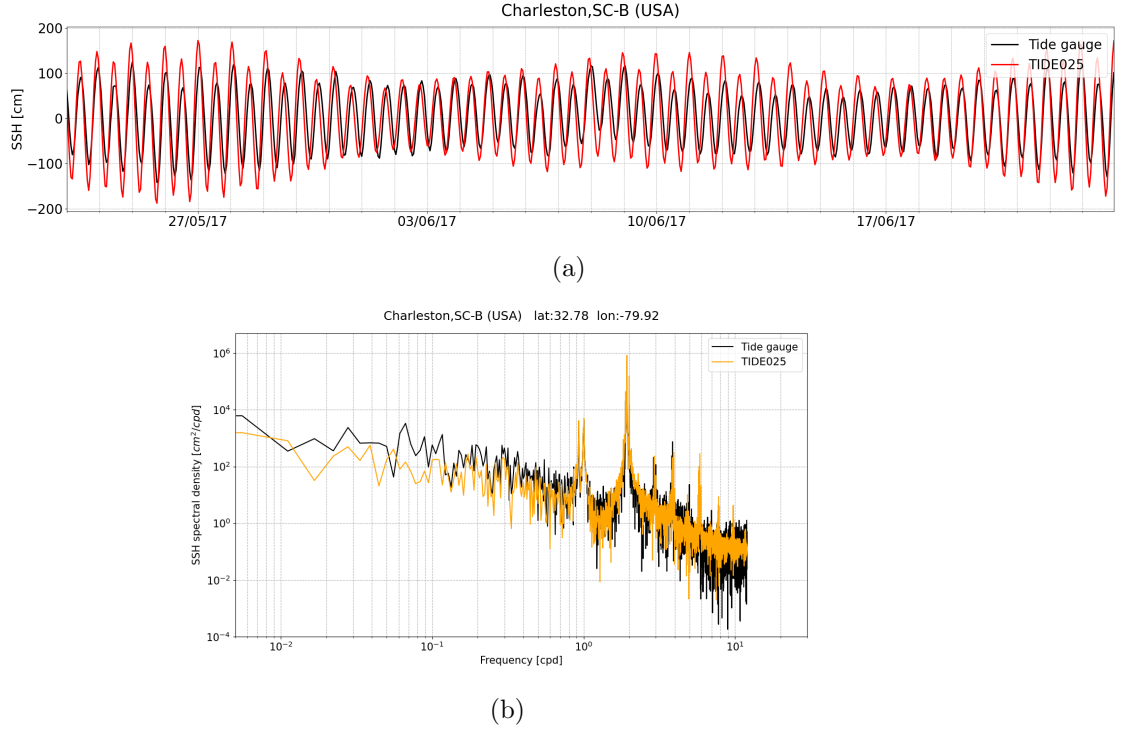
(a)

(b)

Figure 2.17: (a) Example of a typical SSH signal in the North Atlantic region with modelled data from TIDE025 and observed data from tide gauges measurement. The observed station is Charleston (USA) at 32.78°N and 79.92°W. The period of one month allows to appreciate the oscillation of spring and neap tides. (b) Periodogram computed during the period from 24$^{\text{th}}$ April to 20$^{\text{th}}$ December, 2017.

The modelled tides are now described along the coasts at tide gauges locations. In Figure 2.17, an example of SSH comparison is proposed together with its periodogram to summarise the typical differences and similarities between NEMO and observed data: the SSH variability is generally well reproduced by NEMO, with spring and neap tides oscillations that characterise all the plots. In this case the TIDE025 experiment overestimates semidiurnal tidal amplitudes, and the effect is enhanced during spring tides periods where M2 and S2 are summed up. Almost all the simulated timeseries have in common a phase delay compared to observed data. In this region, tide gauges from the UHSLC are point-by-point clustered in three different groups according to their geographical location: different behaviours are indeed presented further south or north than 37°N of the Atlantic coast, and a third group in the Gulf of Mexico is proposed to appreciate the differences between the Atlantic Ocean and a semi-enclosed sea. Figure 2.18 compares the tidal amplitudes and phases computed from the TIDE025 experiment to the observed values computing the amplitude linear regression as

$$A_m = b_1 A_o + b_0 \tag{2.43}$$

where b_0 and b_1 are the random error and regression coefficient, respectively. Figure 2.19 shows the vectorial distance in each site between model simulations and observations, and Table 2.4 summarises the RMSD in each area.

In this region, the modelled amplitudes of M2, K1 and O1 in TIDE025 are in good agreement with respect to observations (Figures 2.18a-e-g), whereas the S2 component is strongly overestimated with an amplitude regression coefficient equal to 1.87 (Figure 2.18c). Looking at the

phases, TIDE025 shows a lag that characterises all the constituents, more for semidiurnal cases than for the diurnal ones. Indeed, it contributes to the vectorial distance of the M2 and S2 components with a RMSD of 36.8 cm and 17.85 cm in the northern Atlantic coast, values more than doubled compared to TPXO. The worse simulation of M2 is found in New York (TG 745) where TIDE025 performs with a vectorial distance of 52 cm far from observation, whereas the better value is in Nantucket (TG 743), where our model works even better than TPXO. Looking now at the diurnal components, the typical amplitudes are smaller and thus the distances between TIDE025 and observations are scaled to few centimetres, but still double with respect to TPXO. The main outlier is the O1 component of St. John's (TG 276) where the d value rises to 7.8 cm. In this area of the Atlantic Ocean, TIDE025_TWD performs better than TIDE025 and improves the vectorial distance by about 1 cm for semidiurnal tides and 0.15 cm for diurnal tides. This difference demonstrates that the TWD has an impact along the coasts through the modification of barotropic currents in the open ocean. On the contrary, the experiment TIDE025_TWD_SAL performs differently according to the geographical location and the harmonic of interest. This experiment shows the worse results in the Bay of Fundy (TG 252 and TG 740), where the M2 vectorial distance is almost double than in TIDE025 case. When these tide gauges are neglected, the RMSD of this area is always the lowest among our experiments, probably due to a correction to the phase lag that reduces the overall d value.

The southern part of the Atlantic Ocean performs in the same way as the northern one, even though the RMSD slightly improves on average with values comparable to TPXO for K1 and O1 components. The worse performance comes from TIDE025 in Wilmington (TG 750) where the distance from data rises up to 72 cm for M2 and is higher than the mean values for all the other components. In this area the TWD parametrization keeps the vectorial distances almost unchanged, whereas the SAL decreases the RMSD down to values comparable with TPXO ones. It is worth noting that the S2 tide is here characterised by smaller amplitudes than M2 but the distance d is of the same order, making the relative error higher and the overall simulation worse.

In the Gulf of Mexico, instead, amplitude values overestimate observations and phase differences confirm a delay of TIDE025 that spreads all over the analysed tides. In this semi-enclosed sea the semidiurnal tides are smaller and characterised by smaller d values compared to the Atlantic Ocean (RMSD of 10 cm for M2 and 7.5 cm for S2), whereas diurnal tides are stronger and their RMSD are consistently worse (up to 6 cm for K1 and O1). The simulation of S2 and O1 is particularly improved when the SAL effect is considered, with the regional RMSD that is more than halved compared to TIDE025.

The vectorial distances associated with TIDE025_TWD experiment are on average smaller than the ones without TWD for all the tidal components, and the RMSD computed over all the observed areas confirms that the parametrization improves the model performance. However, TIDE025_TWD_SAL is the experiment were coastal tidal are closer to observations, with RMSD that are always lower than the other simulations, especially for the S2 component.

M2 (cm)				
Area	TIDE025	TIDE025_TWD	TIDE025_TWD_SAL	TPXO
Gulf of Mexico	9.95	9.93	14.43	1.99
South of 37°N	37.54	36.16	24.24	20.03
North of 37°N	36.80	35.85	41.47	15.52
	(36.89)	(35.90)	(29.98)	(17.05)
TOTAL	29.98	29.10	28.89	14.04
	(29.51)	(28.61)	(23.00)	(14.46)

S2 (cm)				
Area	TIDE025	TIDE025_TWD	TIDE025_TWD_SAL	TPXO
Gulf of Mexico	7.56	7.15	2.66	1.29
South of 37°N	17.29	16.77	7.47	3.31
North of 37°N	17.85	17.02	8.40	2.77
	(16.27)	(15.66)	(8.49)	(2.82)
TOTAL	14.66	14.07	6.53	2.52
	(13.86)	(13.36)	(6.42)	(2.52)

K1 (cm)				
Area	TIDE025	TIDE025_TWD	TIDE025_TWD_SAL	TPXO
Gulf of Mexico	5.35	4.98	4.17	2.54
South of 37°N	1.93	1.89	2.32	2.06
North of 37°N	2.10	1.95	1.87	1.27
	(1.92)	(1.78)	(1.76)	(1.38)
TOTAL	3.65	3.41	3.04	2.04
	(3.70)	(3.46)	(3.08)	(2.10)

O1 (cm)				
Area	TIDE025	TIDE025_TWD	TIDE025_TWD_SAL	TPXO
Gulf of Mexico	6.58	6.34	3.37	2.34
South of 37°N	2.38	2.19	1.61	1.31
North of 37°N	2.84	2.67	2.27	0.82
	(3.11)	(2.91)	(2.04)	(0.89)
TOTAL	4.54	4.35	2.60	1.66
	(4.68)	(4.48)	(2.56)	(1.71)

Table 2.4: RMSD between modelled tides (M2, S2, K1 and O1) and observed data from tide gauges in the North-West Atlantic region. Values in brackets are computed neglecting tide gauges from the Bay of Fundy (TG 252 and TG 740).
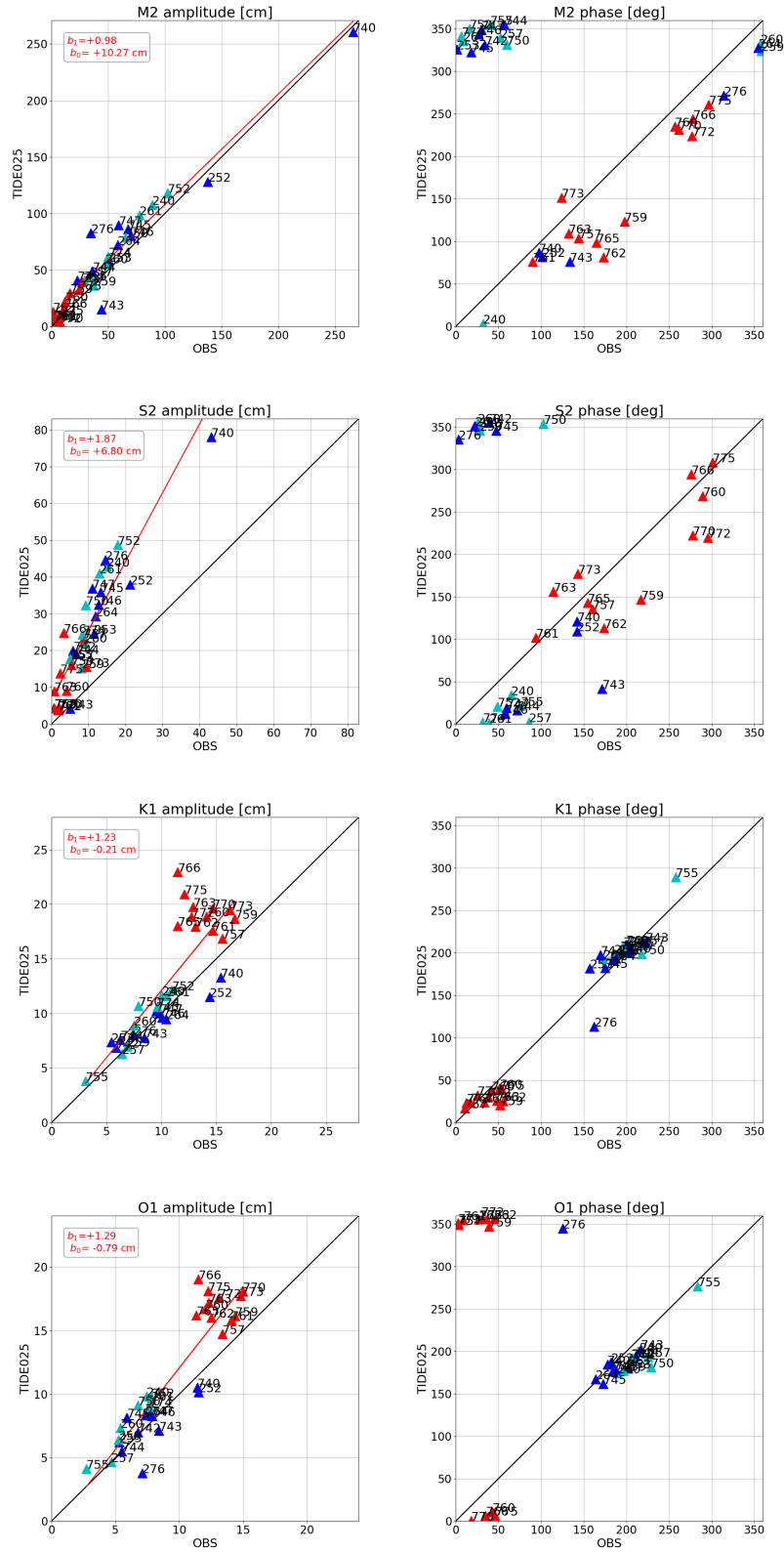
Figure 2.18: Scatter plots of the comparison between TIDE025 experiment and observed data on the North-West Atlantic region. Tidal components are compared looking at their amplitude (*left* column) and phase (*right* column). The red line represents the amplitude linear regression. Tide gauges are clustered together: north of 37°N (*blue*), north of 37°N (*cyan*), Gulf of Mexico (*red*).
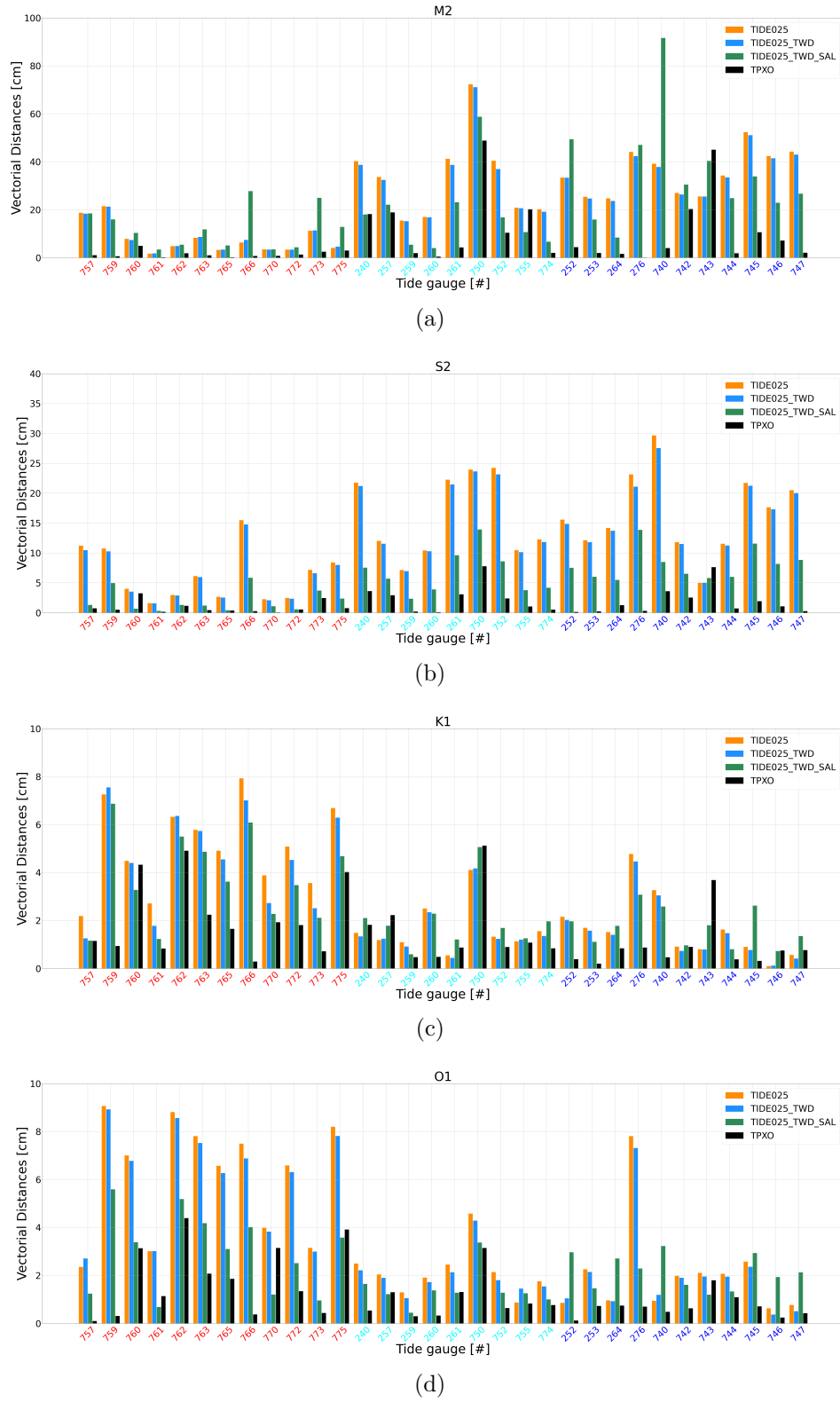
Figure 2.19: Vectorial distances between modelled and observed tidal components on the North-West Atlantic region. Tide gauges are clustered together: north of 37°N (*blue*), north of 37°N (*cyan*), Gulf of Mexico (*red*).
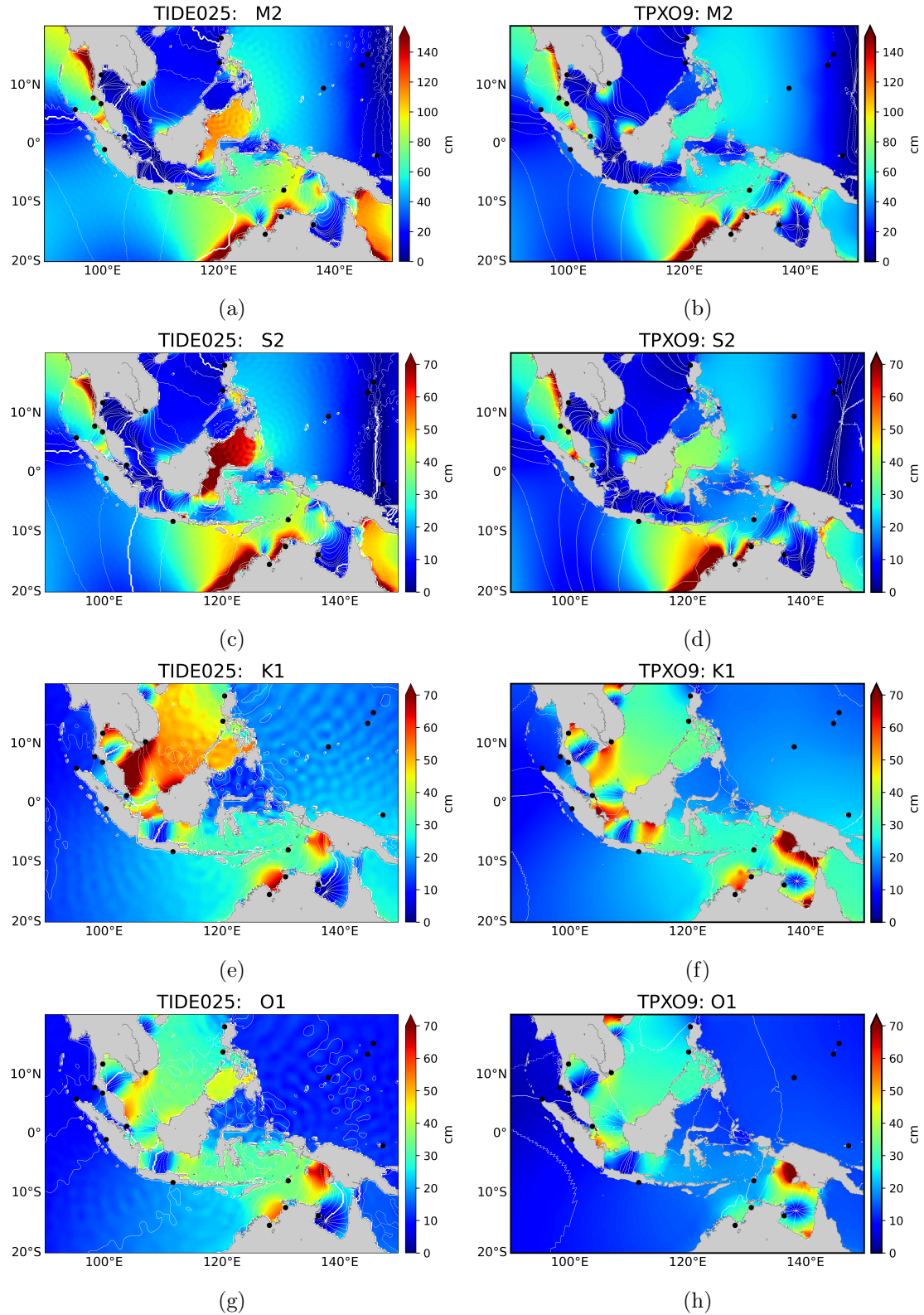
Figure 2.20: Maps in the Indonesian region of tidal amplitude and phase in TIDE025 (*left* column) and TPXO9_v2 (*right* column).

40

Indonesian region

A totally different behavior is simulated in the Indonesian region. This is a complex geographic area characterised by a series of large, deep, semi-enclosed basins connected via numerous narrow straits. Overall, the TIDE025 experiment well reproduces the TPXO atlas in the open ocean regions of the Pacific and Indian oceans, leaving the main differences in the interior seas (Figure 2.20). Here the complex geometry of the coastlines makes the simulation of tides difficult without any data constrain, and the NEMO model overestimates all the considered frequencies, with higher differences in the Coral Sea, the Celebes Sea and Makassar Strait for the semidiurnal components, and in the South China Sea for the K1 component. The sole exception to the general overestimation is the Arafura Sea north of Australia, where the K1 and O1 components are underestimated compared to the TPXO atlas. In TIDE025 internal tides are clearly present at all frequencies and contribute to the sea level amplitude with a wavelength of the order of hundreds of kilometres, whereas in TPXO this phenomenon is totally absent due to the barotropic structure of the model. This signal is partially removed in TIDE025_TWD (Figure 2.21) especially in the South China and Philippines Seas, but the major part of it remains to represent the propagated internal tides that reach the sea surface. Even though the TWD dissipates part of the generated internal tides, it also increases the overall M2 amplitude in the Java Sea, worsening the comparison with TPXO. Indeed, the coastline complexity traps the major part of internal tides within the interior seas making their entire energy available to the local mixing (Koch-Larrouy et al., 2007).
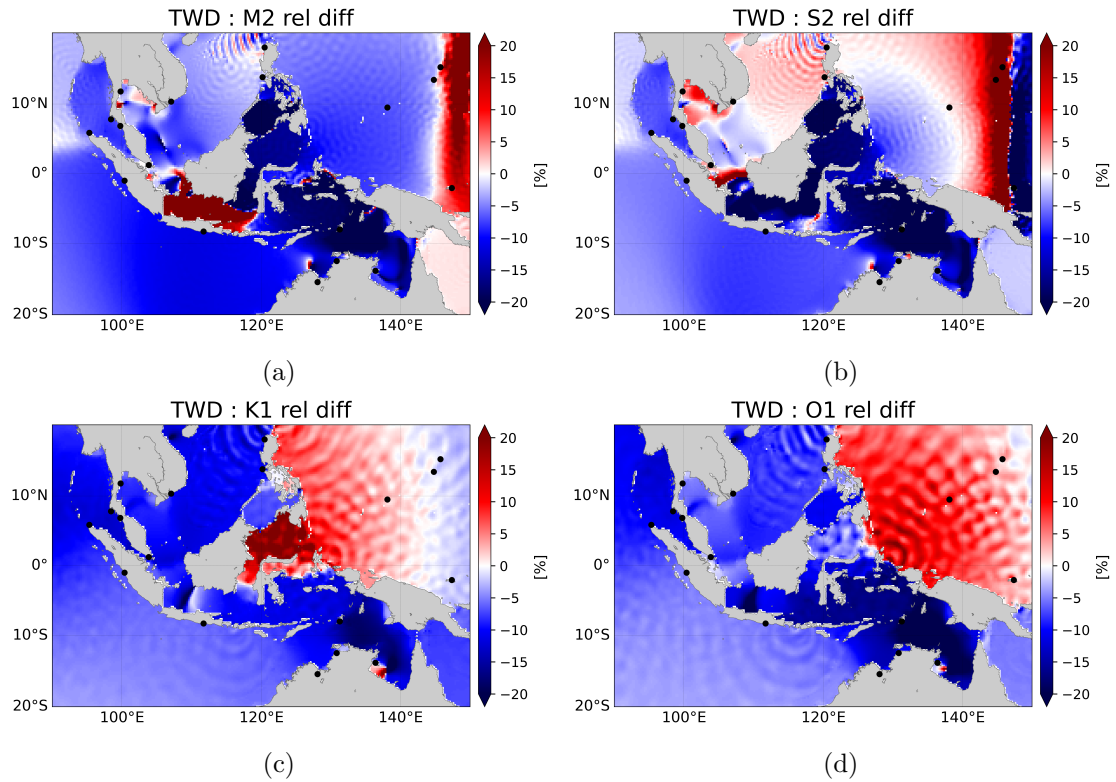

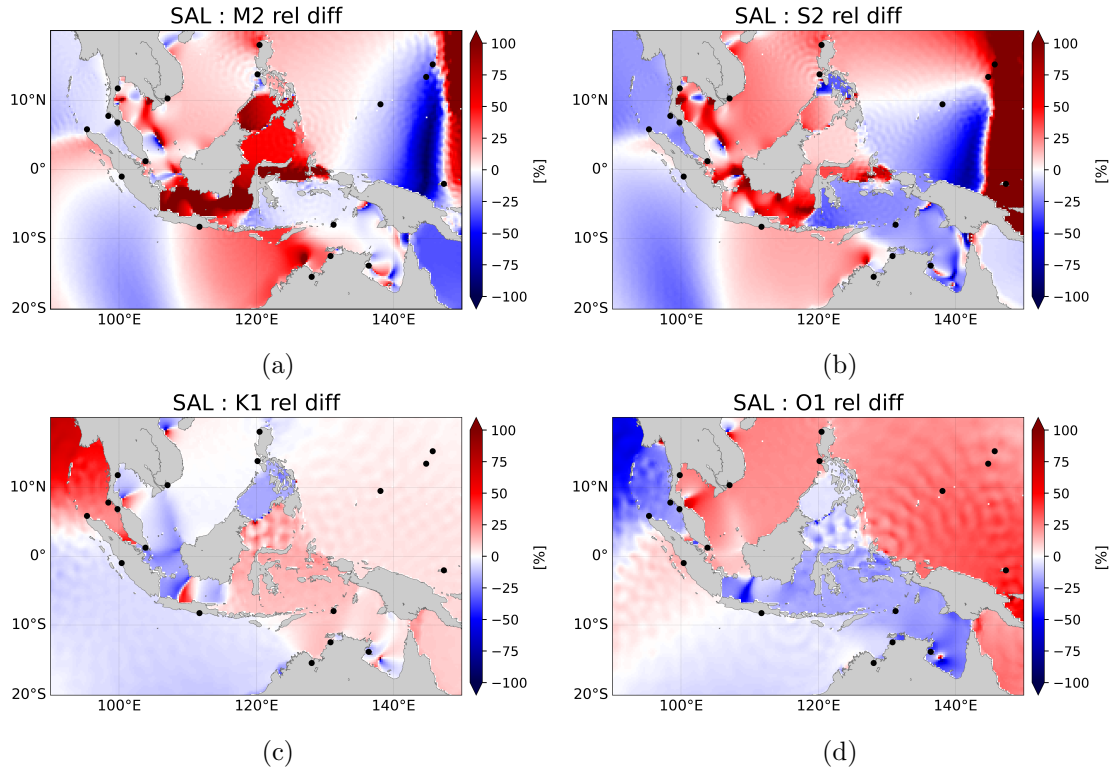Figure 2.21: Maps of tidal amplitude relative differences between TIDE025_TWD and TIDE025 in the Indonesian region.

Figure 2.22: Maps of tidal amplitude relative differences between TIDE025_TWD_SAL and TIDE025_TWD in the Indonesian region.

When SAL parametrization is included in the model (Figure 2.22) its effects at the surface are more intense than the TWD ones (note the different palette compared to Figure 2.21). The SSH relative differences between TIDE025_TWD_SAL and TIDE025_TWD show that semidiurnal tides increase in the South China Sea and Celebes Seas, the Makassar Strait, the Pacific Ocean north of 10°N and in the Indian Ocean south of Java, whereas they weaken in the Banda and Arafura Seas and north of New Guinea. On the contrary, diurnal tides differences are weaker (less than 20%) and generally decrease in the Indian Ocean and increase in the Pacific Ocean. Looking at the interior seas, instead, K1 signal is weaker in the South China Sea and reinforced in the other seas, whereas the O1 component behaves in the opposite way.

Modelled tides along the coast are then validated through the comparison with tide gauges from the UHSLC dataset. Unfortunately, during the period of interest, data are almost missing in the interior seas except in the South China Sea and in the Timor and Arafura Seas, where tide gauges are clustered together, so we enlarged our dataset also considering some neighbour points that are grouped according to the ocean they face (Figure 2.13). Table 2.5 summarises the RMSD computed in each site between models and observations, Figure 2.24 shows the vectorial distance associated with each tidal component in each site, and Figure 2.23 the related scatter plots for amplitudes and phases of TIDE025 with respect to observations.

The geographical complexity of the region makes the tidal simulations very complex, thus the amplitudes are often overestimated or underestimated compared to observations. Despite this difference, the phase biases are widespread and generally show a lag of TIDE025 with respect

to observations. Looking at TIDE025, the South China Sea is the area where the RMSD values are lower than the regional average, except for the K1 case characterised by high amplitudes as well as the highest errors. On the opposite side of the Indonesian region, the Australian coast is characterised by big vectorial distances. In Wyndham (TG 165) the errors of TIDE025 reaches the highest values of 145 cm associated with the M2 component, but also TPXO fails to reproduce these data with a vectorial distance greater than 1 m.

Looking at tide gauges that face on the Indian ocean, the amplitudes are well simulated, apart for Tanjong Pagar, Singapore, (TG 699) that does not really face the ocean, being trapped in the narrow Malacca Strait. On the Pacific side, all the analysed tides have lower errors than the regional average except in the case of Rosslyn Bay (TG 330) on the Australian East coast. Finally, most of the analysed sites show a weak decrease in the biases with observations when the TWD is applied. The TWD improves the model performance on the regional scale, with RMSD values that are always lower in TIDE025_TWD than in TIDE025. The main improvements are detected on diurnal tides, where the RMSD decreases everywhere with an average of about 1 cm, while the semidiurnal tides are improved on average but perform worse in the interior seas.

The overall impact of SAL on the regional tides is to increase the RMSD, but a large variability is observed depending on the area and the tidal component of interest. The worse performance is observed in Darwin, Australia (TG 168), where TIDE025_TWD_SAL has vectorial distances double compared to the other tidal experiments.

M2 (cm)				
Area	TIDE025	TIDE025_TWD	TIDE025_TWD_SAL	TPXO
South China Sea	7.78	9.75	8.08	3.76
Australian coast	78.82	79.89	76.78	51.27
Indian Ocean	36.74	35.09	38.01	3.70
Pacific Ocean	17.76	16.34	30.65	4.00
TOTAL	42.78	42.69	44.25	23.77

S2 (cm)				
Area	TIDE025	TIDE025_TWD	TIDE025_TWD_SAL	TPXO
South China Sea	4.88	5.49	3.07	1.37
Australian coast	36.56	36.55	40.41	24.99
Indian Ocean	16.01	15.72	17.01	1.47
Pacific Ocean	13.00	12.38	14.75	2.60
TOTAL	20.29	20.15	22.24	11.59

K1 (cm)				
Area	TIDE025	TIDE025_TWD	TIDE025_TWD_SAL	TPXO
South China Sea	20.81	18.56	25.61	3.78
Australian coast	17.13	16.74	21.26	9.23
Indian Ocean	8.19	7.88	8.92	1.78
Pacific Ocean	4.66	4.11	3.57	1.12
TOTAL	13.41	12.47	16.18	4.72

O1 (cm)				
Area	TIDE025	TIDE025_TWD	TIDE025_TWD_SAL	TPXO
South China Sea	8.43	8.05	14.73	1.47
Australian coast	16.20	14.30	12.41	5.05
Indian Ocean	11.65	11.17	9.30	2.34
Pacific Ocean	6.86	6.34	3.29	1.36
TOTAL	11.20	10.33	10.40	2.83

Table 2.5: RMSD between modelled tides (M2, S2, K1 and O1) and observed data from tide gauges in the Indonesian region.
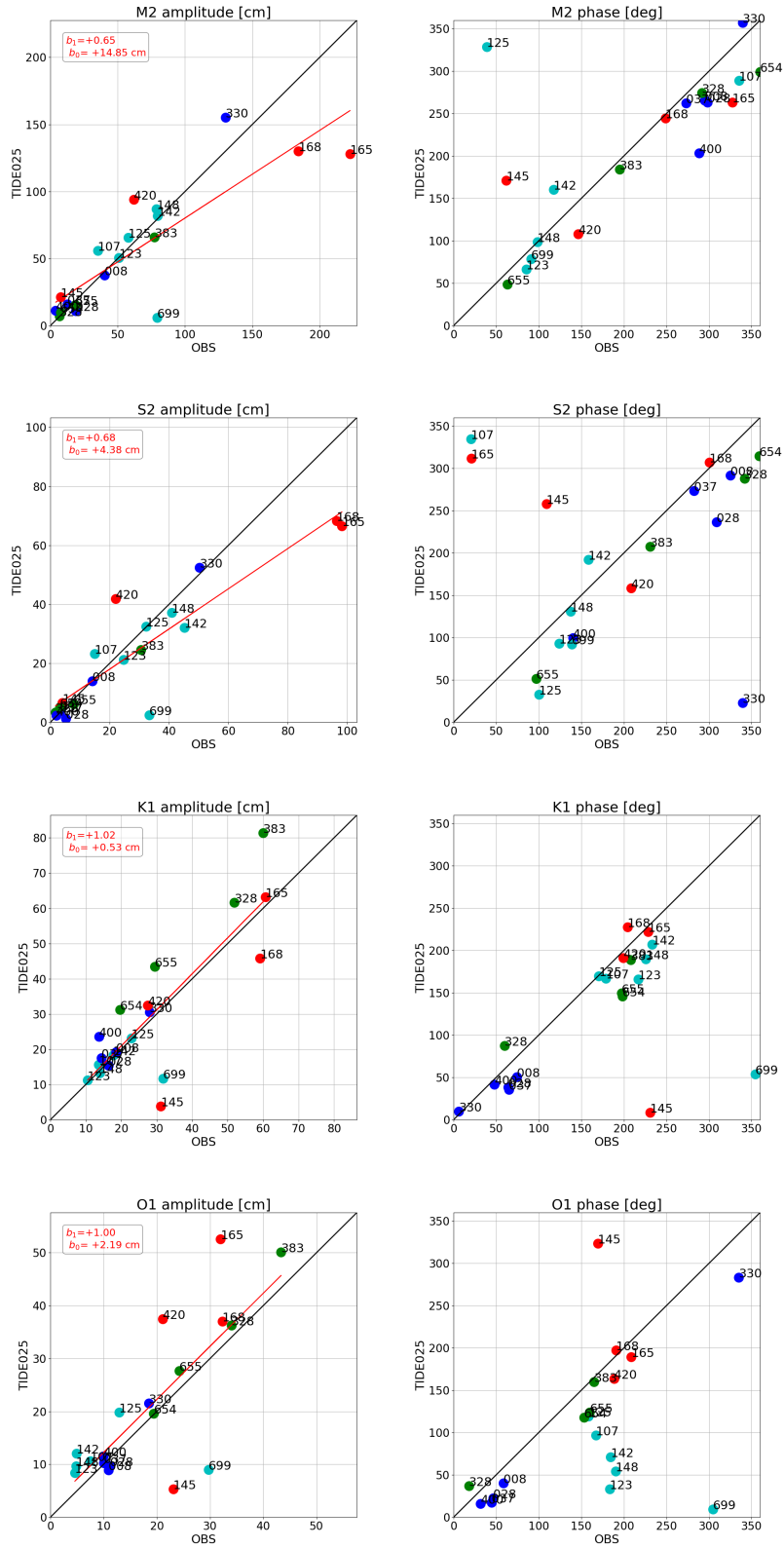
Figure 2.23: Scatter plots of the comparison between TIDE025 experiment and observed data in the Indonesian region. Tidal components are compared looking at their amplitude (*left* column) and phase (*right* column). The red line represents the amplitude linear regression. Tide gauges are clustered together: Indian ocean (*cyan*), Pacific ocean (*blue*), Aurstralian coast (*red*) and South China Sea (*green*).
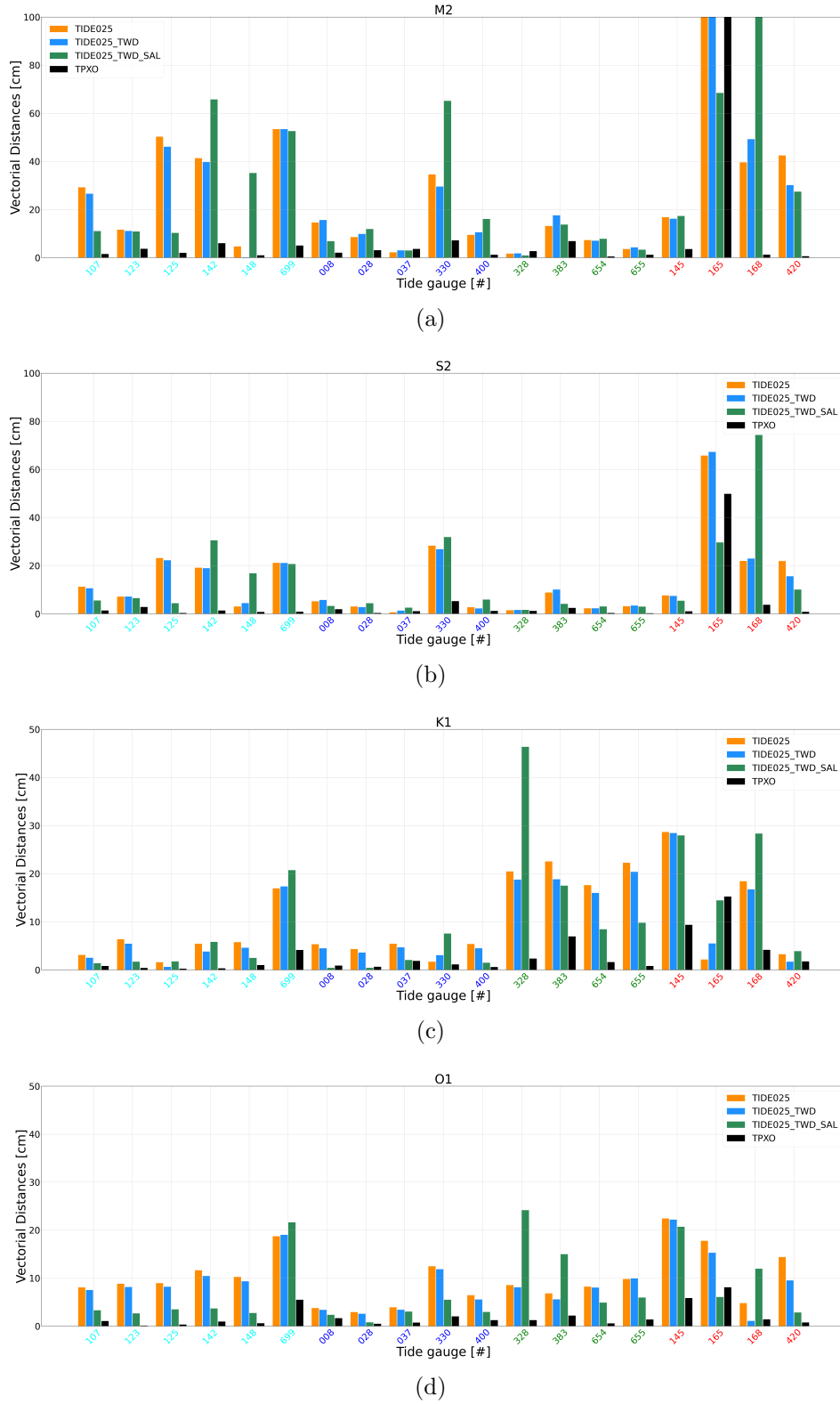
45

Figure 2.24: Vectorial distances between modelled and observed tidal components in the Indonesian region. Tide gauges are clustered together: Indian ocean (*cyan*), Pacific ocean (*blue*), Aurstralian coast (*red*) and South China Sea (*green*).

2.5 Conclusions

In the present work, we used a global configuration of the NEMO model at 1/4° horizontal resolution to integrate four numerical experiments which differ in the tidal forcing, and to assess the accuracy of simulated tides in this global ocean. We found that the tidal energy input increases the total energy budget by about 20% on the global scale, and the simulated tides are in general overestimated compared to the reference barotropic tidal model TPXO. Indeed, the main semidiurnal and diurnal components show regional amplifications especially at higher latitudes, despite the modelled tidal amplitudes properly reproduce the pattern proposed by the TPXO atlases. A possible justification could be the poor representation of sea ice in our configurations. Despite that, the modelled main differences could be caused by the horizontal resolution and the accuracy of the coastlines, that are crucial factors to properly reproduce tides but poorly represented in our model.

We found that our model is lacking some important processes that should be taken into consideration when tides are implemented, and we studied a parametrization to represent internal tides dissipation over rough topography. We are aware that this is just one of the possible processes involved in the interaction between internal tides and topographic features, but we consider it as a good starting point to improve the model performance. Other processes, such as internal tides propagation, reflection or blocking will be further analysed and possibly implemented in future studies.

A new parametrization for the dissipation of internal tides over unresolved bathymetry features is then implemented in NEMO following the work done by Shakespeare et al. (2020). We demonstrated that the tidal energy decreases on the global scale, and the energy lost is the result of the energy conversion from barotropic to baroclinic tides, that in turn break to enhance the ocean mixing near the wave generation site. From the literature we know that this process takes place in the open ocean, and we found that the TWD we used is more efficient in regions of sharp bathymetry roughness than in regions where it is widespread. A possible improvement of the TWD formulation will also include the bathymetry anisotropy with respect to the mean flow orientation as suggested by Choi and Hong (2015).

Looking at the bottom stress distribution, the TWD increases the simulated drag on the open ocean, but at the same time it weakens the barotropic flow in shallow regions causing a general decrease in the bottom friction. This is an interesting implication that deserves a deeper analysis but for the time being confirms the hypothesis that the TWD changes the tidal behavior even near the coasts. Indeed, the comparison with tide gauges data confirms that the TWD decreases the mean vectorial distance between modelled and observed tides in regions of well-known dissipative waves.

We found that the implemented TWD correctly removes internal tides in the Atlantic Ocean, and its efficiency is confirmed looking at the tidal amplitude in the open ocean, where internal tides at the semidiurnal frequency are (at least partially) removed from the SSH. These results are evident in the North-West Atlantic region, where internal tides are dissipated near the New England seamounts, whereas in the Indonesian region the situation is more complex. In this

case we found that the parametrized TWD limited to the dissipative regime is not the proper formulation to be implemented in this area. Indeed, a high variety of islands are here associated with a complex bathymetry of the interior seas, and tides (both barotropic and baroclinic) are often trapped inside and make the simulation more difficult. If we want to improve the baroclinic waves regional representation, we should then act on two main factors: the first is to increase the model resolution, while the second is to include different regimes in the current version of the TWD. The latter solution anyway, needs to know a priori the typical decay time of internal tides, α term in (A.4), rising again the necessity to involve some a priori information about the tidal energy distribution.

Finally, we performed a last simulation to introduce the self-attraction and earth-loading effects of ocean tides. The chosen formulation is a scalar approximation proposed by Accad and Pekeris (1978) making the strong assumption that the SAL phenomena are dominated by a specific spatial scale. The KE decreases slightly when it is globally integrated, but we found that the SAL effect changes with depth, weakening the KE density at the surface and reinforcing it near the bottom. A baroclinic behaviour of this type has not been documented in the literature, at least to our knowledge, however we plan more accurate analysis to understand if this phenomenon is due to physical processes or to the specific approximation applied. Looking at the bottom stress, the main impact is placed in shallow areas and in regions of strong mesoscale activity, as the Gulf Stream and the Antarctic Circumpolar Current.

The SAL effect usually reduces the magnitude of the tidal potential (Arbic et al., 2018), whilst we found that the tidal amplitude is strongly variable depending on the region and the tidal component of interest. In the North-West Atlantic, the comparison with tide gauges data is generally improved by the SAL implementation, whereas in the Indonesian region the simulated tidal quality is strongly space dependent. In the latter region, indeed, the topography is very complex making the scalar approximation prone to large errors. Trying to improve the SAL parametrization, we could then change the β scalar coefficient in (2.22) making it space and time dependent.

Chapter 3

Global tides and Atlantic Overturning Circulation

3.1 Introduction

The tidal forcing acts on the global ocean moving the water volume back and forth with a frequency of one or more cycles per day. The induced motion influences the mean circulation, so that the observed three-dimensional global ocean shows a continuum spectrum of energy that peaks at the near-inertial and tidal frequencies (Garrett and Munk, 1975; Müller et al., 2015) describing the variety of phenomena occurring inside the ocean at different time and spatial scales. These dynamical features interact with each other and generate a direct and inverse cascade of energy between larger and smaller scales.

The interaction between tides and mesoscale eddies or fronts was extensively analysed during the last decades (Chavanne et al., 2010; Callendar et al., 2011; Dunphy and Lamb, 2014; Jensen et al., 2018), and many studies described the impact of the mean flow on the propagation of barotropic and baroclinic tides (Kelly and Lermusiaux, 2016; Kelly et al., 2016; Dossmann et al., 2020). Despite that, only few studies focused on the impact of tidal waves on the mean circulation, and they are mainly limited to coastal areas (Xuan et al., 2016) or near abyssal hills (Shakespeare, 2020). We aim to assess whether the tidal motion influences time scales longer than its typical oscillation, and if it does, how the mean circulation changes on the basin scale.

We focus on the Atlantic Ocean, as its large system of currents plays a crucial role on the global circulation and thus on the global climate system (Frankignoul et al., 2013; Jackson et al., 2015). Within this basin, tides propagate at a dominant semidiurnal frequency and rotate cyclonically around the amphidromic points placed in the middle of the North and South Atlantic. Internal tides in the open ocean are detected at the same frequency and are generated by the interaction of barotropic tides over rough topographic features on the continental shelves (Colosi et al., 2001), the Mid-Atlantic ridge (Vic et al., 2018), or other offshore topographic structures (Löb et al., 2020). These waves are partially dissipated near the generation site, whereas the remaining portion radiates away leading to possible interactions with the mean circulation of the basin.

3.2 The Atlantic Ocean circulation

Looking at time scales longer than the tidal ones, the horizontal circulation of the Atlantic Ocean is characterised by wind-driven currents arranged to form three gyres, two subtropical and one subpolar. The North Atlantic subtropical gyre rotates anticyclonically (opposite to the tidal propagation along the coasts) and its circulation is boundary intensified on the western side to form the Gulf Stream. The other branches are composed by the North Atlantic Current in the north, the Canary Current along the east and the Atlantic North Equatorial Current in the south.

Moving to higher latitudes, the subpolar gyre rotates cyclonically and is constrained into the northern North Atlantic by the North Atlantic Current. In this region the ocean dynamics is very complex, and currents are forced by winds as well as by buoyancy contrasts and overflows from marginal seas (Treguier et al., 2005).

To complete the description, the South Atlantic subtropical gyre rotates cyclonically and is composed by the western boundary intensified Brazil Current, the Antarctic Circumpolar Current, the Benguela Current and the Atlantic South Equatorial Current.

Looking at the vertical circulation, the Atlantic Ocean is characterised by two cells that move different portions of the ocean and are opposite rotating (Figure 3.5 shows how they are simulated in our experiments). These cells contribute to the global Meridional Overturning Circulation (MOC) as a complex dynamical system that transports heat northwards throughout the basins and sinks carbon and nutrients into the deep ocean (Talley, 2013; Cessi, 2019). A sketch of the global overturning is proposed in Figure 3.1 together with the driving processes of the Atlantic MOC.
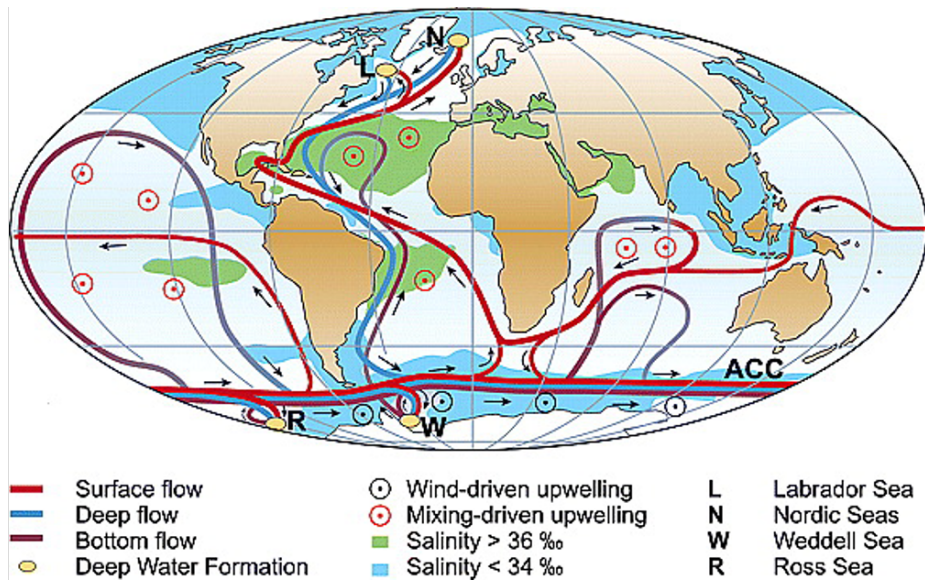

Figure 3.1: Simplified sketch of the global overturning circulation system. Reproduced from Kuhlbrodt et al. (2007).

The first cell moves clockwise and extends in the mid-depth region of the whole basin between around 350 m and 3000 m. In the Antarctic circumpolar region, it is driven by dense Antarctic Bottom Water which is first brought up by mixing and then upwelled to the surface by strong westerly winds (Marshall and Speer, 2012; Hogg et al., 2017). Then the flow moves northward near the surface driven by the Benguela Current, the Gulf Stream, and the North Atlantic Current toward the Arctic Ocean. In this region, intense buoyancy loss and mixing move water from the surface to the deeper ocean to form the North Atlantic Deep Water (Killworth, 1983; Rhein et al., 2002). This water characterises the lower branch of the overturning cell, so the flow returns southward at depth below 2000 m until it reaches again the Southern Ocean.

As stated by Kuhlbrodt et al. (2007) in their extensive review of the driving processes, diapycnal mixing and wind-driven upwelling at the higher latitudes are the main drivers of the Atlantic MOC. Despite that, many other processes contribute to the meridional circulation, such as heat and freshwater fluxes at the surface and internal waves propagation. Other accurate reviews of the Atlantic MOC are proposed by Lozier (2012) and Buckley and Marshall (2016), where the variability of the driving processes and the related heat transport are analysed.

The second overturning cell is weaker than the mid-depth one, moves anticlockwise and lies in the abyssal ocean below 3000 m. It is fed by the formation of Abyssal Antarctic Bottom Water at the highest latitudes of the Antarctic region and is balanced by diapycnal upwelling in the interior of the Atlantic near sloping topography (Mashayek et al., 2015).

The variability of the Atlantic MOC and its role on the global climate system has been widely investigated (Srokosz et al., 2012; Winton et al., 2013; Jackson et al., 2015; Chen and Tung, 2018) and different observational systems have been recently developed to monitor its transport variability Cunningham et al. (2007); Lozier et al. (2017); Frajka-Williams et al. (2019).

In the present study, we are mainly interested to the mid-depth overturning cell since its interaction with tides is expected to be more detectable on decadal time scales.

3.3 Model configuration and experiments

The effects of barotropic and internal tides on the ocean mean circulation was studied using the global ocean general circulation model NEMO v3.6 (Madec and the NEMO team, 2016).

Starting from a reference simulation equivalent to CTR025 described in Chapter 2, we performed a longer experiment, MOCCTRL, initialized in January 1958. The initial conditions were provided by temperature and salinity climatologies from the WOA13_v12 dataset (Locarnini et al., 2013; Zweng et al., 2013), and the ocean started from a rest state. The main difference between CTRL025 and MOCCTRL regarded the sea ice initial condition, that was here based on observed data. The ocean was forced by the JRA55-do reanalysis v1.4 (Tsujino et al., 2018) from 1958, with 3-hour atmospheric fields and daily freshwater runoff information.

Using an analogous configuration of the same model, Iovino et al. (2016) argued that a period of 10 years was long enough to equilibrate the Atlantic mid-depth meridional circulation with transport values comparable to observations. Accordingly, we integrated a period of 22 years after which we separated the experiment in three configurations, simulating the Atlantic circulation

with and without tides from 1980 to 2007:

- in MOCTIDE1 we included the astronomical forcing associated to 11 tidal constituents (M2, S2, K2, N2, K1, O1, Q1, P1, Mm, Mf, M4, see Table 2.1). The resulting experiment was similar to TIDE025 described in Chapter 2, except for the integration period and the bottom turbulent kinetic energy parameter, which was the same of MOCCTRL ($e_b = 2.5 \times 10^{-3}$ m/s in eq (2.24)). The differences between MOCTIDE1 and MOCCTRL were therefore associated only to tidal introduction;

- MOCTIDE2 was equivalent to MOCTIDE1 with the addition of the TWD and the bottom friction correction inside the barotropic mode, as proposed in Sections 2.3.1 and 2.3.2.

Based on previous results on similar configurations (Chapter 2), we considered a spin-up period of 12 months as necessary to stabilize the interactions between tides and the surrounding flow. The analysis is then performed during the 1981-2007 period, storing data on monthly average. We are aware that this span of years is short to properly simulate the deep ocean properties in general, even without tides, but it allows to capture the tidal contribution to the Atlantic MOC transient behaviour.

The main experiment characteristics are then summarised in Table 3.1.

Experiment	Tidal forcing	friction corr	TWD	IC	Period
MOCCTRL	NO	NO	NO	T,S climatology U,V=0	1958 - 2007
MOCTIDE1	YES	NO	NO	MOCCTRL	1980 - 2007
MOCTIDE2	YES	YES	YES	MOCCTRL	1980 - 2007

Table 3.1: Description of the different simulations and their main characteristics.

3.4 Global and Atlantic kinetic energy

The ocean energy balance involves many processes at different temporal and spatial scales (Munk and Wunsch, 1998), so we propose an overview of the tidal effects on the general circulation comparing the total kinetic energy (KE) with respect to its temporal mean component (MKE). To define the scalar quantities of interest, the velocity field is decomposed as its mean and residual terms $\boldsymbol{u} = \langle \boldsymbol{u} \rangle_{3m} + \boldsymbol{u'}$, where the operator $\langle \cdot \rangle_{3m}$ defines the temporal average over three months (one season) of simulation, so the resulting KE and MKE definitions are

$$\langle MKE \rangle_{3m} = \int_{V_{tot}} \frac{1}{2} \rho_0 \left(\langle \boldsymbol{u} \rangle_{3m} \cdot \langle \boldsymbol{u} \rangle_{3m} \right) dV \tag{3.1}$$

$$\langle KE \rangle_{3m} = \int_{V_{tot}} \frac{1}{2} \rho_0 \langle \boldsymbol{u} \cdot \boldsymbol{u} \rangle_{3m} \, dV \tag{3.2}$$

$$= \langle MKE \rangle_{3m} + \int_{V_{tot}} \frac{1}{2} \rho_0 \langle \boldsymbol{u'} \cdot \boldsymbol{u'} \rangle_{3m} \, dV \tag{3.3}$$

Since the KE is computed runtime and seasonally averaged, it includes all the processes with period longer than few model time steps. On the contrary, the MKE is computed from the seasonal mean of the velocity field, where the contribution of eddies, gyres and periodic motions is filtered out due to the time window length. The difference between KE and MKE corresponds then to the eddy kinetic energy (EKE). Table 3.2 reports the temporal mean of all the analysed variables.

Looking at the entire 27-year period, the global KE timeseries in Figure 3.2 have characteristics similar to the shorter experiments analysed in Chapter 2, even though in this case the spring-neap cycle is masked by the temporal average. The interannual variability does not change significantly between the experiments, with weak oscillations during the periods 1985-1986 and 1990-1996, and sharp peaks in 1982, 2003 and 2004. The KE in MOCCTRL (mean 2.318×10^{18} kg m^2/s^2) is in good agreement with the results of Iovino et al. (2016), who used a different configuration of the same model (note that they computed the KE averaged over the global volume per unit of density, so the conversion requires a factor $\rho_0 V_{tot}$). On the other hand, the tidal experiments enhance the KE by about 19.6% (MOCTIDE1) and 16% (MOCTIDE2). In the latter case, as expected, the TWD dissipates part of the tidal energy.

Likewise, the MKE shows a well-defined seasonal variability (Figure 3.3) and the three experiments have comparable values during the entire period, with a negligible mean difference between MOCCTRL and MOCTIDE1 (+0.2%). This result implies that the tidal energy input at the global scale contributes only to the EKE (as expected looking at the tidal timescales) and probably acts to modify eddies, gyres and in general dynamical structures that are neglected by the MKE. A similar result is obtained in the Atlantic Ocean north of 34°S (Figure 3.4), but in this case the MKE is slightly weakened by tides (-1.2%), especially when the TWD is applied (-2.6%). As pointed out in Section 3.5, this is an effect of the averaging over a wide volume and suggests that the mean circulation is slightly weakened.

Kelly et al. (2016) and Pan et al. (2021) demonstrated that in the Atlantic Ocean internal tides interact with the mean flow modifying it and being modified at the same time. Since internal tides strongly interact also with eddies and fronts, these considerations could be linked together: the mean currents could change because of tidal interactions at the mesoscale through a shift of their pathway rather than a modification of their intensity. Indeed, Müller et al. (2010) found that the Gulf Stream flow is splitted differently when tides are implemented in their climatological model, improving the representation of the subpolar front with respect to observations. This hypothesis has no evidence in our simulations, but it would be interesting to study it in other experiments with eddy-resolving configurations.

	MOCCTRL	MOCTIDE1	MOCTIDE2
KE	2.318	2.771	2.688
MKE	1.383	1.385	1.367
MKE*	0.203	0.200	0.198

Table 3.2: Temporal mean of global KE, MKE, and Atlantic MKE (denoted with *) expressed in units of 10^{18} kg m^2/s^2. Data refers to the period 1981-2007.
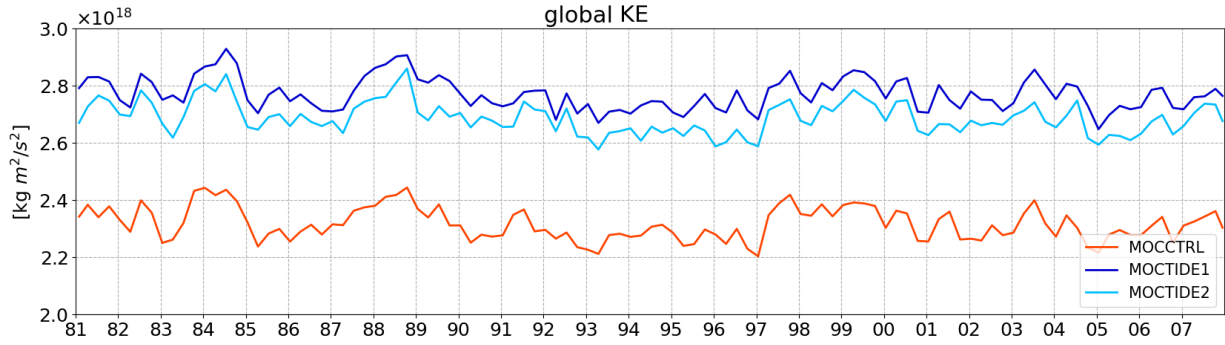
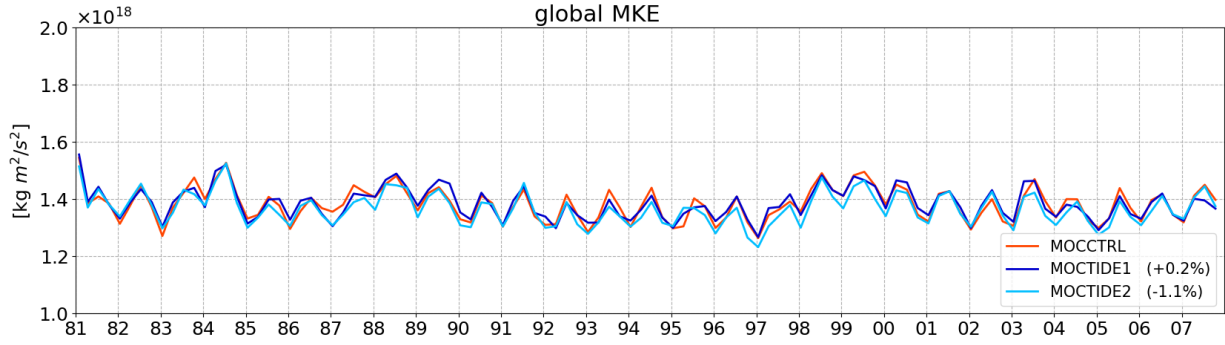Figure 3.2: Timeseries of KE seasonally averaged and globally integrated.

Figure 3.3: Timeseries of seasonal MKE globally integrated. In the legend, each value in brackets corresponds to the mean percentage increment with respect to the reference experiment MOCCTRL.
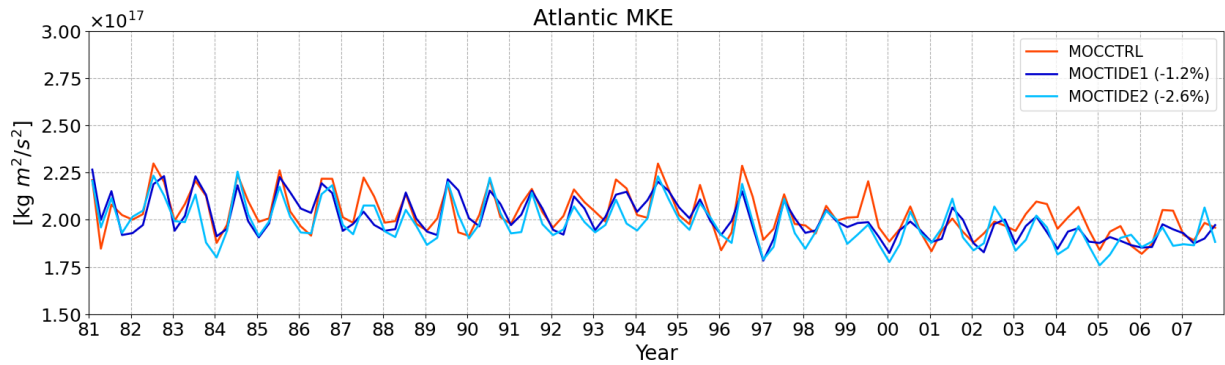

Figure 3.4: Timeseries of seasonal MKE integrated over the Atlantic Ocean north of 34°S. In the legend, each value in brackets corresponds to the mean percentage increment with respect to the reference experiment MOCCTRL.

3.5 Atlantic MOC transport

3.5.1 Climatology and interannual variability

The Atlantic meridional circulation is commonly quantified as the zonally and vertically integrated meridional volume transport in depth coordinates

$$\psi(y,z) = -\int_{-H}^{z} \int_{x_w}^{x_e} v(x,y,z')\, dx\, dz' \tag{3.4}$$

where x_w and x_e are the basin zonal boundaries.

The temporal average over the entire analysis period (1981-2007) is computed for each experiment and the resulting overturning structures are shown in Figure 3.5. Our analysis is limited to the region north of 34°S, where the Atlantic is zonally bounded by land. Indeed, south of this latitude, the obtained transport includes the contribution of the Antarctic Circumpolar Current across the open boundaries, and thus masks the processes that occur within the domain. We are aware that the Southern Ocean plays a crucial role on the global overturning circulation (Wolfe and Cessi, 2010; Marshall and Speer, 2012; Johnson et al., 2019), but using this method we can't appreciate the processes involved in the region.

Despite that, the model well reproduces the structure of the Atlantic MOC (Lumpkin and Speer, 2007; Talley, 2013; Buckley and Marshall, 2016), with a mid-depth cell in the upper portion of the ocean, and an abyssal cell that spans down to the bottom. In particular, the mid-depth cell moves water masses clockwise, with northward transport in the upper limb between the surface and 1000 m depth, and the lower limb that moves southward down to 3400 m. The maximum transport associated to this cell is called AMOC and it is quantified in depth coordinates as

$$\text{AMOC}_z = \max\,\psi(y,z) \quad . \tag{3.5}$$

It represents the balance between the northward and southward flowing waters, moving respectively above and below the depth of maximum overturning (Frajka-Williams et al., 2019).

In our simulations the AMOC_z is always located at 32.5°N and the associated value is 18.36 Sv in MOCCTRL, 17.90 Sv in MOCTIDE1 and 17.80 Sv in MOCTIDE2. These estimates are in good agreement with observations that place the cell maximum around 30°N and its transport between 18 Sv (Lumpkin and Speer, 2007; Talley, 2013) and 19 Sv (Cessi, 2019).

On the other hand, the abyssal cell represents a counterclockwise circulation with northward flow on the lower branch located near the bottom of the ocean. In this case the observed transport is more uncertain, but the value proposed by Talley (2013) (maximum of 7 Sv at 32°S) is far from being reproduced in our experiments, where the cell peaks to 3 Sv north of 30°S.

The overall Atlantic MOC structure is the same between experiments during the 1981-2007 period, but the cells magnitude changes when tides are implemented and Figure 3.6 shows how. The mid-depth cell is weaker in MOCTIDE1 than in MOCCTRL (Figure 3.6a) since the AMOC_z decreases of about 0.66 Sv. The difference is even larger between MOCTIDE2 and MOCCTRL (Figure 3.6b), where the enhanced dissipation of internal tides decreases the AMOC_z of 0.72 Sv.
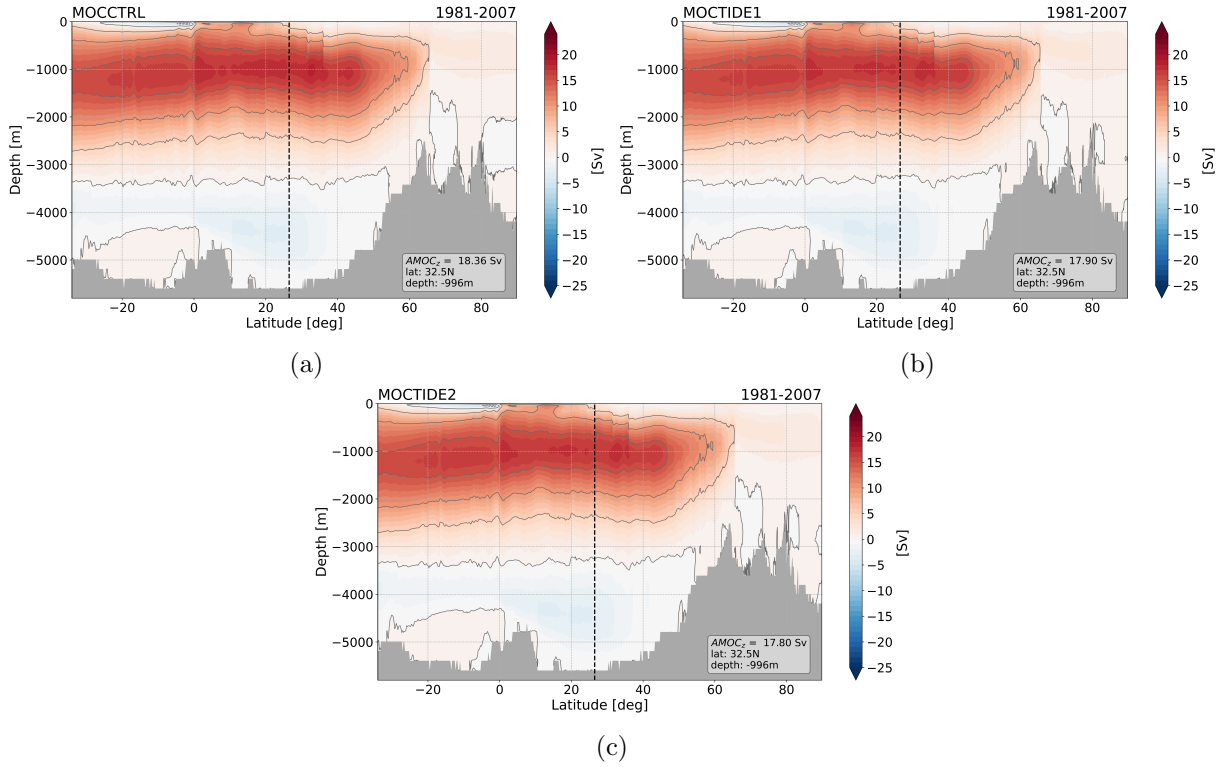
Figure 3.5: Atlantic MOC obtained by (3.4) during the 1981-2007 period: (a) MOCCTRL (b) MOCTIDE1 and (c) MOCTIDE2. Contour lines show 5 Sv intervals, and the black dashed line corresponds to 26.5°N, where the RAPID array is located.

To complete the comparison, the difference between MOCTIDE2 and MOCTIDE1 is small (Figure 3.6c), but it is worth noting that the TWD impact is different above and below 1000 m, corresponding to the typical depth of the first baroclinic mode zero crossing point.

Focusing on MOCCTRL and MOCTIDE1, we computed also the Atlantic MOC annual difference and we found that the tidal forcing enhances or weakens the meridional overturning strength with a big interannual variability. Figure 3.7 shows the annual differences between the two experiments and demonstrates that the tidal impact changes according to the region of interest:

- south of the Equator, tides can intensify the meridional transport (like in 1981, 1989 and 1994, when it is enhanced by 1.5 Sv), or weaken it (as they did in 1982, 1997, 2000 and 2002, when it falls down of 2 Sv);

- moving northward, the perturbations in the tropical region are generally correlated to the South Atlantic, with some exceptions like in 1989 and 1994;

- at the Gulf Stream latitudes between 30°N and 50°N, the meridional transport is always weaker when tides are implemented.

The dynamical system of the Gulf Stream region is probably more complex than the others, with the boundary intensified current that flows northward and barotropic tides that propagate in the opposite direction: on the continental shelf, tides could be trapped as Kelvin waves (Hughes et al.,
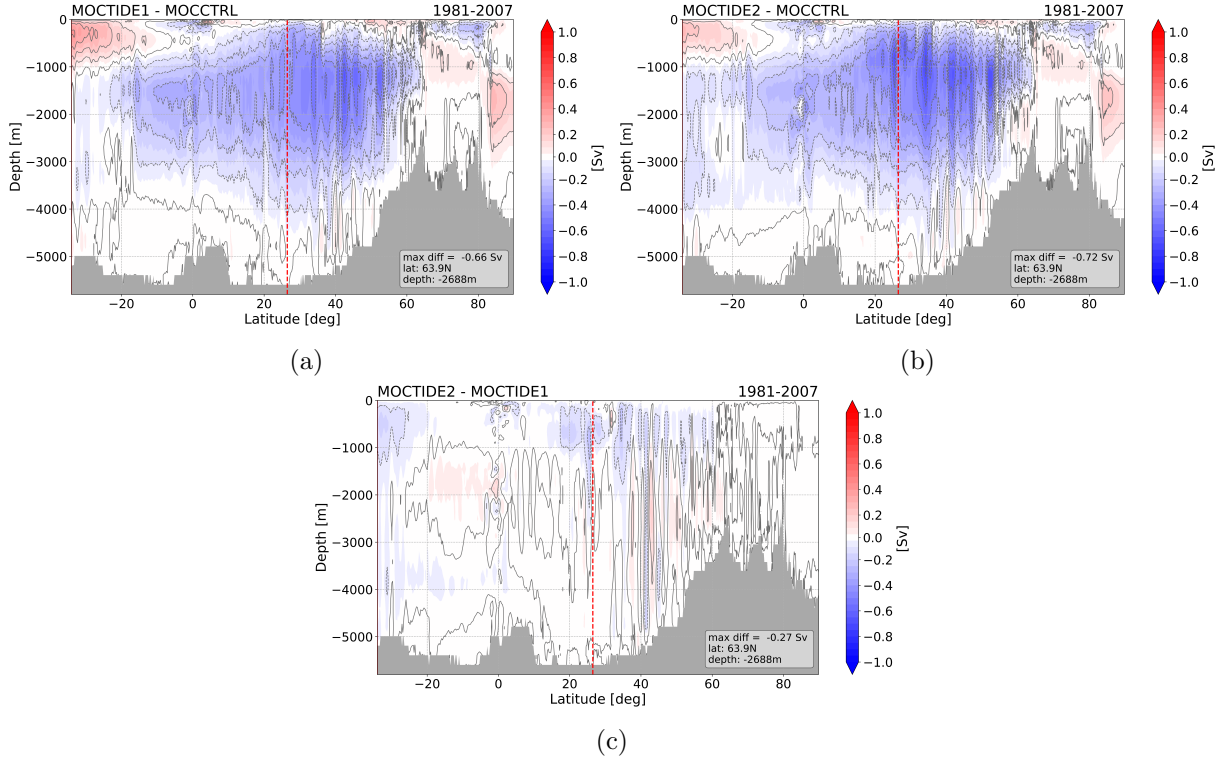
Figure 3.6: Difference of Atlantic MOC during the period 1981-2007: (a) MOCTIDE1 - MOCCTRL, (b) MOCTIDE2 - MOCCTRL, (c) MOCTIDE2 - MOCTIDE1. Contour lines show 0.1 Sv intervals, and the red dashed line corresponds to 26.5°N, where the RAPID array is located.

2019) with a rectified effect as suggested by Thomson and Wilson (1987), while in the open ocean both barotropic and baroclinic tides interact with the mean flow. Many studies investigate the impact of mesoscale eddies and fronts on the internal tides propagation of the region (Rainville and Pinkel, 2006; Kelly et al., 2016; Kelly and Lermusiaux, 2016), while the inverse impact is still poorly analysed. In spite of that, some interesting observations are proposed by Shakespeare and Hogg (2019) and Shakespeare (2020), who demonstrated that internal tides produce a net momentum flux opposite to the surrounding mean flow.
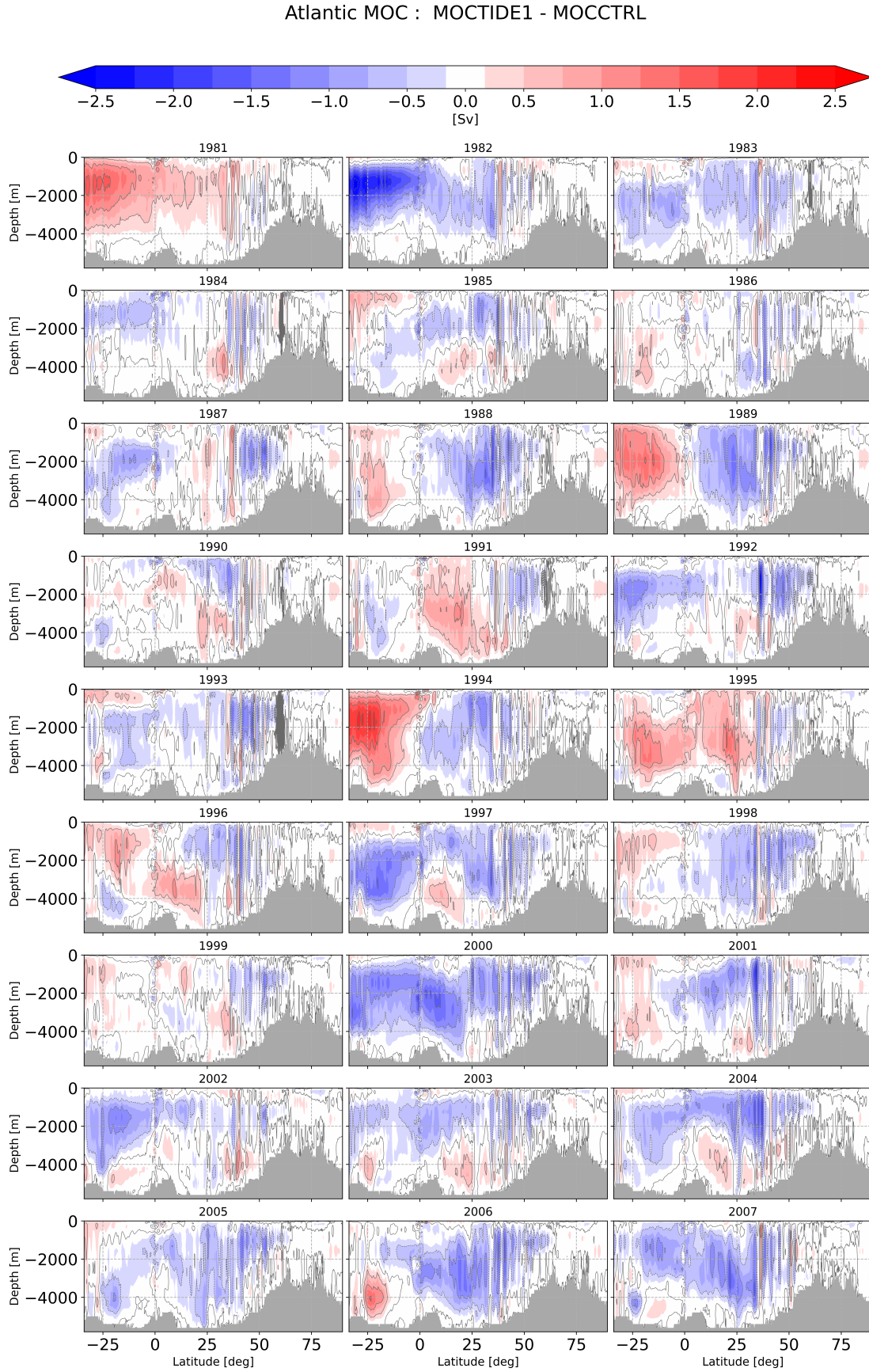
3. Global tides and Atlantic Overturning Circulation

Figure 3.7: Yearly differences of Atlantic MOC between MOCTIDE1 and MOCCTRL during the 1981-2007 period. Contour lines show 0.5 Sv intervals.

58

3.5.2   Volume transport at $26.5°N$

The Atlantic MOC has been widely monitored during the last decades and Frajka-Williams et al. (2019) proposed a complete overview of the continuous observations from mooring arrays at different latitudes. The volume transport simulated in our experiments is here compared to estimates from the RAPID/MOCHA/WBTS program [1] (Cunningham et al., 2007). Within this project moorings and cable data are collected along a zonal section at 26.5°N and the resulting transport is provided from April, 2004 to September, 2018. McCarthy et al. (2015) described the measurements strategy and the related calculation of the AMOC based on geostrophic dynamics, dividing the section in three main regions according to the basin geometry and the dynamical processes involved:

- the western boundary region correspondent to the Florida Strait, where the Gulf Stream (GS hereafter) flows northward between the Florida coast and the Bahamas escarpment west of 76.75°W;

- the surface Ekman layer along the entire section, characterised by wind-driven transport;

- the transatlantic mid-ocean region, extended from the Bahamas (77°W) to Africa (15°W). This region is characterised by the upper mid-ocean (UMO) southward transport, computed from the surface down to around 1100 m, the maximum depth of the intermediate northward flow.

Figure 3.8 shows the vertical profile of the measured and modelled transports at 26.5°N averaged over the 2004-2007 period: positive profile slopes represents a northward flow, while negative slopes represents southward flow. The modelled transports are computed using the procedure proposed for RAPID data by Cunningham et al. (2007). All the profiles get to their maximum value around 1000 m, however our simulations underestimate the observed AMOC of 18.69 Sv. MOCCTRL reaches 16.08 Sv, whereas the presence of tides weakens this value of 0.6 Sv in MOCTIDE1 (coherently with Figure 3.6a), and the TWD reduces transport even more in MOCTIDE2. Likewise, differences between modelled and observed data can be found in the deeper layers, where modelled profiles cross the zero value around 3000 m instead of the observed 4500 m. Such difference might be justified by the simulated period length which is too short to properly reproduce extended deep ocean properties. Finally, it must be noted that Danabasoglu et al. (2014) reported similar biases on many simulations from the Coordinated Ocean-ice Reference Experiments II dataset (CORE2). Our simulations are therefore coherent with other coarse resolution models.

The RAPID product also provides the volume transport for each region above described, so Figure 3.9 shows the timeseries of the simulated transport components compared to RAPID data. Looking at the maximum MOC transport (AMOC, in Figure 3.9a), our experiments underestimate observed data as well as CORE2 experiments and other NEMO configurations (Iovino et al., 2016) do. The timeseries have similar patterns, with tidal presence that reduces the temporal mean

---

[1]RAPID AMOC data are freely available and distributed from www.rapid.ac.uk/rapidmoc.
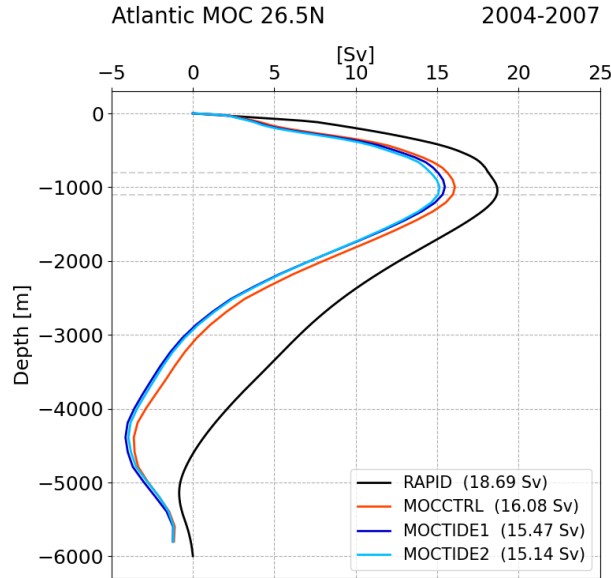
Figure 3.8: AMOC profile for comparison between RAPID and modelled data at 26.5°N from April 2004 to December 2007. The legend reports in brackets the maximum associated to each profile.

from 16.11 Sv (MOCCTRL) to 15.49 Sv (MOCTIDE1). In MOCTIDE2 the transport is further reduced by 1 Sv overall, supporting the hypothesis that internal tide propagation sustains the meridional overturning.

The Ekman transport component (Figure 3.9b) is computed from the surface wind stress and thus is the same for all the experiments, all forced by JRA55 reanalysis. It is in good agreement with the transport provided by RAPID array, based on ERA5 reanalysis data (Hersbach et al., 2020). On the contrary, in our simulations the GS transport is always weaker than in RAPID, with values around 24 Sv compared to 31.75 Sv (Figure 3.9c). It is worth noting that the GS transport in MOCTIDE1 is weaker than MOCCTRL only on average (24.27 Sv compared to 24.86 Sv), because the monthly difference can be reversed. Also the UMO southward transport (Figure 3.9d) is less intense in our experiments (8.9 Sv for MOCTIDE1) than in RAPID data (16.45 Sv), but in this case the differences between the three experiments are weaker than the GS case, especially during the years 2006 and 2007.

The biases of GS and UMO transports are linked to the grid geometry of our configuration, where the narrow (80 km) and shallow (800 m) Florida Strait is poorly described by the model resolution, which is about 25 km at this latitude. Few model points within the strait can't reproduce the entire boundary-intensified northward flow, so a portion of it shifts into the open ocean and is therefore neglected by the GS transport calculation. The excluded flow is instead considered inside the UMO transport, supposed to move southward. To support this hypothesis, note that the biases of GS and UMO simulated transports with respect to RAPID data have the same intensity.

Finally, Figure 3.10 demonstrates that the GS transport could partially overflow out of the Florida Straits even when tides are implemented: indeed, during the entire analysed period the GS transport differences between MOCTIDE1 (MOCTIDE2) and MOCCTRL are anticorrelated
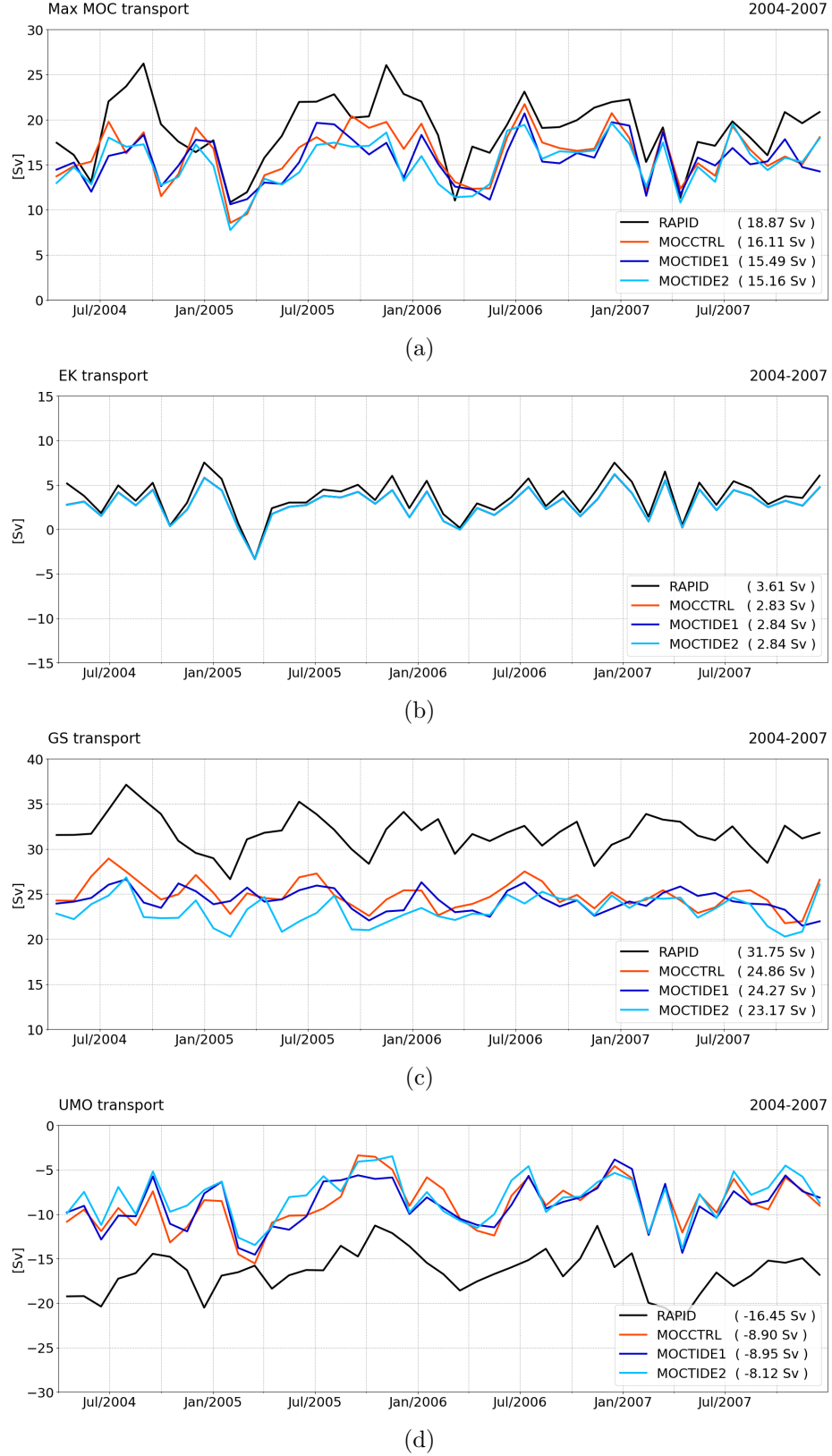
Figure 3.9: Timeseries of the different transport components across 26.5°N computed following RAPID procedure. (a) Maximum transport, AMOC, (b) Ekman transport, (c) GS transport across the Florida Straits, (d) UMO transport. In the legend each value in brackets corresponds to the temporal mean.

to the UMO transport differences. Since tides propagate southward in this region, our hypothesis is that their current may have a rectified effect to slow down the flow within the strait.
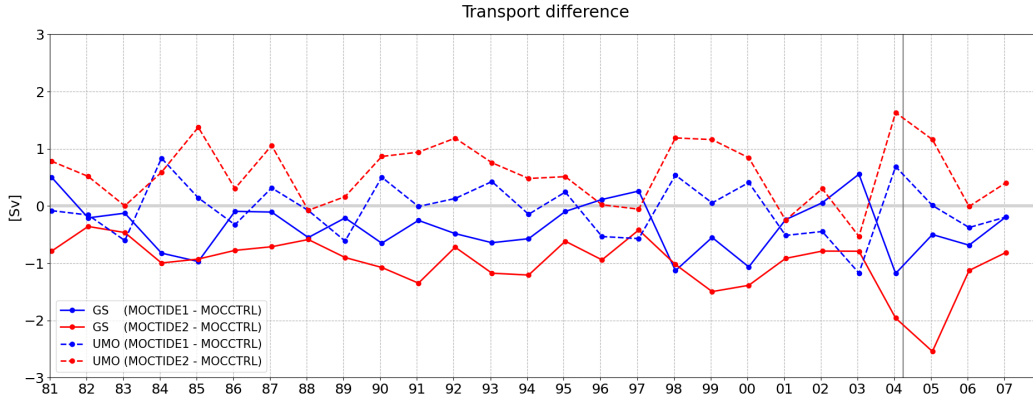

Figure 3.10: Transport differences of GS (solid line) and UMO (dashed line) components between experiments with and without tides: MOCTIDE1 - MOCCTRL (blue) and MOCTIDE1 - MOCCTRL (red). The black thin vertical line corresponds to the RAPID program starting date.

3.6   Atlantic momentum balance

In order to depict a possible impact of tides on the Atlantic MOC, we proceed analysing the zonal momentum balance zonally integrated over the entire basin.

The analysis focuses on one year of the whole simulated period to highlight the differences between MOCTIDE1 and MOCCTRL experiments that are coherent with the climatological mean. Based on Figure 3.7, we chose the year 2000 as the most representative, with a transport change due to tides that interests both the hemispheres and a maximum value (-1.5 Sv) higher than the long period average (-0.66 Sv). Overall, the interpretation of the results is more detailed in the Northern Hemisphere (NH hereafter) due to the lack of information about the modelled Southern Ocean dynamics.

3.6.1   The zonally integrated momentum equation

In order to define the terms that contribute to the momentum balance, we consider the zonal momentum primitive equation

$$\partial_t u + \nabla_3 \cdot (\boldsymbol{u} u) - fv = -\frac{1}{\rho_0} \partial_x p + \frac{1}{\rho_0} \left[\nabla \left(A_h \nabla u \right) + \partial_z \left(A_v \partial_z u \right) \right] \tag{3.6}$$

and we use two operators defined as

$$\langle \cdot \rangle = \frac{1}{T} \int_{t_0}^{t_0+T} (\cdot) \, dt \quad \text{and} \quad \widetilde{(\cdot)} = \int_{x_w}^{x_e} (\cdot) \, dx \tag{3.7}$$

where the former is the temporal average over a period T and the latter is the zonal integration on the basin scale, with $x_w(y,z)$ and $x_e(y,z)$ the basin zonal boundaries.

Applying the temporal average to (3.6) we obtain

$$\frac{\Delta_t u}{T} + \nabla_3 \cdot \langle \boldsymbol{u}u \rangle - f\langle v \rangle = -\frac{1}{\rho_0}\partial_x \langle p \rangle + \frac{1}{\rho_0}\left[\nabla\left(A_h \nabla \langle u \rangle \right) + \partial_z \left(A_v \partial_z \langle u \rangle \right) \right] \tag{3.8}$$

with $\Delta_t u$ being the zonal velocity difference between the initial and final instants.
This equation can be further modified computing its zonal integral to obtain

$$\frac{\Delta_t \widetilde{u}}{T} + \widetilde{\partial_y \langle vu \rangle} + \widetilde{\partial_z \langle wu \rangle} - f\widetilde{\langle v \rangle} = -\frac{1}{\rho_0}\Delta_x \langle p \rangle + \frac{1}{\rho_0}\Delta_x \left(A_h \partial_x \langle u \rangle \right) + \frac{1}{\rho_0}\partial_y \left(\widetilde{A_h \partial_y \langle u \rangle} \right) + \frac{1}{\rho_0}\partial_z \left(\widetilde{A_v \partial_z \langle u \rangle} \right) \tag{3.9}$$

where $\Delta_x(\cdot)$ represents the difference between the eastern and western boundaries values, and the zonal advection term is null according to the no-slip boundary conditions.
The meridional velocity zonally integrated is then balanced by the following formula

$$f\widetilde{\langle v \rangle} = +\frac{1}{\rho_0}\Delta_x \langle p \rangle + \widetilde{\partial_y \langle vu \rangle} + \widetilde{\partial_z \langle wu \rangle} + \mathcal{R} \tag{3.10}$$

where $\mathcal{R}$ represents the sum of the temporal difference $\frac{\Delta_t \widetilde{u}}{T}$ and the diffusive terms.
Moreover, the above notation is useful to describe the temporal average of the streamfunction defined in (3.4) as

$$\langle \psi \rangle(y,z) = -\int_{-H}^{z} \widetilde{\langle v \rangle}(x,y,z')\, dz' \quad . \tag{3.11}$$

and thus justify our choice to study the Atlantic overturning circulation looking at the momentum balance in (3.10). Few considerations are useful to introduce the analysis of each term:

- looking at the pressure term, we expect to analyse the role of tides on the large scale circulation as propagating barotropic and baroclinic waves. Indeed, as tides move across the ocean, they bring pressure perturbations both at the surface and in the interior. Their impact on the pressure difference at the basin boundaries is proposed here for the first time;

- within the advection terms, we include all the dynamical processes of interaction between tides and mesoscale structures as well as mean currents (Dunphy and Lamb, 2014; Kelly and Lermusiaux, 2016; Shakespeare and Hogg, 2019);

- the diffusive terms change due to internal tides breaking through a wide range of processes like wave-wave interaction, mesoscale interaction, topographic scattering (see Figure 1.1). This topic has been widely analysed both at regional and global scales (Ffield and Gordon, 1996; Jayne, 2009; Melet et al., 2016; de Lavergne et al., 2020);

- the zonal flux difference between the beginning and the end of the observed period is sensible to long term tidal constituents.

Hereafter we focus on the contribution of pressure and advection terms (Figures 3.11b to 3.11d) as the most suitable to change with tides on the basin scale. Despite of that, we are aware that zonal fluxes and diffusive processes are non-negligible to fully understand the tidal impact on the Atlantic circulation (Figure 3.11e), so they will be subject to future research.
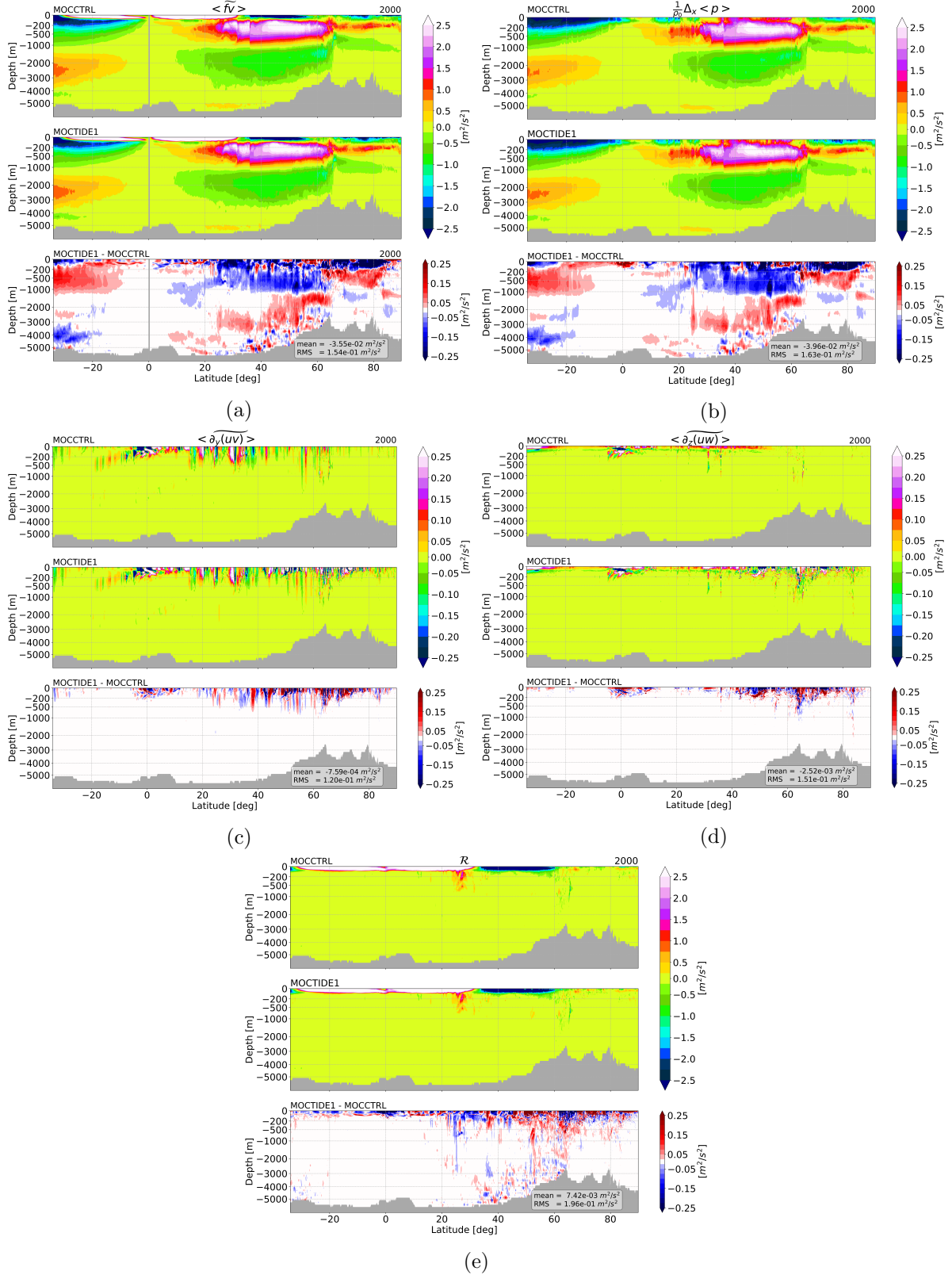
Figure 3.11: Sections of the zonal momentum balance zonally integrated during the year 2000 of MOCCTRL and MOCTIDE1 experiments: (a) Coriolis term along the meridional direction, (b) pressure gradient term, (c) horizontal advection term along the meridional direction, (d) vertical advection term and (e) sum of the residual terms. Note that the vertical axes are stretched in the upper portion of the ocean, and the palettes in (c) and (d) are one order of magnitude weaker than the others.

The meridional circulation of the Atlantic Ocean is presented in Figure 3.11a (note the flow opposite sign between the SH and NH due to the Coriolis factor). The momentum flux is organized in four layers: near the surface the circulation is wind-driven and the flow direction depends on latitude, while in the interior layers the flow direction is uniform. In the upper layer, Trade winds move surface waters away from the equator and Westerlies drive them southward. In the intermediate layer, the momentum flux moves northward between 100 and 1000 m, and its strongest region is placed between 200 and 500 m. The deep layer extends between 1000 and 3500 m and is characterised by southward momentum flux with maximum strength of 1 m^2/s^2 around 2000 m. Finally, in the abyssal layer the flow moves northward again, with maximum flux intensity of 0.6 m^2/s^2. The resulting flow depicts the overturning cells described in Section 3.5, even though in the figure they are partially masked at tropical latitudes by the small Coriolis factor. Differently from the rest of the basin, north of 65°N the circulation is heavily weakened by topographic constrains like the Denmark Strait and the Faroe-Shetland Channel.

When tides are included into the dynamical system, south of 65°N the momentum flux weakens both towards north and south, and its zero-crossing depth matches the depth associated to the AMOC_z around 1000 m. On the contrary, the flow is reinforced north of 65°N between 200 and 500 m, suggesting that tides contribute to the Nordic Seas dynamics differently from the rest of the Atlantic basin.

3.6.2 Tidal impact on the geostrophic balance

Kanzow et al. (2010) demonstrated that the Atlantic MOC is balanced by the pressure difference between the eastern and western boundaries more than by the northward Ekman transport. The same result was confirmed by our simulations in Figure 3.11b, where the pressure component $\Delta_x \langle p \rangle$ is the main driver of the momentum balance in the interior of the ocean, with values that are one order of magnitude higher compared to the other terms in (3.10) (Figures 3.11c-d-e). Therefore, both the simulations are in geostrophic balance below 200 m.

The differences between boundary values can be further analysed decomposing the pressure field according to (2.15) as the sum of its hydrostatic (barotropic, p_s) and dynamical (baroclinic, p_h) components[2] . Figure 3.12 shows that both $\Delta_x \langle p_s \rangle$ and $\Delta_x \langle p_h \rangle$ change with depth from the surface to the bottom: the former decreases uniformly, while the latter has a vertical profile of the first baroclinic mode with zero-crossing depth around 1000 m. Moreover, the boundary differences of p_h are one order of magnitude higher than the ones related to p_s, contributing to the momentum balance between 200 m and 500 m with 3.0 m^2/s^2.

Looking at the differences between the experiments, we found that tides modify both pressure components: indeed, surface tides elevation changes the modelled SSH and therefore p_s, while internal tides dissipation modifies the water density through processes such as diapycnal mixing, and therefore p_h. Accordingly, their difference between eastern and western boundaries changes too, with values of the order of 10^{-1} m^2/s^2 (bottom panels of Figure 3.12). However, the main

---

[2]In this chapter the dynamical pressure term notation is different than in Chapter 2 (where it is called p') to mark the difference between the vertical integration computed within its definition and the temporal integration computed in (3.10).

distinction concerns the depth that these variations reach: surface tides cause differences to the upper 200 m, whereas internal tides change the ocean stratification even in the interior.

The main impact of tides on the overturning circulation is then to change the ocean stratification at the lateral boundaries, being the main cause of geostrophic balance perturbation. The origin of this impact is far from trivial, since the temporal mean of pressure perturbations induced by tides is zero (Shakespeare and Hogg, 2019). It requires to understand whether the density changes are due to local diapycnal mixing, to other tidal processes in the ocean interior, or a combination thereof.

Trying to assess where tides mostly change the density field, Figure 3.13 depicts maps of potential temperature and salinity differences vertically integrated over the entire depth. In these maps the vertical integration makes the tidal differences stronger in the open ocean than on the shelves, but it also allows to better interpret data in terms of pressure variations. Both temperature and salinity differences are roughly uniform south of 30°N and north of 50°N. Between these latitudes, instead, the Gulf Stream and the North Atlantic Current strongly interact with propagating tides and produce coherent variations of the water properties, so that where the water column gets warmer it becomes saltier.

The tidal impact on the pressure field demonstrates that tides change the water stratification, thus, to investigate further their role on the ocean circulation we should look at the impact on the buoyancy balance. Unfortunately, this analysis requires to implement a new diagnostic within the NEMO model, so we plan to work on this in future research projects. Nevertheless, we would like to argue here three possible mechanisms that could drive the observed differences between MOCTIDE1 and MOCCTRL:

- first, internal tides enhance the diapycnal mixing near the continental slopes and the topographic structures, changing in turn the density field. The tidally induced mixing near the bottom has been widely analysed in coastal regions, but it is still a debated topic for the open ocean, both on regional and global scales (Naveira Garabato et al., 2004; de Lavergne et al., 2019);

- second, tides propagate southward as Kelvin waves along the continental shelf, and their rectified effect could generate a density anomaly down to 1000 m along the shelf (Thomson and Wilson, 1987; Fevrier et al., 2007);

- third, tides could slightly change the mean circulation pathway maintaining its original intensity (as pointed out in Section 3.4). In a complex dynamical system like the North Atlantic Ocean, a weak difference in the currents trajectory could modify the exchange of heat and salt between the open ocean and the marginal seas. This interpretation is supported by Müller et al. (2010), who found that tides shift the subpolar front to the north changing the pathway of the North Atlantic Current. Therefore, in the Labrador Sea the sea surface temperature becomes cooler and the water fresher, improving in both cases the comparison with observations. Similar behaviours of temperature and salinity are also evident during the analysed period in MOCTIDE1 (Figure 3.13).

It is worth noting that the last process can modify the water properties over the entire basin, but the main perturbations are placed along the boundaries, coherently with the observed pressure differences.

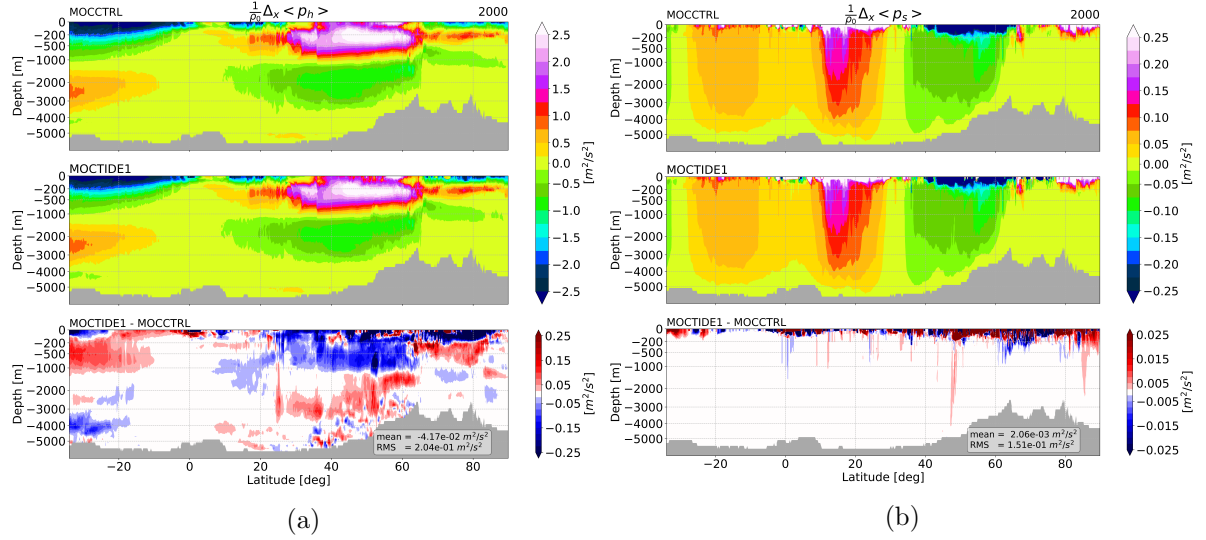Figure 3.12: Sections of the zonal momentum balance zonally integrated during the year 2000 of MOCCTRL and MOCTIDE1 experiments: (a) dynamical pressure gradient term, p_h, (b) hydrostatic pressure gradient term, p_s.
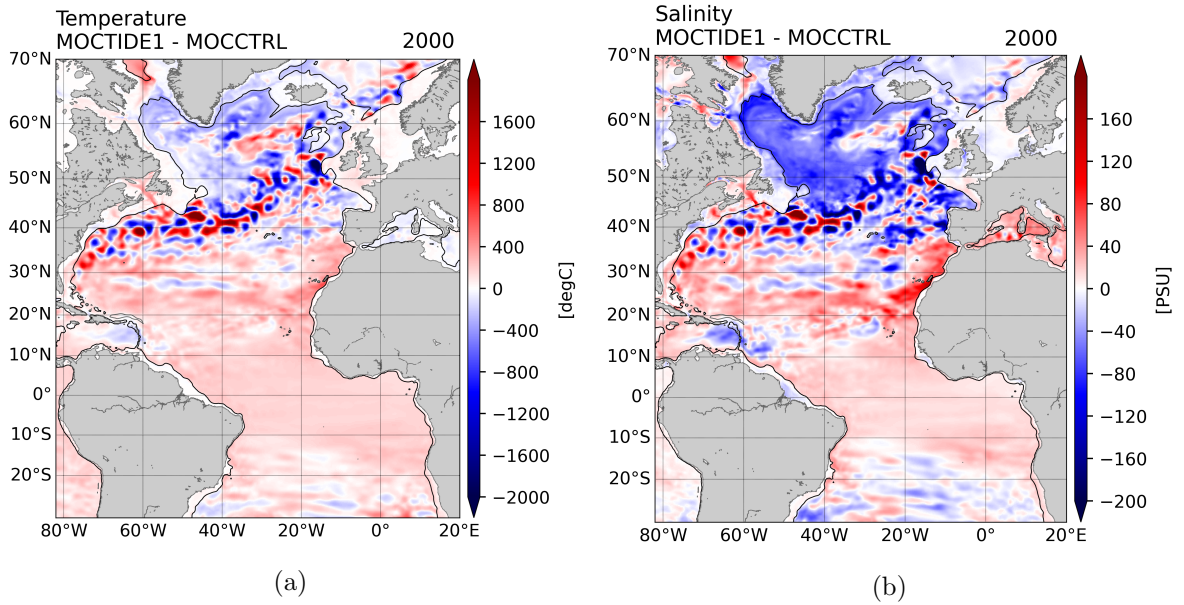

Figure 3.13: Maps of the difference between MOCTIDE1 and MOCCTRL : (a) vertically integrated potential temperature and (b) vertically integrated salinity. Temporal mean over the year 2000.

3.6.3 Tidal impact on the advection terms

Tides contribute to the momentum balance changing also the horizontal and vertical advection terms, respectively $\widetilde{\partial_y \langle vu \rangle}$ and $\widetilde{\partial_z \langle wu \rangle}$. These terms are better analysed when they are decomposed in time as

$$\widetilde{\partial_y \langle vu \rangle} = \partial_y \widetilde{(\langle v \rangle \langle u \rangle)} + \widetilde{\partial_y \langle v'u' \rangle} \tag{3.12}$$

$$\widetilde{\partial_z \langle wu \rangle} = \partial_z \widetilde{(\langle w \rangle \langle u \rangle)} + \widetilde{\partial_z \langle w'u' \rangle} \tag{3.13}$$

with (u', v', w') being the velocity deviations from the temporal mean. The mean advection terms are associated to gyres and mean currents of the ocean, while the residual components, also called Reynolds stresses, are related to dynamical features like mesoscale structures, eddies and tides interacting with each other.

The mean advection terms are presented in Figure 3.14a and Figure 3.14b. In general, these terms are characterised by root mean squared (RMS) tidal differences that are negligible with respect to the RMS differences of pressure (one order of magnitude weaker). The horizontal component, $\partial_y \widetilde{(\langle v \rangle \langle u \rangle)}$ (Figure 3.14a), has the same spatial distribution in MOCCTRL and MOCTIDE1, with positive and negative values alternated above 1000 m over the entire basin. The differences between the two experiments maintain the same horizontal pattern, while along the vertical they focus on the upper 200 m in the equatorial area and extend down to 1000 m in the subtropical region. The tidal impact has a RMS intensity of $10^{-2} \mathrm{m}^2/\mathrm{s}^2$ with maximum values of the order of 10^{-1} $\mathrm{m}^2/\mathrm{s}^2$. On the contrary, the mean vertical component $\partial_z \widetilde{(\langle w \rangle \langle u \rangle)}$ has a different spatial distribution, being weaker and much more localised between the equator and 40°N (Figure 3.14b). The tidal impact on this term is restrict to the equatorial region.

On the other hand, Reynolds stresses are shown in Figure 3.14c and Figure 3.14d. Their differences between the experiments are larger than the mean advection terms, suggesting an intense internal tide activity. Indeed, tides perturb the residual advection terms both directly, by the presence of tidal currents or the interaction between internal tides and topography (Shakespeare and Hogg, 2019), or indirectly, when internal tides interact with the mesoscale features changing their structure (Kelly and Lermusiaux, 2016). The overall tidal impact on the Reynolds stresses is as large as the impact on pressure, with RMS values of the order of 10^{-1} $\mathrm{m}^2/\mathrm{s}^2$.

It is worth noting that eddies typically have small vertical velocity, so their contribution to the vertical residual advection is small too (McWilliams, 2008), making the differences between experiments directly associated to the tidal activity. Along the horizontal direction, instead, the contributions of tides and mesoscale to advection are mixed together, making difficult to distinguish which of the two causes the differences between MOCCTRL and MOCTIDE1.

Figure 3.14c depicts the horizontal residual term $\widetilde{\partial_y \langle v'u' \rangle}$. The highest values in MOCCTRL (0.08 $\mathrm{m}^2/\mathrm{s}^2$) are localised in the equatorial region and between 30°N and 40°N, where the GS forms eddies that interact with each other. Differently, in MOCTIDE1 the horizontal residual term shows weaker mesoscale structures in the GS region, while high positive and negative terms characterise the region north of 40°N.

The vertical residual advection $\widetilde{\partial_z \langle w'u' \rangle}$ has a very different spatial distribution in Figure 3.14d,

with intense fluxes near the surface ($0.2 \text{ m}^2/\text{s}^2$) spreading at all latitudes south of 50°N. The presence of tides enhances the momentum flux in the North Atlantic Ocean, north of 40°N, with a RMS intensity of $10^{-1} \text{ m}^2/\text{s}^2$.

To summarise, tides change the vertical and horizontal advection terms with the same intensity applied on the pressure terms, but in this case the differences are randomly organised within the domain, giving a null net contribution to the total momentum balance.

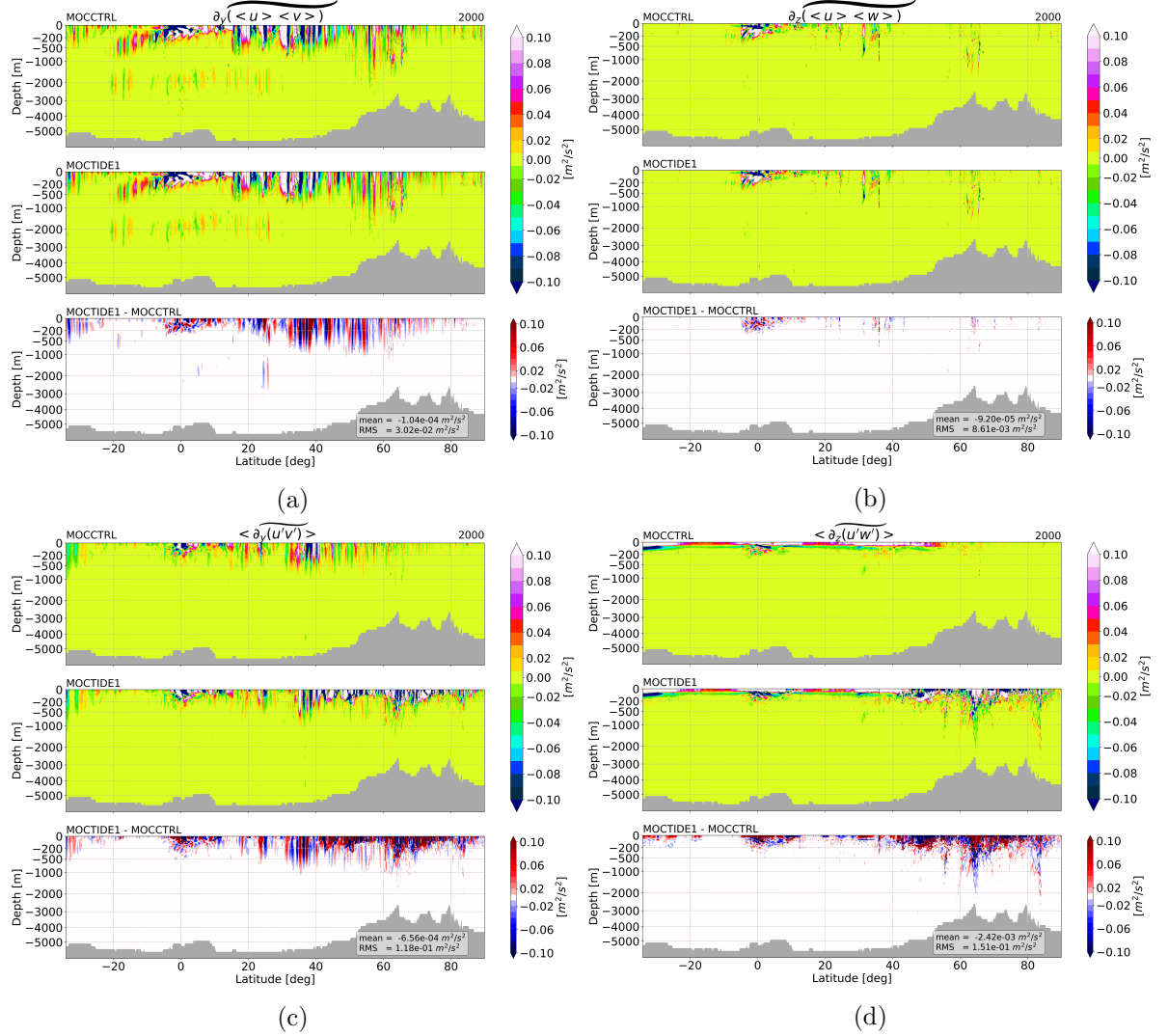Figure 3.14: Sections of the zonal momentum balance zonally integrated during the year 2000 of MOCCTRL and MOCTIDE1 experiments: (a) mean component of the horizontal advection term along the meridional direction, (b) mean component of the vertical advection term, (c) residual component of the horizontal advection term along the meridional direction and (d) residual component of the vertical advection term.

69

3.7   Conclusions

In this chapter we studied the impact of tides on the meridional overturning circulation of the Atlantic Ocean on decadal time scales, using three global simulations of the NEMO model at 1/4° of horizontal resolution analysed during the period from 1981 to 2007. The first experiment was initialised in 1958 in order to properly reproduce a mid-depth overturning cell in the Atlantic Ocean. The other experiments started in 1980 from the reference configuration (MOCCTRL) and were characterised by the addition of the tidal forcing (MOCTIDE1), a topographic wave drag and a numerical modification of the bottom friction (MOCTIDE2).

Comparing the first two experiments we analysed the effect of tides on the Atlantic MOC, and we found that it is on average weakened of about 0.66 Sv even though the interannual difference can strongly change in amplitude and sign. This is particularly evident in the SH, where the yearly perturbation contributes to the meridional transport changing the overall value by 1.5 Sv. On the contrary, the differences at mid and high latitudes are more uniform in time, and the meridional transport including tides is generally weaker. This condition occurs especially in the Gulf Stream and North Atlantic Current regions, where internal tides and mesoscale structures evolve and interact with each other.

Moreover, the Atlantic MOC further decreases when the TWD dissipates a portion of the modelled internal tides (-0.72 Sv), suggesting that the propagation of such waves could contribute to maintain the overturning circulation on basin scale.

We compared the modelled transport at 26.5°N with the RAPID/MOCHA array during the period from 2004 to 2007, and we found that the overall transport is underestimated, with 16.08 Sv compared to the observed 18.69 Sv. Moreover, following the RAPID decomposition, our model simulates a weaker transport compared to data both in the Florida Strait and in the upper portion of the open ocean, suggesting that a part of the modelled GS northward transport overflows out of the strait. This phenomenon is enhanced by tides, and the perturbations to the GS and UMO transport components are found to be anticorrelated.

Looking at the kinetic energy, we found that the addition of tides doesn't change the mean kinetic energy on the global scale, while the entire tidal energy input contributes to the EKE and probably acts to strength eddies and gyres. This statement appears to be contradictory with respect to the above considerations and led us to further investigate the momentum balance zonally integrated over the entire basin. According to the literature, we demonstrated that the overturning circulation is geostrophically balanced by the difference of pressure between the eastern and western boundaries, and we found that even the perturbations induced by tides are mostly related to the pressure field. Indeed, the tidal impact on the advection terms is mostly placed in the upper 500 m of the ocean, without being organised in space to give a net contribution to the total momentum budget.

Finally, we proposed three possible mechanisms that could explain the tidal contribution to set the dynamical pressure difference between the lateral boundaries of the Atlantic Ocean: the first one is related to the tidal diapycnal mixing near the solid boundaries, the second one regards a possible rectification of tides on the continental shelf, and the last one involves the interaction

between tides and eddies as a driver to change the mean currents pathway and thus impact on the distribution of heat and salt over the entire basin. The latter process acts on the entire basin and its main effects are boundary intensified, concurring to be the most suitable factor that changes the dynamical pressure.

Chapter 4

Mediterranean Sea Overturning Circulation

In the present chapter the overturning circulation of the Mediterranean Sea is described using the reanalysis dataset of Simoncelli et al. (2017) for the 1987-2013 period, computing the meridional and zonal streamfunctions both in the classical, Eulerian, and in the residual frameworks. The concept of residual zonal (meridional) circulation has never been applied in this region and adds to the mean flow the contribution of velocity structures with zero time or meridional (zonal) averages but nonzero fluxes, leading to a more inclusive representation of the transports across the basin.

The preliminary part of this work was the object of my master thesis, where I computed the Eulerian and the residual streamfunctions of the Mediterranean circulation during the whole reanalysis period, and the computation was carried on in my PhD studies analysing the streamfunctions variability. In addition, considering the importance of the water exchange between the Atlantic Ocean and the Mediterranean Sea, I analysed the horizontal transport vertically integrated over two layers down to the Gibraltar Strait depth, and I distinguished its divergent and rotational components.

As the applied methodology has never been used in the Mediterranean contest, the obtained results improved the comprehension of the Mediterranean Sea circulation, and was therefore published in Pinardi et al. (2019). My contribution to the paper can be summarized in the postprocessing of reanalysis data, their analysis and graphic visualization. The fundamental work of interpreting the results and contextualize them in the Mediterranean framework has been achieved thanks to the experience and expertise of prof. Nadia Pinardi and prof. Paola Cessi.

Finally, the overturning interannual variability was further analised in Section 2.4 of the Copernicus Marine Service Ocean State Report, Issue 4 (von Schuckmann et al., 2020). Within this section, the Mediterranean Overturning Index is defined as a measure of the strength of the Mediterranean Eulerian clockwise overturning circulation, computed separately for the eastern and western subbasins.

The Mediterranean Sea Overturning Circulation

NADIA PINARDI

Department of Physics and Astronomy, University of Bologna, and Istituto nazionale di Geofisica e Vulcanologia, Bologna, Italy

PAOLA CESSI

Scripps Institution of Oceanography, University of California, San Diego, La Jolla, California

FEDERICA BORILE

Department of Physics and Astronomy, University of Bologna, and Centro EuroMediterraneo sui Cambiamenti Climatici, Bologna, Italy

CHRISTOPHER L. P. WOLFE

School of Marine and Atmospheric Sciences, Stony Brook University, State University of New York, Stony Brook, New York

(Manuscript received 11 December 2018, in final form 12 April 2019)

ABSTRACT

The time-mean zonal and meridional overturning circulations of the entire Mediterranean Sea are studied in both the Eulerian and residual frameworks. The overturning is characterized by cells in the vertical and either zonal or meridional planes with clockwise circulations in the upper water column and counterclockwise circulations in the deep and abyssal regions. The zonal overturning is composed of an upper clockwise cell in the top 600 m of the water column related to the classical Wüst cell and two additional deep clockwise cells, one corresponding to the outflow of the dense Aegean water during the Eastern Mediterranean Transient (EMT) and the other associated with dense water formation in the Rhodes Gyre. The variability of the zonal overturning before, during, and after the EMT is discussed. The meridional basinwide overturning is composed of clockwise, multicentered cells connected with the four northern deep ocean formation areas, located in the Eastern and Western Mediterranean basins. The connection between the Wüst cell and the meridional overturning is visualized through the horizontal velocities vertically integrated across two layers above 600 m. The component of the horizontal velocity associated with the overturning is isolated by computing the divergent components of the vertically integrated velocities forced by the inflow/outflow at the Strait of Gibraltar.

1. Introduction

The overturning circulation of the global ocean plays a key role in setting the stratification of different basins because it regulates the ocean carbon budgets and provides the mechanism for the supply of oxygen and other tracers from the surface to the deep ocean. The conceptual framework of the global overturning circulation has recently advanced, indicating a middepth clockwise overturning cell that connects the Northern Hemisphere deep water formation areas to the wind-driven Southern Ocean upwelling (Toggweiler and Samuels 1993; Gnanadesikan 1999; Lumpkin and Speer 2007; Marshall and Speer 2012; Talley 2013) and an abyssal counterclockwise overturning cell driven by bottom-enhanced diapycnal mixing that balances Antarctic bottom water formation. In other words, the global meridional
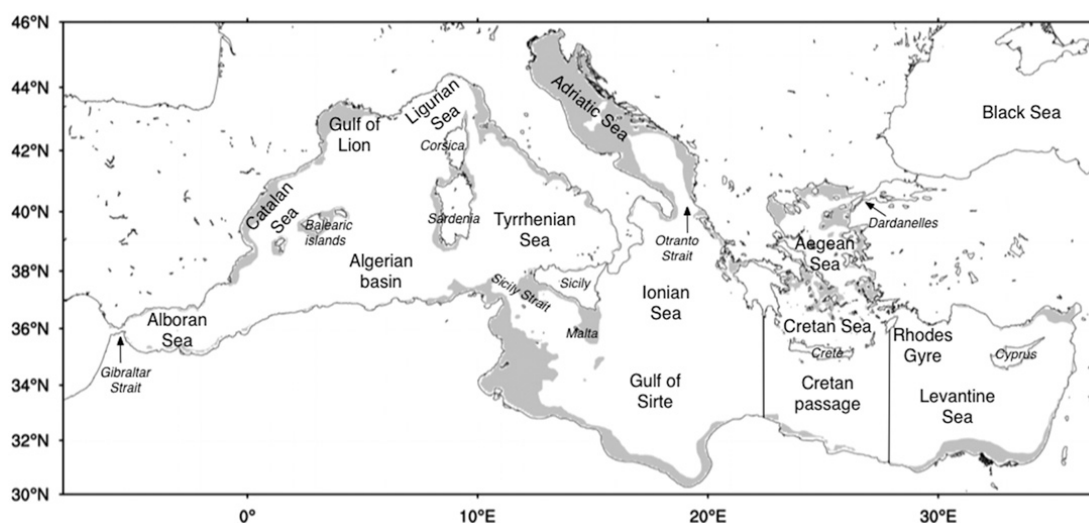

FIG. 1. The Mediterranean Sea with the names of the geographical locations used in the text. Gray areas specify the continental shelf down to 200-m depth.

overturning circulation has been depicted as composed of counterrotating meridional cells, and a recent overview is offered by Cessi (2019).

This new picture has emphasized the importance of adiabatic, along-isopycnal motion in the clockwise intermediate-depth overturning, with Ekman transport and eddy-flux of buoyancy in the Antarctic Circumpolar Current playing a fundamental role (Marshall and Radko 2003; Wolfe and Cessi 2010). In contrast, diapycnal mixing is important in the dynamics of the counterclockwise abyssal cell (Nikurashin and Vallis 2011).

Much of the understanding of the global overturning circulation dynamics has been advanced by using the concept of *residual* circulation (Andrews et al. 1987; Marshall and Radko 2003). Taking the meridional overturning as an example, the velocity is averaged in density layers of thickness h and can be decomposed into its mean and eddy components, that is,

$$\frac{\overline{vh}}{\overline{h}} = \overline{v} + \frac{\overline{v'h'}}{\overline{h}}, \tag{1}$$

where the overbar indicates the zonal and time average, and the prime indicates departures from the zonal and time average. The left-hand side of Eq. (1) is the *thickness-weighted* or *residual* velocity in the chosen layer; the first term on the right-hand side (rhs) is the traditional, Eulerian-average velocity; and the second term is the velocity due to large-scale circulation gyres, standing waves, and transient eddies. The advantage of the residual framework is that it includes the contribution of eddy fluxes due to velocity structures with zero time or zonal averages, but nonzero fluxes [the second term on the rhs of Eq. (1)]. Thus, the residual velocity is

representative of the transport of scalars, such as temperature, salinity, and density (Plumb and Mahlman 1987; Bachman and Fox-Kemper 2013). From the thickness-weighted velocity in Eq. (1) a transport streamfunction is calculated in density and latitude coordinates. In this paper the residual overturning circulation of the Mediterranean Sea is studied and compared to the Eulerian overturning circulation.

The geometry and bathymetry of the Mediterranean Sea is described in Fig. 1. Several ~500-m-deep sills subdivide the basin into areas where different processes dominate. The narrow (~7-km width) and shallow (300-m depth) Gibraltar Strait sill connects the Mediterranean to the Atlantic. The exchange at the Strait is characterized by a baroclinic two-layer flow related to the energy and buoyancy budget of the semienclosed basin (Cessi et al. 2014). This two-layer flow provides low-salt waters to the Mediterranean, balancing the increasing salt time tendency due to evaporation at the air–sea interface, thus helping to maintain a stratification in the basin. The wide and shallow (~500-m depth) Sicily Strait sill divides the Western Mediterranean (WMED) from the Eastern Mediterranean (EMED), allowing only surface and intermediate waters to be exchanged. The EMED has two marginal seas of its own, the Adriatic and the Aegean Sea, where deep waters are formed. Deeper sills (~800-m depth) connect the Adriatic and Aegean Seas to the EMED through the Otranto and four Cretan Sea Straits, among which the Kasos and Antikythira Straits are 1000 and 700 m deep, allowing dense waters to exit the Cretan Sea.

The Mediterranean Sea has been called a miniature ocean for climate studies (Bethoux et al. 1999; Tsimplis et al. 2006) because it is a basin with deep and intermediate

mass formation processes generating a vigorous vertical circulation. The WMED overturning circulation is connected to the deep water formation areas of the Gulf of Lion (Schott and Leaman 1991; Houpert et al. 2016) and an overall understanding of its structure is still lacking. The semienclosed geometry of the Mediterranean Sea enables a zonal overturning cell connecting the two-layer flow at the Strait of Gibraltar to remote areas of the Eastern Mediterranean basin (Pinardi et al. 2006). The zonal circulation of the Mediterranean Sea was described for the first time by Wüst (1961) analyzing a vertical section of salinity, and by Zavatarelli and Mellor (1995) in terms of the Eulerian zonal transport streamfunction obtained with a coarse-resolution numerical model.

The traditional picture of the EMED overturning considered the Adriatic Sea as the only source of deep water formation (Zavatarelli and Mellor 1995), but after 1995 it has become clear that two EMED meridional cells are possible, one with the downwelling branch in the Adriatic Sea and the other in the Aegean Sea. Between 1988 and 1998, a climatic event, termed the Eastern Mediterranean Transient (EMT; Roether et al. 1996; Klein et al. 1999, 2000; Manca et al. 2003; Gertman et al. 2006) was observed, characterized by the formation of very dense waters in the Aegean Sea outflowing through the Cretan Straits and filling the abyssal plain of the EMED. The overturning circulation linked to the Adriatic Sea has been the subject of recent studies (Verri et al. 2018; Somot et al. 2006), and the overturning circulation generated from both the Adriatic and Aegean Sea sources has been discussed by Amitai et al. (2017). There is no description of the overturning circulation generated by the intermediate and deep water formation in the Rhodes Gyre area (see Fig. 1), although this formation process has been documented (Pinardi et al. 2015; Hecht and Gertman 2001). In this work, we show for the first time the role of the Rhodes Gyre water mass formation area in the EMED overturning circulation.

The first multiscale descriptions of the meridional overturning circulation that included the Aegean deep water source were given by Robinson et al. (2001), Tsimplis et al. (2006), and Pinardi and Masetti (2000). These early studies outline a Mediterranean Sea overturning composed of three main spatial scales: basin scale, subbasin-scale gyres, mesoscale eddies, and standing waves. However, this amount of work produced a qualitative scientific synthesis and not a quantitative estimate of the transport streamfunction. Although we are aware that other scales might also be important, such as the submesoscales (Pinardi et al. 2016; Pascual et al. 2017) and the baroclinic tides generating mixing (Morozov et al. 2002), there is no dataset currently available to investigate these high-frequency components.

The zonal and meridional overturning circulations in the Mediterranean Sea have received attention in the context of simulations of paleoceanographic scenarios, where atmospheric forcing and sill depths were varied in simplified and coarse-resolution general circulation models (Myers 2002; Alhammoud et al. 2010). These studies showed the importance of the Gibraltar sill depth and the value of the net water balance (today with evaporation largely overcoming precipitation) in determining the overturning circulation. Non-eddy-resolving simulations (Pisacane et al. 2006; Amitai et al. 2017) were also used to study the stability of the EMED overturning cells as a function of the strength of the two different deep water formation sources, that is, the Adriatic and Aegean Seas, showing that multiple equilibria are possible depending on the dominance of one deep water source over the other.

A comprehensive description of the zonal and meridional overturning circulation of the Mediterranean Sea for the present climate is still missing. The goal of this work is to describe the observational evidence of the time-mean meridional and zonal overturning system in the Mediterranean Sea with an eddy-resolving model that assimilates data. We use part of an eddy-resolving reanalysis dataset (Simoncelli et al. 2017), spanning the period from 1987 to 2013, to characterize the basin-scale overturning circulation and compute the residual transport streamfunction to understand the role played by eddies and permanent gyres. The key questions are: 1) What is the structure of the zonal and meridional overturning circulations in the Mediterranean Sea? 2) What is the contribution of eddying/gyre motion to that structure? 3) What are the connections between the zonal and the meridional overturning circulation? 4) What is the variability of the Mediterranean overturning before and after the EMT?

The paper starts with section 2 briefly describing the reanalysis dataset. Section 3 presents the analysis of the zonal overturning circulation compared with Wüst (1961) schematic, documenting the vertical density structure of the basin. Section 4 analyses the meridional overturning circulation in the WMED and EMED. Section 5 explores the connection between the zonal and meridional overturning circulation. Section 6 presents the EMT influence of the Mediterranean zonal overturning circulation. Section 7 offers a discussion and conclusions.

2. The reanalysis dataset

A reanalysis is a three-dimensional retrospective estimate of the ocean dynamical variables obtained through a data assimilative numerical experiment

([Masina and Storto 2017](#)). In this work, we used the Copernicus Marine Environment Monitoring Service reanalysis of the Mediterranean area ([Simoncelli et al. 2017](#)), which provided daily mean fields for over 27 years, from 1987 to 2013.

The reanalysis modeling component uses the Nucleus for European Modelling of the Ocean (NEMO), version 3.2, ocean general circulation model ([Madec 2008](#)) that solves the primitive equations on the sphere using the [Jackett and McDougall (1995)](#) equation of state. The horizontal grid has a resolution of $1/16° \times 1/16°$, and the vertical grid has 72 unevenly spaced levels from the surface to a maximum depth of 5000 m. Since the model uses vertical partial cells, the thickness of the bottom layer is allowed to vary as a function of the geographical location to yield a better representation of the bathymetry. The model domain covers the entire Mediterranean Sea and a portion of the Atlantic Ocean in order to resolve salinity and heat exchanges through the Gibraltar Strait ([Oddo et al. 2009](#)). Specifically, the model domain spans from 18.125°W to 36.25°E in longitude and from 30.1875° to 45.9375°N in latitude. The Mediterranean part of the domain is illustrated in [Fig. 1](#). The model is forced by interactive momentum, heat, and freshwater fluxes forced by the ERA-Interim atmospheric fields ([Dee et al. 2011](#)) and climatological precipitation from [Xie and Arkin (1997)](#).

The data assimilation system uses a three-dimensional variational method developed by [Dobricic and Pinardi (2008)](#). The assimilated data consist of in situ observations from conductivity–temperature–depth (CTD), expendable bathythermograph (XBT), mechanical bathythermograph (MBT), bottle, and Argo data as well as remotely sensed data from satellite sea surface temperature and along-track altimetry (TOPEX/Poseidon, *ERS-1* and *-2*, *Envisat*, *Jason-1* and *-2*). The in situ data were contained in the MEDAR/MEDATLAS dataset ([Maillard et al. 2005](#)) and other datasets collected by the authors along the years. These data are now part of the SeaDataNet European archive (https://www.seadatanet.org/). Gridded maps of sea surface temperatures derived from satellite data are not directly assimilated into the model, but were used to correct iteratively the heat flux at the air–sea interface. The background error multivariate correlation matrix was estimated from a historical model simulation and varied seasonally in 13 regions of the Mediterranean Sea each having different characteristics ([Dobricic et al. 2005](#)).

The reanalysis was initialized in January 1985 using a January temperature and salinity climatology obtained from the historical dataset of in situ data collected from year 1900 to the beginning of the reanalysis. The years 1985–86 are considered as a spinup period for the system and are not used in the following analysis.

3. The Mediterranean overturning circulation from salinity and density mapping

a. Vertical salinity mapping

In a landmark study, [Wüst (1961)](#) described the mean intermediate and deep circulation for the whole Mediterranean, by analyzing the principal water masses of the basin. He used the "core method," which entails following the positions of intermediate maxima and minima of salinity, oxygen, and temperature. His results were in the form of handmade figures that are still considered a qualitative representation of the Mediterranean vertical distributions of salt and temperature and its related zonal and vertical circulation. In particular, some of his figures show longitudinal sections of salinity that were used to infer the zonal and vertical velocities associated with the first characterization of the zonal overturning circulation of the Mediterranean Sea. Hypothesizing an advective/diffusive dynamical balance, Wüst indicated the direction and depth of the two-layer flow throughout a zonal Mediterranean section [top panels of [Figs. 2](#) and [3](#), reproduced from [Wüst (1961)](#)]. The upper eastward branch is composed of Atlantic Water (AW; [Malanotte-Rizzoli et al. 1997](#)) that crosses the Sicily Strait up to the Levantine basin. The lower westward returning branch, between 150 and 500 m, is composed of saltier Mediterranean waters, called Levantine Intermediate Waters (LIW; [Theocharis et al. 1993](#); [Ben Ismail et al. 2014](#)).

The 1987–2013 salinity mean field is computed at approximately the same section as Wüst's and the comparison is provided in [Figs. 2](#) and [3](#) (bottom panels). The similarities between the old description and the new estimate are striking, except the new estimate gives a more homogeneous deep water column and a weaker LIW tongue in winter. Salinity values are consistent between the two analyses even if the LIW and deep salinity values are 0.1 psu higher in the new estimate than in Wüst's dataset both in the WMED and the EMED, probably due to the positive salinity climate trend documented by many authors of 0.001 psu yr^{-1} (e.g., [Vargas-Yáñez et al. 2017](#)).

b. Vertical density mapping

One approach to determine the pathways of the overturning circulation is to examine maps of potential density and the associated velocity field ([Talley 2013](#)). We introduce our analysis by considering a vertical transect in the Mediterranean zonal direction and vertical meridional sections across the four deep water formation areas. In their study of a previous Mediterranean Sea reanalysis dataset, [Pinardi et al. (2015)](#) confirmed the existence of four well-defined water mass
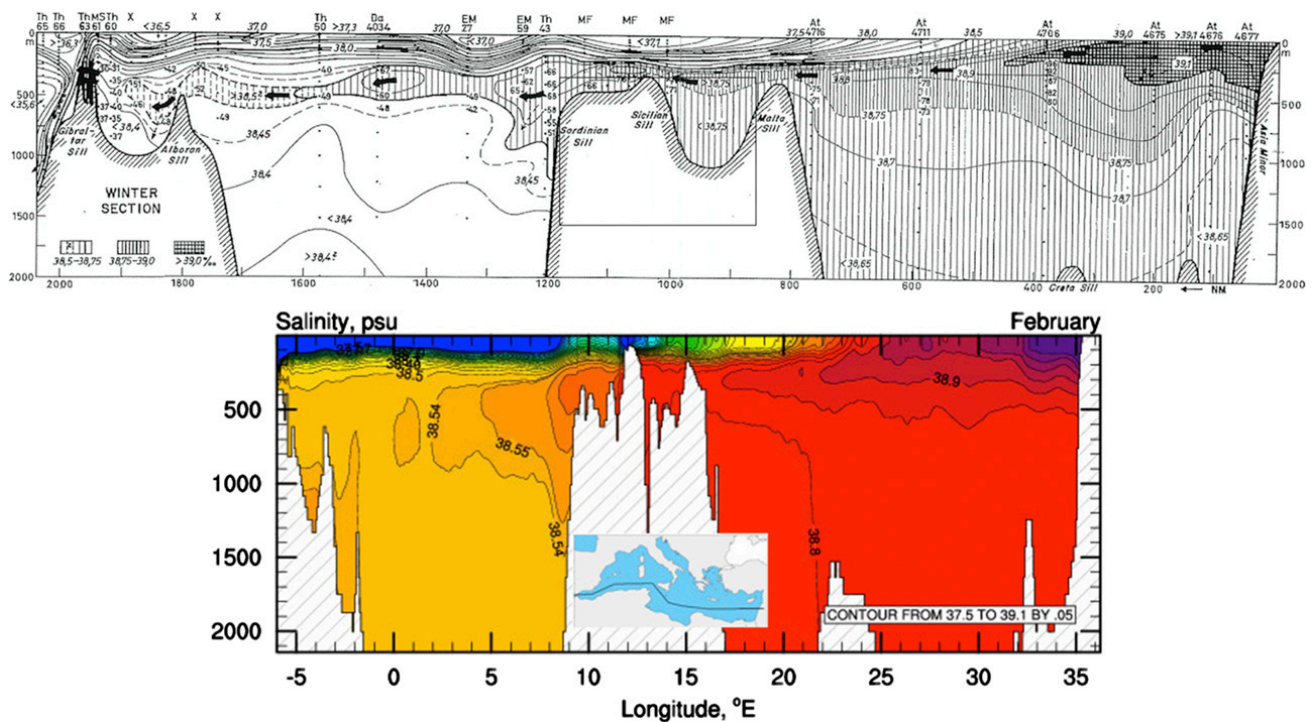
FIG. 2. (top) Zonal section of the salinity along the axis of the Levantine intermediate current for the winter season from Wüst (1961). (bottom) Polyline zonal section of the salinity from a reanalysis climatology in February. The location of the section is shown in the inset.

formation areas: the Gulf of Lion Gyre in the WMED (Leaman and Schott 1991), the southern Adriatic, the Cretan Sea, and the Rhodes Gyre in the EMED (Velaoras et al. 2014). Since the densest waters in the Mediterranean are found as shallow as 500 m below the surface, the potential density referenced to the surface, σ_0, is a useful variable to use in this analysis.

A zonal transect of σ_0 similar to Wüst's longitudinal section of Figs. 2 and 3 is shown in Fig. 4. West of longitude 6°W, fresh Atlantic Waters ($\sigma_0 < 27.3 \, \text{kg m}^{-3}$) enter the Mediterranean Sea, while east of 20°E intermediate isopycnals rise to the surface. The densest waters ($\sigma_0 > 29.2 \, \text{kg m}^{-3}$) are stored in the abyssal plains of the EMED. Below the depth of 500 m, isopycnals of $\sigma_0 \sim 29.15$ and $\sigma_0 \sim 29.225 \, \text{kg m}^{-3}$ are flat, with a larger stratification in the deep EMED water column. The circulation that can be deduced from this figure corresponds to that obtained with the salinity sections of Figs. 2 and 3, except that the subsurface return flow is now along the 28.1–29.1 kg m^{-3} isopycnals, crossing the basin east–west at depths between 150 and 400 m.

Meridional transects connecting the deep water formation areas and the southern boundary of the basin are shown in Fig. 5. All the formation areas show an upwelling of the 29.05 kg m^{-3} isopycnal up to 200 m, indicating the potential for winter ventilation. The pycnocline is located between 200 and 300 m. The EMED contains the densest waters, in particular in the Cretan Sea where densities rise

to 29.3 kg m^{-3} (Velaoras et al. 2014). Isopycnals outside the water formation areas are flat in the middle of the basin, while downwelling (upwelling) occurs along the southern Mediterranean coasts above (below) 200–250 m with the exception of the Cretan Sea transect.

The overall density analysis of meridional sections shows the emergence of two distinct meridional areas: 1) above 200 m, the northern regions are dominated by the outcropping of isopycnals and the southern regions are dominated by AW flow, and 2) below 300 m, the deep isopycnals downwell from the open ocean formation areas toward the coasts and upwell on the southern shores, with the exception of the Cretan Passage section. From these density sections it is not possible to draw a complete picture of the deep circulation of the basin. Therefore the smoothed time-mean vertical velocity was calculated at 1000 m, that is, an interface deep enough to be affected only by the vertical motion of the deep water masses (a qualitatively similar picture is found at 500 m).

The model vertical velocity field is displayed in Fig. 6. Along the four sections shown in Fig. 5, the mean vertical velocity shows downwelling along the northern shores and upwelling in the southern coasts, strongly enhanced near the boundary. This is not surprising, since enhanced mixing and friction is found near rough topography, associated with vertical motion. Thus, large downwelling motions are likely to be found near areas of intense mixing, such as deep water formation regions. It is interesting to note that
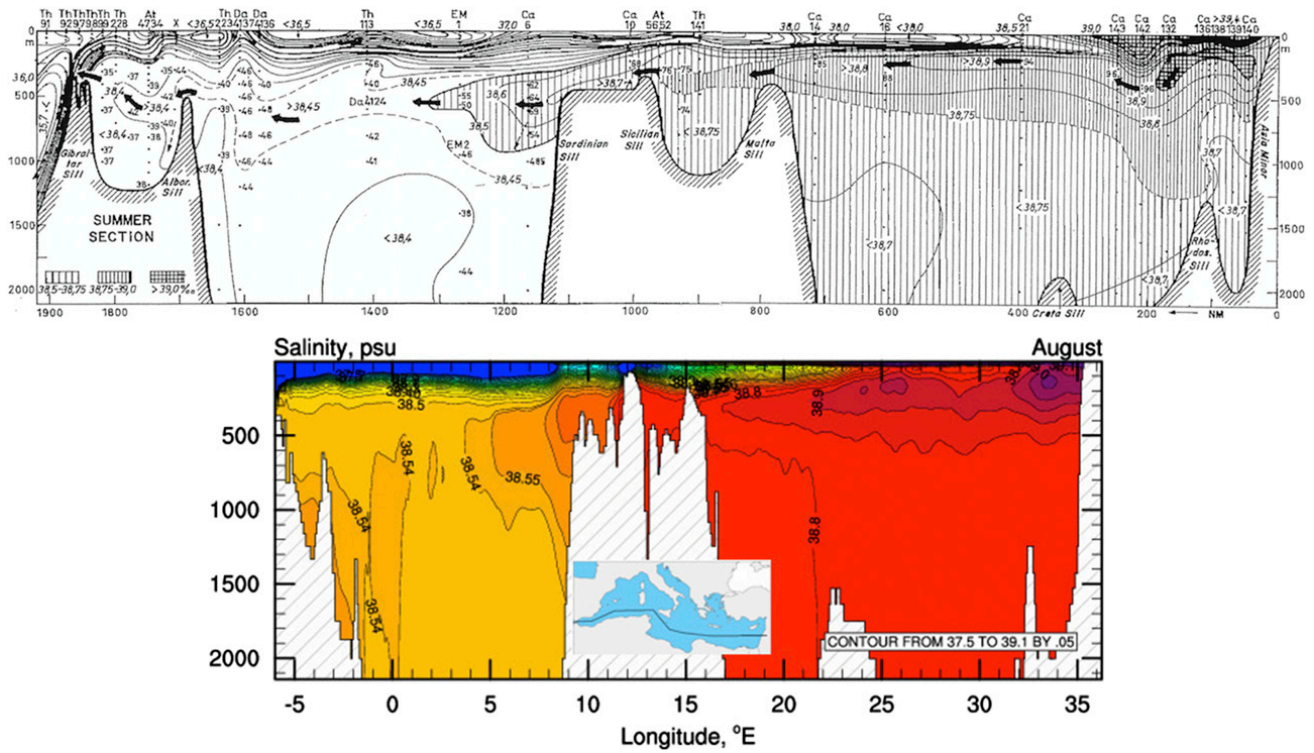
FIG. 3. (top) Zonal section of the salinity along the axis of the Levantine intermediate current for the summer season from Wüst (1961). (bottom) Polyline zonal section of the salinity from a reanalysis climatology in August. The location of the section is shown in the inset.

there are subregional differences, especially in the Alboran Sea, Ionian Sea, and the Cretan Passage.

Recently, Waldman et al. (2018) has also looked at the areas of downwelling that were most likely associated with the overturning circulation of the Mediterranean Sea. They report measurements of downwelling motion along the northern escarpment of the Gulf of Lion, which is in agreement with our model results. However, they cannot estimate all areas with observations. Our work extends their finding that overturning circulation downwelling is localized in the northern boundary current areas, that is, the Liguro–Provençal current for the Gulf of Lion and the Asia Minor current in the northern Levantine basin, [for the nomenclature, see Pinardi et al. (2015)]. Deep upwelling is instead found along most of the southern Mediterranean coastlines, which might be connected to abyssal overturning or to the return flow of the upper water column overturning.

To better understand the basin-scale overturning, we will now compute the streamfunctions in the vertical plane and relate them back to this downwelling–upwelling system along the boundaries of the domain.

4. The Mediterranean Sea overturning system

To understand the mean vertical circulation of the Mediterranean Sea, we compute the time-mean zonal and meridional Eulerian and residual streamfunctions associated with the velocity field estimate provided by the reanalysis.

The Eulerian meridional (zonal) streamfunction is calculated by integrating the meridional (zonal) velocity v (u) first in the vertical direction, then in the zonal (meridional) direction, and finally averaging over the reanalysis period. The resulting streamfunctions are

$$\psi_{\text{zon}}(x,z) \equiv -\frac{1}{T}\int_{t_0}^{t_1}\int_{y_{B_1}}^{y_{B_2}}\int_{-H}^{z} u(x,y,\tilde{z},t)\,d\tilde{z}\,dy\,dt, \quad (2)$$

$$\psi_{\text{mer}}(y,z) \equiv -\frac{1}{T}\int_{t_0}^{t_1}\int_{x_{B_1}}^{x_{B_2}}\int_{-H}^{z} v(x,y,\tilde{z},t)\,d\tilde{z}\,dx\,dt, \quad (3)$$

where y_{B_1} and y_{B_2} are the meridional boundaries, x_{B_1} and x_{B_2} are the zonal boundaries, $T = t_1 - t_0$ is the temporal averaging interval, and H is the bottom bathymetry. With these definitions, positive (negative) values represent clockwise (counterclockwise) circulations in the vertical plane.

To include the transport associated with the contributions from eddies, gyres, and standing waves, the residual streamfunctions ψ^* are defined from the velocities integrated in density (σ_0) space, rather than depth, then integrated in one horizontal direction and then averaged in time, as follows:
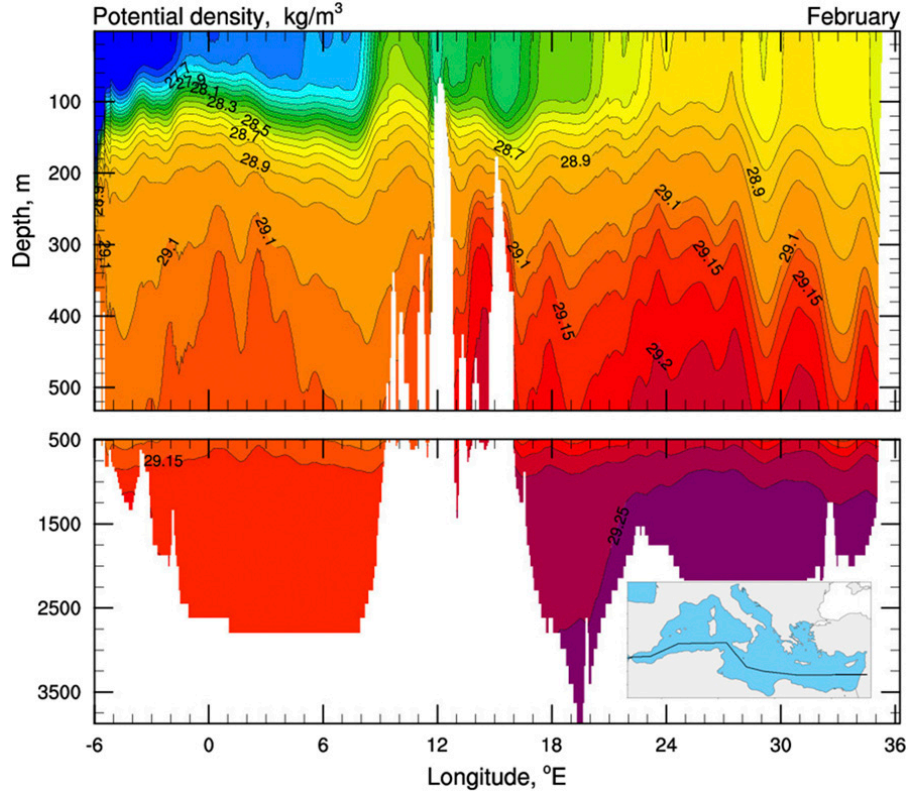
FIG. 4. Polyline zonal section of the potential density σ_0 for a climatological February average. The location of the section is shown in the inset.

$$\psi_{\text{zon}}^{*}(x, \tilde{\sigma}) = \frac{1}{T}\int_{t_0}^{t_1}\int_{y_{B_1}}^{y_{B_2}}\int_{-H}^{0}\mathcal{H}[\tilde{\sigma} - \sigma(x, y, z, t)]$$
$$\times u(x, y, z, t)\, dz\, dy\, dt, \qquad (4)$$

$$\psi_{\text{mer}}^{*}(y, \tilde{\sigma}) = \frac{1}{T}\int_{t_0}^{t_1}\int_{x_{B_1}}^{x_{B_2}}\int_{-H}^{0}\mathcal{H}[\tilde{\sigma} - \sigma(x, y, z, t)]$$
$$\times v(x, y, z, t)\, dz\, dx\, dt, \qquad (5)$$

where $\mathcal{H}$ is the Heaviside function. This is the streamfunction corresponding to the thickness weighted averaged velocity defined in Eq. (1) and, formally, in Young (2012). With these definitions, ψ^{*} is the transport occurring below the isopycnal $\tilde{\sigma}$, which in turn is a function of all three spatial dimensions plus time. Within the residual framework, the natural vertical coordinate is $\tilde{\sigma}$, but we remapped ψ^{*} onto a depth-like coordinate ζ in order to ease the comparison with the Eulerian representation, whose natural vertical coordinate is depth. The definition of ζ is

$$\zeta(x, \tilde{\sigma}) \equiv -\frac{1}{T}\frac{1}{y_{B_2} - y_{B_1}}\int_{t_0}^{t_1}\int_{\mathbf{y}_{B_1}}^{\mathbf{y}_{B_2}}\mathcal{H}[\tilde{\sigma} - \sigma(x, y, z, t)]\, dy\, dt,$$
$$(6)$$

$$\zeta(y, \tilde{\sigma}) \equiv -\frac{1}{T}\frac{1}{x_{B_2} - x_{B_1}}\int_{t_0}^{t_1}\int_{\mathbf{x}_{B_1}}^{\mathbf{x}_{B_2}}\mathcal{H}[\tilde{\sigma} - \sigma(x, y, z, t)]\, dx\, dt.$$
$$(7)$$

This mapping implies a distribution of $\tilde{\sigma}$ which is given by

$$\tilde{\sigma}(\mathbf{x}, \zeta) = \zeta^{-1}[\zeta(\mathbf{x}, \tilde{\sigma})], \qquad (8)$$

where $\mathbf{x} = x$ or $\mathbf{x} = y$ for the zonal and meridional streamfunctions, respectively (see the appendix). The quantity $\tilde{\sigma}$ is contoured together with ψ^{*} to show the location of potential density surfaces used in the mapped coordinates.

a. Zonal overturning circulation

Figure 7 shows the Eulerian mean ψ_{zon} and residual ψ_{zon}^{*} averaged over the entire period of the reanalysis.

The Eulerian zonal overturning (top panel of Fig. 7) is characterized by three structures: the first is a shallow clockwise cell, above the 29.1 kg m^{-3} potential density surface, corresponding to AW flowing eastward and LIW flowing westward. We called this shallow overturning circulation the Wüst cell. Below 300–700 m, two other cells dominate, one in the WMED and the other in the EMED. In the WMED, a counterclockwise cell
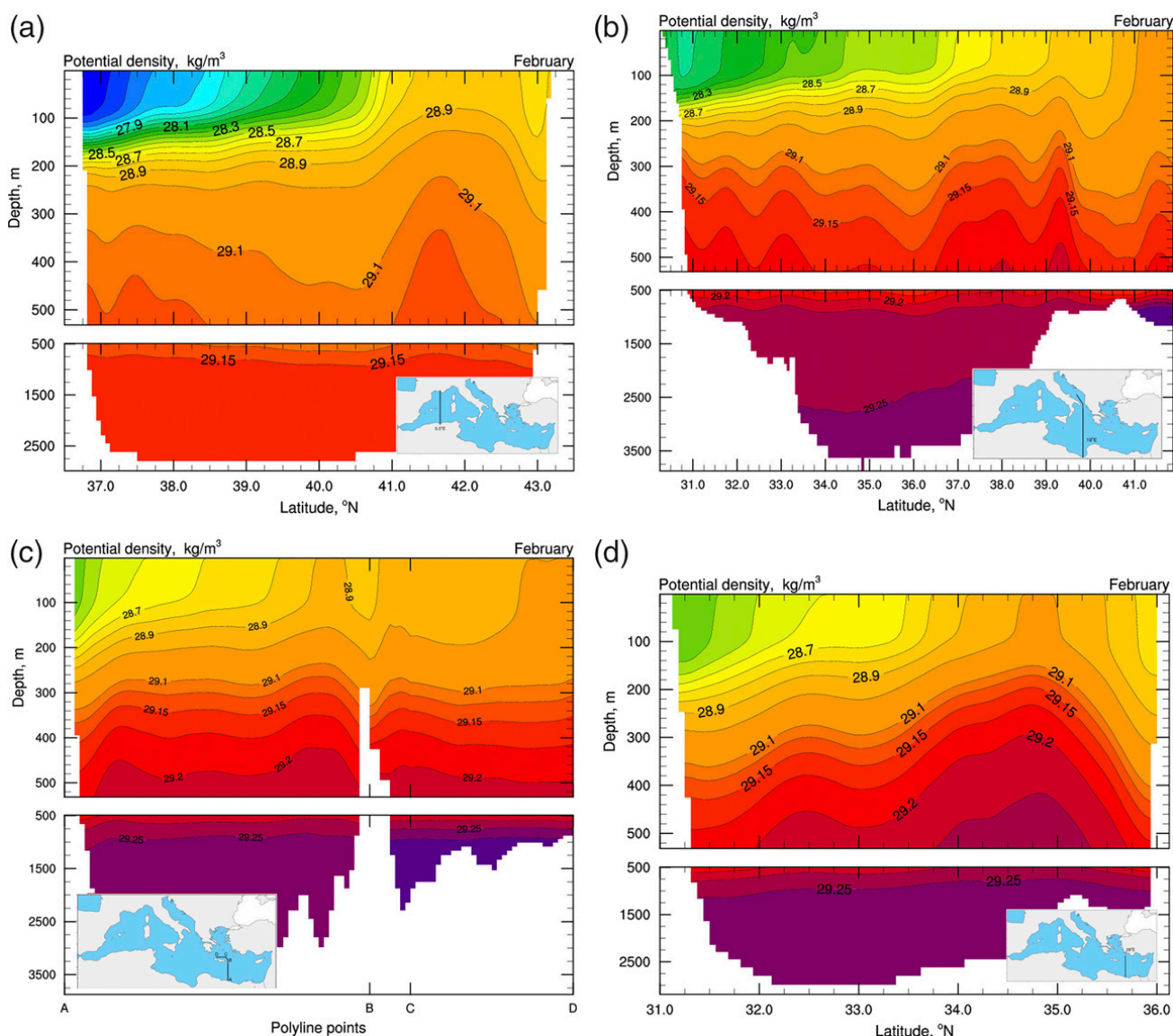
80

FIG. 5. Sections of the potential density σ_0 during climatological February along (a) 5.5°, (b) 19°, (c) 26°, and (d) 28°E. The locations of the sections are shown in the bottom-corner inset of each panel.

occupies the region below 700 m, while in the EMED a multiple centers clockwise cell extends to the bottom. The WMED deep zonal counterclockwise cell fills the region east of 5°W, occupying the deep regions of the Alboran Sea, the Algerian basin, and the Tyrrhenian Sea, the latter located at about 10°–15°E. The EMED deep clockwise cell maximum is centered at the longitude of the Aegean deep water outflow, that is, 22°E, and it is connected with the surface intensified Wüst cell. Several other subsurface clockwise cells exist in the Levantine, disconnected from the surface. The clockwise cell centered at approximately 28°E is notably associated with the dense water formation processes occurring in the Rhodes Gyre area.

The residual streamfunction (bottom panel of Fig. 7) shows the different dynamical balances dominating the deep WMED and EMED overturning cells due to the transport by permanent gyres, standing waves and transient eddies [the second term in Eq. (1)]. The WMED deep counterclockwise residual overturning is stronger than its Eulerian counterpart indicating that the transport by stationary gyres and eddies reinforces the mean abyssal vertical circulation. The residual velocities (tangent to the streamfunction by definition) cross the isopycnals indicating that diapycnal mixing is important for the maintenance of this cell. In the Tyrrhenian Sea, the residual overturning circulation mostly flows along isopycnals indicating a more adiabatic balance. But it is in the EMED where the major differences between
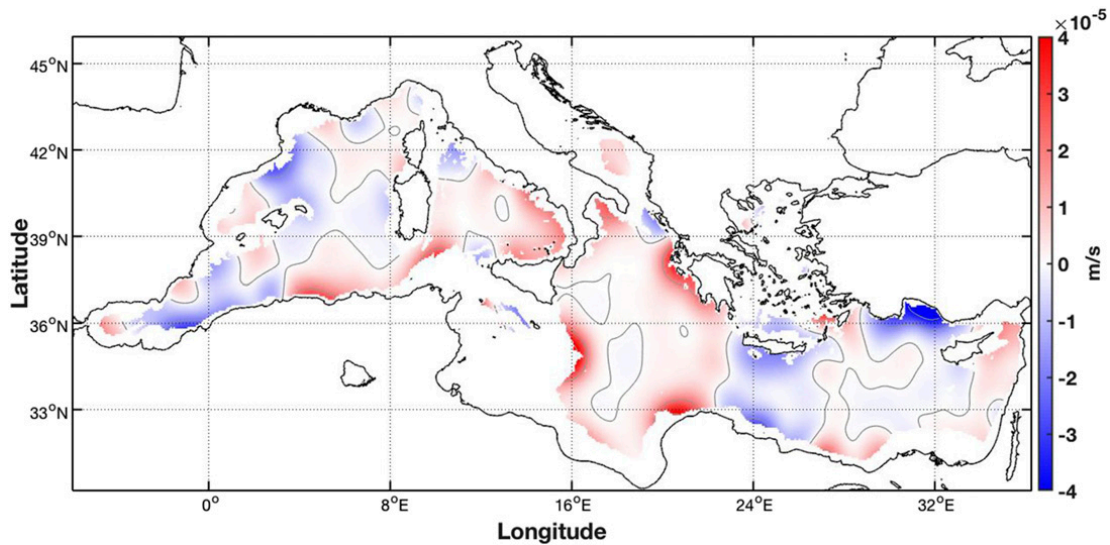
FIG. 6. Vertical velocity at 1000 m smoothed with 75 iterations of a Gaussian filter, which applies a weighted average of the 24 nearest points to each grid point.

Eulerian and residual zonal overturning appear. The residual circulation is weaker at depth than the Eulerian counterpart, and a detectable residual counterclockwise circulation emerges. The large and deep Eulerian clockwise cell is broken down in two parts in the residual representation: the deep overturning at 22°E is along isopycnals, while the circulation around the secondary maxima located approximately in the Rhodes Gyre area of 28°E is across isopycnals. The deep to abyssal zonal overturning circulation of the EMED is strongly influenced by the transport due to the eddy/permanent gyres component. In our analysis, the Aegean deep water source is apparent in the zonal overturning cell of the Mediterranean Sea, because our dataset straddles the period of the EMT event. This feature will be further discussed in section 6.

Values of the zonal overturning circulation counterclockwise and clockwise cells are on the order of 1 Sv ($1 Sv \equiv 10^6 m^3 s^{-1}$) in both the WMED and the EMED. The surface Wüst cell is stronger in the Eulerian mean than in the residual form, supporting the conclusion that the eddy field in the first 300 m weakens the zonal transport of the Wüst cell.

In synthesis, the major outcomes of the zonal overturning circulation analysis are 1) the revisited Wüst cell occupies the first 500 m of the water column and is weakened by the gyre/eddy components of the transport field; 2) a clockwise deep cell is present in the region of the Aegean outflow, dominated by along isopycnal motion, and a weaker, less deep clockwise cell is present in the Rhodes Gyre area; and 3) the permanent gyre/eddy transport field strengthens the deep overturning counterclockwise cells of the zonal overturning.

b. Meridional overturning circulation

We now discuss the meridional streamfunction, comparing the Eulerian mean ψ_{mer} and residual ψ^*_{mer} previously defined in Eqs. (3) and (5). We first show the WMED and EMED and then the whole basin-scale meridional overturning system. The streamfunction for the WMED considers a zonal averaging up to a section in the Sicily Strait and the one for the EMED an averaging carried out from the same section up to the Levantine basin coastlines.

1) THE WESTERN MERIDIONAL OVERTURNING CIRCULATION

The Eulerian WMED overturning circulation is shown in Fig. 8. It consists of a clockwise cell composed of several maxima, from approximately 100 m down to a depth of 2000 m. The second, opposite cell is counterclockwise, occupying the deep Algerian basin areas. The large positive values in the upper 500 m, south of 37°N, correspond to the Gibraltar Strait inflow.

The residual WMED meridional overturning changes this picture, showing only two well-separated counter-rotating cells, both stronger than their Eulerian counterparts. For the clockwise cells, the Eulerian streamfunction indicates a volume transport approximately of 0.36 Sv, while the residual counterpart is 0.88 Sv. For the counterclockwise cells, the minimum of -0.22 Sv in the Eulerian framework is increased to -0.7 Sv in the residual streamfunction. The boundary between the two cells is at approximately 39°N, that is, the latitude marking the division between the permanent cyclonic gyre of the Gulf of Lion and the eddy-dominated anticyclonic area of the
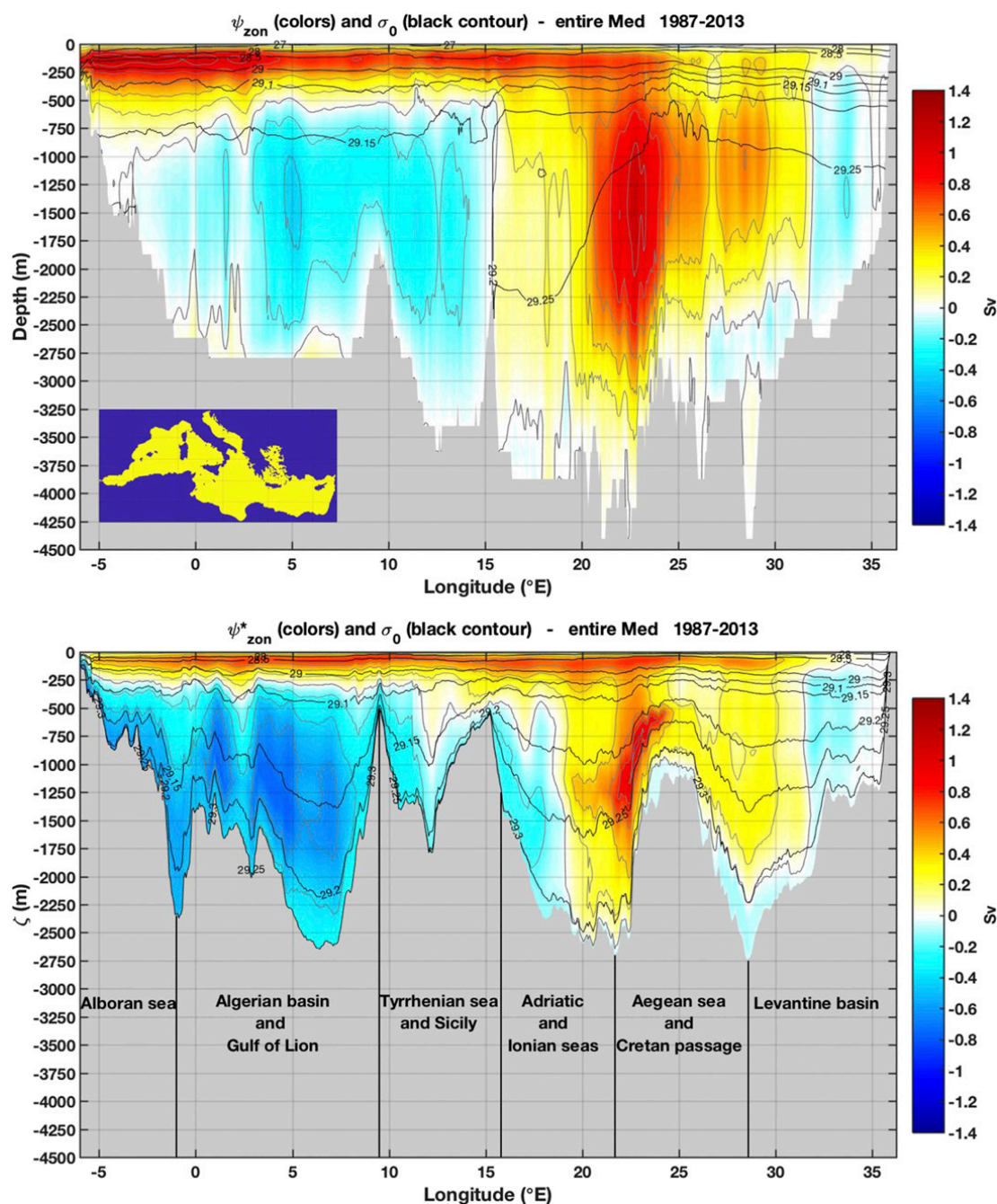
FIG. 7. (top) Eulerian and (bottom) residual zonal streamfunction, integrated over the latitudinal extension of the basin and averaged in time over the years 1987–2013. The gray contour lines and the colors show streamfunction values at 0.2-Sv intervals. The black contours are isopycnal surfaces of $\tilde{\sigma}$ (kg m^{-3}) (top) latitudinally and time averaged and (bottom) calculated from Eq. (8). The gray areas mark (top) the deepest bathymetry level and (bottom) the highest density-layer found over each latitudinal section of the basin. The different regions of the Mediterranean considered in the latitudinal averaging are described over the gray area in the bottom panel.

Algerian current described by Pinardi et al. (2015). The clockwise northern cell is associated with the deep water formation areas in the northern basin, normally centered around 41°–42°N. The downwelling branch of the clockwise cell occurs near along the northern boundary of the domain, where vertical velocities are negative, as illustrated in Fig. 6. The western Mediterranean deep water formation and spreading phenomena is an eddy dominated process, documented in several papers (Madec et al. 1996; Demirov and Pinardi 2007; Send and Testor 2017). Thus, the residual overturning is stronger than the Eulerian mean.
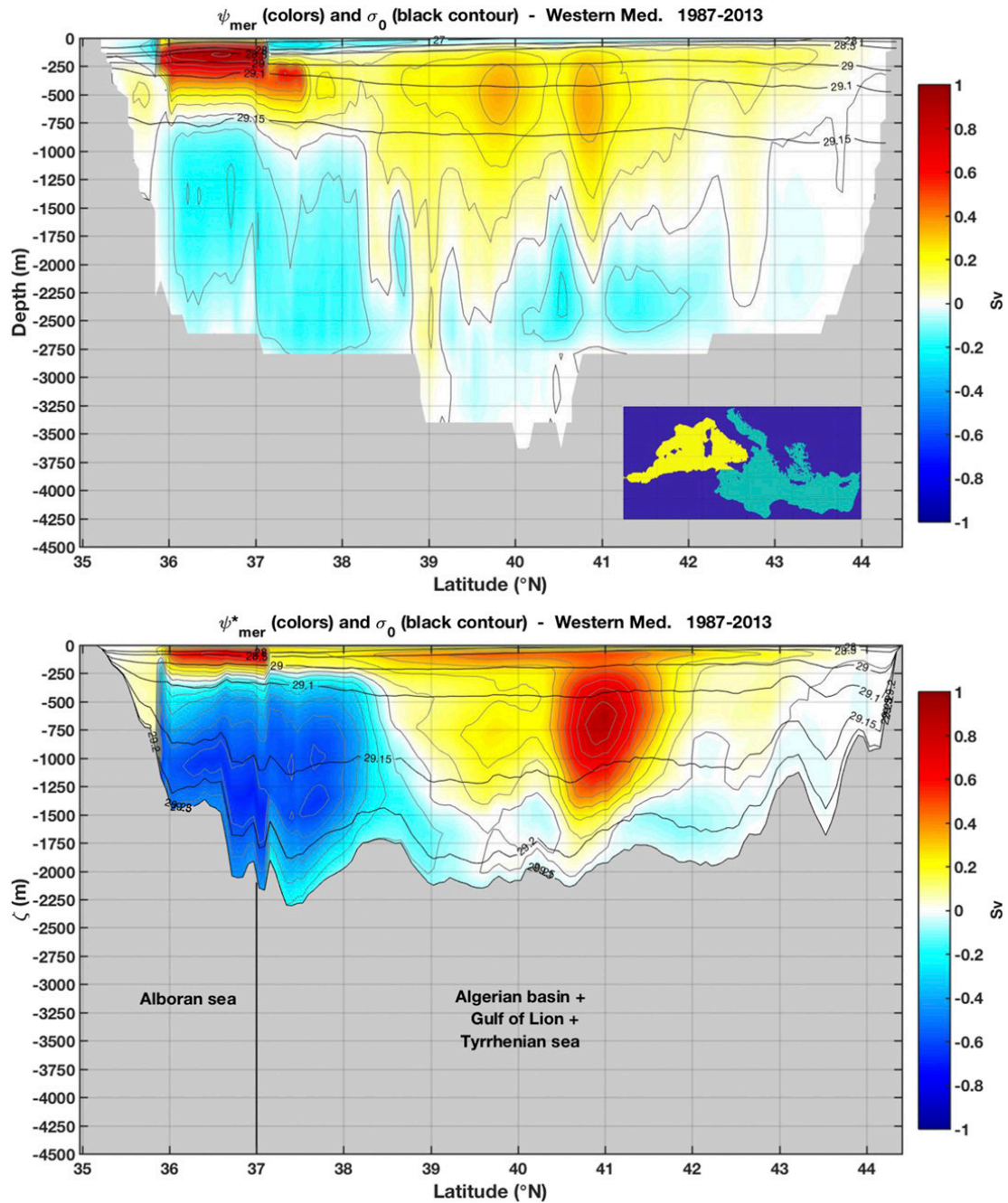
FIG. 8. (top) Eulerian and (bottom) residual meridional streamfunction for the WMED, integrated in longitude over the yellow region shown in the inset and averaged in time over the years 1987–2013. The gray contour lines and the colors show streamfunction values at 0.1-Sv intervals. The black contours are isopycnal surfaces of $\tilde{\sigma}$ (kg m^{-3}) (top) longitudinally and time averaged and (bottom) calculated from Eq. (8). The gray areas mark (top) the deepest bathymetry level and (bottom) the highest density-layer depth found over each longitudinal section of the basin. The different regions of the Mediterranean considered in the longitudinal averaging are described over the gray area in the bottom panel.

The residual southern counterclockwise cell extends from approximately 300 m to the bottom and it is stronger than the northern clockwise cell. The downwelling branch of this abyssal cell is located along the northern African escarpment, below the upwelling branch illustrated in Fig. 6. The residual overturning, for both counterclockwise and clockwise cells, crosses isopycnals, indicating that diapycnal mixing dominates the WMED meridional overturning circulation.

2) THE EASTERN MERIDIONAL OVERTURNING
CIRCULATION

We now consider a spatial domain bounded in the zonal direction by the Sicily Strait and the Adriatic, Balcanic, Turkish, and Levantine basin coasts. To have an overall expression of the EMED basin-scale vertical circulation, both deep water formation marginal sea areas are included, that is, the Adriatic and the Aegean Sea. The Eulerian and residual EMED overturning circulations are shown in Fig. 9.

With reference to the Eulerian framework (top panel of Fig. 9), the upper 250 m of the water column are occupied by a counterclockwise surface cell, which we interpret to be associated with the Ekman transport and its shallow return flow. This surface counterclockwise cell is interrupted at 36.5°N due to the physical gap of the Sicily Strait at this latitude. Below 250 m a clockwise multicentered overturning cell is present. In general we can distinguish between two clockwise centers, one extending southward of 36.5°N and the other north of it. North of 36.5°N, the overturning streamfunction is connected to the Adriatic and Aegean deep water formation areas with the maximum centered at about 37°N, corresponding to the Aegean deep water formation area (Cretan Sea). The northward maximum extension of this clockwise cell includes the Adriatic Sea deep water formation regions with transports about 0.1 Sv, in agreement with the recent estimates of Verri et al. (2018). It is clear that this northern clockwise center is weaker than the Aegean one, probably due to the specific time period chosen. In fact, from 1989 to 1998 the EMT deep water formation event is known to coincide with smaller southern Adriatic deep water formation rates (Amitai et al. 2017).

South of 36.5°N, several clockwise overturning centers exist, with maxima between 250- and 1000-m depth, some of them extending to almost 3000 m. These cells are associated with the Aegean Sea deep water formation area, its outflow during the EMT and the Levantine Deep Water formation processes in the Rhodes Gyre. Velaoras et al. (2014) report that dense water outflow from the Aegean continued between 2000 and 2010 thus contributing to give a large overturning in this area. These clockwise cells add up to approximately 0.5–0.6 Sv at the latitudes of 34°–36°N.

A deep counterclockwise Eulerian cell occupies the depth below 1000 m in the meridional region of the Ionian Sea (north of 35°N). It is bounded by the $\sigma_0 \sim 29.2 \, \mathrm{kg \, m^{-3}}$ isopycnal surface, below which the stratification is weak. This deep cell has been described before (Zavatarelli and Mellor 1995; Pisacane et al. 2006; Verri et al. 2018) and it is stronger than the Eulerian WMED deep counterclockwise cell, probably due to the deeper bathymetry of the eastern basin.

In the residual framework (bottom panel of Fig. 9) the vertical circulation appears quite different, as it is the case for the WMED. The clockwise part of the streamfunction is subdivided into three major cells: the weakest is connected to the Adriatic Sea water formation areas, the second to the Aegean Sea, and the third, south of 35.5°N, is connected to the Aegean dense water outflow and the Rhodes Gyre dense water formation area. The southern residual clockwise cells extend over most of the water column and the deep counterclockwise cell has practically disappeared. While the clockwise overturning cell north of 36.5°N is essentially the same in the Eulerian and residual framework, the southern residual circulation is dipolar and stronger than in the Eulerian description, adding up to ~0.7 Sv in each center. The second clockwise center, located between 35.5° and 36.5°N, corresponds to the areas where the Aegean Sea dense waters formation occurs, and to the Rhodes Gyre formation area around 36.5°N. The southernmost positive maximum, located between 33° and 35°N, corresponds geographically to the so-called Cretan Passage, where the dense Aegean Seawater outflows and to the southern Rhodes Gyre. All the clockwise residual circulations are cross-isopycnals indicating that diapycnal mixing processes are important over the whole basin. It is noteworthy that the EMED southern clockwise cell has never been depicted before.

3) THE MERIDIONAL BASIN-SCALE
OVERTURNING SYSTEM

In Fig. 10 we analyze the Eulerian and residual meridional overturning circulation for the whole Mediterranean Sea. The Eulerian basin-scale streamfunction (top panel of Fig. 10) shows the superposition of the WMED and EMED clockwise cells occupying the depths between ~100–250 and 1000 m with cell boundaries reaching 2000 m. The maximum value of 1 Sv is reached in the regions south of 38°N. The WMED clockwise cells (north of 38°N) are weaker than their EMED counterparts, while the WMED abyssal counterclockwise circulation is the largest.

The residual basin-scale meridional overturning brings a balance between the southern and northern clockwise cells. The WMED clockwise maximum is 0.9 Sv, larger than in the Eulerian framework and comparable to the southern one, 0.76 Sv, corresponding to the Cretan Passage and Levantine basin overturning. The basin-scale residual counterclockwise deep to abyssal circulation has an absolute value of the transport around 0.5 Sv, about half of the clockwise counterparts.

5. Connection between the zonal and the meridional overturning

There is evidence that the LIW, occupying the layer between 150 and 500 m, impacts the deep water
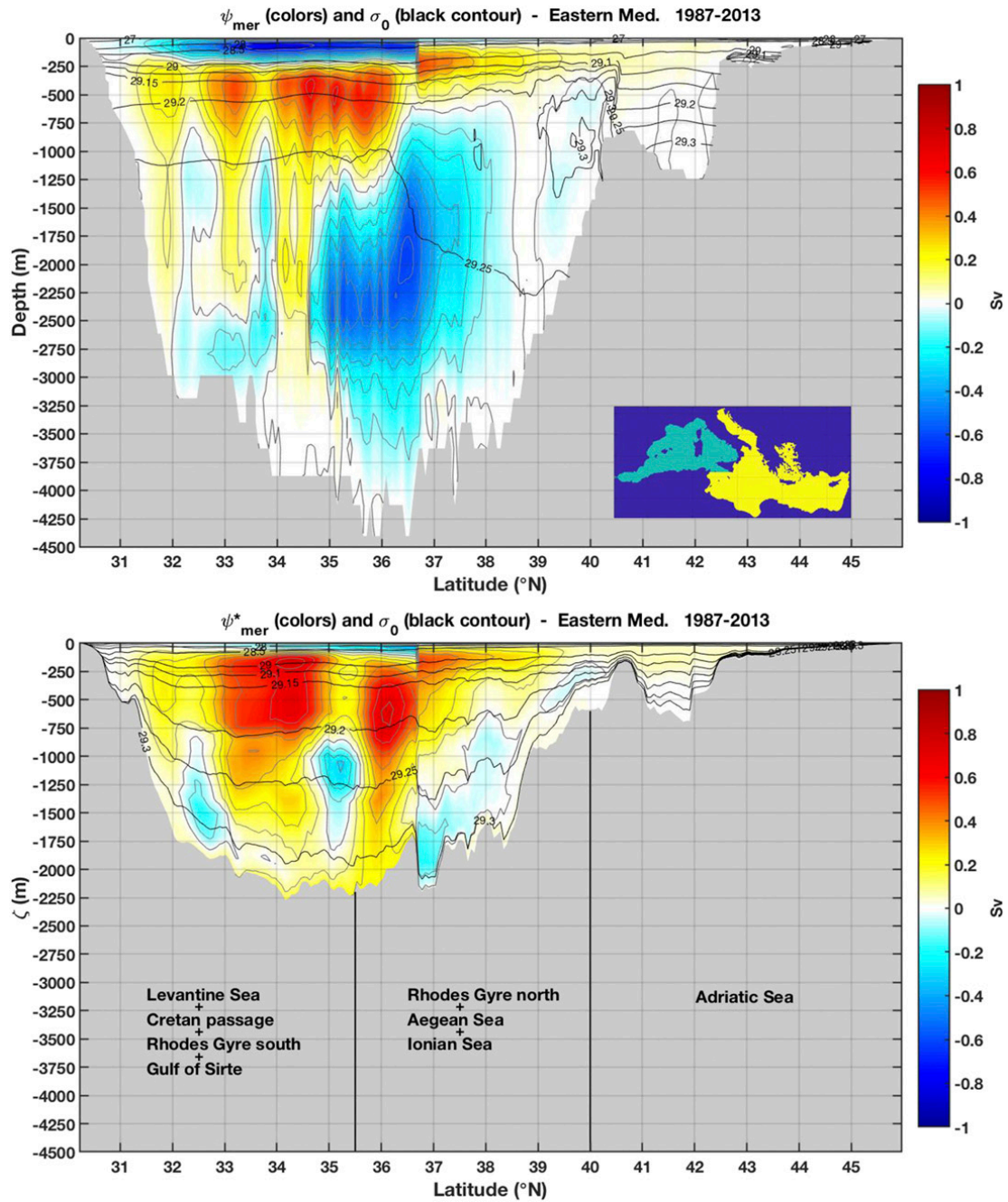
FIG. 9. (top) Eulerian and (bottom) residual meridional streamfunction of the EMED, integrated in longitude over the yellow region shown in the inset and averaged in time over the years 1987–2013. The gray contour lines and the colors show streamfunction values at 0.1-Sv intervals. The black contours are isopycnal surfaces of $\tilde{\sigma}$ (kg m^{-3}) (top) longitudinally and time averaged and (bottom) calculated from Eq. (8). The gray areas mark (top) the deepest bathymetry level and (bottom) the highest density layer depth found over each longitudinal section of the basin. The different regions of the Mediterranean considered in the longitudinal averaging are described over the gray area in the bottom panel.

formation processes (Wu and Haines 1996) in the WMED. Published results showed that LIW increases the salinity of the waters exposed to the winter cooling influencing the deep water mass formation in the Aegean, Adriatic, and Gulf of Lion areas (Klein et al. 2000; Theocharis et al. 2002; Schroeder et al. 2016). The Western Mediterranean Transition (WMT) has been

recently documented that connects the changes of the WMED deep water formation rates to the saltier LIW arriving from the EMED, after the EMT (Zunino et al. 2012).

In addition, the AW, occupying the upper-layer (0–150 m), also influences the deep water properties and formation rates. Malanotte-Rizzoli et al. (1997) found that,
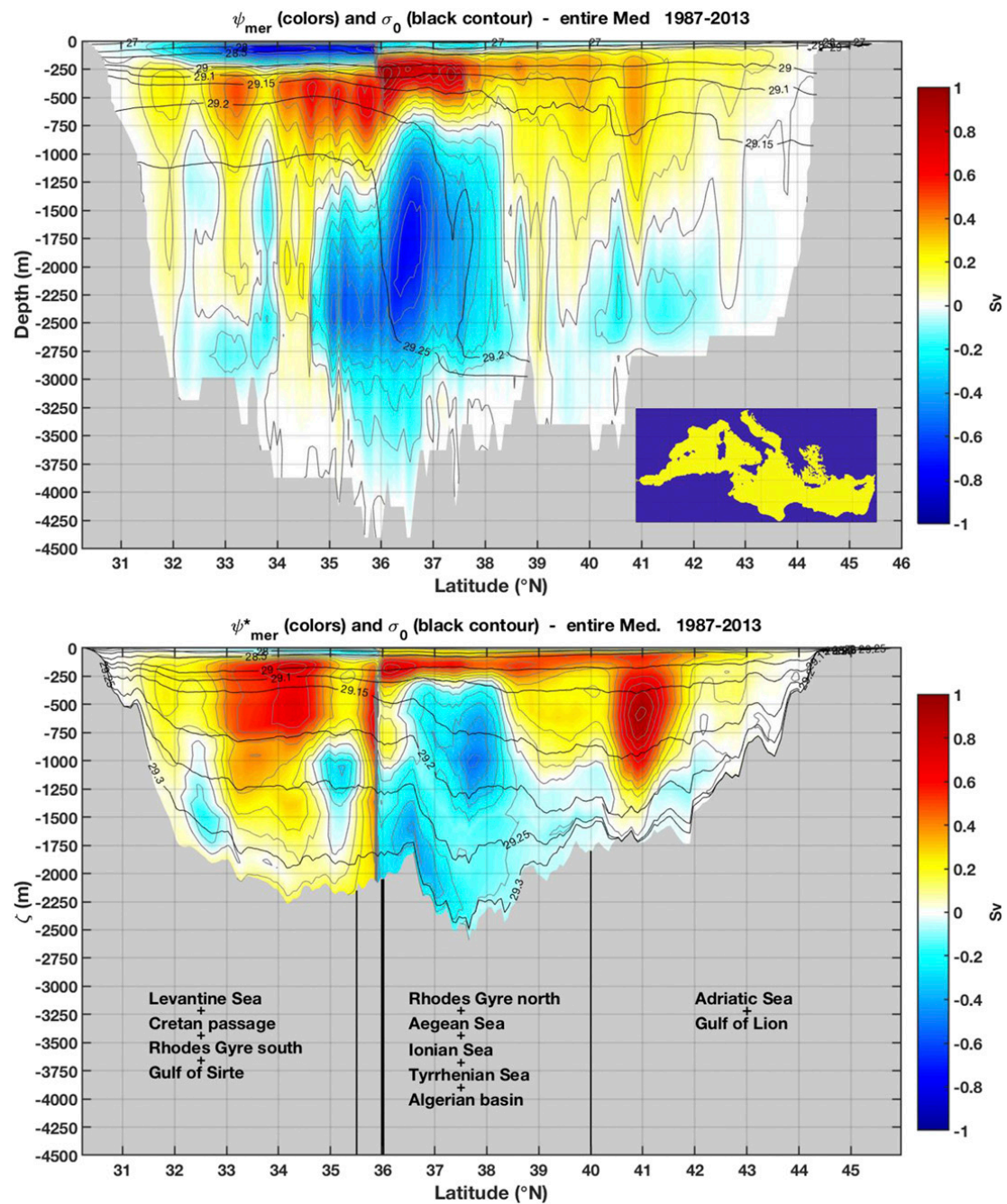
FIG. 10. (top) Eulerian and (bottom) residual meridional streamfunction of the entire Mediterranean Sea, integrated in longitude over the yellow region shown in the inset and averaged in time over the years 1987–2013. The gray contour lines and the colors show streamfunction values at 0.1-Sv intervals. The black contours are isopycnal surfaces of $\tilde{\sigma}$ (kg m^{-3}) (top) longitudinally and time averaged and (bottom) calculated from Eq. (8). The gray areas mark (top) the deepest bathymetry level and (bottom) the highest density layer depth found over each longitudinal section of the basin. The different regions of the Mediterranean considered in the longitudinal averaging are described over the gray area in the bottom panel. The thick vertical black line indicates the Gibraltar Strait location.

during the EMT the diversion of AW toward the Adriatic Sea was an important factor determining the deep water formation in the Rhodes Gyre and the subsequent formation of high-density waters in the Aegean Sea. The AW diversion was due to a specific gyre in the Northern Ionian Sea, so-called Northern Ionian Gyre (NIG) that lasted a decade, from 1987 to 1996, documented for the first time by Pinardi and Navarra (1993) and recently discussed in great details by Reale et al. (2016). After the 1987–96 period the NIG reversed and AW reached again the Levantine while the EMT ended.

Since the flow of AW and LIW composes the Wüst cell, there could be important interactions between the zonal and meridional overturning dynamics of the basin. In this section we start to explore the connection between the Wüst cell and the meridional cells by looking at the horizontal flow field in the upper and lower branches of the cell and separating the divergent and rotational components of the flow field. The divergent component is connected to the inflow–outflow system at Gibraltar and it contributes to the vertical downwelling–upwelling components of the meridional overturning of the basin.

Considering the inflow–outflow system at the Gibraltar Strait (5.5°W, figure not shown), we found that the zero crossing of the zonal velocity is located around 150 m and the outflow extends slightly lower than 600 m. The time-mean value of the inflow is 0.92 Sv, while the outflow is 0.88 Sv for a net transport of 0.04 Sv, which is in close agreement with the literature (Baschek et al. 2001). We analyze the horizontal circulation in two vertical layers, the first extending from the surface to $z_1 = 150$ m and the second from z_1 to $z_2 = 600$ m. Specifically, we define the transports and the vertically averaged velocities:

$$(U_k, V_k) = \int_{z_k}^{z_{k-1}} (u\Delta y, v\Delta x)\, dz, \qquad (9)$$

$$(u_k, v_k) = \frac{1}{\Delta z_k} \int_{z_k}^{z_{k-1}} (u, v)\, dz, \qquad (10)$$

where (u, v) is the horizontal velocity field; Δx and Δy are the model grid cells in the longitudinal and latitudinal directions, respectively; $k = 1, 2$ are the vertical layer labels (increasing downward) with z_0 equal to the sea surface, taken approximately at $z_0 = 0$; and Δz_k is the layer thickness. The transport field and the vertically averaged velocities are shown in Fig. 11.

The upper-layer flow is characterized by intensified current segments that, starting from the Gibraltar Strait, can be traced up to the Levantine basin (top panel of Fig. 11). We can recognize some of the well-known structures of the surface circulation of the Mediterranean Sea, as described in details by Pinardi et al. (2015). The westward lower-layer flow of the Wüst cell is composed of jet segments that bring LIW and other intermediate waters toward the Strait of Gibraltar (bottom panel of Fig. 11). To note is the intensified branch of the lower-layer flow along the Libyan coasts.

To understand the effects of this two-layer flow field on the overturning circulation we need to disentangle the divergent and rotational component of the flow field.

The divergent component is associated with the vertical velocity component of the overturning cells (Fig. 6).

We subdivide the two-layer transport vector in the two components:

$$(U_k, V_k) = (U_{k,\phi}, V_{k,\phi}) + (U_{k,\chi}, V_{k,\chi}), \qquad (11)$$

where $(U_{k,\phi}, V_{k,\phi})$ is the divergent component of the transport, while $(U_{k,\chi}, V_{k,\chi})$ is the divergenceless or rotational component. The divergent and rotational components of the transport are related to the velocity potential ϕ_k and streamfunction χ_k by

$$U_{k,\phi} = \delta_i \phi_k, \quad V_{k,\phi} = \delta_j \phi_k \qquad (12)$$

and

$$U_{k,\chi} = -\delta_j \chi_k, \quad V_{k,\chi} = \delta_i \chi_k, \qquad (13)$$

respectively. The symbols δ_i and δ_j indicate the (dimensionless) difference between two adjacent points in the longitudinal and latitudinal direction respectively. The equation for the velocity potential is defined as

$$(\delta_i^2 + \delta_j^2)\phi_k = \delta_i U_k + \delta_j V_k, \qquad (14)$$

while for the rotational component,

$$(\delta_i^2 + \delta_j^2)\chi_k = \delta_i V_k - \delta_j U_k. \qquad (15)$$

The solution of Eq. (14) is subject to nonhomogeneous boundary conditions, given by the normal velocity at the Gibraltar Strait, that is,

$$(\delta_i \phi_k, \delta_j \phi_k) \cdot \hat{\mathbf{n}} = \mathbf{U}_k \cdot \hat{\mathbf{n}} \qquad (16)$$

at all the points corresponding to the Gibraltar entrance, while the normal velocity to the solid boundary is zero everywhere else: all of the Gibraltar inflow–outflow is attributed to the divergent component of the velocity. The solutions of Eq. (15) are subject to homogenous boundary conditions everywhere, including the Gibraltar Strait. This implies that all the χ_k streamlines are closed.

The potential function ϕ_k and the velocity vecto, $(1/\Delta z_k)[(U_{k,\phi}/\Delta x), (V_{k,\phi}/\Delta y)]$ are shown in the top panels of Fig. 12. The potential field is large-scale, except at Gibraltar and the Sicily Strait where it intensifies. Because the velocity associated with the velocity potential singles out the component with horizontal divergence, it describes the overturning circulation, both zonal and meridional. However, the *total* velocity is the sum of the potential and rotational components, and the latter steers the flow into large-scale gyres subdividing
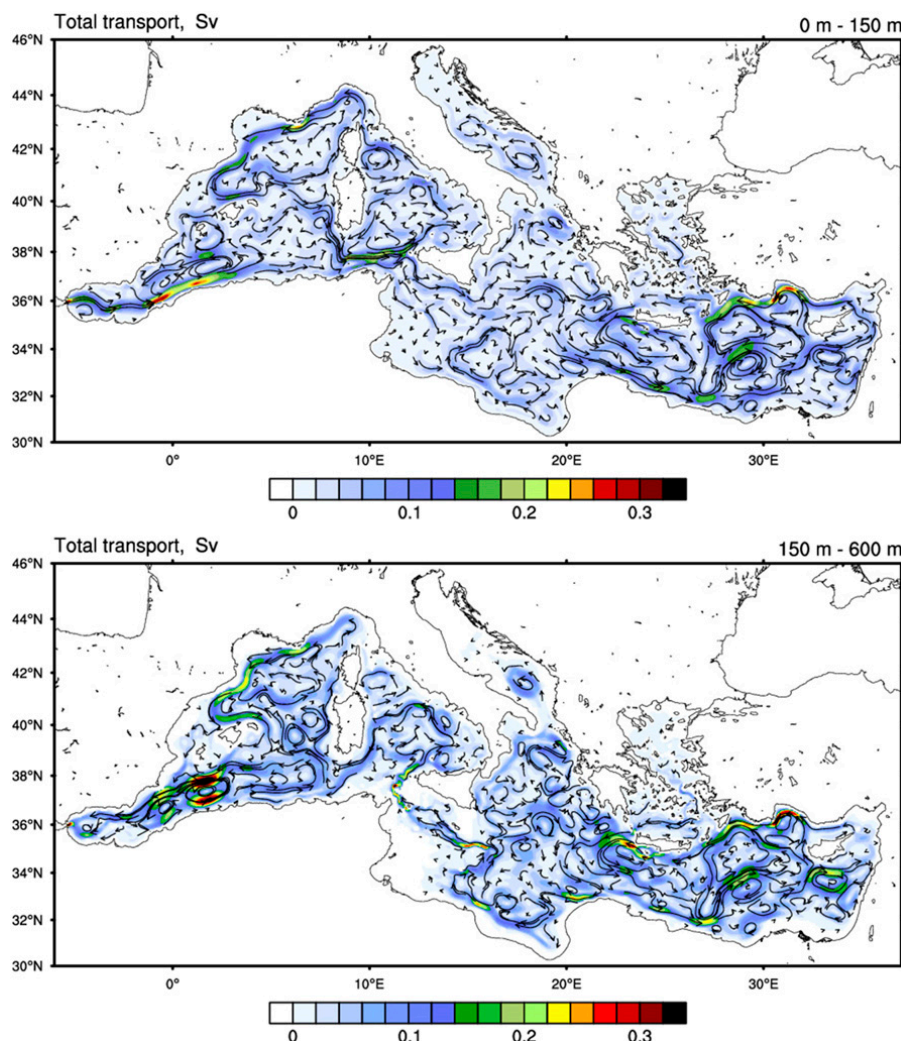
FIG. 11. Two-layer horizontal transport (U_i, V_i), integrated (top) from the surface to 150 m and (bottom) from 150 to 600 m. The colors indicate transport amplitude (Sv). The vertically averaged velocity (u_k, v_k) is shown by arrows (m s^{-1}), represented using a curved line tangent to the instantaneous flow in the neighborhood of the grid point. A variably sized arrowhead at one end of the line points in the direction of the flow. For more information see https://www.ncl.ucar.edu/Document/Graphics/Resources/vc.shtml#vcGlyphStyle.

the basin into several opposite circulation components (bottom panels of Fig. 12). In the upper layer (bottom-left panel of Fig. 12), the flow field is characterized by cyclonic large-scale gyres in the WMED and the Levantine Sea, and one anticyclonic in the Ionian Sea. The rotational velocity component of the NIG is weak and broken into opposite sign eddies or subbasin-scale gyres probably due to the time averaging in the period of NIG reversal [the 1987–96 NIG was anticyclonic, the 1997–2013 NIG is cyclonic, as shown in Pinardi et al. (2015)]. In the lower-layer flow field (bottom-right panel of Fig. 12), the gyres are at smaller scales and multicentered. It is clear that the flow shown in Fig. 11 is equally composed by both the potential and rotational components of the velocity field.

6. The EMT influence on the Mediterranean zonal overturning

Now that the general overturning structure is defined over the whole 1987–2013 reanalysis period, we can analyze some aspects of the interannual variability of the zonal residual overturning circulation shown in the bottom panel of Fig. 7. One of the deep clockwise cells in the EMED is centered at the longitude of the Aegean deep water outflow, that is, 22°E, and it is connected to the EMT event.

Roether et al. (2014) defined the characteristics of the EMT: the Aegean Sea, which up to 1987 had only formed intermediate-depth water masses, began to discharge unusually dense waters in the EMED. The large Aegean water outflow started in 1992 and lasted until
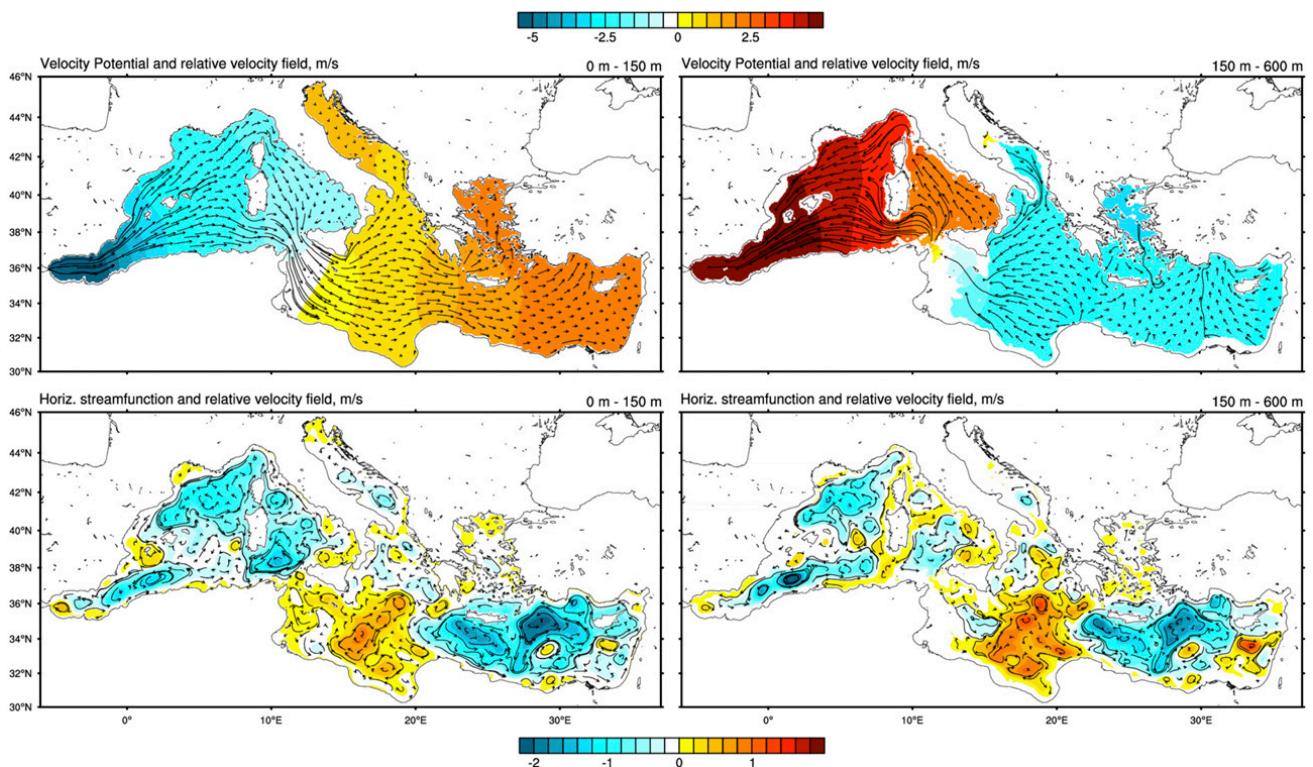
FIG. 12. The (top) divergent and (bottom) rotational components of the horizontal transport field integrated (left) from the surface to 150 m and (right) from 150 to 600 m. Colors in the background indicate the velocity potential and streamfunction (Sv). The top color bar refers to the top row and the bottom color bar refers to the bottom row. Velocity vectors, $(1/\Delta z_k)[(U_k/\Delta x), (V_k/\Delta y)]$ (m s^{-1}), are represented using a curved line tangent to the instantaneous flow in the neighborhood of the grid point. A variably sized arrowhead at one end of the line points in the direction of the flow. For more information see https://www.ncl.ucar.edu/Document/Graphics/Resources/vc.shtml#vcGlyphStyle.

1995 (Roether et al. 2014), so that we consider the interval between 1991 and 1996 to be the EMT peak period, with 1987–90 the onset period and 1997–2013 the decay phase. The Aegean outflow during the peak phase was 10 times that in the two neighboring periods.

The average residual zonal streamfunction for these three periods is shown in Fig. 13. In the onset phase the deep clockwise cell at the Aegean Sea longitude of 22°E is weak (~0.9 Sv) and relatively shallow, only down to 750 m. During the EMT peak phase, the clockwise cell moved deeper, down to 2750 m and more, and its amplitude almost tripled, up to ~2.4 Sv. During the decay phase the anticlockwise cell detached from the Wüst cell, stabilized between 500 and 1750 m and weakened back to ~1 Sv.

We then conclude that the EMT is the source of the deep anticlockwise Wüst cell in the EMED and that the interannual variability of deep water mass formation events in the Aegean is an important forcing for the clockwise cells of the zonal overturning circulation.

7. Conclusions

This paper analyzes the Mediterranean Sea large-scale overturning circulation in its zonal and meridional components. The basin-scale vertical circulation was studied using the Eulerian and residual circulation frameworks, with the latter including the contribution from permanent gyres, eddies and standing waves. This analysis was made possible by the availability of an eddy-resolving reanalysis of the whole basin (Simoncelli et al. 2017).

Starting with the zonal overturning circulation, we documented the Wüst cell, well reproduced by the reanalysis in the salinity and density sections, thus giving a general validation of the reanalysis data. The zonal Eulerian streamfunction shows a new, deep clockwise cell in the region of the Aegean deep water outflow, where the Wüst cell goes down to 3000-m depth. In the residual framework this cell flows largely along isopycnals indicating an almost adiabatic buoyancy balance of deep water outflow from the Aegean. In the Levantine Sea, two other clockwise cells are present, one at the location of the EMT dense water overflow and the other in the Rhodes Gyre area. These clockwise zonal overturning cells are new and we argue that one of them is connected to the EMT dominating the deep water formation processes in the Levantine Sea for almost a decade, from 1989 to 1998.
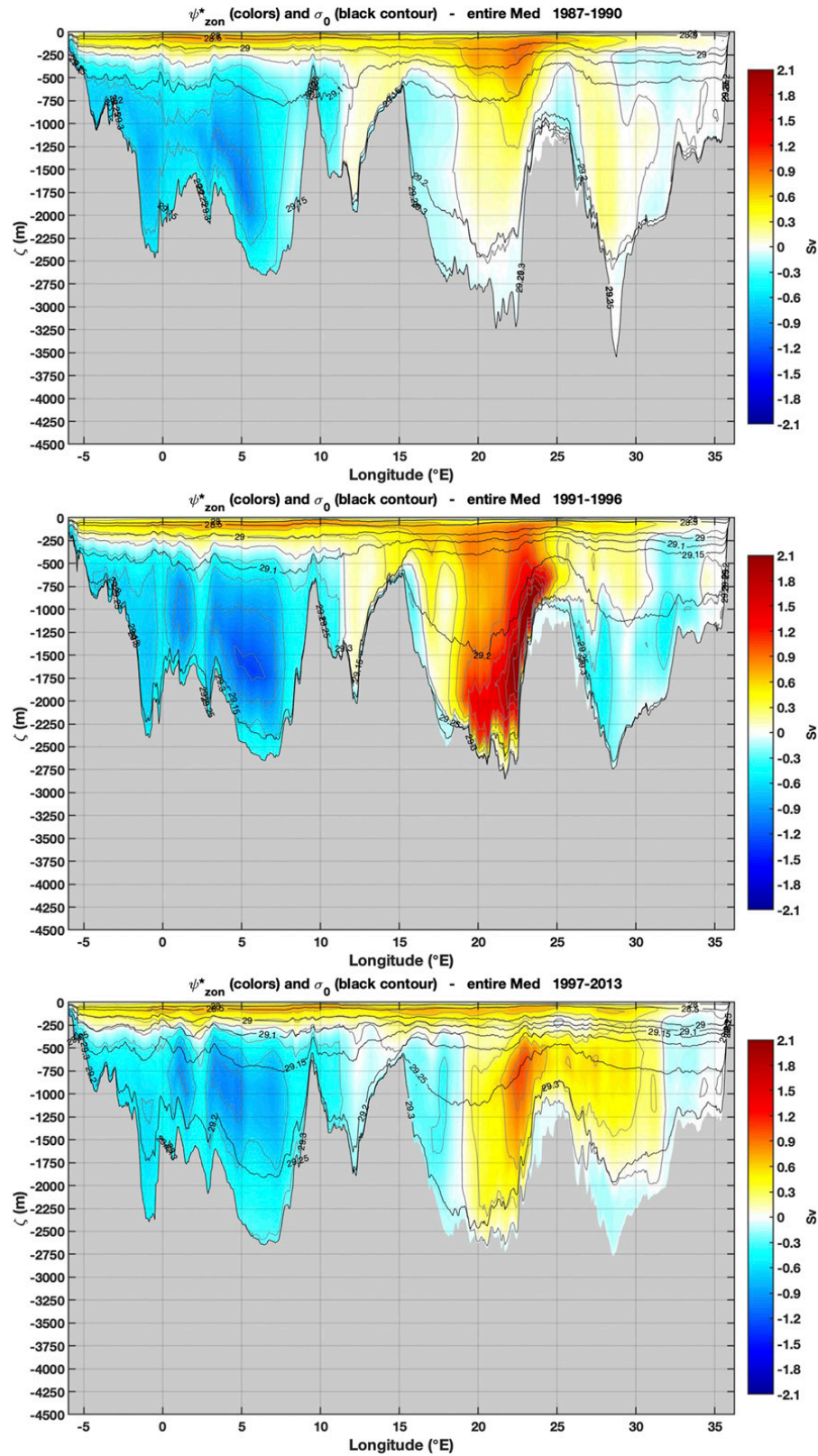
FIG. 13. The residual zonal overturning circulation averaged over different years of the EMT phenomena: (top) the onset period from 1987 to 1990, (middle) the peak period from 1990 to 1996, and (bottom) the decay phase from 1997 to 2013. The gray contour lines show streamfunction values at 0.3-Sv intervals.

The meridional overturning circulation of the whole Mediterranean has been analyzed for the first time. In summary, the meridional overturning circulation can be characterized as follows: 1) the WMED meridional overturning circulation is dominated by two clockwise cells, that is, a clockwise cell connected to the deep formation area in the Gulf of Lion and a counterclockwise cell located in the abyssal regions of the southern basin, and 2) the EMED is dominated by three clockwise cells associated with the three deep and intermediate water formation areas and a weak counterclockwise cell.

In the Eulerian framework, the clockwise overturning is multicentered occupying the depths between 250 and 2500 m. The EMED clockwise vertical circulation is dominated by the Aegean, Cretan Passage, and Rhodes Gyre overturning, with a weak Adriatic Sea contribution. The WMED clockwise overturning reaches a maximum of 0.36 Sv while the EMED meridional clockwise overturning reaches 0.5–0.6 Sv. Conversely, the counterclockwise abyssal overturning is stronger in the WMED than EMED.

In the residual framework, the clockwise meridional cells are characterized by large cross-isopycnal flows, leading to the conclusion that diabatic mixing is an important component of the basin buoyancy balance. This differs from the middepth Atlantic meridional overturning circulation balance, which shows a largely adiabatic residual flow (Marshall and Speer 2012). The limited meridional extent of the Mediterranean Sea might be the cause of the major role of diapycnal mixing.

The Wüst cell has been connected for the first time to the meridional overturning by studying the divergent and rotational components of the two-layer flow field composing the clockwise vertical flow field. The divergent part of the transport that produces the vertical velocities composing the downwelling and upwelling branches of the meridional circulation is shown to be at large scales and intensified in the Alboran Sea and Sicily Strait. Such a divergent flow field is steered by the rotational transport in the basin, giving rise to jet segments and local divergences. In accordance with the results of Waldman et al. (2018) downwelling areas are found along the northern shelf of the basin where intense boundary currents develop, that is, the Asia Minor current and the Liguro–Provençal current.

Last, we discuss the EMT influence on the residual zonal clockwise cell: it is found that the strength of the deep clockwise zonal cell in the area of the Aegean Sea outflow changes in phase with the different phases of the EMT, reaching 2.4-Sv maxima during the peak phase of the climatic event.

In conclusion, our analysis of the Mediterranean Sea global overturning circulation has revealed several new features, not discussed before to the best of our knowledge. Specifically, we highlight the multiple meridional clockwise cells of the EMED, the abyssal counterclockwise vertical circulation of the WMED and the structure of the Wüst cell that is composed of the classical shallow cell in the upper ~600 m of the water column and two deep clockwise zonal cells, one out of the Aegean and the other corresponding to the Rhodes Gyre. This study gives rise to many new questions that should be answered in the future, for example, what is the role played by the deep vertical counterclockwise cell in the WMED? What is the seasonal and interannual variability of the divergent part of the flow field? How is such large buoyancy mixing balance produced?

Finally, future investigations of the overturning circulation of the Mediterranean Sea should analyze how this active vertical circulation is connected to the basin-scale air–seawater, heat and momentum exchanges and how did this change in the past. This would finally elucidate the potential for oxygen depletion in the Mediterranean Sea as well as in other semienclosed seas of the World Ocean.

APPENDIX

A Conservative Remapping Of Level-Coordinate Models

We describe the procedure used to remap a vertical profile from depth coordinates into potential density coordinates, using the convention for variable names and grid layers similar to those used in the MITgcm (Marshall et al. 1997a,b).

The NEMO model utilizes the Arakawa C-type grid (Mesinger and Arakawa 1976; Arakawa and Lamb 1977), which places scalar quantities at the center of each cell volume, and shifts vectorial fields by half a cell width in the three directions so that vector fields are defined at the edges of the cell volumes.

The vertical index k increases *downward*, thus the cell boundaries (faces) are located at z_k^f and $k_1^f = 0$ is the surface. There are K cells and $K + 1$ faces. The distance between the faces of the kth cell face is $\Delta z_k^f = z_k^f - z_{k+1}^f > 0$. The fraction of the grid cell occupied by water is h_{ck}, where $h_{ck} = 1$ represents a cell full of

water, $h_{ck} = 0$ a cell totally inside the topography, and $0 < h_{ck} \leq 1$ a partial cell near the bottom boundary.

The value of the potential density carried by the model represents the average of σ over the kth grid cell:

$$\sigma_k = \frac{1}{h_{ck}\Delta z_k^f}\int_{z_k^f - \delta z_k^f}^{z_k^f} \sigma\, dz, \qquad (A1)$$

where

$$\delta z_k^f = (\Delta z_k^f - \Delta z_{k+1}^f)h_{ck} > 0. \qquad (A2)$$

Fields are remapped from height into isopycnal coordinates using the piecewise parabolic method (PPM; Colella and Woodward 1984; Carpenter et al. 1990).

a. Building the interpolator

To specify uniquely a parabola describing the variable distribution $\hat{\sigma}_k(z)$ over the kth volume cell $z_{k+1}^f \leq z \leq z_k^f$, three quantities are necessary:

- the average of σ over the entire cell, $\langle\sigma\rangle_k$;
- the potential density at the top of the cell, σ_{Tk}; and
- the potential density at the bottom of the cell, σ_{Bk}.

Using a notation similar to that of Colella and Woodward (1984) and Carpenter et al. (1990), this parabola is defined as

$$\hat{\sigma}_k(\zeta_k) \equiv \langle\sigma\rangle_k + \Delta\sigma_k \zeta_k + \sigma_{6k}\left(\frac{1}{12} - \zeta_k^2\right), \qquad (A3)$$

where

$$\zeta_k \equiv \frac{z - z_k^f}{\delta z_k^f} + \frac{1}{2},$$

$$\langle\sigma\rangle_k \equiv \frac{\Delta z_k^f}{z_k^f - z_{k+1}^f}\sigma_k,$$

$$\Delta\sigma_k \equiv \sigma_{Tk} - \sigma_{Bk},$$

$$\sigma_{6k} \equiv 6\left(\langle\sigma\rangle_k - \frac{\sigma_{Tk} + \sigma_{Bk}}{2}\right).$$

Note that $-1/2 \leq \zeta_k \leq 1/2$. An equivalent formulation to Eq. (A3) is

$$\hat{\sigma}_k(z) = \sigma_{Tk} + 2(\sigma_{Bk} + 2\sigma_{Tk} - 6\langle\sigma\rangle_k)\frac{z - z_k^f}{\delta z_k^f}$$

$$+ 6\left(\frac{\sigma_{Bk} + \sigma_{Tk}}{2} - \langle\sigma\rangle_k\right)\left(\frac{z - z_k^f}{\delta z_k^f}\right)^2. \qquad (A4)$$

A commonly used second-order accurate estimate of face quantities is the average of the adjacent cells:

$$\sigma_{Bk} \equiv \frac{\sigma_k + \sigma_{k+1}}{2}, \qquad (A5)$$

$$\sigma_{Tk} \equiv \frac{\sigma_{k-1} + \sigma_k}{2}. \qquad (A6)$$

When these definitions are used, we find

$$\Delta\sigma_k = \frac{\sigma_{k-1} - \sigma_{k+1}}{2},$$

$$\sigma_{6k} = 6\left(\langle\sigma\rangle_k - \frac{\sigma_{k-1} + 2\sigma_k + \sigma_{k+1}}{4}\right),$$

and the resulting interpolator is continuous and second-order accurate. More information is required at the upper and lower boundaries: we assume insulating boundary conditions so that $\sigma_{T1} = \sigma_1$ and $\sigma_{Bk} = \sigma_k$. With these assumptions, we obtain

$$\Delta\sigma_1 = \frac{\sigma_1 - \sigma_2}{2},$$

$$\Delta\sigma_k = \frac{\sigma_{k-1} - \sigma_k}{2},$$

$$\sigma_{6,1} = 6\left(\langle\sigma\rangle_1 - \frac{3\sigma_1 + \sigma_2}{4}\right),$$

$$\sigma_{6k} = 6\left(\langle\sigma\rangle_k - \frac{\sigma_{k-1} + 3\sigma_k}{4}\right).$$

b. Monotonicity

It is important for many tracers that the interpolation scheme does not produce values outside the range of the original values. In this case, if the data to be interpolated are monotonic, then the interpolator should be monotonic as well. The PPM interpolation scheme will be monotonic if the first derivative of $\hat{\sigma}_k(\zeta_k)$ does not change sign in the interval $-1/2 \leq \zeta_k \leq 1/2$. If $\hat{\sigma}_k(\zeta_k)$ does change sign, the face values σ_T and σ_B can be adjusted to restore monotonicity at the expense of a loss of continuity and second-order accuracy. There are several cases to consider:

1) If $\sigma_{6k} = 0$, the interpolator is linear and thus monotonic.
2) If $\sigma_{6k} \neq 0$, then the $\hat{\sigma}_k'(\zeta_k)$ changes sign at $\zeta_* = \Delta\sigma_k/2\sigma_{6k}$.
   If $\zeta_* \geq 1/2$ or $\zeta_* \leq -1/2$, the interpolator is monotonic in $-1/2 \leq \zeta_k \leq 1/2$. Otherwise:

(i) If $\zeta_* > 0$, we can move the zero in $\hat{\sigma}'_k(\zeta_k)$ upward to $\zeta = 1/2$ by adjusting σ_{Tk} to obtain

$$\sigma_{Tk} = \frac{3\langle\sigma\rangle_k - \sigma_{Bk}}{2}. \tag{A7}$$

(ii) If $\zeta_* < 0$, we can move the zero in $\hat{\sigma}'_k(\zeta_k)$ downward to $\zeta = -1/2$ by adjusting σ_{Bk}, resulting in

$$\sigma_{Bk} = \frac{3\langle\sigma\rangle_k - \sigma_{Tk}}{2}. \tag{A8}$$

(iii) If $\zeta_* = 0$, we split the difference and adjust both face values to $\sigma_{Bk} = \sigma_{Tk} = \langle b \rangle_k$. Then $\Delta\sigma_k = \sigma_{6k} = 0$ and the interpolator is constant.

c. Transforming into potential density coordinates

Once an interpolator is constructed for potential density σ and some other field ϕ the ϕ field can be binned into potential density coordinates by analytically integrating the interpolator. The potential density coordinate is defined by specifying the edges of the potential density grid σ_n^f. Then the isopycnal thickness and field integrated over the nth potential density bin is

$$h_n = \int_{\sigma_n^f \le \sigma(z) \le \sigma_{n+1}^f} dz, \tag{A9}$$

$$\phi_n = \int_{\sigma_n^f \le \sigma(z) \le \sigma_{n+1}^f} \phi \, dz, \tag{A10}$$

respectively. Each vertical cell, k, can be handled independently. For example, considering a fixed k and n, the two integrals above are given in terms of the interpolation variable by

$$h_n = \delta z_k^f \int_{\sigma_n^f \le \sigma_k(\zeta) \le \sigma_{n+1}^f} d\zeta, \tag{A11}$$

$$\phi_n = \delta z_k^f \int_{\sigma_n^f \le \sigma_k(\zeta) \le \sigma_{n+1}^f} \phi \, d\zeta. \tag{A12}$$

Evaluating these integrals amounts to finding the values of ζ for which $-1/2 \le \zeta < 1/2$ and $\sigma_n^f \le \sigma_k(\zeta) \le \sigma_{n+1}^f$.

REFERENCES

Alhammoud, B., P. T. Meijer, and H. A. Dijkstra, 2010: Sensitivity of Mediterranean thermohaline circulation to gateway depth: A model investigation. *Paleooceanography*, **25**, PA2220, https://doi.org/10.1029/2009PA001823.

Amitai, Y., Y. Ashkenazy, and H. Gildor, 2017: Multiple equilibria and overturning variability of the Aegean-Adriatic Seas. *Global Planet. Change*, **151**, 49–59, https://doi.org/10.1016/j.gloplacha.2016.05.004.

Andrews, D. G., J. R. Holton, and C. B. Leovy, 1987: *Middle Atmosphere Dynamics*. International Geophysics Series, Vol. 40, Academic Press, 489 pp.

Arakawa, A., and V. Lamb, 1977: Computational design of the basic dynamical processes of the UCLA general circulation model. *Methods Comput. Phys.*, **17**, 173–265, https://doi.org/10.1016/B978-0-12-460817-7.50009-4.

Bachman, S., and B. Fox-Kemper, 2013: Eddy parameterization challenge suite I: Eady spindown. *Ocean Modell.*, **64**, 12–28, https://doi.org/10.1016/j.ocemod.2012.12.003.

Baschek, B., U. Send, J. G. Lafuente, and J. Candela, 2001: Transport estimates in the Strait of Gibraltar with a tidal inverse model. *J. Geophys. Res.*, **106**, 31 033–31 044, https://doi.org/10.1029/2000JC000458.

Ben Ismail, S., K. Schroeder, C. Sammari, G. P. Gasparini, M. Borghini, and L. Aleya, 2014: Interannual variability of water mass properties in the Tunisia–Sicily Channel. *J. Mar. Syst.*, **135**, 14–28, https://doi.org/10.1016/j.jmarsys.2013.06.010.

Bethoux, J., B. Gentili, P. Morin, E. Nicolas, C. Pierre, and D. Ruiz-Pino, 1999: The Mediterranean Sea: a miniature ocean for climatic and environmental studies and a key for the climatic functioning of the North Atlantic. *Prog. Oceanogr.*, **44**, 131–146, https://doi.org/10.1016/S0079-6611(99)00023-3.

Carpenter, R. L. J., K. K. Droegemeier, P. R. Woodward, and C. E. Hane, 1990: Application of the Piecewise Parabolic Method (PPM) to meteorological modeling. *Mon. Wea. Rev.*, **118**, 586–612, https://doi.org/10.1175/1520-0493(1990)118<0586:AOTPPM>2.0.CO;2.

Cessi, P., 2019: The global overturning circulation. *Annu. Rev. Mar. Sci.*, **11**, 249–270, https://doi.org/10.1146/annurev-marine-010318-095241.

——, N. Pinardi, and V. Lyubartsev, 2014: Energetics of the semienclosed basins with two-layer flows at the strait. *J. Phys. Oceanogr.*, **44**, 967–979, https://doi.org/10.1175/JPO-D-13-0129.1.

Colella, P., and P. R. Woodward, 1984: The Piecewise Parabolic Method (PPM) for gas-dynamical simulations. *J. Comput. Phys.*, **54**, 174–201, https://doi.org/10.1016/0021-9991(84)90143-8.

Dee, D. P., and Coauthors, 2011: The ERA-Interim reanalysis: Configuration and performance of the data assimilation system. *Quart. J. Roy. Meteor. Soc.*, **137**, 553–597, https://doi.org/10.1002/qj.828.

Demirov, E. K., and N. Pinardi, 2007: On the relationship between the water mass pathways and eddy variability in the Western Mediterranean Sea. *J. Geophys. Res.*, **112**, C02024, https://doi.org/10.1029/2005JC003174.

Dobricic, S., and N. Pinardi, 2008: An oceanographic three-dimensional variational data assimilation scheme. *Ocean Modell.*, **22**, 89–105, https://doi.org/10.1016/j.ocemod.2008.01.004.

——, ——, M. Adani, A. Bonazzi, C. Fratianni, and M. Tonani, 2005: Mediterranean Forecasting System: An improved assimilation scheme for sea-level anomaly and its validation. *Quart. J. Roy. Meteor. Soc.*, **131**, 3627–3642, https://doi.org/10.1256/qj.05.100.

Gertman, I., N. Pinardi, Y. Popov, and A. Hecht, 2006: Aegean Sea water masses during the early stages of the Eastern Mediterranean Climatic Transient (1988–90). *J. Phys. Oceanogr.*, **36**, 1841–1859, https://doi.org/10.1175/JPO2940.1.

Gnanadesikan, A., 1999: A simple predictive model for the structure of the oceanic pycnocline. *Science*, **283**, 2077–2079, https://doi.org/10.1126/science.283.5410.2077.

Hecht, A., and I. Gertman, 2001: Physical features of the eastern Mediterranean resulting from the integration of POEM data

with Russian Mediterranean cruises. *Deep-Sea Res. I*, **48**, 1847–1876, https://doi.org/10.1016/S0967-0637(00)00113-8.

Houpert, L., and Coauthors, 2016: Observations of open-ocean deep convection in the northwestern Mediterranean Sea: Seasonal and interannual variability of mixing and deep water masses for the 2007–2013 period. *J. Geophys. Res. Oceans*, **121**, 8139–8171, https://doi.org/10.1002/2016JC011857.

Jackett, D. R., and T. J. McDougall, 1995: Minimal adjustment of hydrographic profiles to achieve static stability. *J. Atmos. Oceanic Technol.*, **12**, 381–389, https://doi.org/10.1175/1520-0426(1995)012<0381:MAOHPT>2.0.CO;2.

Klein, B., G. Roether, B. B. Manca, D. Bregant, V. Beitzel, V. Kovancevic, and A. Luchetta, 1999: The large deep water transient in the eastern Mediterranean. *Deep-Sea Res. I*, **46**, 371–414, https://doi.org/10.1016/S0967-0637(98)00075-2.

——, W. Roether, G. Civitarese, M. Gačič, B. B. Manca, and M. R. d'Alcala, 2000: Is the Adriatic returning to dominate the production of Eastern Mediterranean Deep Water? *Geophys. Res. Lett.*, **27**, 3377–3380, https://doi.org/10.1029/2000GL011620.

Leaman, K. D., and F. A. Schott, 1991: Hydrographic structure of the convective regime in the Gulf of Lions: Winter 1987. *J. Phys. Oceanogr.*, **21**, 575–598, https://doi.org/10.1175/1520-0485(1991)021<0575:HSOTCR>2.0.CO;2.

Lumpkin, R., and K. Speer, 2007: Global ocean meridional overturning. *J. Phys. Oceanogr.*, **37**, 2550–2562, https://doi.org/10.1175/JPO3130.1.

Madec, G., 2008: NEMO ocean engine. Note du Pole de modelisation 27, Institut Pierre-Simon Laplace, 209 pp.

——, F. Lott, P. Delecluse, and M. Crepon, 1996: Large scale preconditioning of deep-water formation in the northwestern Mediterranean Sea. *Phys. Oceanogr.*, **26**, 1393–1408, https://doi.org/10.1175/1520-0485(1996)026<1393:LSPODW>2.0.CO;2.

Maillard, C., and Coauthors, 2005: A Mediterranean and Black Sea oceanographic database and network. *Boll. Geofis. Teor. Appl.*, **46** (4), 329–343.

Malanotte-Rizzoli, P., and Coauthors, 1997: A synthesis of the Ionian Sea hydrography, circulation and water mass pathways during POEM-Phase I. *Prog. Oceanogr.*, **39**, 153–204, https://doi.org/10.1016/S0079-6611(97)00013-X.

Manca, B. B., G. Budillon, P. Scarazzato, and L. Ursella, 2003: Evolution of dynamics in the eastern Mediterranean affecting water mass structures and properties in the Ionian and Adriatic Sea. *J. Geophys. Res.*, **108**, 8102, https://doi.org/10.1029/2002JC001664.

Marshall, J., and T. Radko, 2003: Residual-mean solutions for the Antarctic Circumpolar Current and its associated overturning circulation. *J. Phys. Oceanogr.*, **33**, 2341–2354, https://doi.org/10.1175/1520-0485(2003)033<2341:RSFTAC>2.0.CO;2.

——, and K. Speer, 2012: Closure of the meridional overturning circulation through southern ocean upwelling. *Nat. Geosci.*, **5**, 171–180, https://doi.org/10.1038/ngeo1391.

——, A. Adcroft, C. Hill, L. Perelman, and C. Heisey, 1997a: A finite-volume, incompressible Navier-Stokes model for studies of the ocean on parallel computers. *J. Geophys. Res.*, **102**, 5753–5766, https://doi.org/10.1029/96JC02775.

——, C. Hill, L. Perelman, and A. Adcroft, 1997b: Hydrostatic, quasi-hydrostatic, and nonhydrostatic ocean modeling. *J. Geophys. Res.*, **102**, 5733–5752, https://doi.org/10.1029/96JC02776.

Masina, S., and A. Storto, 2017: Reconstructing the recent past ocean variability: Status and perspective. *J. Mar. Res.*, **75**, 727–764, https://doi.org/10.1357/002224017823523973.

Mesinger, F., and A. Arakawa, 1976: *Numerical Methods Used in Atmospheric Models*. Vol. 1, GARP Publ. Series, Vol. 17, 64 pp.

Morozov, E. G., K. Trulsen, M. G. Velarde, and V. I. Vlasenko, 2002: Internal tides in the Strait of Gibraltar. *J. Phys. Oceanogr.*, **32**, 3193–3206, https://doi.org/10.1175/1520-0485(2002)032<3193:ITITSO>2.0.CO;2.

Myers, P. G., 2002: Flux-forced simulations of the paleocirculation of the Mediterranean. *Paleoceanography*, **17**, 1009, https://doi.org/10.1029/2000PA000613.

Nikurashin, M., and G. Vallis, 2011: A theory of deep stratification and overturning circulation in the ocean. *J. Phys. Oceanogr.*, **41**, 485–502, https://doi.org/10.1175/2010JPO4529.1.

Oddo, P., M. Adani, N. Pinardi, C. Fratianni, M. Tonani, and D. Pettenuzzo, 2009: A nested Atlantic–Mediterranean Sea general circulation model for operational forecasting. *Ocean Sci.*, **5**, 461–473, https://doi.org/10.5194/os-5-461-2009.

Pascual, A., and Coauthors, 2017: A multiplatform experiment to unravel meso- and submesoscale processes in an intense front (AlborEx). *Front. Mar. Sci.*, **4**, 39, https://doi.org/10.3389/fmars.2017.00039.

Pinardi, N., and A. Navarra, 1993: Baroclinic wind adjustment processes in the Mediterranean Sea. *Deep-Sea Res. II*, **40**, 1299–1326, https://doi.org/10.1016/0967-0645(93)90071-T.

——, and E. Masetti, 2000: Variability of the large scale general circulation of the Mediterranean Sea from observations and modelling: A review. *Palaeogeogr. Palaeoclimatol. Palaeoecol.*, **158**, 153–173, https://doi.org/10.1016/S0031-0182(00)00048-1.

——, E. Arneri, A. Crise, M. Ravaioli, and M. Zavatarelli, 2006: The physical, sedimentary and ecological structure and variability of shelf areas in the Mediterranean Sea. *The Global Coastal Ocean*, A. R. Robinson, and K. Brink, Eds., *The Sea—Ideas and Observations on Progress in the Study of the Seas*, Vol. 14B, Harvard University Press, 1243–1330.

——, and Coauthors, 2015: Mediterranean Sea large-scale low-frequency ocean variability and water mass formation rates from 1987 to 2007: A retrospective analysis. *Prog. Oceanogr.*, **132**, 318–332, https://doi.org/10.1016/j.pocean.2013.11.003.

——, and Coauthors, 2016: Marine rapid environmental assessment in the Gulf of Taranto: A multiscale approach. *Nat. Hazards Earth Syst. Sci.*, **16**, 2623–2639, https://doi.org/10.5194/nhess-16-2623-2016.

Pisacane, G., V. Artale, S. Calmanti, and V. Rupolo, 2006: Decadal oscillations in the Mediterranean Sea: A result of the overturning circulation variability in the eastern basin? *Climate Res.*, **31**, 257–271, https://doi.org/10.3354/cr031257.

Plumb, R., and J. Mahlman, 1987: The zonally averaged transport characteristics of the GFDL general circulation/transport model. *J. Atmos. Sci.*, **44**, 298–327, https://doi.org/10.1175/1520-0469(1987)044<0298:TZATCO>2.0.CO;2.

Reale, M., A. Crise, R. Farneti, and R. Mosetti, 2016: A process study of the Adriatic-Ionian System baroclinic dynamics. *J. Geophys. Res. Oceans*, **121**, 5872–5887, https://doi.org/10.1002/2016JC011763.

Robinson, A. R., W. G. Leslie, A. Theocharis, and A. Lascaratos, 2001: Mediterranean Sea circulation. *Encyclopedia of Ocean Sciences*, J. H. Steele, S. A. Thorpe, and K. K. Turekian, Eds., Academic Press, 1689–1706.

Roether, W., B. B. Manca, B. Klein, D. Bregant, D. Georgopoulos, V. Beitzel, V. Kovačević, and A. Luchetta, 1996: Recent changes in the Eastern Mediterranean Deep Waters. *Science*, **271**, 333–335, https://doi.org/10.1126/science.271.5247.333.

——, B. Klein, and D. Hainbucher, 2014: The eastern Mediterranean transient. *The Mediterranean Sea: Temporal Variability*

and Spatial Patterns, *Geophys. Monogr.*, Vol. 202, Amer. Geophys. Union, 75–83.

Schott, F., and K. D. Leaman, 1991: Observation with moored acoustic Doppler current profilers in the convection regime in the Golfe du Lion. *J. Phys. Oceanogr.*, **21**, 558–574, https://doi.org/10.1175/1520-0485(1991)021<0558:OWMADC>2.0.CO;2.

Schroeder, K., J. Chiggiato, H. Bryden, M. Borghini, and S. Ben Ismail, 2016: Abrupt climate shift in the western Mediterranean Sea. *Sci. Rep.*, **6**, 23 009, https://doi.org/10.1038/srep23009.

Send, U., and P. Testor, 2017: Direct observations reveal the deep circulation of the western Mediterranean Sea. *J. Geophys. Res. Oceans*, **122**, 10 091–10 098, https://doi.org/10.1002/2016JC012679.

Simoncelli, S., C. Fratianni, N. Pinardi, A. Grandi, M. Drudi, P. Oddo, and S. Dobricic, 2017: Mediterranean Sea physical reanalysis (MEDREA 1987-2015). Copernicus Monitoring Environment Marine Service, https://doi.org/10.25423/medsea_reanalysis_phys_006_004.

Somot, S., F. Sevault, and M. Déqué, 2006: Transient climate change scenario simulation of the Mediterranean Sea for the twenty-first century using a high-resolution ocean circulation model. *Climate Dyn.*, **27**, 851–879, https://doi.org/10.1007/s00382-006-0167-z.

Talley, L. D., 2013: Closure of the global overturning circulation through the Indian, Pacific, and Southern Oceans: Schematics and transports. *Oceanography*, **26**, 80–97, https://doi.org/10.5670/oceanog.2013.07.

Theocharis, A., D. Georgopoulos, A. Lascaratos, and K. Nittis, 1993: Water masses and circulation in the central region of the Eastern Mediterranean: Eastern Ionian, South Aegean and Northwest Levantine, 1986–1987. *Deep-Sea Res. II*, **40**, 1121–1142, https://doi.org/10.1016/0967-0645(93)90064-T.

——, B. Klein, K. Nittis, and W. Roether, 2002: Evolution and status of the Eastern Mediterranean Transient. *J. Mar. Syst.*, **33–34**, 91–116, https://doi.org/10.1016/S0924-7963(02)00054-4.

Toggweiler, J. R., and B. Samuels, 1993: Is the magnitude of the deep outflow from the Atlantic Ocean actually governed by Southern Hemisphere winds? *The Global Carbon Cycle*, M. Heimann, Ed., NATO ASI Series, Vol. 15, Springer, 303–331.

Tsimplis, M. N., and Coauthors, 2006: Changes in the oceanography of the Mediterranean Sea and their link to climate variability. *Mediterranean Climate Variability*, P. Lionello, P. Malanotte-Rizzoli, and R. Boscolo, Eds., Developments in Earth and Environmental Sciences, Vol. 4, Elsevier, 227–282, https://doi.org/10.1016/S1571-9197(06)80007-8.

Vargas-Yáñez, M., and Coauthors, 2017: Updating temperature and salinity mean values and trends in the Western Mediterranean: The RADMED project. *Prog. Oceanogr.*, **157**, 27–46, https://doi.org/10.1016/j.pocean.2017.09.004.

Velaoras, D., G. Krokos, K. Nittis, and A. Theocharis, 2014: Dense intermediate water outflow from the Cretan Sea: A salinity driven, recurrent phenomenon, connected to thermohaline circulation changes. *J. Geophys. Res. Oceans*, **119**, 4797–4820, https://doi.org/10.1002/2014JC009937.

Verri, G., N. Pinardi, P. Oddo, S. A. Ciliberti, and G. Coppini, 2018: River runoff influences on the Central Mediterranean overturning circulation. *Climate Dyn.*, **50**, 1675–1703, https://doi.org/10.1007/s00382-017-3715-9.

Waldman, R., N. Brüggemann, A. Bosse, M. Spall, S. Somot, and F. Sevault, 2018: Overturning the Mediterranean thermohaline circulation. *Geophys. Res. Lett.*, **45**, 8407–8415, https://doi.org/10.1029/2018GL078502.

Wolfe, C., and P. Cessi, 2010: What sets the strength of the mid-depth stratification and overturning circulation in eddying ocean models? *J. Phys. Oceanogr.*, **40**, 1520–1538, https://doi.org/10.1175/2010JPO4393.1.

Wu, P., and K. Haines, 1996: Modelling the dispersal of Levantine Intermediate Water and its role in Mediterranean deep water formation. *J. Geophys. Res.*, **101**, 6591–6607, https://doi.org/10.1029/95JC03555.

Wüst, G., 1961: On the vertical circulation of the Mediterranean Sea. *J. Geophys. Res.*, **66**, 3261–3271, https://doi.org/10.1029/JZ066i010p03261.

Xie, P., and P. A. Arkin, 1997: Global precipitation: A 17-year monthly analysis based on gauge observations, satellite estimates, and numerical model outputs. *Bull. Amer. Meteor. Soc.*, **78**, 2539–2558, https://doi.org/10.1175/1520-0477(1997)078<2539:GPAYMA>2.0.CO;2.

Young, W. R., 2012: An exact thickness-weighted average formulation of the Boussinesq equations. *J. Phys. Oceanogr.*, **42**, 692–707, https://doi.org/10.1175/JPO-D-11-0102.1.

Zavatarelli, M., and G. L. Mellor, 1995: A numerical study of the Mediterranean Sea circulation. *J. Phys. Oceanogr.*, **25**, 1384–1414, https://doi.org/10.1175/1520-0485(1995)025<1384:ANSOTM>2.0.CO;2.

Zunino, P., K. Schroeder, M. Vargas-Yáñez, G. Gasparini, L. Coppola, M. García-Martínez, and F. Moya-Ruiz, 2012: Effects of the Western Mediterranean transition on the resident water masses: Pure warming, pure freshening and pure heaving. *J. Mar. Syst.*, **96–97**, 15–23, https://doi.org/10.1016/j.jmarsys.2012.01.011.

Chapter 5

NEMO 1/16°: preliminary results

5.1 Introduction

The spatial variability in the tidal periodic motion of the ocean is generally low, due to its astronomical origin. However, barotropic tides are intensified where the basin geometry is particularly complex (as Aiken (2008) notes for the Chilean Inland Sea), and when flowing over rough topography they generate tidal waves with low-mode components whose length scale is comparable to mesoscale eddies (Garrett and Kunze, 2007). Baroclinic tides interact with dynamical features and contribute to mixing the ocean, redistributing energy at the global scale and shaping the ocean circulation on continental shelves (Dunphy and Lamb, 2014).

Thus, the impact of tides in a general ocean circulation model can vary according to the accuracy of the resolved topography and the simulated dynamical structures. Arbic (2021) detailed the progress made concerning the introduction of tides into ocean models summarising the comparison between model results and observations, while Buijsman et al. (2020) focused on the roles of horizontal surface resolution and internal tide damping. Increasing the resolution is computationally very demanding, and only a few global three-dimensional models have been developed that include the simultaneous forcing of tides and atmosphere with a horizontal resolution finer than 1/10°. The first was the HYCOM model (Arbic et al., 2010; Shriver et al., 2012), and other examples include the Max Plank Institute Ocean Model (Müller et al., 2012; Li et al., 2015), the GFDL Generalized Ocean Layered Model (Waterhouse et al., 2014) and the Massachusetts Institute of Technology general circulation model (Rocha et al., 2016; Fu et al., 2021).

In this chapter, we describe the implementation of tidal forcing in a global eddy-resolving configuration of the NEMO model. A similar configuration has already been analysed by Kodaira et al. (2016), but they used a prescribed stratification letting tidal motions to evolve freely. Differently, we included the atmospheric forcing and enhanced the resolution both horizontally, from 1/12° to 1/16°, and vertically, from 19 to 98 levels.

The increased resolution in the experiment described below leads to many differences from the coarser TIDE025 experiment described in Chapter 2, in which the ocean tides are simulated with 1/4° resolution and 75 vertical levels. First, the local variability of tides is enhanced in coastal regions, as the coastline geometry and the bottom topography are now more accurate and

realistic. Second, many vertical modes are now resolved due to the increased vertical resolution, and thus more internal waves are generated, propagated and dissipated in the ocean. These waves interact with eddies and mesoscale fronts that were not included in TIDE025.

Egbert and Ray (2000) estimated that approximately 25-30% of the total tidal dissipation occurs in the open ocean, near areas of rough topography where barotropic tides interact with the bathymetry, thus generating internal tides (Melet et al., 2013; Timko et al., 2017). The rate of energy conversion from the barotropic to baroclinic tides has been found to be very sensitive to both the horizontal grid spacing and the modelled bottom topography (Niwa and Hibiya, 2011), and the dissipation processes occur both near and far from the generation site. Internal tides enhance the local turbulent mixing due to their shear instability near the site, while when propagating further away they can nonlinearly interact with the background internal waves and mesoscale eddies (St. Laurent and Garrett, 2002).

5.2 Model configuration and experiments

The simulations are performed using the NEMO model v3.6 (Madec and the NEMO team, 2016) with a horizontal resolution of 1/16° and 98 vertical levels. The configuration, called GLOB16, uses a non-uniform tripolar grid that ranges from 78°S to 90°N, with a correspondent grid size of 6.9 km at the equator and of about 2-3 km in the polar regions (Iovino et al., 2016).

The model's bathymetry is based on a combination of the ETOPO2 data set (of Commerce, 2006) for the deep ocean, GEBCO (IOC and BODC, 2003) for the continental shelves and BEDMAP2 (Fretwell et al., 2013) for the Antarctic region. The vertical dimension is discretized using the z^* vertical coordinate system (Adcroft and Campin, 2004) with levels unevenly spaced. They have a minimum thickness of 1 m at the surface and a maximum of 160 m in the deep ocean. This formulation enables height coordinates to be rescaled according to the variability of the sea surface, and thus avoids the problem of vanishing surface levels under the large sea-surface displacement induced by tides. Partial steps are used to more accurately represent the bottom topography (Barnier et al., 2006).

The momentum and tracer equations are solved every 200 seconds, while the sea surface elevation and the barotropic transports are computed using a shorter time step of 2 seconds through the split-explicit time stepping scheme (see Section 2.3). The surface forcing is provided by JRA55-do v1.4 reanalysis (Tsujino et al., 2018) at 55 km, with a frequency of 3 hours for atmospheric fields and monthly river runoff averaged from 1965 to 2016.

Differences with the eddy-permitting model are mainly related to the resolution-dependent parameters: the viscous processes are parametrised horizontally using a bilaplacian operator with a coefficient of 5×10^{11} m^4/s, while the lateral tracer mixing is laplacian and follows isoneutral surfaces with a coefficient of 80 m^2/s. At the surface, the turbulent kinetic energy below the mixed layer decreases exponentially, with a length scale of 0.5 m at the equator and 30 m poleward of 40°.

Following the experiments in Chapter 2, the first run is now referred to as CTRL16 and reproduces the general ocean circulation without the tidal forcing. The simulation starts from a state

of rest in January 2016, with initial conditions provided by temperature and salinity climatologies from the WOA13_v12 dataset (Locarnini et al., 2013; Zweng et al., 2013), and ends in June 2017, giving a total period of 18 months. Like CTRL025, this experiment is initialized without observed sea-ice conditions, and thus the sea ice concentration is based on the climatological sea surface temperature.

The bottom friction formulation follows (2.24) as in CTRL025 case: the bottom background kinetic energy parameter e_b is set to 2.5×10^{-3} m^2/s^2, but now the friction coefficient C_d is spatially constant and equal to 2.5×10^{-3}.

The second simulation, TIDE16, is configured as CTRL16 with the addition of tidal forcing associated with 11 tidal components, as in TIDE025 (M2, N2, S2, K2, K1, O1, P1, Q1, Mm, Mf and M4). As in TIDE025, we propose to resolve most of the processes that occur near the bottom and thus we neglect the bottom turbulent kinetic energy parameter in (2.24). We note that this is a controversial approximation because the breaking of internal waves and low-mode turbulence are partially resolved regardless of the resolution (Arbic et al., 2010). Thus, we have planned the implementation of a TWD parametrization for further analysis with the GLOB16 configuration.

The implementation of tides in TIDE16 does not induce numerical instabilities in regions known for high tidal amplitudes, which represents an important difference from the TIDE025 experiment (where local changes to the original bathymetry were necessary) and suggests that the increased horizontal resolution contributes to maintain model stability when an additional barotropic forcing is applied.

5.3 Results

5.3.1 Kinetic energy analysis

We present a preliminary analysis of the impact of tides on the global KE. The differences between the CTRL16 and TIDE16 experiments are globally integrated every five days, and the results are compared to the coarser-resolution experiments of CTRL025 and TIDE025. Our focus is on the role of tides, while Iovino et al. (2016) provided an extensive analysis of the impact of the increased resolution.

The global KE of the CTRL16 experiment increases linearly during the first simulated year and then becomes stable with a mean value of around 3.39×10^{18} kg m^2/s^2 (Figure 5.1). However, in TIDE16 the KE reaches an equilibrium value of 4.16×10^{18} kg m^2/s^2, but continuously oscillates with a characteristic period of 15 days, which is associated with spring and neap tides. We disregard 2016 data because of the initial model adjustment, and during the remaining months the impact of tides results in a KE increase of about 20%. The KE values obtained in CTRL16 and TIDE16 are comparable and are greater than in CTRL025 and TIDE025 (Figure 2.7), confirming that the increase in the horizontal and vertical resolution leads to a broader range of dynamical processes, which then enhance the kinetic energy of the ocean.

The KE density is computed for different layers (0-100m, 100-500m, 500-3000m, 3000-5000m), as in Figure 5.2, and the same periodic motion is detected at all depths. Moving down from the

surface, the ocean KE decreases due to the weaker velocity, but the differences between TIDE16 and CTRL16 remain qualitatively the same.

In the final two months of the simulation, high- and low-resolution experiments are compared by dividing the KE into its temporal mean (MKE) and eddy (EKE) components. Their mean values are summarised in Table 5.1. Figure 5.3 shows that CTRL16 and TIDE16 (CTRL025 and TIDE025) have almost the same MKE, while the EKE is significantly enhanced when tides are implemented, with a mean value in the TIDEs experiments increased by approximately 50% compared to the CTRLs. Although the tidal energy input is a well-known number in the real ocean (3.5 TW according to Munk and Wunsch (1998)), in numerical models it strongly varies due to the interaction between tides and bottom topography, coastal shelves, basin resonances and dynamical structures, all of which are modified by the grid resolution. Therefore, by increasing the resolution in TIDE16 compared to TIDE025, more dynamical structures that are averaged out by the MKE are resolved and interact with tides.

	CTRL16	**TIDE16**	**CTRL025**	**TIDE025**
MKE	2.02	2.05	1.74	1.72
EKE	1.41	2.17	0.78	1.28
KE	3.43	4.22	2.52	3.00

Table 5.1: Temporal mean of global KE, MKE and EKE expressed in units of 10^{18} kg/m^{2}s^2. Data refers to the experiments CTRL025, TIDE025, CTRL16 and TIDE16 during the period from April 25th to June 23th, 2017.
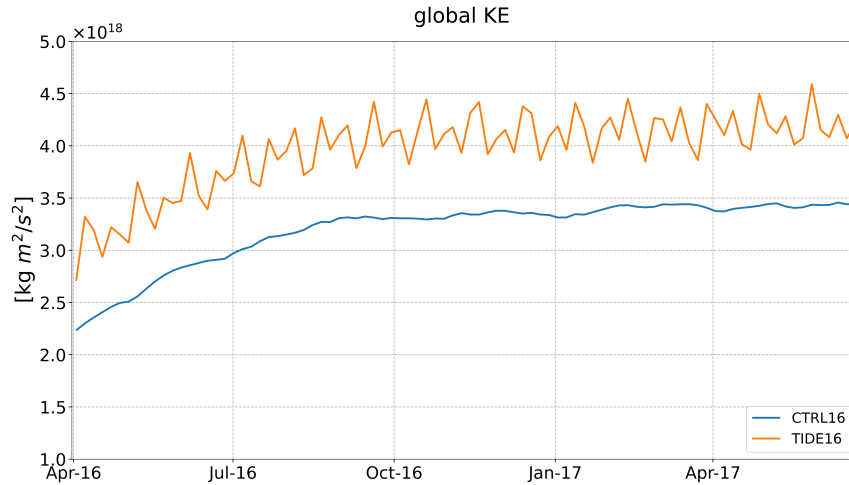
Figure 5.1: Timeseries of the global KE of CTRL16 and TIDE16 experiments during the period from April, 2016 to June, 2017.

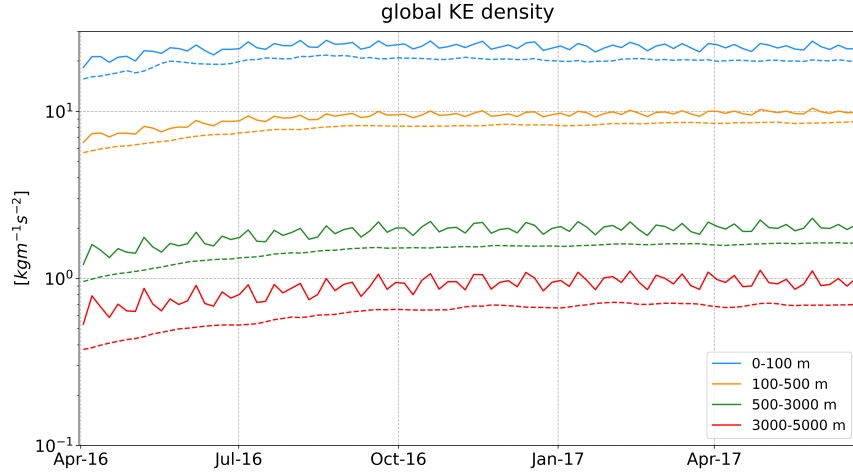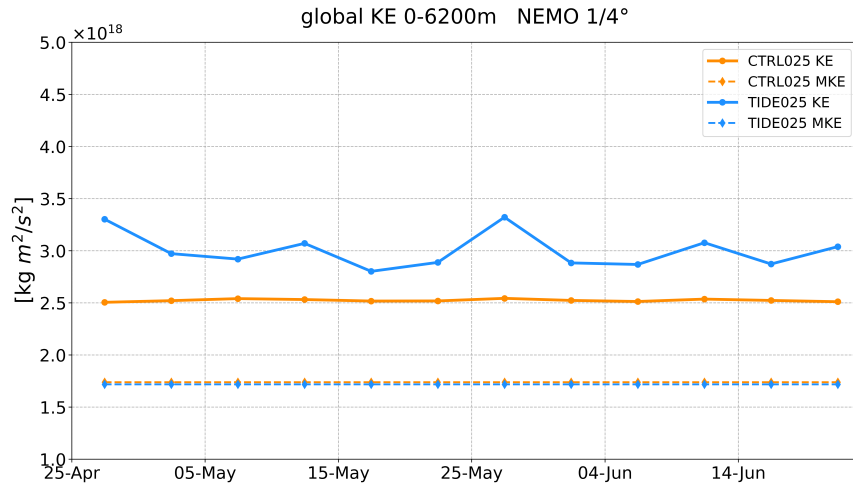Figure 5.2: Timeseries of the global KE density in different layers of TIDE16 (solid lines) and CTRL16 (dashed lines) during the period from April, 2016 to June, 2017.

(a)
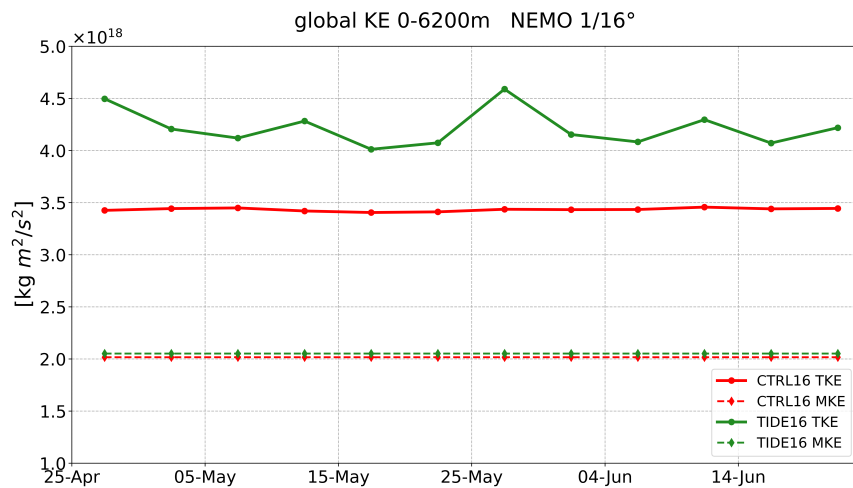
(b)

Figure 5.3: Timeseries of the global KE and MKE in (a) CTRL16 and TIDE16, (b) CTRL025 and TIDE025 experiments. The analysed period corresponds to the last two months of the higher resolution experiments, from April 25th to July 3rd, 2017.

101
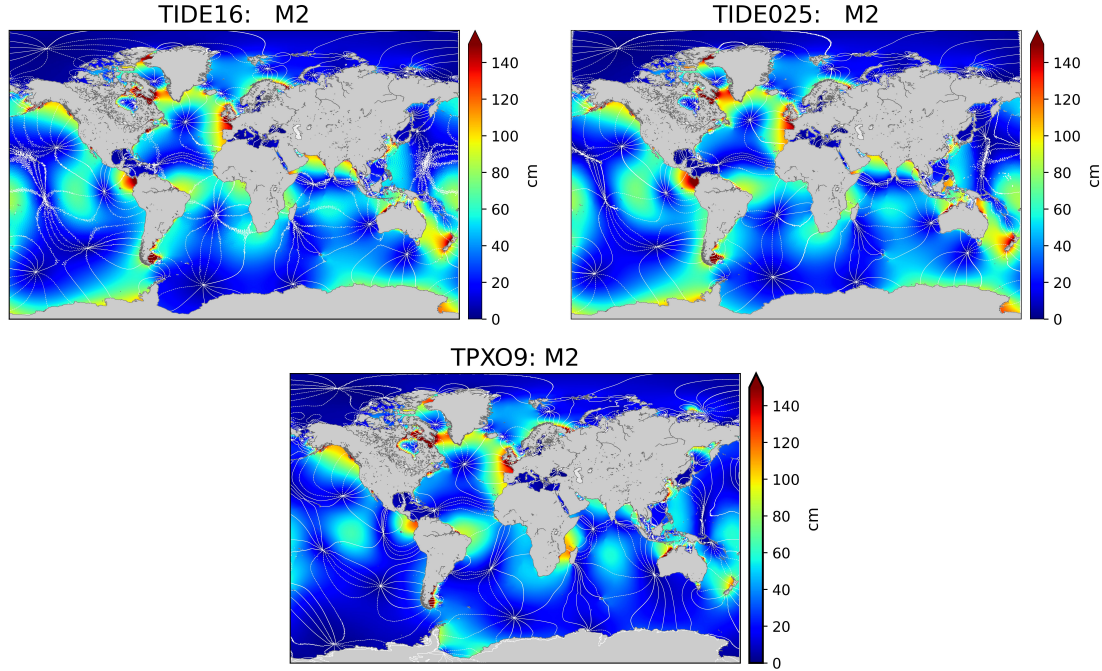
Figure 5.4: Global maps of M2 tidal amplitude and phase in TIDE16 (top left), TIDE025 (top right) and TPXO9 (bottom) during the period from January 1st to July 3rd, 2017.

5.3.2 Sea level analysis

A global overview of the modelled tidal amplitudes in TIDE16 is presented in Figure 5.4 and Figure 5.5. The model output is analysed using the method of Foreman et al. (2009). We compute the harmonic analysis using hourly data of the SSH from January 1st to July 3rd, 2017, and extrapolate the implemented 11 tidal constituents from the total signal. Consistent with the analysis in Chapter 2, the main semidiurnal (M2, S2) and diurnal (K1, O1) components are analysed using the TPXO barotropic tidal model as a reference.

The M2 principal semidiurnal lunar component is the strongest in global terms, with maximum values that exceed 150 cm in coastal areas such as the Hudson Strait and the European, Patagonian and north-west Australian shelves. Figure 5.4 shows the M2 amplitude computed from TIDE16, TIDE025 and TPXO, and demonstrates that the NEMO configurations have qualitatively the same geographical distribution and therefore the same differences compared to TPXO. The tidal amplitude is typically enhanced along the coasts, but in our experiments an area further offshore than TPXO is included, with a resulting overestimation almost everywhere in the open ocean. The main biases are found on the African Atlantic coast, the Arabian Sea, the Gulf of Benguela, the Australian shelf and the Mozambique Channel, and all are positive except for the Mozambique Channel.

The Antarctic region is particularly sensitive to ice shelf presence, as Rosier et al. (2014) noted, and this represents a special case as the behaviour of the simulated amplitude is opposite to that of TPXO. NEMO simulates higher M2 amplitudes along the entire Antarctic coast except for the Weddell Sea and the coasts east of it, where the values are below 40 cm. Conversely, the
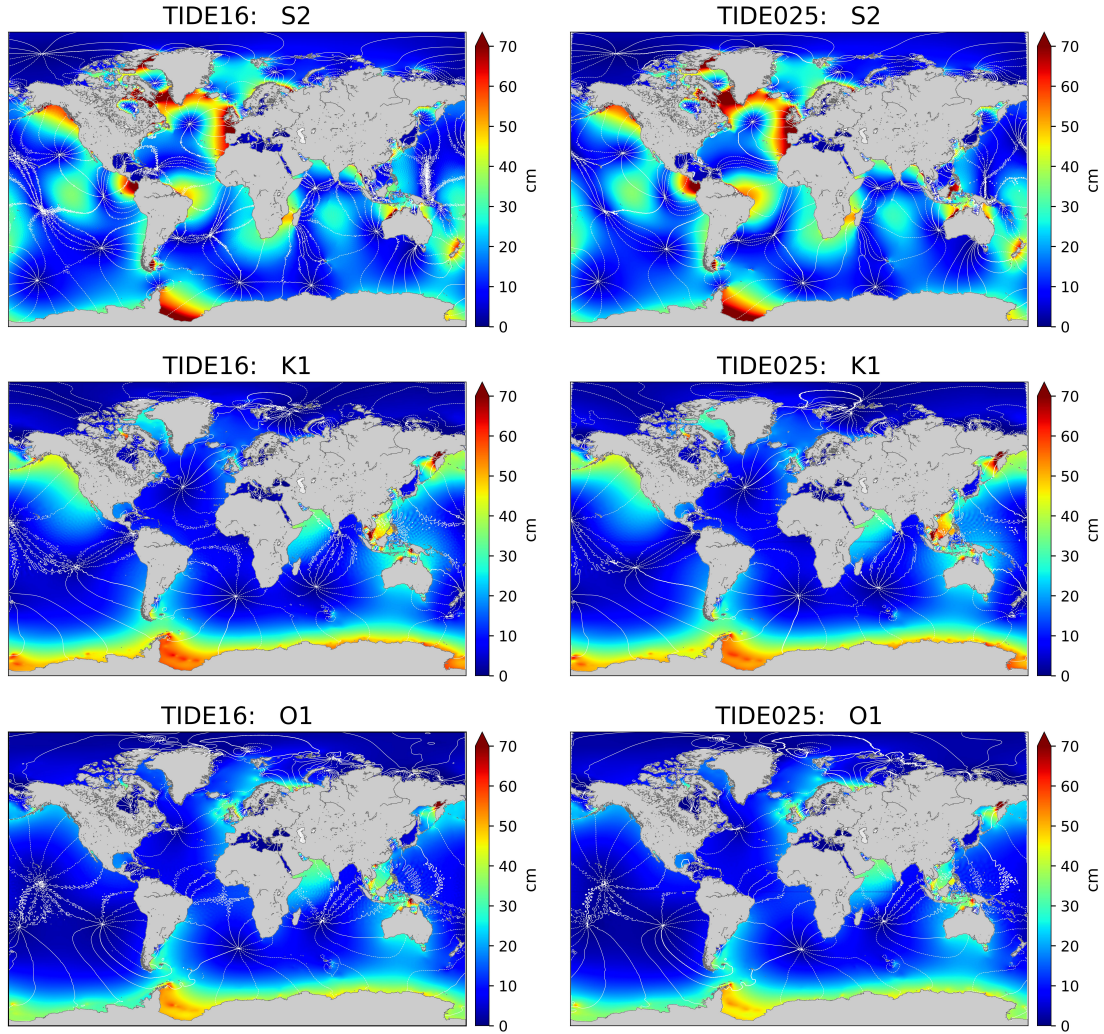
Figure 5.5: Global maps of S2, K1 and O1 tidal amplitudes and phases computed from TIDE16 (left column) and TIDE025 (right column) experiments during the period from January 1ˢᵗ to July 3ʳᵈ, 2017.

amplitudes recorded by TPXO are all below 20 cm, with the only exception being the Weddell Sea. The amphidromic points also illustrate this, as for example our model places one point in the Southern Ocean around 150°E, but is completely absent from the TPXO atlas. The common behaviour of TIDE025 and TIDE16 suggests that in this region the biases of NEMO may not be due to the model resolution, but rather to unrealistic initial sea-ice conditions. Comparing the M2 tide of TIDE16 and TIDE025, we identify three main differences:

- the M2 amplitude is significantly weakened in the Celebes Sea and Makassar Strait inside the Indonesian region, where the amplitude of TIDE16 is almost half that of TIDE025;

- TIDE16 tends to restrict the high amplitude regions along the coasts, and particularly offshore of Panama and in the Labrador Sea;

- in the open ocean more ripples are observed in the amplitude of TIDE16 than in TIDE025. The wavelengths for semidiurnal (diurnal) tides are the same and are associated with an increased number of resolved baroclinic tides, which reach the surface and contribute to

the sea level variability. This phenomenon is mainly evident in the Philippines Sea, but influences the entire global ocean .

These assessments of M2 can be generalised to S2 (Figure 5.5), the principal semidiurnal solar component, which appears to be the least accurately simulated when compared to TPXO (Figure 2.10). Here, TIDE16 only reduces the bias in the Celebes Sea by halving the amplitude simulated in TIDE025, while enhancing the amplitude of the baroclinic tides at the S2 frequency that are detected at the sea surface, particularly in the Southern hemisphere.

Internal tides propagate in the open ocean with a typical wavelength that is inversely proportional to their frequency, corresponding to about 130 km for semidiurnal tides and 260 km for diurnal tides, thus rendering the K1 and O1 waves more detectable in global maps.

In terms of diurnal frequencies, the increased resolution enhances the amplitude of both K1 and O1 in the Southern Ocean. The general behaviour of the NEMO model is then to overestimate TPXO tidal amplitudes at all frequencies, particularly in polar regions. If the biases in TIDE025 at a coarse resolution are mainly induced by the ocean circulation, the differences in TIDE16 may be related to the interaction between tides and mesoscale dynamical processes. In both cases the lack of an initial sea ice condition contributes to increasing the tidal amplitude (St-Laurent et al., 2008) and the errors in the Southern Ocean.

A validation of the modelled tides is proposed for the North-West Atlantic and the Indonesian regions (Figure 5.6) and tide gauges observations from the University of Hawaii Sea Level Centre (Caldwell et al., 2015) are considered as a reference (Appendix B).

(a)   (b)
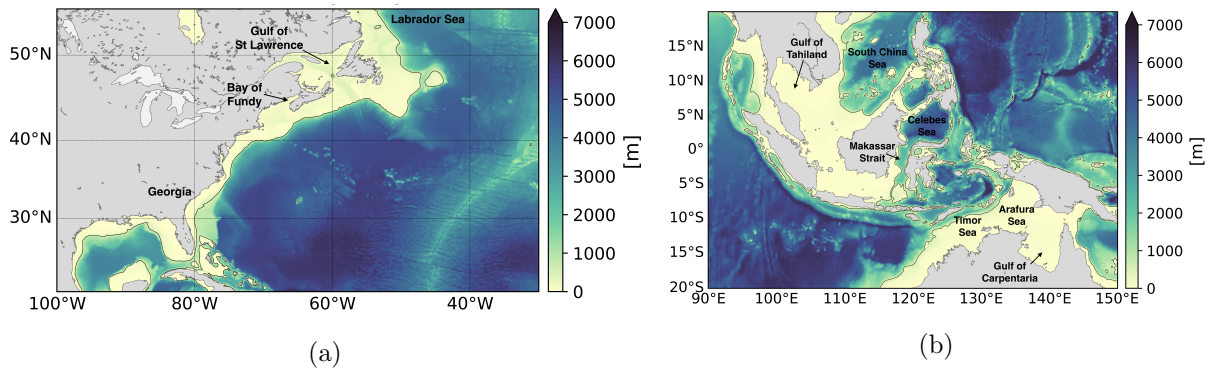
Figure 5.6: Maps of the GLOB16 bathymetry of the selected regions, North-West Atlantic Ocean (*left*) and Indonesian region (*right*). Contour black lines represent the isolines of 500 m.

North-West Atlantic region

Semidiurnal tides are dominant in the North-West Atlantic region, with highest amplitudes along the coasts of Georgia, in the Bay of Fundy and in the Gulf of St Lawrence (Figure 5.7). In these areas TIDE16 simulates semidiurnal amplitudes higher than TIDE025, with M2 maximum values of 4.0 m compared to 2.5 m, and thus increases the biases in terms of TPXO (Figure 2.14).
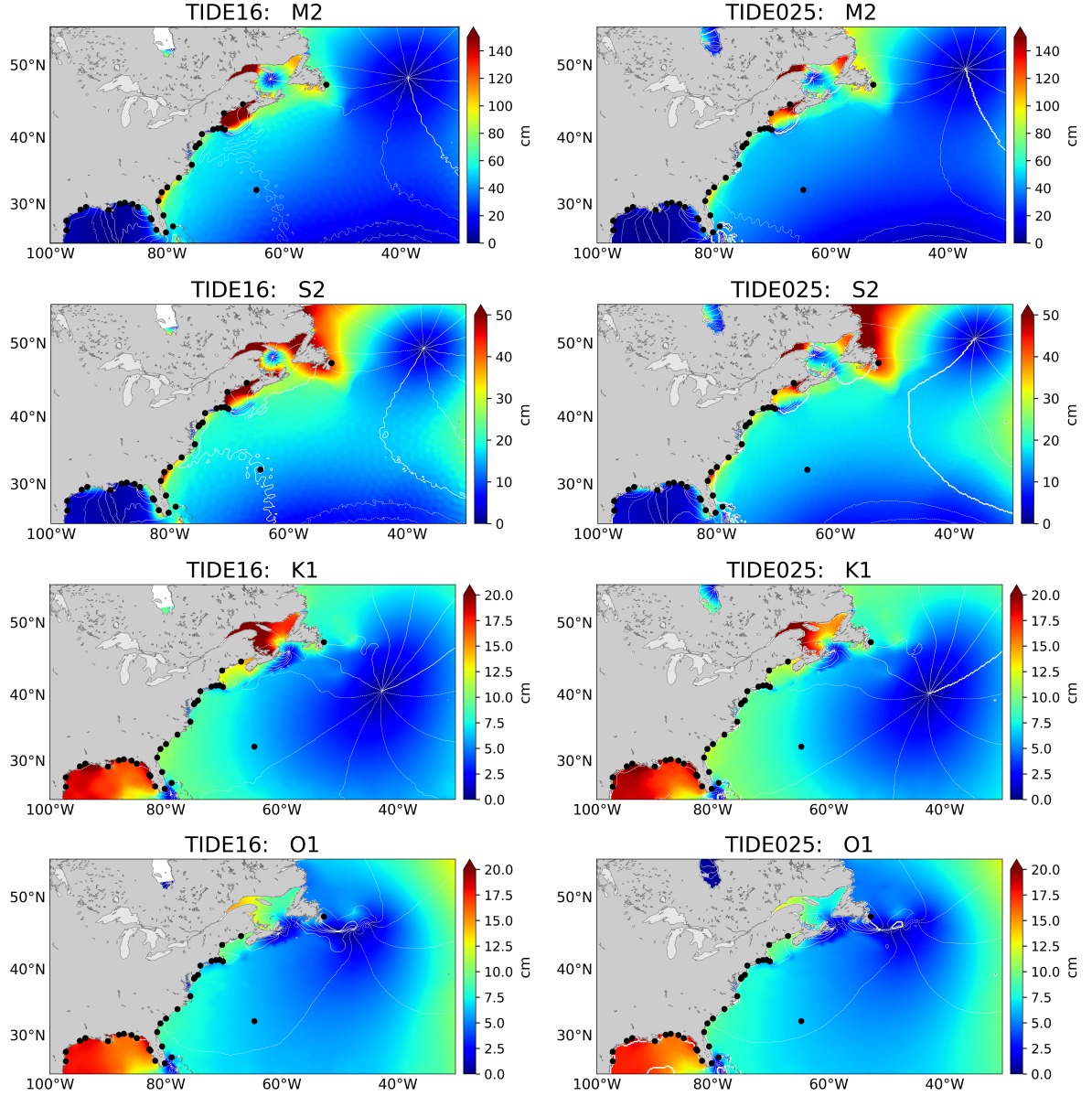
Figure 5.7: Maps of tidal amplitudes and phases in the North-West Atlantic region computed from TIDE16 (*left* column) and TIDE025 (*right* column) experiments during the period from January 1st to July 3rd, 2017. Black dots represent the location of tide gauges data analysed in the text.

The same behaviour is associated with the differences of diurnal tides, even though they are more localised in the Gulf of St Lawrence. This gulf has a very complex geometry and one of the highest sea surface oscillations in the world: it contains two amphidromic points inside it (M2 and S2) and just outside (K1 and O1), and their locations are closer to TPXO in TIDE16 than in TIDE025. Contrary to the general trend, TIDE16 weakens the S2 amplitude in the Labrador Sea, thus making it more comparable to TPXO.

Moving offshore, TIDE16 fails to reproduce the amplitude damping on the continental shelf and propagates numerous internal tides from the slope to the open ocean. Although this region is known for internal tide propagation (Colosi et al., 2001), their contribution to the sea level is probably overestimated and should be damped in future simulations with the GLOB16

configuration.

The model output can then be validated along the coasts by comparing the amplitudes of TIDE16 with tide gauge data, clustered into three groups according to their geographical location (2.13). As in the lower resolution cases, different model behaviours are observed south or north of 37°N of the Atlantic coast, and a third group in the Gulf of Mexico is proposed, which can highlight the differences between the Atlantic Ocean and a semi-enclosed sea.

Figure 5.8 provides a preliminary comparison between TIDE025 and TIDE16, by considering scatter plots of tidal amplitude and phase at grid points closer to the tide gauges locations: the two experiments simulate almost the same semidiurnal amplitudes, while the diurnal amplitudes are slightly lower in TIDE16. The main differences are associated with the semidiurnal tides of Portland (TG 252) and Eastport (TG 740) tide gauges, in the Gulf of St Lawrence. Likewise, the phase plots behave similarly to the amplitude ones, with a weak delay of K1 and O1 in TIDE16, while M2 and S2 correspond closely.

The vectorial distances between the modelled and observed tides are then computed following the formulation in (2.41) and are shown in Figure 5.9. The RMSD (2.42) is computed for each subregion, as summarised in Table 5.2:

- north of 37°N, TIDE16 performs better than TIDE025 for M2, S2 and K1 with the exception of the outlier tide gauges in Portland and Eastport. Figure 5.8 shows that in the two experiments these points are characterised by strong amplitude differences, as indicated by the linear regression coefficient (1.39 for M2 and 1.21 for S2). It is worth noting that when they are neglected from the analysis of M2, the RMSD total value of TIDE16 decreases from 42.71 cm to 29.96 cm;

- south of 37°N, TIDE16 is closer to the observations at the S2 and K1 frequencies that have lower RMSD values, while TIDE025 performs better for the M2 and O1 components;

- in the Gulf of Mexico, TIDE16 is generally poorer than TIDE025, apart from the K1 component where the RMSD decreases from 5.36 cm in TIDE025 to 4.86 cm in TIDE16.

On average, in the North-West Atlantic region TIDE16 improves the S2 and K1 simulation when the Gulf of St Lawrence is not considered in the analysis, whereas TIDE025 performs better for the M2 and O1 components. Although we expected TIDE16 to be closer to observations than TIDE025, this result highlights that the eddy-resolving grid is probably not fine enough to resolve the dissipative processes that limit tidal amplification near the coast. Therefore, some parametrizations (such as the TWD) should be implemented in the future.

M2 (cm)			
Area	TIDE16	TIDE025	TPXO
Gulf of Mexico	16.86	9.83	1.88
South of 37°N	39.94	36.01	19.66
North of 37°N	60.76	35.36	15.59
	(31.89)	(35.78)	(17.04)
TOTAL	42.71	28.83	13.92
	(29.96)	(28.49)	(14.30)

S2 (cm)			
Area	TIDE16	TIDE025	TPXO
Gulf of Mexico	9.22	7.45	1.38
South of 37°N	16.98	17.72	4.06
North of 37°N	21.97	17.91	2.82
	(14.49)	(16.42)	(3.04)
TOTAL	16.70	14.81	2.85
	(13.54)	(14.05)	(2.91)

K1 (cm)			
Area	TIDE16	TIDE025	TPXO
Gulf of Mexico	4.86	5.36	2.51
South of 37°N	1.38	1.72	1.49
North of 37°N	1.76	2.11	1.20
	(1.75)	(2.04)	(1.31)
TOTAL	3.24	3.63	1.87
	(3.31)	(3.69)	(1.93)

O1 (cm)			
Area	TIDE16	TIDE025	TPXO
Gulf of Mexico	7.61	6.53	2.27
South of 37°N	2.68	2.38	1.29
North of 37°N	2.86	2.51	0.78
	(3.10)	(2.72)	(0.85)
TOTAL	5.15	4.45	1.61
	(5.31)	(4.58)	(1.67)

Table 5.2: RMSD between modelled tides (M2, S2, K1 and O1) and observed data from tide gauges in the North-West Atlantic region. Values in brackets are computed neglecting tide gauges from the Bay of Fundy (TG 252 and TG 740).
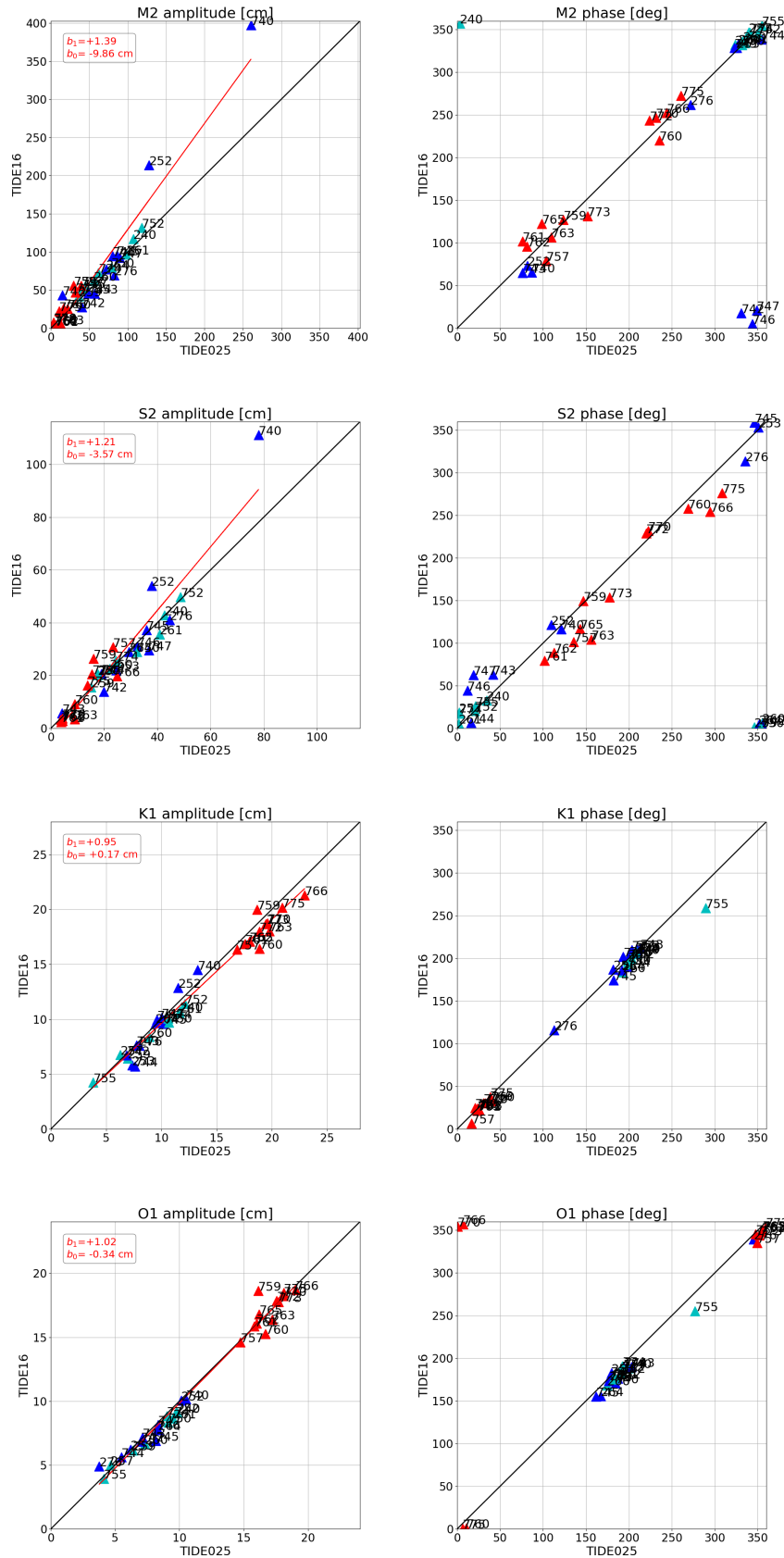
Figure 5.8: Scatter plots of the tidal amplitude (*left*) and phase (*right*) at tide gauges locations in the North-West Atlantic computed for TIDE16 and TIDE025 experiments during the period from January 1st to July 3rd, 2017. Dots of the same color represent tide gauges of the same area: Atlantic coast north of 37°N (blue), Atlantic coast south of 37°N (cyan) and Gulf of Mexico (red). 108

Figure 5.9: Vectorial distances between modelled and observed tidal components in the North-West Atlantic Ocean during the period from January 1st to July 3rd, 2017. Tide gauges of the same area have the same color: Atlantic coast north of 37°N (blue), Atlantic coast south of 37°N (cyan) and Gulf of Mexico (red).
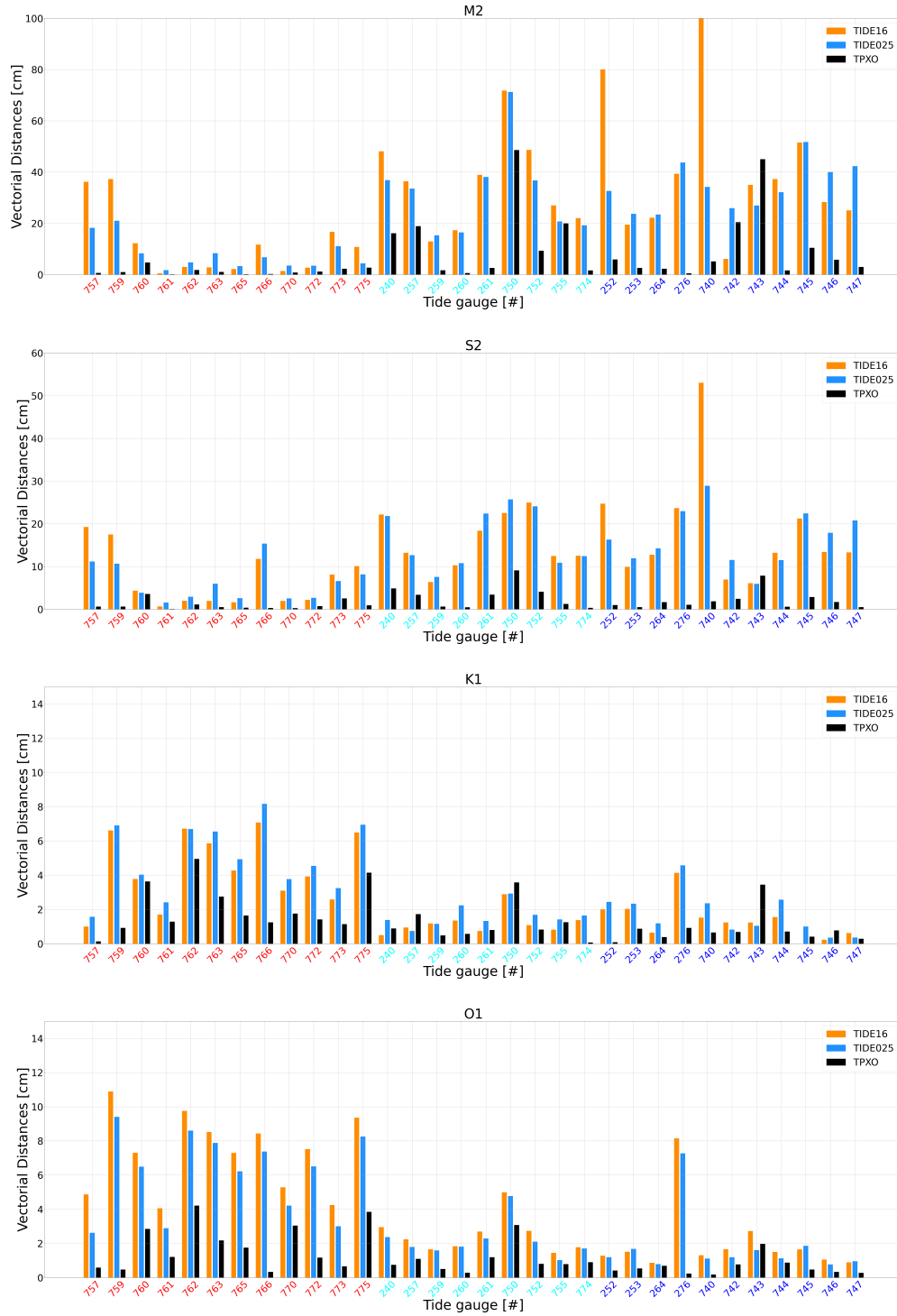
Indonesian region

Totally different behaviour is simulated in the Indonesian region, where more than 16000 islands influence the passage of water flowing from the Pacific Ocean to the Indian Ocean. This region is characterised by a series of large, deep, semi-enclosed basins that are connected to very shallow seas via narrow straits and thus create sharp topography gradients.

Figure 5.10 shows that the overall region is characterised by internal tides, which are detectable at the sea surface as ripples of constant wavelength that change according to the tidal frequency. The specific basin geometry means that once these waves are generated they remain confined within the semi-enclosed area before radiating away.
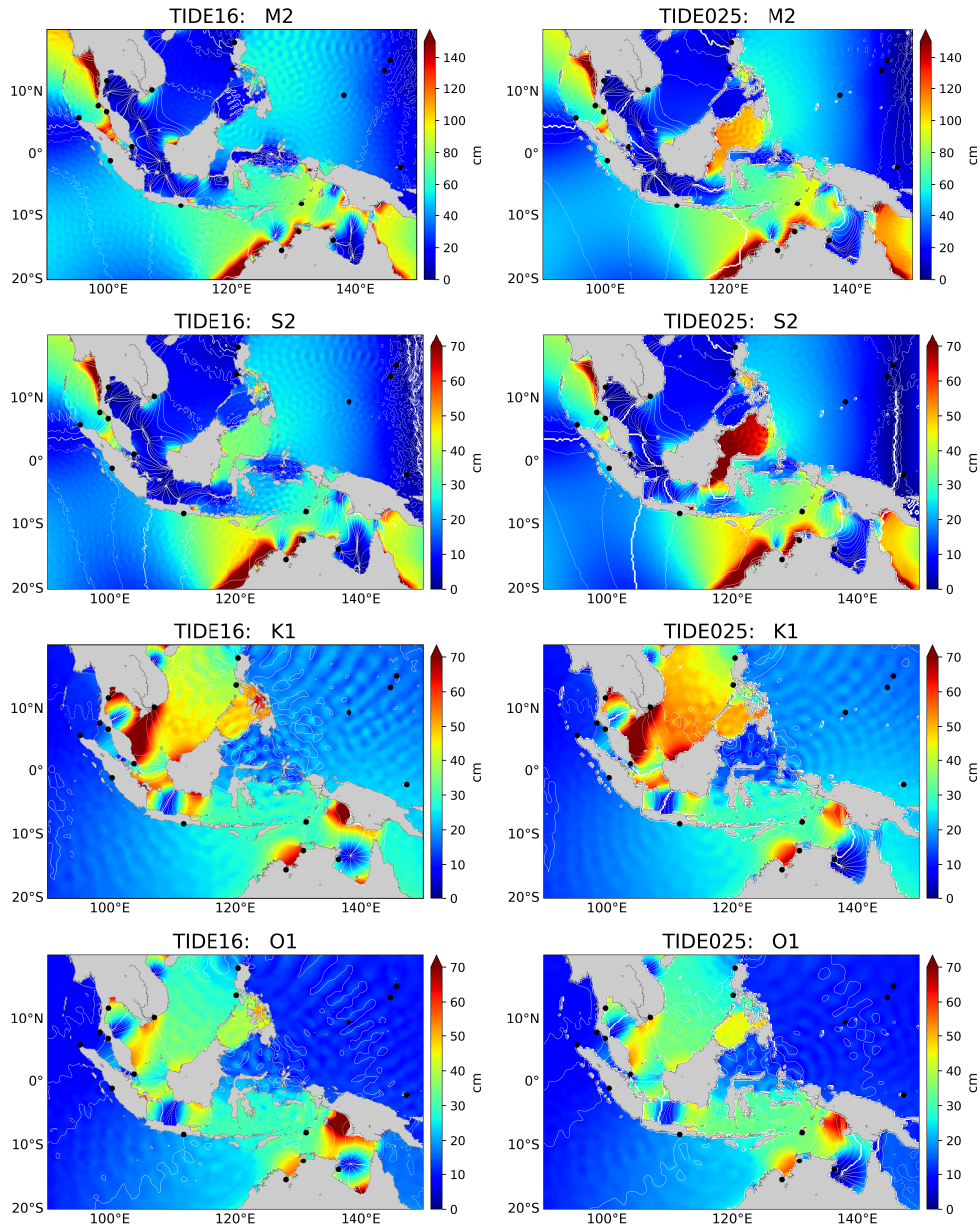
Figure 5.10: Maps of tidal amplitudes and phases in the Indonesian region computed from TIDE16 (*left* column) and TIDE025 (*right* column) experiments during the period from January 1st to July 3rd, 2017. Black dots represent the location of tide gauges data analysed in the text.

The major differences between TIDE16 and TIDE025 are in the Celebes Sea and the Makassar Strait, where the M2 amplitude is reduced from 110 cm to 60 cm (S2 from 70 cm to 35 cm) and becomes closer to those of the TPXO atlases (Figure 2.20). Other areas where TIDE16 performs better than TIDE025 include the North Australian shelf in the Arafura Sea and the Gulf of Carpentaria, where TIDE16 accurately reproduces both diurnal and semidiurnal amplitudes and places two amphidromic points (K1 and O1) that are absent from TIDE025. However, TIDE16 performs worse than TIDE025 in areas such as the Gulf of Thailand, where the biases of K1 and O1 with TPXO are higher.

The model resolution means that TIDE16 resolves more internal tides than TIDE025 both in the interior seas and in the open ocean, leading to a stronger interaction between them and mesoscale structures. Koch-Larrouy et al. (2007) suggest that the induced internal tidal mixing can change the properties of waters from the Pacific Ocean, and thus warrants further analysis. Tides modelled along the coast are then validated through a comparison with tide gauges. Unfortunately, during the period of interest, most data are missing for the interior seas, except for the South China Sea and the Timor and Arafura Seas, where tide gauges are clustered together. We therefore enlarged our dataset to consider tide gauges located nearby in the Pacific and Indian Oceans.

The two experiments behave in the same way at the tide gauge locations in the simulation of tidal amplitude, therefore the linear regression coefficient between the two is 0.96 for diurnal tides and 1.18 for semidiurnal tides (Figure 5.11). To evaluate the differences, the vectorial distances of the main tidal constituents are computed for each tide gauge (Figure 5.12), and the subregion RMSDs are summarised in Table 5.3:

- along the coasts of the South China Sea, TIDE16 performs worse than TIDE025, increasing the RMSD of M2, S2 and O1. The poorest value is derived from the M2 simulation, where the RMSD of TIDE16 is double that of TIDE025. Note that the semidiurnal RMSDs are forced by the high vectorial distances associated with the Vung Tau tide gauge (TG 383) on the Vietnam coast;

- on the North-West Australian shelf, both the experiments show strong vectorial distances, as associated with the Wyndham (TG 165) tide gauge, but on average TIDE16 can better reproduce K1 and O1 diurnal tides.

- on the coasts facing the Indian Ocean, TIDE16 is closer to observed data at the diurnal frequencies, particularly when we consider the poor simulation given by TIDE025 at Tanjong Pagar (TG 699) inside the Malacca Strait. Conversely, TIDE025 has a lower RMSD for M2 and S2.

- in the Pacific Ocean, TIDE025 is closer to tide gauges data than TIDE16, with the K1 component being the only exception.

On average, TIDE16 improves the K1 and O1 simulations in the Indonesian region (and around it) along with the generation of diurnal internal tides that reaches the sea surface, while TIDE025 is closer to the observed data at semidiurnal frequencies.

M2 (cm)			
Area	TIDE16	TIDE025	TPXO
South China Sea	15.27	7.36	3.05
Australian coast	91.81	77.83	51.09
Indian Ocean	41.69	36.57	3.57
Pacific Ocean	27.10	17.90	4.32
TOTAL	50.65	42.35	23.67

S2 (cm)			
Area	TIDE16	TIDE025	TPXO
South China Sea	6.99	5.15	1.64
Australian coast	46.05	37.87	25.87
Indian Ocean	17.28	16.89	2.52
Pacific Ocean	13.16	12.38	2.56
TOTAL	24.43	20.93	12.05

K1 (cm)			
Area	TIDE16	TIDE025	TPXO
South China Sea	20.45	20.80	2.94
Australian coast	11.69	15.31	10.87
Indian Ocean	6.27	9.18	2.36
Pacific Ocean	4.89	5.45	3.45
TOTAL	11.64	13.22	5.62

O1 (cm)			
Area	TIDE16	TIDE025	TPXO
South China Sea	9.49	8.79	1.52
Australian coast	14.97	15.21	3.92
Indian Ocean	9.14	11.45	2.17
Pacific Ocean	6.93	6.19	2.07
TOTAL	10.26	10.79	2.52

Table 5.3: RMSD between modelled tides (M2, S2, K1 and O1) and observed data from tide gauges in the Indonesian region.
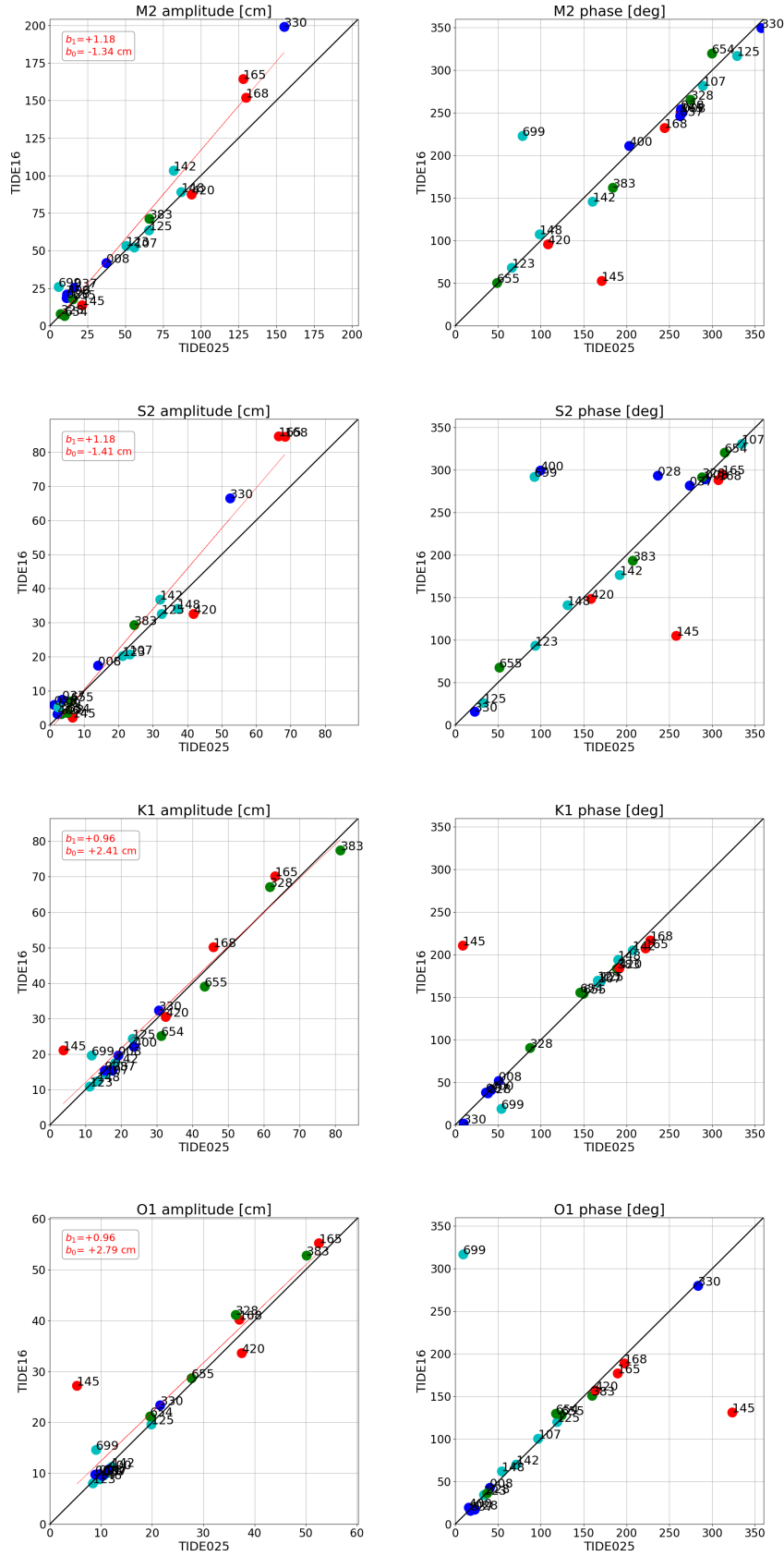
Figure 5.11: Scatter plots of the tidal amplitude (*left*) and phase (*right*) at tide gauges locations in the Indonesian region computed for TIDE16 and TIDE025 experiments during the period from January 1$^{\text{st}}$ to July 3$^{\text{rd}}$, 2017. Dots of the same color represent tide gauges of the same area: South China Sea (green), North-West Australian shelf (red), Pacific Ocean (blue) and Indian Ocean (cyan).
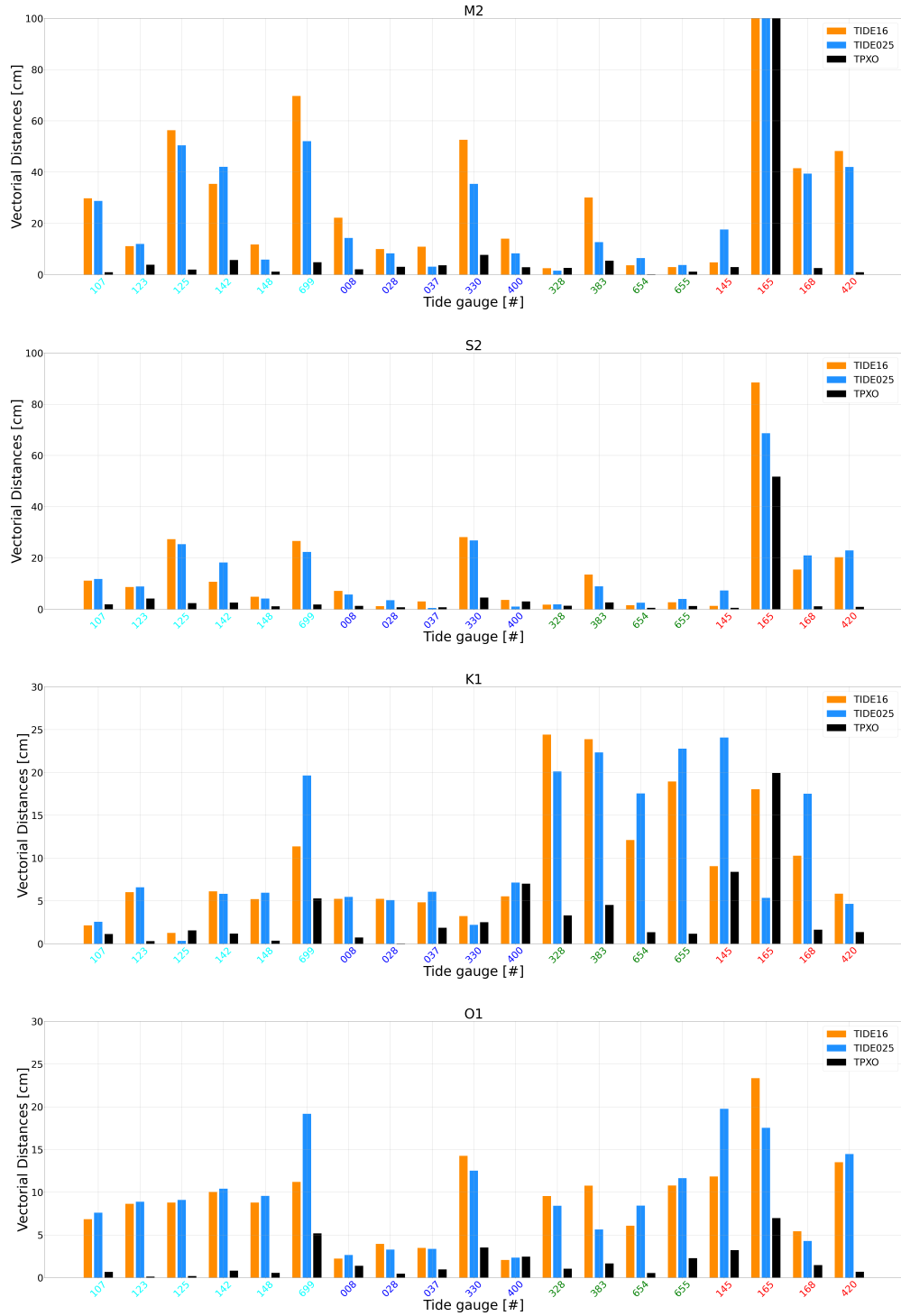
Figure 5.12: Vectorial distances between modelled and observed tidal components in the Indonesian region during the period from January 1st to July 3rd, 2017. Tide gauges of the same area have the same color: South China Sea (green), North-West Australian shelf (red), Pacific Ocean (blue) and Indian Ocean (cyan).

5.4   Conclusions

In this chapter, we describe for the first time the implementation of tides in GLOB16, a global eddy-resolving configuration of the NEMO model with a horizontal resolution of 1/16° and 98 vertical levels. The increased resolution implies a higher level of accuracy in the coastline geometry and the bottom topography, two factors that in principle can improve the tidal simulation. One tidal experiment (TIDE16) is then integrated for 18 months and compared to a similar experiment without tides (CTRL16), with consideration of the global KE and the simulated tides in the North-West Atlantic Ocean and the Indonesian region. Iovino et al. (2016) provided a description of the ocean dynamics, and the tidal effect on the ocean circulation will be considered in future studies.

We first point out that the tidal energy strongly varies according to the grid resolution, generally interacting with dynamical structures that are averaged out by the MKE, leaving the mean circulation unperturbed. When tides are implemented, the global MKE increases by about 1% from the reference value of CTRL16, while the EKE shows an oscillation typical of spring-neap tides and a mean value that enhances the reference one of about 50%.

Second, we compute the harmonic analysis of the SSH of TIDE16 and compare the results with TIDE025. The modelled amplitudes increase or decrease according to the region of interest and the considered harmonic component: the main improvements are found for the Celebes Sea and the Makassar strait, where TIDE16 simulates values close to the TPXO atlases, while the poorest simulations are in terms of the M2 and S2 frequencies in the Gulf of St Lawrence, Canada. In general, TIDE16 resolves more intense internal tides, both at diurnal (K1 and O1) and semidiurnal (M2 and S2) frequencies. These waves in turn interact with the surrounding flow, are enhanced by eddies and fronts at the mesoscale and contribute to the interior mixing (Koch-Larrouy et al., 2007). On average, TIDE16 overestimates the tidal amplitudes compared to the altimeter data-constrained model TPXO, suggesting that the topographic wave drag should for example be included as an additional term of internal wave dissipation.

Third, we compare the simulated tides with tide gauge data from the North-West Atlantic Ocean and in the Indonesian region. Along the Atlantic coast, TIDE16 performs better than TIDE025 at the M2 and S2 frequencies, while in the Indonesian region a better comparison with the observations is only found for K1.

Finally, the broad difference in the Southern Ocean between the modelled tides and TPXO is probably due to two main factors related to ice simulation. In our experiments, the initial sea ice conditions are based on the sea surface temperature climatology rather than on observed data, and the ice shelves are missing although recent studies have demonstrated their importance in tide modelling.

Chapter 6

Conclusions and future work

6.1 Summary

Tides are one of the longest observed phenomena in the ocean. Despite this, understanding the processes they affect is still a topic of debate within the scientific community. In the open ocean, indeed, barotropic and baroclinic tides interact with the bottom topography and the surrounding flow and they trigger a cascade of energy from larger to smaller scales that is difficult to reproduce in global numerical models. This thesis aims to deepen the study of tides from a dynamical point of view, improving their simulation in a general circulation model and analysing what are their effects on the overturning circulation of the ocean.

For this purpose, we performed different simulations using the ocean general circulation model NEMO forced by both atmospheric fields and astronomical tidal potential, including a broad spectrum of 11 tidal constituents. In Chapters 2 and 5 we compared tidal and non-tidal experiments using two global configurations with different horizontal and vertical resolutions: the former is eddy-permitting at $1/4°$ with 75 vertical levels (TIDE025), while the latter is eddy-resolving at $1/16°$ with 98 vertical levels (TIDE16). This latter one is, at least to our knowledge, the global NEMO simulation at the highest resolution that includes tides.

From the energetic point of view, we found that the tidal energy input increases the global kinetic energy by about 18% in TIDE025 and 22% in TIDE16. However, this difference is detected only when the kinetic energy is computed with sufficient temporal resolution including dynamical processes at very high frequencies (below hourly).

As our first objective is to assess the accuracy of simulated tides, we computed the harmonic analysis of the modelled SSH and compared maps of the four principal tidal components (M2, S2, K1, O1) to atlases provided by the barotropic assimilative tidal model TPXO. Even though TIDE16 enhances the accuracy of coastline geometry and bottom topography with respect to TIDE025, both the experiments overestimate tidal amplitudes compared to observations, especially at high latitudes. We also compared the modelled tides to in situ observations from the UHSLC dataset. We focused the analysis on two regions of interest, the North-West Atlantic Ocean and the Indonesian region: the former is characterised by semidiurnal tides and is a well-known region of internal waves dissipative regime (Zilberman et al., 2009), while the latter has a

6. Conclusions and future work

very complex bathymetry and broad range of tidal harmonics, representing a challenging region to test the model (Ray et al., 2005). In these regions, TIDE025 and TIDE16 perform differently according to the considered harmonics. Indeed, in the North-West Atlantic region semidiurnal tides are closer to observations in TIDE16 than in TIDE025, while in the Indonesian region TIDE16 performs worse at all frequencies, except for K1 component.

Moreover, TIDE16 resolves a higher number of baroclinic modes and then a larger number of internal tides propagating from the bottom to the surface of the ocean. The lower-mode internal tides are simulated also in TIDE025, giving evidence that the model resolves a portion of the interaction between barotropic tides and rough bathymetry. However, these processes are multi-scale and their unresolved component must be parametrized to have a correct tidal energy distribution (Arbic et al., 2010).

To improve the model performance, in Chapter 2 we implemented a TWD parametrization in the eddy-permitting configuration in order to introduce a sink of the tidal energy associated to unresolved internal tide generation processes over rough topography. We followed the formulation proposed by Shakespeare et al. (2020) for dissipating semidiurnal internal tides. The TWD is based on the computation of unresolved roughness and bottom water stratification, and it is more intense where bottom stratification is stronger and roughness is sharp. Moreover, we modified the bottom friction numerical formulation to improve its coherency with the analytical definition when barotropic tides contribute to the bottom flow. Both implementations were included in TIDE025_TWD experiment.

In TIDE025_TWD the total KE decreases on the global scale compared to TIDE025 (-4%), consistently with the implemented dissipation of internal tides, even though its temporal mean remains higher than the reference simulation without tides. The TWD improves the modelled SSH in the Atlantic region with respect to TIDE025, whereas in the Indonesian region the formulation is too simple to represent the complexity of the region and decrease the biases with respect to data.

In order to make the tidal simulations more realistic, we also implemented a SAL parametrization to introduce the effects of gravitational self-attraction and earth-loading induced by oceanic tides. In TIDE025_TWD_SAL experiment we included a SAL scalar formulation, based on the assumption that these phenomena are dominated by a specific spatial scale. We found that the impact on the SSH strongly depends on the region and the tidal constituent of interest, therefore it is necessary to refine the formulation to make results obtained with SAL comparable to the literature.

The answer to the first scientific question that motivates this thesis was achieved in Chapter 3, where we extended the eddy-permitting simulations to decadal time scales and analysed the overturning circulation in the Atlantic Ocean. We computed the meridional streamfunction from 1981 to 2007 and we found that tides weaken the AMOC (-2.5% of the reference value) during the analysed period. Nevertheless, the interannual differences strongly change in both amplitude and sign especially in the SH. However, in the NH the differences are more uniform in time. The AMOC further decreases (-3% when the TWD dissipates part of the tidal energy, suggesting that

the propagation of internal tides contributes to sustain the overturning circulation.

When we compared modelled data with the RAPID/MOCHA array at 26.5°N, we found that the model underestimates the observed meridional transport (16.08 Sv in the reference simulation, compared to the observed 18.69 Sv). Moreover, when tides are implemented, part of the northward transport associated to the GS flows outside the Florida Strait weakening the observed UMO southward transport.

To better analyse the dynamical processes involved in the Atlantic MOC reduction by tides, we computed the zonally integrated momentum balance. As illustrated by the meridional stream-function, tides decrease the baroclinic transport throughout the water column, both northward (between the surface and 1000 m) and southward (in the deeper layers). The overturning circulation is geostrophically balanced by the pressure difference at the zonal boundaries (Kanzow et al., 2010) and we found that most of the tidal contribution to the momentum balance impacts on this term. This is because tides change the density distribution of the whole water column at the lateral boundaries of the domain. Tides modify also the advective momentum flux, but their contribution focuses in the upper 500 m leaving the deep ocean unperturbed.

The answer to the second scientific question was given in Chapter 4, where we analysed the overturning circulation in the Mediterranean Sea both in the traditional, Eulerian, and the residual frameworks including the contribution of the mesoscale fronts, eddies and gyres. This analysis was never used before in a marginal sea. The zonal circulation is composed by three cells mainly forced by adiabatic processes: a shallow clockwise cell extending from the Gibraltar Strait to the Levantine Sea, and two deep cells which characterise the WMED and EMED, counterclockwise and clockwise respectively. In the WMED, a meridional clockwise cell is forced in the Gulf of Lion by deep water formation processes, while an abyssal counterclockwise cell characterises the southern portion of the subbasin. The EMED, instead, has multicentred clockwise cells forced by water formation events and strongly influenced by diapycnal processes. Finally, we presented the connection between zonal and meridional overturning cells computing the divergent component of the horizontal flow. Such component drives the vertical circulation and is steered by the rotational transport in the basin. Lastly, we analysed the impact of a transient climatic event as the EMT on the overturning circulation strength.

6.2 Conclusions and future works

This thesis represents a step toward the understanding of tides and their role on the general circulation of the ocean. We implemented a TWD in an eddy-permitting configuration of the NEMO model following the Shakespeare et al. (2020) formulation limited to the case of dissipating internal waves. The TWD improves the comparison with observed data in the North-West Atlantic Ocean, whereas it enhances the errors in the Indonesian region, characterised by more complex tidal dynamics.

We propose this parametrization as a necessary starting point to include the interaction processes between tides and unresolved bottom topography in the NEMO model. Nevertheless, the

6. Conclusions and future work

implementation could be carried further extending the range of processes, or taking into consideration the incidence angle between the tidal flow and the topographic structures (i.e., roughness anisotropy), or including different regimes of propagating and bottom-trapped waves. We also assessed the necessity to improve the SAL parametrization using an iterative approach to make the formulation time and space dependent.

In this study we described some preliminary results on the addition of tides in an eddy-resolving configuration of the NEMO model. Despite the increased accuracy of the coastline geometry and bottom topography, the simulation of tides strongly depends on the region of interest, especially in case of intense interaction between tides and resolved mesoscale structures. We plan to improve this configuration in future research projects, implementing a TWD parametrization for dissipating and propagating waves.

After the preliminary phase of model assessment, we studied the impact of tides in the general circulation of the ocean focusing on the Atlantic basin, where we computed the meridional streamfunction in different experiments with and without the tidal forcing. We found that the tidally induced water stratification weakens the overturning circulation compared to the reference value. Furthermore, in the tidal experiment with TWD the reduction is even stronger, suggesting that internal tides contribute to the overturning strength.

Using diagnostics of the zonally integrated momentum balance, we demonstrated that the variations induced by tides are mostly due to the pressure difference between the zonal boundaries. In turn, the pressure at the boundaries is determined by local buoyancy changes acting to weaken the zonally integrated meridional transport over the entire basin. Our result confirms the necessity to analyse the buoyancy momentum balance to identify how tides influence the ocean circulation, and points out the importance of parametrizing unresolved tidal diapycnal processes in ocean general circulation models.

The entire momentum budget could be improved considering also the surface intensified tidal effects, as the diffusive terms and the zonal flow variation. Moreover, it would be interesting to study the AMOC circulation in an eddy-resolving configuration, looking at a larger range of interaction processes between tides, topography and mesoscale structures.

Finally, we described the overturning circulation in the Mediterranean Sea, giving evidence for the first time to the connection between meridional and zonal circulation. We identified the processes that force each circulation cell with particular emphasis to the mesoscale and the role of a transient climatic event. The implementation of a TWD could also be useful to improve tidal simulations in the Mediterranean Sea, with particular emphasis in the area west of the Gibraltar Strait, where two submarine sills (Camarinal and Espartel sills) strongly influence the inflow of Atlantic water.

Appendix A

TWD formulation

The main hypothesis and the complete topographic wave stress parametrization defined in Shakespeare et al. (2020) are summarised in the following. The relevant equations are

$$\frac{\partial \boldsymbol{u}}{\partial t} + \boldsymbol{u} \cdot \nabla \boldsymbol{u} + f\,\hat{\boldsymbol{z}} \times \boldsymbol{u} = -\nabla p + \boldsymbol{F} + b\hat{\boldsymbol{z}} \tag{A.1a}$$

$$\nabla \cdot \boldsymbol{u} = 0 \tag{A.1b}$$

$$\frac{\partial b}{\partial t} + \boldsymbol{u} \cdot \nabla b = 0 \tag{A.1c}$$

where $\boldsymbol{u} = (u, v, w)$ is the total velocity, p is the dynamic pressure, b is the buoyancy, f is the Coriolis parameter, and $\boldsymbol{F} = (F_x, F_y, 0)$ is the spatially uniform body force.

The formulation is based on the following assumptions:

- the observed fluid is inviscid on an f-plane

- the ocean boundaries are described by a rigid lid at the surface $z = 0$ and a bottom bathymetry $z = -H + h(x, y)$, where $-H$ is the mean bathymetry on regional scale and h is the small amplitude roughness ($h \ll H$);

- the roughness is supposed to be isotropic, and can be defined in the Fourier domain as $\widehat{h}(K)$, where K is the horizontal wavenumber;

- a periodic body forcing $\boldsymbol{F}$ (in this case the astronomical tidal forcing) is the only source of energy acting across larger-scale bathymetry;

- all dynamic fields are decomposed in their spatial mean oscillation and the residual component as

$$\boldsymbol{u}(\boldsymbol{x}, z, t) = \langle \overline{\boldsymbol{u}} \rangle(t) + \boldsymbol{u}'(\boldsymbol{x}, z, t) \tag{A.2}$$

where the angle brackets denote the horizontal average, so $\langle \overline{\boldsymbol{u}} \rangle$ corresponds to the space independent barotropic flow in the region of interest;

- the barotropic tidal flow is spatially uniform over topographic scales and generates baroclinic waves with horizontal scales smaller than 100 km. The small amplitude approximation is

A. TWD formulation

then valid near the bottom and asymptotically, when the vertical wavenumber, m, satisfies the relation $mh \ll 1$.

According to these considerations, the authors first analyse the mean flow equations and derive its momentum equation neglecting advection and viscous terms

$$\frac{\partial \langle \overline{\boldsymbol{u}} \rangle}{\partial t} + f\,\hat{\boldsymbol{k}} \times \langle \overline{\boldsymbol{u}} \rangle = -\frac{1}{H} \langle p'_{-H} \nabla h \rangle + \boldsymbol{F} \quad . \tag{A.3}$$

This formula demonstrates that the spatial-mean flow $\langle \overline{\boldsymbol{u}} \rangle$ is determined by the balance between the body force and the bottom pressure interaction with the bathymetry.

Then the baroclinic flow equations are considered with the addition of a drag term as a zeroth-order dissipation

$$\frac{\partial \boldsymbol{u}'}{\partial t} + \langle \overline{\boldsymbol{u}} \rangle \cdot \nabla \boldsymbol{u}' + f\,\hat{\boldsymbol{k}} \times \boldsymbol{u}' = -\nabla p' + b'\hat{\boldsymbol{k}} - \alpha \boldsymbol{u}' \tag{A.4a}$$

$$\nabla \cdot \boldsymbol{u}' = 0 \tag{A.4b}$$

$$\frac{\partial b'}{\partial t} + \langle \overline{\boldsymbol{u}} \rangle \cdot \nabla b' + N^2 w' = -\alpha b' \tag{A.4c}$$

where α is a decay time parameter. This parameter is used here to represent both locally dissipating waves (when α has a finite value in a deep ocean with $H \to \infty$) and propagating waves (meaning that $\alpha \to 0$). The topographic stress parametrization derives then from the FFT analysis of the relation between the dynamic pressure term, $\langle p'|_{-H} \nabla h \rangle / H$, and the baroclinic dissipation term $\alpha \boldsymbol{u}'$.

In the limit of weak dissipation on regional scales ($\alpha \ll f$) the baroclinic motion is characterised by a vertical wavenumber, m, and a related decay-weighted vertical wavenumber, γ, defined as

$$m = \omega K \sqrt{\frac{N^2 - \omega^2}{\omega^2 - f^2}} \tag{A.5a}$$

$$\gamma = \alpha\,m\,\frac{\omega\,(2N^2 - \omega^2 - f^2)}{2\,(N^2 - \omega^2)\,(\omega^2 - f^2)} \tag{A.5b}$$

that contribute to define the parameter r^* as

$$r^* = \frac{1}{4\pi A} \int_0^{+\infty} |\hat{h}(K)|^2 \frac{K^2}{|\omega|} \sqrt{(N^2 - \omega^2)(\omega^2 - f^2)} \coth(imH + \gamma H)\, dK \quad . \tag{A.6}$$

This formulation of r^* is comprehensive of different possible wave regimes (Figure A.1) but it is difficult to implement in ocean models, however it can be simplified depending on the wave dissipation strength, γH, and the oscillation frequency, ω. Together with the roughness root-mean-square h_{rms} and its height-weight-mean wavenumber $\overline{K}$ defined in (2.36) and (2.37), these variables identify different regimes and produce the formulas summarised in Table A.1.

It is worth noting that when the frequency conditions are stronger and $f \ll \omega \ll N$, the formulation for dissipative waves simplifies to the coefficient proposed by Jayne and St. Laurent (2001), confirming a good agreement with previous TWD schemes but without the need of any additional

scaling parameters.

Regime	Frequency regime	dissipation strength	Stress coefficient
Locally dissipating waves	$f < \omega < N$	$\gamma H \to \infty$	$r_1^* = \frac{1}{2} N \, h_{rms}^2 \overline{K} F_1(\omega)$ $F_1(\omega) = \frac{\sqrt{(N^2-\omega^2)(\omega^2-f^2)}}{N|\omega|}$
Propagating waves	$f < \omega < N$	$\gamma H \to 0$	$r_2^* = \frac{1}{2} N \, h_{rms}^2 \overline{K} F_1(\omega) - i \frac{\omega}{H} h_{rms}^2 F_2(\omega \ln 2)$ $F_2(\omega) = \frac{\omega^2-f^2}{\omega^2}$
Bottom trapped waves	$\omega < f$	$\gamma H \to 0$	$r_3^* = \frac{1}{2} i N \, h_{rms}^2 \overline{K} \frac{f}{\omega} F_3(\omega)$ $F_3(\omega) = \frac{\sqrt{(N^2-\omega^2)(f^2-\omega^2)}}{N|\omega|}$

Table A.1: Summary of the possible solutions for the topographic wave parameter (A.6) in different regimes. The key factors are the dynamical characteristics of the generated waves together with the ocean depth and stratification.
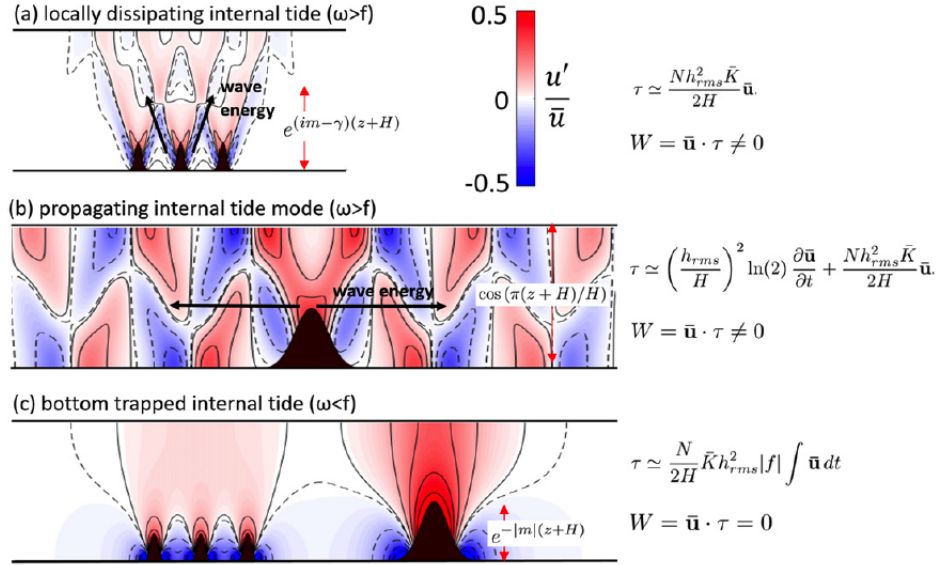
Figure A.1: Schematic of the dynamical regimes, from Shakespeare et al. (2020). *(a)* Locally dissipating wave regime: small topographic scale features generate waves that dissipate near to their generation site without encountering the ocean surface. In this case internal tides extract from the barotropic mode the energy and move it vertically. *(b)* Propagating mode regime typically dominates on large scale topographic structures, when internal tides are generated but propagate away. Even in this case some energy is extracted from the barotropic tide, but now it is propagated horizontally. *(c)* Bottom-trapped internal tides regime is associated with both large and small topographic scales, when they generate waves that do not propagate nor dissipate energy from the mean flow. The contour shows a snapshot of the in-page horizontal perturbation velocity as a fraction of the velocity magnitude without topography.

A. TWD formulation

Appendix B

Tide gauges list

#TG	Station	Country	Lat (deg)	Lon (deg)
240	Fernandina Beach	USA	30.67	-81.47
252	Portland,ME	USA	43.66	-70.25
253	Newport,RI	USA	41.51	-71.33
257	Settlement Point-B	Bahamas	26.69	-78.98
259	Bermuda-B	United Kingdom	32.37	-64.70
260	Duck Pier,NC	USA	36.18	-75.75
261	Charleston,SC-B	USA	32.78	-79.92
264	Atlantic City,NJ	USA	39.35	-74.42
276	St. John's-B	Canada	47.57	-52.70
740	Eastport,ME	USA	44.90	-66.98
742	Woods Hole,MA	USA	41.52	-70.67
743	Nantucket,MA	USA	41.28	-70.10
744	New London,CT	USA	41.35	-72.09
745	New York,NY	USA	40.70	-74.02
746	Cape May,NJ	USA	38.97	-74.96
747	Lewes,DE	USA	38.78	-75.12
750	Wilmington,NC	USA	34.23	-77.95
752	Fort Pulaski,GA	USA	32.03	-80.90
755	Virginia Key,FL	USA	25.73	-80.16
757	Naples,FL	USA	26.13	-81.81
759	St. Petersburg, FL	USA	27.76	-82.63
760	Apalachicola,FL	USA	29.73	-84.98
761	Panama City Beach	USA	30.21	-85.88
762	Pensacola,FL	USA	30.40	-87.21
763	Dauphin Island, AL	USA	30.25	-88.08
765	Grand Isle,LA	USA	29.26	-89.96
766	Sabine Pass N,TX	USA	29.73	-93.87
770	Corpus Cristi,TX	USA	27.58	-97.22
772	Port Isabel,TX	USA	26.06	-97.22
773	Clearwater Bch,FL	USA	27.98	-82.83
774	Port Canaveral, FL	USA	28.41	-80.59
775	Galveston,Pier 21	USA	29.31	-94.79

Table B.1: List of tide gauges in the North-West Atlantic region, characterised by hourly data continuously recorded for 9 months, from April to December, 2017. Data selected from the University of Hawai'i Sea Level Centre (UHSLC) tide gauges database (Caldwell et al., 2015).

#TG	Station	Country	Lat (deg)	Lon (deg)
008	Yap-B	Fd. St. Micronesia	9.51	138.13
028	Saipan-B	N. Mariana Islands	15.23	145.74
037	Pago Bay, Guam	USA	13.43	144.80
107	Padang-B	Indonesia	-1.00	100.38
123	Sabang	Indonesia	5.89	95.32
125	Prigi	Indonesia	-8.28	111.73
142	Langkawi	Malaysia	6.87	99.77
145	Groote Eylandt	Australia	-13.86	136.42
148	Ko Taphao Noi	Thailand	7.83	98.42
165	Wyndham	Australia	-15.45	128.10
168	Darwin	Australia	-12.47	130.85
328	Ko Lak	Thailand	11.79	99.82
330	Rosslyn Bay	Australia	-23.16	150.79
383	Vung Tau-B	Vietnam	10.34	107.07
400	Lombrum, Manus Is.	Papua New Guinea	-2.04	147.38
420	Saumlaki	Indonesia	-7.98	131.29
654	Currimao	Philippines	17.99	120.49
655	Lubang	Philippines	13.82	120.20
699	Tanjong Pagar	Singapore	1.26	103.85

Table B.2: List of tide gauges in the Indonesian region, characterised by hourly data continuously recorded for 9 months, from April to December, 2017. Data selected from the University of Hawai'i Sea Level Centre (UHSLC) tide gauges database (Caldwell et al., 2015).

Bibliography

Accad, Y. and Pekeris, C. L. (1978). Solution of the tidal equations for the m2 and s2 tides in the world oceans from a knowledge of the tidal potential alone. *Philosophical Transactions of the Royal Society of London. Series A, Mathematical and Physical Sciences*, 290:235–266.

Adcroft, A. and Campin, J.-M. (2004). Rescaled height coordinates for accurate representation of free-surface flows in ocean circulation models. *Ocean Modelling*, 7(3):269–284.

Agresti, V. (2018). *Effects of tidal motion on the Mediterranean Sea General Circulation,*. PhD thesis, University of Bologna.

Aiken, C. M. (2008). Barotropic tides of the chilean inland sea and their sensitivity to basin geometry. *Journal of Geophysical Research: Oceans*, 113(C8).

Amante, C. and Eakins, B. W. (2009). Etopo1 global relief model converted to panmap layer format. *NOAA-National Geophysical Data Center*.

Andrews, D. G., Holton, J. R., and Leovy, C. B. (1987). *Middle Atmosphere Dynamics*, volume 127. Academic Press, Orlando, San Diego, New York, Austin, Boston, London, Sydney, Tokyo, Toronto.

Arbic, B. K. (2021). *Incorporating Tides and Internal Gravity Waves within Global Ocean General Circulation Models*, volume in press. AGU book.

Arbic, B. K., Alford, M. H., Ansong, J. K., Buijsman, M. C., Ciotti, R. B., Farrar, J. T., and Hallberg, R. W. (2018). A primer on global internal tide and internal gravity wave continuum modeling in hycom and mitgcm. *New Frontiers In Operational Oceanography*, pages 306–391.

Arbic, B. K., Garner, S. T., Hallberg, R. W., and Simmons, H. L. . (2004). The accuracy of surface elevations in forward global barotropic and baroclinic tide models. *Deep-Sea Research II*, 51:3069–3101.

Arbic, B. K., Wallcraft, A. J., and Metzger, E. J. (2010). Concurrent simulation of the eddying general circulation and tides in a global ocean model. *Ocean Modelling*, 32:175–182.

Barnier, B., Madec, G., Penduff, e. a. T., Molines, J.-M., Treguier, A.-M., Le Sommer, J., Beckmann, A., Biastoch, A., Böning, C., Dengg, J., Derval, C., Durand, E., Gulev, S., Remy, E., Talandier, C., Theetten, S., Maltrud, M., McClean, J., and De Cuevas, B. (2006). Impact of

partial steps and momentum advection schemes in a global ocean circulation model at eddy-permitting resolution. *Ocean Dynamics*, 56(5):543–567.

Bell, T. H. (1975). Topographically generated internal waves in the open ocean. *Journal of Geophysical Research*, 80:320–327.

Blanke, B. and Raynaud, S. (1997). Kinematics of the pacific equatorial undercurrent: An eulerian and lagrangian approach from gcm results. *Journal of Physical Oceanography*, 27(6):1038 – 1053.

Buckley, M. W. and Marshall, J. (2016). Observations, inferences, and mechanisms of the atlantic meridional overturning circulation: A review. *Reviews of Geophysics*, 54(1):5–63.

Bühler, O. and Holmes-Cerfon, M. (2011). Decay of an internal tide due to random topography in the ocean. *Journal of Fluid Mechanics*, 678.

Buijsman, M. C., Stephenson, G. R., Ansong, J. K., Arbic, B. K., Green, J. M., Richman, J. G., Shriver, J. F., Vic, C., Wallcraft, A. J., and Zhao, Z. (2020). On the interplay between horizontal resolution and wave drag and their effect on tidal baroclinic mode waves in realistic global ocean simulations. *Ocean Modelling*, 152:101656.

Caldwell, P. C., Merrifield, M. A., and Thompson, P. R. (2015). Sea level measured by tide gauges from global oceans — the joint archive for sea level holdings (ncei accession 0019568). Dataset Version 5.5, NOAA National Centers for Environmental Information.

Callendar, W., Klymak, J. M., and Foreman, M. G. G. (2011). Tidal generation of large sub-mesoscale eddy dipoles. *Ocean Science*, 7(4):487–502.

Carter, G. S., Fringer, O., and Zaron, E. D. (2012). Regional models of internal tides. *Oceanography*, 25(2):56–65.

Cartwright, D. (1999). *Tides: A Scientific History.* Cambridge University Press, Cambridge.

Cessi, P. (2019). The global overturning circulation. *Annual Review of Marine Science*, 11(1):249–270. PMID: 30606095.

Chavanne, C., Flament, P., Luther, D., and Gurgel, K.-W. (2010). The surface expression of semidiurnal internal tides near a strong source at hawaii. part ii: Interactions with mesoscale currents. *Journal of Physical Oceanography*, 40(6):1180 – 1200.

Chen, X. and Tung, K.-K. (2018). Global surface warming enhanced by weak atlantic overturning circulation. *Nature*, 559(7714):387–391.

Choi, H.-J. and Hong, S.-Y. (2015). An updated subgrid orographic parameterization for global atmospheric forecast models. *Journal of Geophysical Research: Atmospheres*, 120(24):12445–12457.

Colosi, J. A., Beardsley, R. C., Lynch, J. F., Gawarkiewicz, G., Chiu, C.-S., and Scotti, A. (2001). Observations of nonlinear internal waves on the outer new england continental shelf during the summer shelfbreak primer study. *Journal of Geophysical Research: Oceans*, 106(C5):9587–9601.

Cunningham, S. A., Kanzow, T., Rayner, D., Baringer, M. O., Johns, W. E., Marotzke, J., Longworth, H. R., Grant, E. M., Hirschi, J. J.-M., Beal, L. M., Meinen, C. S., and Bryden, H. L. (2007). Temporal variability of the atlantic meridional overturning circulation at 26.5°n. *Science*, 317(5840):935–938.

Danabasoglu, G., Yeager, S. G., Bailey, D., Behrens, E., Bentsen, M., Bi, D., Biastoch, A., Böning, C., Bozec, A., Canuto, V. M., Cassou, C., Chassignet, E., Coward, A. C., Danilov, S., Diansky, N., Drange, H., Farneti, R., Fernandez, E., Fogli, P. G., Forget, G., Fujii, Y., Griffies, S. M., Gusev, A., Heimbach, P., Howard, A., Jung, T., Kelley, M., Large, W. G., Leboissetier, A., Lu, J., Madec, G., Marsland, S. J., Masina, S., Navarra, A., George Nurser, A., Pirani, A., y Mélia, D. S., Samuels, B. L., Scheinert, M., Sidorenko, D., Treguier, A.-M., Tsujino, H., Uotila, P., Valcke, S., Voldoire, A., and Wang, Q. (2014). North atlantic simulations in coordinated ocean-ice reference experiments phase ii (core-ii). part i: Mean states. *Ocean Modelling*, 73:76–107.

de Lavergne, C., Falahat, S., Madec, G., Roquet, F., Nycander, J., and Vic, C. (2019). Toward global maps of internal tide energy sinks. *Ocean Modelling*, 137:52–75.

de Lavergne, C., Vic, C., Madec, G., F., R., Waterhouse, A. F., Whalen, C. B., Cuypers, Y., Bouruet-Aubertot, P., Ferron, B., and Hibiya, T. (2020). A parameterization of local and remote tidal mixing. *Journal of Advences in Modeling Earth Systems*, 12(e2020MS002065).

Dossmann, Y., Shakespeare, C., Stewart, K., and Hogg, A. M. (2020). Asymmetric internal tide generation in the presence of a steady flow. *Journal of Geophysical Research: Oceans*, 125(10):e2020JC016503. e2020JC016503 10.1029/2020JC016503.

Dunphy, M. and Lamb, K. G. (2014). Focusing and vertical mode scattering of the first mode internal tide by mesoscale eddy interaction. *Journal of Geophysical Research: Oceans*, 119(1):523–536.

Dushaw, B. D., Howe, B. M., Cornuelle, B. D., Worcester, P. F., and Luther, D. S. (1995). Barotropic and baroclinic tides in the central north pacific ocean determined from long-range reciprocal acoustic transmissions. *Journal of Physical Oceanography*, 25(4):631 – 647.

Egbert, G., Bennet, A. F., and Foreman, M. G. G. (1994). Topex/poseidon tides estimated using a global inverse model. *Journal of Geophysical Research*, 99:24821–24852.

Egbert, G. and Erofeeva, S. (2002). Efficient inverse modeling of barotropic ocean tides. *Journal of Atmospheric and Oceanic Technology*, 19:183–204.

Egbert, G. and Ray, R. (2000). Signifcant dissipation of tidal energy in the deep ocean inferred from satellite altimeter data. *Nature*, 405:775–778.

Egbert, G. D. and Ray, R. D. (2001). Estimates of m2 tidal energy dissipation from topex/poseidon altimeter data. *Journal of Geophysical Research: Oceans*, 106:22475–22502.

Egbert, G. D., Ray, R. D., and Bills, B. G. (2004). Numerical modeling of the global semidiurnal tide in the present day and in the last glacial maximum. *Journal of Geophysical Research*, 109(C03003).

Einšpigel, D. and Martinec, Z. (2017). Time-domain modeling of global ocean tides generated by the full lunisolar potential. *Ocean Dynamics*, 67(2):165–189.

Falahat, S. and Nycander, J. (2015). On the generation of bottom-trapped internal tides. *Journal of Physical Oceanography*, 45(2):526 – 545.

Fevrier, S., Sirven, J., and Herbaut, C. (2007). Interaction of a coastal kelvin wave with the mean state in the gulf stream separation area. *Journal of Physical Oceanography*, 37(6):1429 – 1444.

Ffield, A. and Gordon, A. L. (1996). Tidal mixing signatures in the indonesian seas. *Journal of Physical Oceanography*, 26(9):1924 – 1937.

Foreman, M. G. G., Cherniawsky, J. Y., and Ballantyne, V. A. (2009). Versatile harmonic tidal analysis: Improvements and applications. *Journal of Atmospheric and Oceanic Technology*, 26(4):806 – 817.

Frajka-Williams, E., Ansorge, I. J., Baehr, J., Bryden, H. L., Chidichimo, M. P., Cunningham, S. A., Danabasoglu, G., Dong, S., Donohue, K. A., Elipot, S., Heimbach, P., Holliday, N. P., Hummels, R., Jackson, L. C., Karstensen, J., Lankhorst, M., Le Bras, I. A., Lozier, M. S., McDonagh, E. L., Meinen, C. S., Mercier, H., Moat, B. I., Perez, R. C., Piecuch, C. G., Rhein, M., Srokosz, M. A., Trenberth, K. E., Bacon, S., Forget, G., Goni, G., Kieke, D., Koelling, J., Lamont, T., McCarthy, G. D., Mertens, C., Send, U., Smeed, D. A., Speich, S., van den Berg, M., Volkov, D., and Wilson, C. (2019). Atlantic meridional overturning circulation: Observed transport and variability. *Frontiers in Marine Science*, 6:260.

Frankignoul, C., Gastineau, G., and Kwon, Y.-O. (2013). The influence of the amoc variability on the atmosphere in ccsm3. *Journal of Climate*, 26(24):9774 – 9790.

Fretwell, P., Pritchard, H. D., Vaughan, D. G., Bamber, J. L., Barrand, N. E., Bell, R., Bianchi, C., Bingham, R. G., Blankenship, D. D., Casassa, G., Catania, G., Callens, D., Conway, H., Cook, A. J., Corr, H. F. J., Damaske, D., Damm, V., Ferraccioli, F., Forsberg, R., Fujita, S., Gim, Y., Gogineni, P., Griggs, J. A., Hindmarsh, R. C. A., Holmlund, P., Holt, J. W., Jacobel, R. W., Jenkins, A., Jokat, W., Jordan, T., King, E. C., Kohler, J., Krabill, W., Riger-Kusk, M., Langley, K. A., Leitchenkov, G., Leuschen, C., Luyendyk, B. P., Matsuoka, K., Mouginot, J., Nitsche, F. O., Nogi, Y., Nost, O. A., Popov, S. V., Rignot, E., Rippin, D. M., Rivera, A., Roberts, J., Ross, N., Siegert, M. J., Smith, A. M., Steinhage, D., Studinger, M., Sun, B., Tinto, B. K., Welch, B. C., Wilson, D., Young, D. A., Xiangbin, C., and Zirizzotti, A. (2013). Bedmap2: improved ice bed, surface and thickness datasets for antarctica. *The Cryosphere*, 7(1):375–393.

Fu, H., Wu, X., Li, W., Zhang, L., Liu, K., and Dan, B. (2021). Improving the accuracy of barotropic and internal tides embedded in a high-resolution global ocean circulation model of mitgcm. *Ocean Modelling*, 162:101809.

Fu, L.-L., Christensen, E. J., Yamarone Jr., C. A., Lefebvre, M., Ménard, Y., Dorrer, M., and Escudier, P. (1994). Topex/poseidon mission overview. *Journal of Geophysical Research: Oceans*, 99(C12):24369–24381.

Garner, S. T. (2004). A topographic drag closure built in an analytical base flux. *Journal of Atmospheric Science*, 62:2302–2315.

Garrett, C. and Kunze, E. (2007). Internal tide generation in the deep ocean. *Annual Review of Fluid Mechanics*, 39(1):57–87.

Garrett, C. and Munk, W. (1975). Space-time scales of internal waves: A progress report. *Journal of Geophysical Research (1896-1977)*, 80(3):291–297.

Green, J. A. M. and Nycander, J. (2013). A comparison of tidal conversion parameterizations for tidal models. *Journal of Physical Oceanography*, 43(1):104 – 119.

Haley, P. J. and Lermusiaux, P. F. J. (2010). Multiscale two-way embedding schemes for free-surface primitive equations in the "multidisciplinary simulation, estimation and assimilation system". *Ocean Dynamics*, 60:1497–1537.

He, R. and Wilkin, J. L. (2006). Barotropic tides on the southeast new england shelf: A view from a hybrid data assimilative modeling approach. *Journal of Geophysical Research: Oceans*, 111(C8).

Hendershott, M. C. (1972). The Effects of Solid Earth Deformation on Global Ocean Tides. *Geophysical Journal International*, 29(4):389–402.

Hersbach, H., Bell, B., Berrisford, P., Hirahara, S., Horányi, A., Muñoz-Sabater, J., Nicolas, J., Peubey, C., Radu, R., Schepers, D., Simmons, A., Soci, C., Abdalla, S., Abellan, X., Balsamo, G., Bechtold, P., Biavati, G., Bidlot, J., Bonavita, M., De Chiara, G., Dahlgren, P., Dee, D., Diamantakis, M., Dragani, R., Flemming, J., Forbes, R., Fuentes, M., Geer, A., Haimberger, L., Healy, S., Hogan, R. J., Hólm, E., Janisková, M., Keeley, S., Laloyaux, P., Lopez, P., Lupu, C., Radnoti, G., de Rosnay, P., Rozum, I., Vamborg, F., Villaume, S., and Thépaut, J.-N. (2020). The era5 global reanalysis. *Quarterly Journal of the Royal Meteorological Society*, 146(730):1999–2049.

Hogg, A. M., Spence, P., Saenko, O. A., and Downes, S. M. (2017). The energetics of southern ocean upwelling. *Journal of Physical Oceanography*, 47(1):135 – 153.

Hughes, C. W., Fukumori, I., Griffies, S. M., Huthnance, J. M., Minobe, S., Spence, P., Thompson, K. R., and Wise, A. (2019). Sea level and the role of coastal trapped waves in mediating the influence of the open ocean on the coast. *Surveys in Geophysics*, 40(6):1467–1492.

IOC, I. and BODC (2003). *Centenary Edition of the GEBCO Digital Atlas, published on CD-ROM on behalf of the Intergovernmental Oceanographic Commission and the International Hydrographic Organization as part of the General Bathymetric Chart of the Oceans.* British Oceanographic Data Centre, Liverpool, UK.

Iovino, D., Masina, S., Storto, A., Cipollone, A., and Stepanov, V. N. (2016). A 1/16° eddying simulation of the global nemo sea-ice–ocean system. *Geoscientific Model Development*, 9(8):2665–2684.

Jackson, L. C., Kahana, R., Graham, T., Ringer, M. A., Woollings, T., Mecking, J. V., and Wood, R. A. (2015). Global and european climate impacts of a slowdown of the amoc in a high resolution gcm. *Climate Dynamics*, 45(11):3299–3316.

Jayne, S. R. (2009). The impact of abyssal mixing parameterizations in an ocean general circulation model. *Journal of Physical Oceanography*, 39(7):1756 – 1775.

Jayne, S. R. and St. Laurent, L. C. (2001). Parametrizing tidal dissipation over rough topography. *Geophysicsl Research Letters*, 8(811-814).

Jensen, T. G., Shulman, I., Wijesekera, H. W., Anderson, S., and Ladner, S. (2018). Submesoscale features and their interaction with fronts and internal tides in a high-resolution coupled atmosphere-ocean-wave model of the bay of bengal. *Ocean Dynamics*, 68(3):391–410.

Johnson, H. L., Cessi, P., Marshall, D. P., Schloesser, F., and Spall, M. A. (2019). Recent contributions of theory to our understanding of the atlantic meridional overturning circulation. *Journal of Geophysical Research: Oceans*, 124(8):5376–5399.

Kang, D. (2012). *Energy Conservation*. InTech.

Kang, D. and Fringer, O. (2012). Energetics of barotropic and baroclinic tides in the monterey bay area. *Journal of Physical Oceanography*, 42:272–290.

Kantha, L. H. (1995). Barotropic tides in the global oceans from a nonlinear tidal model assimilating altimetric tides: 1. model description and results. *Journal of Geophysical Research: Oceans*, 100(C12):25283–25308.

Kanzow, T., Cunningham, S. A., Johns, W. E., Hirschi, J. J.-M., Marotzke, J., Baringer, M. O., Meinen, C. S., Chidichimo, M. P., Atkinson, C., Beal, L. M., Bryden, H. L., and Collins, J. (2010). Seasonal variability of the atlantic meridional overturning circulation at 26.5 °n. *Journal of Climate*, 23(21):5678 – 5698.

Käse, R. H. and Krauß, W. (1996). The gulf stream, the north atlantic current, and the origin of the azores current. In Krauß, W., editor, *The Warmwatersphere of the North Atlantic Ocean*, pages 291–337. ARRAY(0xde269f8), Berlin, Germany.

Kelly, S. M. and Lermusiaux, P. F. J. (2016). Internal-tide interactions with the gulf stream and middle atlantic bight shelfbreak front. *Journal of Geophysical Research: Oceans*, 121(8):6271–6294.

Kelly, S. M., Lermusiaux, P. F. J., Duda, T. F., and Haley, P. J. (2016). A coupled-mode shallow-water model for tidal analysis: Internal tide reflection and refraction by the gulf stream. *Journal of Physical Oceanography*, 46(12):3661 – 3679.

Killworth, P. D. (1983). Deep convection in the world ocean. *Reviews of Geophysics*, 21(1):1–26.

Koch-Larrouy, A., Madec, G., Bouruet-Aubertot, P., Gerkema, T., Bessières, L., and Molcard, R. (2007). On the transformation of pacific water into indonesian throughflow water by internal tidal mixing. *Geophysical Research Letters*, 34(4).

Kodaira, T., Thompson, K. R., and Bernier, N. B. (2016). Prediction of m2 tidal surface currents by a global baroclinic ocean model and evaluation using observed drifter trajectories. *Journal of Geophysical Research: Oceans*, 121(8):6159–6183.

Kuhlbrodt, T., Griesel, A., Montoya, M., Levermann, A., Hofmann, M., and Rahmstorf, S. (2007). On the driving processes of the atlantic meridional overturning circulation. *Reviews of Geophysics*, 45(2).

Kuhlmann, J., Dobslaw, H., and Thomas, M. (2011). Improved modeling of sea level patterns by incorporating self-attraction and loading. *Journal of Geophysical Research: Oceans*, 116(C11).

Kunze, E. (2017). The internal-wave-driven meridional overturning circulation. *Journal of Physical Oceanography*, 47(11):2673 – 2689.

Lahaye, N., Gula, J., and Roullet, G. (2019). Sea surface signature of internal tides. *Geophysical Research Letters*, 46(7):3880–3890.

Laplace, P. S. (1776). Recherches sur plusieurs points du système du monde. mémoires de l'académie royale des sciences paris. *Reprinted in Oeuvres Complètes de Laplace, Gauthier-Villars, Paris, 9 (1893)*, 89:177–264.

Le Provost, C., Bennet, A. F., and Cartwright, D. E. (1995). Ocean tides for and from topex/poseidon. *Science*, 267(5198):639–642.

Ledwell, J. R., Montgomery, E. T., Polzin, K. L., St. Laurent, L. C., Schmitt, R. W., and Toole, J. M. (2000). Evidence for enhanced mixing over rough topography in the abyssal ocean. *Nature*, 403(6766):179–182.

Legg, S. (2014). Scattering of low-mode internal waves at finite isolated topography. *Journal of Physical Oceanography*, 44(1):359 – 383.

Li, Z., von Storch, J.-S., and Müller, M. (2015). The m2 internal tide simulated by a 1/10 ° ogcm. *Journal of Physical Oceanography*, 45(12):3119 – 3135.

Löb, J., Köhler, J., Mertens, C., Walter, M., Li, Z., von Storch, J.-S., Zhao, Z., and Rhein, M. (2020). Observations of the low-mode internal tide and its interaction with mesoscale flow south of the azores. *Journal of Geophysical Research: Oceans*, 125(11):e2019JC015879. e2019JC015879 10.1029/2019JC015879.

Locarnini, R. A., Mishonov, A. V., Antonov, J. I., Boyer, T. P., Garcia, H. E., Baranova, O. K., Zweng, M. M., Paver, C. R., Reagan, J. R., Johnson, D. R., Hamilton, M., and Seidov, D. (2013). World ocean atlas 2013, volume 1: Temperature, edited by: Levitus, s. and mishonov, a. Technical Report 40, NOAA Atlas NESDIS 73, Silver Spring, MD, USA.

Lozier, M. S. (2012). Overturning in the north atlantic. *Annual Review of Marine Science*, 4(1):291–315. PMID: 22457977.

Lozier, M. S., Bacon, S., Bower, A. S., Cunningham, S. A., de Jong, M. F., de Steur, L., deYoung, B., Fischer, J., Gary, S. F., Greenan, B. J. W., Heimbach, P., Holliday, N. P., Houpert, L., Inall, M. E., Johns, W. E., Johnson, H. L., Karstensen, J., Li, F., Lin, X., Mackay, N., Marshall, D. P., Mercier, H., Myers, P. G., Pickart, R. S., Pillar, H. R., Straneo, F., Thierry, V., Weller, R. A., Williams, R. G., Wilson, C., Yang, J., Zhao, J., and Zika, J. D. (2017). Overturning in the subpolar north atlantic program: A new international ocean observing system. *Bulletin of the American Meteorological Society*, 98(4):737 – 752.

Lueck, R. G. and Mudge, T. D. (1997). Topographically induced mixing around a shallow seamount. *Science*, 276(5320):1831–1833.

Lumpkin, R. and Speer, K. (2007). Global ocean meridional overturning. *Journal of Physical Oceanography*, 37(10):2550 – 2562.

Lyard, F. H., Allain, D. J., Cancet, M., Carrère, L., and Picot, N. (2021). Fes2014 global ocean tide atlas: design and performance. *Ocean Science*, 17(3):615–649.

MacKinnon, J. A., Zhao, Z., Whalen, C. B., Waterhouse, A. F., Trossman, D. S., Sun, O. M., Laurent, L. C. S., Simmons, H. L., Polzin, K., Pinkel, R., Pickering, A., Norton, N. J., Nash, J. D., Musgrave, R., Merchant, L. M., Melet, A. V., Mater, B., Legg, S., Large, W. G., Kunze, E., Klymak, J. M., Jochum, M., Jayne, S. R., Hallberg, R. W., Griffies, S. M., Diggs, S., Danabasoglu, G., Chassignet, E. P., Buijsman, M. C., Bryan, F. O., Briegleb, B. P., Barna, A., Arbic, B. K., Ansong, J. K., and Alford, M. H. (2017). Climate process team on internal wave–driven ocean mixing. *Bulletin of the American Meteorological Society*, 98(11):2429 – 2454.

Madec, G. and the NEMO team (2016). *NEMO ocean engine - version 3.6 stable*. Note du Pole de modelisation de l'Institut Pierre-Simon Laplace No 27, issn no 1288-1619 edition.

Maraldi, C., Galton-Fenzi, B., Lyard, F., Testut, L., and Coleman, R. (2007). Barotropic tides of the southern indian ocean and the amery ice shelf cavity. *Geophysical Research Letters*, 34(18).

Marshall, J. and Radko, T. (2003). Residual-mean solutions for the Antarctic Circumpolar Current and its associated overturning circulation. *J. Phys. Oceanogr.*, 33:2341–2354.

Marshall, J. and Speer, K. (2012). Closure of the meridional overturning circulation through southern ocean upwelling. *Nature Geoscience*, 5(3):171–180.

Mashayek, A., Ferrari, R., Nikurashin, M., and Peltier, W. R. (2015). Influence of enhanced abyssal diapycnal mixing on stratification and the ocean overturning circulation. *Journal of Physical Oceanography*, 45(10):2580 – 2597.

McCarthy, G., Smeed, D., Johns, W., Frajka-Williams, E., Moat, B., Rayner, D., Baringer, M., Meinen, C., Collins, J., and Bryden, H. (2015). Measuring the atlantic meridional overturning circulation at 26°n. *Progress in Oceanography*, 130:91–111.

McWilliams, J. C. (2008). The nature and consequences of oceanic eddies. *Ocean modeling in an eddying regime*, 177:5–15.

Melet, A., Legg, S., and Hallberg, R. (2016). Climatic impacts of parameterized local and remote tidal mixing. *Journal of Climate*, 29(10):3473 – 3500.

Melet, A., Nikurashin, M., Muller, C., Falahat, S., Nycander, J., Timko, P. G., Arbic, B. K., and Goff, J. A. (2013). Internal tide generation by abyssal hills using analytical theory. *Journal of Geophysical Research: Oceans*, 118(11):6303–6318.

Müller, M. (2013). On the space- and time-dependence of barotropic-to-baroclinic tidal energy conversion. *Ocean Modelling*, 72:242–252.

Müller, M., Arbic, B. K., Richman, J. G., Shriver, J. F., Kunze, E. L., Scott, R. B., Wallcraft, A. J., and Zamudio, L. (2015). Toward an internal gravity wave spectrum in global ocean models. *Geophysical Research Letters*, 42(9):3474–3481.

Müller, M., Cherniawsky, J. Y., Foreman, M. G. G., and von Storch, J.-S. (2012). Global m2 internal tide and its seasonal variability from high resolution ocean circulation and tide modeling. *Geophysical Research Letters*, 39(19).

Müller, M., Haak, H., Jungclaus, J., Sündermann, J., and Thomas, M. (2010). The effect of ocean tides on a climate model simulation. *Ocean Modelling*, 35(4):304–313.

Munk, W. (1997). Once again: once again-tidal friction. *Progress in Oceanography*, 40:7–35.

Munk, W. and Wunsch, C. (1998). Abyssal recipes ii: energetics of tidal and wind mixing. *Deep Sea Research I*, 45:1977–2010.

Naveira Garabato, A. C., Oliver, K. I. C., Watson, A. J., and Messias, M.-J. (2004). Turbulent diapycnal mixing in the nordic seas. *Journal of Geophysical Research: Oceans*, 109(C12).

Nikurashin, M. and Legg, S. (2011). A mechanism for local dissipation of internal tides generated at rough topography. *Journal of Physical Oceanography*, 41(2):378 – 395.

Niwa, Y. and Hibiya, T. (2011). Estimation of baroclinic tide energy available for deep ocean mixing based on three-dimensional global numerical simulations. *Journal of Oceanography*, 67(4):493–502.

Nugroho, D., Koch-Larrouy, A., Gaspar, P., Lyard, F., Reffray, G., and Tranchant, B. (2018). Modelling explicit tides in the indonesian seas: An important process for surface sea water properties. *Marine Pollution Bulletin*, 131:7–18. Special Issue: Indonesia seas management.

of Commerce, U. D. (2006). 2-minute gridded global relief data (etopo2) v2.

Palmer, T. N., Shutts, G. J., and Swinbank, R. (1986). Alleviation of a systematic westerly bias in general circulation and numerical weather prediction models through an orographic gravity wave drag parameterization. *Royal Meteorological Society*.

Pan, Y., Haley, P. J., and Lermusiaux, P. F. (2021). Interactions of internal tides with a heterogeneous and rotational ocean. *Journal of Fluid Mechanics*, 920:A18.

Pereira, A. F., Castro, B. M., Calado, L., and da Silveira, I. C. A. (2007). Numerical simulation of m2 internal tides in the south brazil bight and their interaction with the brazil current. *Journal of Geophysical Research: Oceans*, 112(C4).

Pinardi, N., Cessi, P., Borile, F., and Wolfe, C. L. P. (2019). The mediterranean sea overturning circulation. *Journal of Physical Oceanography*, 49(7):1699 – 1721.

Pinardi, N., Zavatarelli, M., Adani, M., Coppini, G., Fratianni, C., Oddo, P., Simoncelli, S., Tonani, M., Lyubartsev, V., Dobricic, S., and Bonaduce, A. (2015). Mediterranean sea large-scale low-frequency ocean variability and water mass formation rates from 1987 to 2007: A retrospective analysis. *Progress in Oceanography*, 132:318–332. Oceanography of the Arctic and North Atlantic Basins.

Rainville, L. and Pinkel, R. (2006). Propagation of low-mode internal waves through the ocean. *Journal of Physical Oceanography*, 36(6):1220 – 1236.

Ray, R. D. (1998). Ocean self‚Äêattraction and loading in numerical tidal models. *Marine Geodesy*, 21(3):181–192.

Ray, R. D., Egbert, G. D., and Erofeeva, S. (2005). A brief overview of tides in the indonesian seas. *Oceanography*, 18(4).

Ray, R. D. and Mitchum, G. T. (1996). Surface manifestation of internal tides generated near hawaii. *Geophysical Research Letters*, 23(16):2101–2104.

Reef, K. R. G., Roos, P. C., Schuttelaars, H. M., and Hulscher, S. J. M. H. (2020). Influence of back-barrier basin geometry on multiple tidal inlet systems: The roles of resonance and bottom friction. *Journal of Geophysical Research: Earth Surface*, 125(3):e2019JF005261. e2019JF005261 10.1029/2019JF005261.

Rhein, M., Fischer, J., Smethie, W. M., Smythe-Wright, D., Weiss, R. F., Mertens, C., Min, D.-H., Fleischmann, U., and Putzka, A. (2002). Labrador sea water: Pathways, cfc inventory, and formation rates. *Journal of Physical Oceanography*, 32(2):648 – 665.

Robertson, R. and Ffield, A. (2008). Baroclinic tides in the indonesian seas: Tidal fields and comparisons to observations. *Journal of Geophysical Research: Oceans*, 113(C7).

Rocha, C. B., Chereskin, T. K., Gille, S. T., and Menemenlis, D. (2016). Mesoscale to submesoscale wavenumber spectra in drake passage. *Journal of Physical Oceanography*, 46(2):601 – 620.

Rosier, S. H. R., Green, J. A. M., Scourse, J. D., and Winkelmann, R. (2014). Modeling antarctic tides in response to ice shelf thinning and retreat. *Journal of Geophysical Research: Oceans*, 119(1):87–97.

Schiller, A. and Fiedler, R. (2007). Explicit tidal forcing in an ocean general circulation model. *Geophysicsl Research Letters*, 34(L03611).

Schureman, P. (1958). *Manual of Harmonic Analysis and Prediction of Tides*. United States Government Printing Office.

Shakespeare, C. J. (2020). Interdependence of internal tide and lee wave generation at abyssal hills: Global calculations. *Journal of Physical Oceanography*, 50(3):655 – 677.

Shakespeare, C. J., Arbic, B. K., and Hogg, A. M. (2020). The drag on the barotropic tide due to the generation of baroclinic motion. *Journal of Physical Oceanography*, 50:3467–3481.

Shakespeare, C. J. and Hogg, A. M. (2019). On the momentum flux of internal tides. *Journal of Physical Oceanography*, 49(4):993 – 1013.

Shchepetkin, A. F. and McWilliams, J. C. (1995). The regional oceanic modeling system (roms): a split-explicit, free-surface, topography-following-coordinate oceanic model. *Ocean Modelling*, 9:347–404.

Shihora, L., Sulzbach, R., Dobslaw, H., and Thomas, M. (2022). Self-attraction and loading feedback on ocean dynamics in both shallow water equations and primitive equations. *Ocean Modelling*, 169:101914.

Shriver, J. F., Arbic, B. K., Richman, J. G., Ray, R. D., Metzger, E. J., Wallcraft, A. J., and Timko, P. G. (2012). An evaluation of the barotropic and internal tides in a high-resolution global ocean circulation model. *Journal of Geophysical Research: Oceans*, 117(C10).

Simoncelli, S., Fratianni, C., Pinardi, N., Grandi, A., Drudi, M., Oddo, P., and Dobricic, S. (2017). Mediterranean sea physical reanalysis (medrea 1987-2015).

Srokosz, M., Baringer, M., Bryden, H., Cunningham, S., Delworth, T., Lozier, S., Marotzke, J., and Sutton, R. (2012). Past, present, and future changes in the atlantic meridional overturning circulation. *Bulletin of the American Meteorological Society*, 93(11):1663 – 1676.

St. Laurent, L. C. and Garrett, C. (2002). The role of internal tides in mixing the deep ocean. *Journal of Physical Oceanography*, 32:2882–2899.

St-Laurent, P., Saucier, F. J., and Dumais, J.-F. (2008). On the modification of tides in a seasonally ice-covered sea. *Journal of Geophysical Research: Oceans*, 113(C11).

Stacey, M. W., Pond, S., and Nowak, Z. P. (1995). A numerical model of the circulation in knight inlet, british columbia, canada. *Journal of Physical Oceanography*, 25(6):1037 – 1062.

Stammer, D., Ray, R., Andersen, O., Arbic, B., Bosch, W., Carrere, L., Cheng, Y., Chinn, D., Dushaw, B., Egbert, G., Erofeeva, S., Fok, H., Green, J., Griffths, S., King, M., Lapin, V. Lemoine, F., Luthcke, S., F., L., Morison, J., Müller, M., Padman, L., Richman, J., Shriver, J., Shum, C., Taguchi, E., and Yi, Y. (2014). Accuracy assessment of global barotropic ocean tide models. *Reviews of Geophysics*, 52(5198):243–282.

Talley, L. D. (2013). Closure of the global overturning circulation through the indian, pacific, and southern oceans: schematics and transports. *Oceanography*, 26(1).

Thomson, R. E. and Wilson, R. E. (1987). Coastal countercurrent and mesoscale eddy formation by tidal rectification near an oceanic cape. *Journal of Physical Oceanography*, 17(11):2096 – 2126.

Thorpe, S. A. (2001). Internal wave reflection and scatter from sloping rough topography. *Journal of Physical Oceanography*, 31(2):537 – 553.

Timko, P. G., Arbic, B. K., Goff, J. A., Ansong, J. K., Smith, W. H., Melet, A., and Wallcraft, A. J. (2017). Impact of synthetic abyssal hill roughness on resolved motions in numerical global ocean tide models. *Ocean Modelling*, 112:1–16.

Treguier, A. M., Theetten, S., Chassignet, E. P., Penduff, T., Smith, R., Talley, L., Beismann, J. O., and Böning, C. (2005). The north atlantic subpolar gyre in four high-resolution models. *Journal of Physical Oceanography*, 35(5):757 – 774.

Tsujino, H., Urakawa, S., Nakano, H., Small, R. J., Kim, W. M., Yeager, S. G., Danabasoglu, G., Suzuki, T., Bamber, J. L., Bentsen, M., Böning, C. W., Bozec, A., Chassignet, E. P., Curchitser, E., Boeira Dias, F., Durack, P. J., Griffies, S. M., Harada, Y., Ilicak, M., Josey, S. A., Kobayashi, C., Kobayashi, S., Komuro, Y., Large, W. G., Le Sommer, J., Marsland, S. J., Masina, S., Scheinert, M., Tomita, H., Valdivieso, M., and Yamazaki, D. (2018). Jra-55 based surface dataset for driving ocean–sea-ice models (jra55-do). *Ocean Modelling*, 130:79–139.

Vic, C., Garabato, A. C. N., Green, J. A. M., Spingys, C., Forryan, A., Zhao, Z., and Sharples, J. (2018). The lifecycle of semidiurnal internal tides over the northern mid-atlantic ridge. *Journal of Physical Oceanography*, 48(1):61 – 80.

Von Karman, T. (1931). Mechanical similitude and turbulence. *Technical memorandums National Advisory Commitee for Aeronautics*.

von Schuckmann, K., Traon, P.-Y. L., and et al. (2020). Copernicus marine service ocean state report, issue 4. *Journal of Operational Oceanography*, 13(sup1):S1–S172.

Waterhouse, A. F., MacKinnon, J. A., Nash, J. D., Alford, M. H., Kunze, E., Simmons, H. L., Polzin, K. L., Laurent, L. C. S., Sun, O. M., Pinkel, R., Talley, L. D., Whalen, C. B., Huussen, T. N., Carter, G. S., Fer, I., Waterman, S., Garabato, A. C. N., Sanford, T. B., and Lee, C. M. (2014). Global patterns of diapycnal mixing from measurements of the turbulent dissipation rate. *Journal of Physical Oceanography*, 44(7):1854 – 1872.

Winters, K. B. and Armi, L. (2014). Topographic control of stratified flows: upstream jets, blocking and isolating layers. *Journal of Fluid Mechanics*, 753:80–103.

Winton, M., Griffies, S. M., Samuels, B. L., Sarmiento, J. L., and Frölicher, T. L. (2013). Connecting changing ocean circulation with changing climate. *Journal of Climate*, 26(7):2268 – 2278.

Wolfe, C. L. and Cessi, P. (2010). What sets the strength of the middepth stratification and overturning circulation in eddying ocean models? *Journal of Physical Oceanography*, 40(7):1520 – 1538.

Wunsch, C. and Ferrari, R. (2004). Vertical mixing, energy and the general circulation of the ocean. *Annual Review of Fluid Mechanics*, 36:281–314.

Xuan, J., Yang, Z., Huang, D., Wang, T., and Zhou, F. (2016). Tidal residual current and its role in the mean flow on the changjiang bank. *Journal of Marine Systems*, 154:66–81. Changjiang (Yangtze River) Estuary and Adjacent Marine Environment.

Zalesak, S. T. (1979). Fully multidimensional flux-corrected transport algorithms for fluids. *Journal of Computational Physics*, 31(3):335–362.

Zaron, E. D. and Egbert, G. D. (2006). Estimating open-ocean barotropic tidal dissipation: The hawaiian ridge. *Journal of Physical Oceanography*, 36(6):1019 – 1035.

Zhao, Z., Alford, M. H., MacKinnon, J. A., and Pinkel, R. (2010). Long-range propagation of the semidiurnal internal tide from the hawaiian ridge. *Journal of Physical Oceanography*, 40(4):713 – 736.

Zilberman, N. V., Becker, J. M., Merrifield, M. A., and Carter, G. S. (2009). Model estimates of m2 internal tide generation over mid-atlantic ridge topography. *Journal of Physical Oceanography*, 39(10):2635 – 2651.

Zweng, M. M., Reagan, J. R., Antonov, J. I., Locarnini, R. A., Mishonov, A. V., Boyer, T. P., Garcia, H. E., Baranova, O. K., Johnson, D. R., Seidov, D., and Biddle, M. M. (2013). World ocean atlas 2013, volume 2: Salinity, edited by: Levitus, s. and mishonov, a. Technical Report 39, NOAA Atlas NESDIS 74, Silver Spring, MD, USA.